Parameter Estimation of a High-Voltage Transformer using Pseudo-Random Impulse Sequence Perturbation

Daniel Marc Banks

Thesis presented in partial fulfilment of the requirements for the degree of
Master of Engineering (Electrical) in the Faculty of Engineering at
Stellenbosch University.

Supervisors: Mr J.C. Bekker & Prof. H.J. Vermeulen
Department of Electrical and Electronic Engineering

December 2022

Acknowledgements

I want to thank my family for their constant support throughout my research, most of all my mother, Marietjie Banks, for her endless check-ins and phone calls and without whom I would not be the man I am today. I would like to thank my friends for their words of encouragement and distractions whenever I needed them. I want to thank my supervisors Mr J.C. Bekker and Prof. H.J. Vermeulen as well as my unofficial ”supervisor”, Dr F.M. Mwaniki for the hours of dedication, guidance and meetings throughout the past 18 months. Finally, I would like to thank my research partner (and friend) Ian Gerber for the endless interesting debates and discussions regarding our research and for being a trustworthy voice of reason.

Plagiaatverklaring / *Plagiarism Declaration*

1. Plagiaat is die oorneem en gebruik van die idees, materiaal en ander intellektuele eiendom van ander persone asof dit jou eie werk is.
   Plagiarism is the use of ideas, material and other intellectual property of another's work and to present is as my own.
2. Ek erken dat die pleeg van plagiaat 'n strafbare oortreding is aangesien dit 'n vorm van diefstal is.
   I agree that plagiarism is a punishable offence because it constitutes theft.
3. Ek verstaan ook dat direkte vertalings plagiaat is.
   I also understand that direct translations are plagiarism.
4. Dienooreenkomstig is alle aanhalings en bydraes vanuit enige bron (ingesluit die internet) volledig verwys (erken). Ek erken dat die woordelikse aanhaal van teks sonder aanhalingstekens (selfs al word die bron volledig erken) plagiaat is.
   Accordingly all quotations and contributions from any source whatsoever (including the internet) have been cited fully. I understand that the reproduction of text without quotation marks (even when the source is cited) is plagiarism
5. Ek verklaar dat die werk in hierdie skryfstuk vervat, behalwe waar anders aangedui, my eie oorspronklike werk is en dat ek dit nie vantevore in die geheel of gedeeltelik ingehandig het vir bepunting in hierdie module/werkstuk of 'n ander module/werkstuk nie.
   I declare that the work contained in this assignment, except where otherwise stated, is my original work and that I have not previously (in its entirety or in part) submitted it for grading in this module/assignment or another module/assignment.

Abstract

Transformers are essential devices to the power system. Transformer applications include transmission services, monitoring of line voltages and currents, and distribution services. High-voltage test transformers are commonly used in environments when high voltages are required to test power system equipment. Due to the cost of large transformers and their importance to the power system, it is essential to monitor their health and condition to ensure nominal grid operation. Access to an equivalent-circuit model that represents the physical construction of the transformer aids in condition monitoring and identifying the location of faults. Due to the proliferation of renewable generation, there are increased harmonics in the power system. Therefore, there is a growing need for equivalent-circuit models that provide physical representation and accuracy over a wide range of frequencies. System identification can be applied to transformers to develop wideband equivalent-circuit models from measured data. In this project, a methodology for determining wideband models for transformer windings and a high-voltage test transformer is presented.

The Pseudo-Random Impulse Sequence (PRIS) signal is a wideband excitation signal for system identification in the power system environment. The PRIS perturbation arrangement is applied to two cascaded transformer winding models in simulation. Successful offline perturbation of transformer winding models with the PRIS signal is verified through good correlations between the simulated and analytically derived frequency responses of the input impedance and voltage ratios. The performance of various optimisation algorithms are investigated and compared. The algorithms are applied to various approaches, namely, frequency-domain, time-domain, or modal decomposition, in combination with various cost function formulations. It is found that although the time-domain and modal decomposition approaches perform superior, frequency-domain estimation that makes use of the model's frequency responses derived analytically is the most computationally efficient.

A PRIS source is built and subsequently applied to perturb a practical 7.5kVA, 230V/100kV high-voltage test transformer. The transformer measurements show minimal noise up to 20kHz. Four equivalent-circuit model topologies are investigated to identify a suitable model and associated parameters that best reproduces the transformer measurements. It is found that a single-section low-voltage winding and a six-section high-voltage winding model topology are of a high enough order to represent the number of observed resonances up to 10kHz. The measured frequency responses and estimated frequency responses produced by the model show a good correlation, with discrepancies below 1kHz due to the lack of any frequency-dependent model parameters.

Uittreksel

Transformators is baie belangrike toestelle in die kragstelsel, en word gebruik vir transmissie doeleindes, om lyn spannings en fout strome te meet, en ook vir distrubisie doeleindes. Hoogspannings transformators word oor die algemeen gebruik in omgewings waar hoë-spannings benodige word om kragstelsel toerusting te toets. Omdat groot transformators duur is en 'n belangrike komponent in die kragstelsel is, is dit belangrik om transformators deurgaans te monitor om nominale werking te verseker. Toegang tot die ekwivalente stroombaan model wat die fisiese bou van die transformator beskryf help om die kondisie van transformators te monitor en foute binne die transformator te vind. As gevolg van die verspreiding van hernubare opwekking, is daar verhoogde harmonieke in die kragstelsel. Daarom is daar 'n groeiende behoefte aan ekwivalente stroombaanmodelle wat nie net fisiese voorstelling verskaf nie, maar wat ook akkuraatheid oor 'n wye reeks frekwensies verskaf. Stelselidentifisering kan toegepas word om transformators te beskryf deur wyeband modelle te onwtikkel. In hierdie projek word 'n metode om akkurate modelle vir transformator windings en 'n hoogspannings toets transformator voorgestel.

Die Pseudo-Lukrake Impuls Volgorde (PLIV) sein is 'n breëband opwekkings sein wat vir stelsel bepalings studies gebruik kan word in die kragtselsel. Die PLIV opwekking stelsel is aangewend op twee kaskade winding transformator modelle in simulasie. Suksesvolle vanlyn perturbasie van die transformator windings met die PLIV sein is geverifieer deur goeie korrelasie tussen die gesimuleerde en analitiese frekwensie uittrees van die intree impedansie en spannings verhoudings. Die optrede van verskeie optimiserings algoritmes word ondersoek en vergelyk. Die algoritmes word toegepas op verskeie benaderings, naamlik frekwensie-domein, tyd-domein en modale ontbinding, tesame met verskeie koste funksie samestellings. Dit is bevind dat alhoewel die tyd-domein en modale ontbinding benaderings beter presteer, die analities berekende frekwensie-domein oordragfunksies van die model meer koste effektief is.

'n PLIV bron is en daarna aangewand om 'n 7.5kVA, 230V/100kV hoogspannings toets transformator te versteur. Die metings van die transformator toon minimale geraas tot 20kHz. Vier ekwivalente stroombaanmodel topologieë is ondersoek om die mees gepaste model en bypassende parameters te verkry. Dit is bevind dat 'n enkel-seksie lae-spanning winding en ses-seksie hoë-spannings winding model topologie van 'n hoog genoeg orde is om die aantal waargeneemde resonansies tot 10kHz voor te stel. Die gemete frekwensie gedrag en afgeskatte frekwensie gedrag vanaf die model toon goeie korrelasie, met verskille onder 1kHz wat volg uit die tekort aan frekwensie-afhanklike parameters.

Publications

This research has generated the following publications:

- D. M. Banks, J. C. Bekker, and H. J. Vermeulen, “Parameter estimation of a two-section transformer winding model using pseudo-random impulse sequence perturbation,” in *2021 56th International Universities Power Engineering Conference (UPEC)*, 2021, pp. 1–6.
- D. M. Banks, J. C. Bekker, and H. J. Vermeulen, “Parameter estimation of a three-section winding model using intrinsic mode functions,” in *2022 IEEE International Conference on Environment and Electrical Engineering and 2022 IEEE Industrial and Commercial Power Systems Europe (EEEIC / I&CPS Europe)*, 2022, pp. 1–6.

Contents

List of Figures

List of Tables

Nomenclature

Acronyms and abbreviations

SQP	Sequential Quadratic Programming
MMF	Magnetomotive Force
HV	High Voltage
LV	Low Voltage
HVOC	High-Voltage Open-Circuit
HVSC	High-Voltage Short-Circuit
LVOC	Low-Voltage Open-Circuit
LVSC	Low-Voltage Short-Circuit
LVHV	Low-Voltage to High-Voltage
HVLV	High-Voltage to Low-Voltage
DUT	Device Under Test
PSD	Power Spectral Density
DFT	Discrete Fourier Transform
PRIS	Pseudo-Random Impulse Sequence
SNR	Signal-to-Noise Ratio
PRBS	Pseudo-Random Binary Sequence
LFSR	Linear Feedback Shift Register
MSE	Mean Squared Error
MAE	Mean Absolute Error
RMSE	Root Mean Squared Error
MAPE	Mean Absolute Percentage Error
NRMSE	Normalised Root Mean Squared Error
EMD	Empirical Mode Decomposition
IMF	Intrinsic Mode Function
EEMD	Ensemble Empirical Mode Decomposition
PCB	Printed Circuit Board
FPGA	Field Programmable Gate Array
PWM	Pulse-Width Modulated
IEMD	Inferred Empirical Mode Decomposition
GA	Genetic Algorithm
PSO	Particle-Swarm Optimisation
iIMF	inferred Intrinsic Mode Function
HPC	High Performance Computing cluster
ADC	Analogue-to-Digital Converter
LPF	Low-Pass Filter
WNRMSE	Weighted Normalised Root Mean Squared Error

Chapter 1

Introduction

This chapter presents some background on the importance of transformers and transformer modelling, leading to the motivation for the research. The chapter continues by presenting the project objectives and concludes by presenting the structure of the chapters to follow.

1.1. Project motivation and description

Transformers are essential devices to the power system, for industrial applications as well as residential electrical consumers. The use of transformers dates back to the late 1800s and its applications have only broadened since then [1]. The power system makes use of an extensive number of power transformers in the transmission system, voltage and current transformers to monitor the line currents and voltages for protection purposes as well as distribution transformers for supply to residential zones [2]. High-voltage test transformers are commonly operated in step-up mode and used in an environment when high voltages are required to test power system equipment such as transmission cables, insulation and transformers [3]. The cost of large transformers and their contribution to the power system makes it an important task to ensure the health and safety of these devices. Having access to accurate equivalent-circuit models of transformers can provide insight into the processes that take place within the device as well as improve the simulation accuracy in cases where the transformer behaviour needs to be investigated.

The need for accurate wideband equivalent-circuit transformer models is further motivated by the rise of renewable generation in the power system. The harmonics introduced by inverter-based renewables mean that transformers are being operated at voltages with a high level of high-frequency harmonic content [4]. Being able to model the transformer for wideband harmonic frequencies aids in understanding the effect these harmonics have on transformer operation.

System identification is the field of study whereby mathematical models are developed to represent systems using measurements of the relevant system's input and output signals [5]. This area of research has been applied extensively in the field of power system equipment for transient studies, frequency response analysis, fault detection and condition monitoring [6–9].

The system identification process consists of the following steps [5]:

1. **Measure and retrieve information from the target system:** This can be done from nominal system operation or through wideband excitation of the system.
2. **Choose a model structure that best represents the target system:** A mathematical modelling approach is adopted whereby a model structure is chosen and then represented analytically in terms of the model parameters.
3. **Estimating the model's unknown parameters:** This is most commonly done through an optimisation algorithm that minimises a cost function that represents the difference between the outputs of the target system and the outputs generated from the model.
4. **Validate the model:** Once the model parameters have been selected the validation step assesses how well the model represents the system. The model may be inaccurate due to an inappropriate model structure choice, or insufficient system perturbation such that the recorded measurements do not reflect the true responses of the system or the optimisation was unable to solve for the parameters [10].

This research pays specific attention to the first three steps in the system identification process. The following summarises the application of the first three steps within the context of this research:

1. **Measure and retrieve information from the target system:** Many wideband perturbation signals have been developed and implemented in literature for exciting transformers over a wide frequency range, including the swept sine and Pseudo-Random Binary Sequence (PRBS) [11–14]. The Pseudo-Random Impulse Sequence (PRIS) is a wideband perturbation signal recently introduced by Mwaniki *et al.* [15] that can be generated efficiently and provides high degrees of controllability within the power system environment. The original intent of the signal is to be used for *in situ*, i.e. online, excitations. However, the aim of this research is to investigate the application of the PRIS signal as a suitable source of perturbation to obtain wideband measurements of transformers and transformer winding models in an offline perturbation arrangement.
2. **Choose a model structure that best represents the target system:** Modelling a transformer typically consists of a topology of circuit elements that attempt to reproduce the electromagnetic behaviour that exists within the core and windings, as well as their interactions with one another [16]. The basic equivalent-circuit model is not sufficient to model the responses of a transformer at high frequencies.

Some approaches propose models that adapt the basic equivalent-circuit to be suited to wideband applications [17, 18]. Other approaches begin by modelling a single winding and extend these models by including core effects and additional windings to arrive at a complete transformer model [11, 14]. The latter approach makes strong efforts to ensure the physical interpretability of the circuit elements of the model for diagnostic and condition monitoring purposes. This research makes an effort to apply the PRIS perturbation to transformer winding models in simulation prior to practical implementation. The model topologies used in simulations are mathematically derived and used to validate the PRIS perturbation simulations. Finally, various case studies are performed to identify a suitable model topology for a 7.5kVA, 230V/100kV high-voltage test transformer.

3. **Estimating the model's unknown parameters:** Various methodologies have been proposed for estimating the parameters of wideband transformer models. Keyhani *et al.* [8] performed maximum likelihood estimation on a six-section transformer winding model. Unique solutions could only be estimated if the initial values are close to the target values, or if sectional voltage measurements were included. Brozio *et al.* [19] used a constrained Sequential Quadratic Programming (SQP) optimisation algorithm to estimate the parameters of a two-winding distribution transformer from measured frequency responses. Time-domain signals were not employed due to computational limitations and the overall simplicity of representing the frequency responses analytically. In a more recent contribution, Chanane *et al.* [14, 20, 21] applied metaheuristic optimisation algorithms to estimate the parameters of a fully interleaved continuous-disc winding. This research considers various optimisation algorithms using frequency-domain, time-domain, or modal decomposition approaches to determine the parameter estimation procedures that supply reliable and computationally efficient results for determining the parameters of transformer windings and two-winding transformer models.

1.2. Project objectives

The project comprises two main objectives. The first is to use the PRIS signal in simulation to perform perturbation and parameter estimation. The second objective is to apply the arrangement and results from the simulated findings to a practical environment. This gives rise to the following research objectives:

- **Literature review:** Perform a literature review to determine the topologies and transformer modelling approaches for wideband characterisation. To review signal processing techniques and understand the spectral properties of perturbation signals. Finally, to present various optimisation algorithms and cost function formulations to perform parameter estimation.

- **Simulated perturbation:** Perform simulations using the PRIS perturbation arrangement on transformer winding models for the purpose of validating the PRIS signal as well as to gain insight into the excitation of transformer winding models in an offline perturbation arrangement.
- **Parameter estimation approaches:** Following perturbation, the parameter estimation process is investigated through the use of various optimisation algorithms and measurement approaches. These approaches use either time-domain data, frequency-domain data, or a method of modal decomposition to estimate the parameters of a transformer winding model. These approaches are investigated to determine a suitable optimisation methodology for practical implementation.
- **PRIS source hardware design:** The source design is a collective effort amongst three research students. All constituents of the source are discussed and detail is provided for the hardware sections that were designed as part of this project. The source is validated by comparing the measured perturbation voltage and current for a simple load to the expected simulation outputs.
- **Practical perturbation:** The source is used to perturb a 7.5kVA, 230V/100kV high-voltage test transformer, the measurement equipment and perturbation arrangement is discussed as well as the solutions to challenges encountered during testing. A total of six frequency-domain measurements are recorded for subsequent use in characterisation and parameter estimation.
- **Characterisation and parameter estimation of a high-voltage transformer:** Derive an equivalent circuit that is able to reproduce the frequency responses measured from the high-voltage transformer. This involves selecting or developing a model with a high enough order to match the number of resonant points within the measurements and then performing parameter estimation to identify the parameters such that the frequency responses of the model and measurements match.

1.3. Thesis structure

The remainder of the thesis is structured as follows:

- **Chapter 2:** Chapter 2 presents the literature review relevant to the research area within this thesis. Different transformer models are presented, followed by an overview of perturbation signals and their spectral properties. Finally, various cost function formulations, optimisation algorithms, and empirical mode decomposition are discussed as they pertain to parameter estimation.

- **Chapter 3:** Chapter 3 describes the hardware specifications and design methodology for a PRIS source. The source is subsequently validated against a simulated PRIS arrangement.
- **Chapter 4:** Chapter 4 focuses on implementing PRIS perturbation arrangements on two transformer winding models in simulation. The analytical expressions for the input impedances are derived and used to validate the success of the PRIS perturbation. The first model makes use of the simulated perturbations to obtain model parameters based on frequency-domain responses, whilst the second model is made more complex to mimic a more practical environment. The simulations are subsequently used in frequency-domain, time-domain, and modal decomposition parameter estimation methodologies, and the results are critically interpreted.
- **Chapter 5:** Chapter 5 outlines the implementation of the PRIS source to excite a practical high-voltage test transformer. The frequency-domain measurements are presented and used to identify a suitable model. The parameter estimation methodology is presented and applied to three case studies, wherein the results are presented and discussed.
- **Chapter 6:** Chapter 6 concludes the thesis by summarising the conclusions that can be drawn from the results presented in Chapters 3 through 5. The chapter is concluded by providing recommendations for further avenues of research.

Chapter 2

Literature Review

The literature study consists of four sections. The first section summarises the transformer models used in past research along with the advantages and drawbacks of each. Section two presents the theory of spectral estimation to extract the relevant frequency-domain information. The third section focuses on common perturbation signals used in the characterisation and system identification of power system equipment. Section four concludes the chapter by discussing some common cost function formulations, optimisation algorithms and describes the process of empirical mode decomposition.

2.1. Transformer models

This section provides an overview of transformer models and transformer model structures, the models are divided into three subsections. It begins with the basic low-frequency transformer model, followed by wideband models with similar topologies to the low-frequency model with some adaptations, and finally, models that cater to the higher order resonances as often observed in wideband transformer frequency responses.

2.1.1. Basic transformer model

The most basic form of the transformer equivalent circuit is shown in Fig. 2.1, this is commonly used for the simulation and modelling of the low-frequency and steady-state responses of a transformer. The low-frequency model extends the concepts of an ideal transformer by including the following practical corrections [22]:

- The windings have resistance and thus I^2R losses, the real losses in the winding are represented by parameters R_1 and R_2.
- The core permeability, μ_c, is finite and thus an exciting Magnetomotive Force (MMF) is required to establish the mutual flux linking the primary and secondary windings of the transformer. The exciting current of the core, I_e, is represented by a shunt inductance L_m in parallel with a core-loss resistance R_c.

- The magnetic flux, Φ_c, is not entirely confined to the core. The leakage flux is accounted for through the leakage inductances L_1 and L_2.

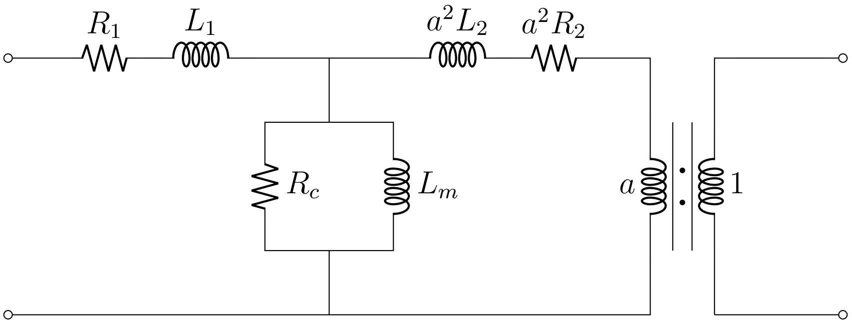

Figure 2.1: The basic low-frequency equivalent-circuit transformer model.

It is important to note that the representation of the excitation branch by linear circuit elements, is an approximation. In practical transformers, the excitation current is determined by the physical characteristics of the core material which is saturable and exhibits hysteric properties. The permeability of the core, μ_c is dependent on the applied MMF and is time-varying due to the hysteresis curve of the material. This implies that the inductance L_m varies with the saturation of the core material [19, 23]. Thus, to apply a linear approximation of the magnetizing inductance an effective value for the core permeability, μ_c, and thus inductance L_m is required. The resistance, R_c, accounts for the losses within the core due to frequency-dependent hysteresis and eddy-currents [18, 23].

The values of both R_c and L_m are traditionally determined at rated voltage and frequency and assumed to remain constant. It is therefore limited to representing the transformer in the regions around the operating point where these effective values were determined [18, 19, 23]. In practice, the parameters of this model can be determined by performing the open-circuit and short-circuit tests on the transformer at rated frequency.

2.1.2. Basic transformer model adapted for wideband applications

If a transformer is analysed at a higher than rated frequency, the capacitances between the windings, the windings to ground, and inter-turn become important. The inter-turn capacitance and winding to ground capacitance are shown graphically in Fig. 2.2.

If each capacitance associated with a single turn in the transformer is modelled the model topology becomes large and complex to solve. Thus lumped representations of these capacitances are added to the basic low-frequency equivalent-circuit model to adapt it to modelling transformers in the harmonic frequency range, where typical power quality measurements are taken up until the 40^{th} or 63^{rd} harmonic [13, 17, 19, 24–26].

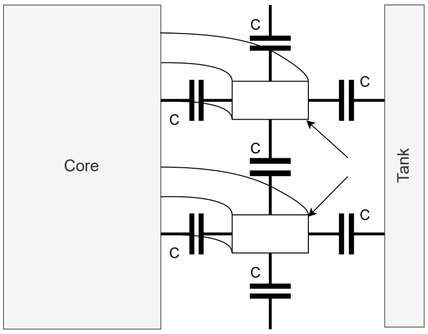

Figure 2.2: Graphical representation showing the internal winding capacitances as often included in transformer models for wideband applications [17].

Fig. 2.3 shows the adapted model, where the solid lines represents the model as presented by Slemon [27] and the dashed lines represents the additional components summarised by Aponte *et al.* [17]. The capacitance C_{12} is included as the inter-winding capacitance. Capacitors C_{g1} and C_{g2} are referred to by Brozio [19] as lumped representations of both the inter-turn and winding-to-ground capacitance. Whilst Aponte *et al.* [17] represented the lumped inter-turn capacitance by the capacitors C_{s1} and C_{s2}, and represented the capacitance associated with the magnetic core sheets by the capacitor C_m. Capacitors C_{12}, C_{s2}, and C_{g2} are related to the secondary winding of the transformer, however, are all transformed to the primary side to facilitate analysis of the equivalent circuit.

Vermeulen *et al.* [13] used the model represented by the solid lines in Fig. 2.3 as a basis to predict the voltage transformation ratio in the frequency range of 100Hz to 10kHz for a 110V/11kV step-up transformer. The results for the step-up transformer show good correlation up to 10kHz. Olivier *et al.* [25] used a cascaded connection of the model shown in Fig. 2.3 to predict the frequency response of a cascaded connection between two 440V/110kV high-voltage transformers and reported good results up to 1.5kHz.

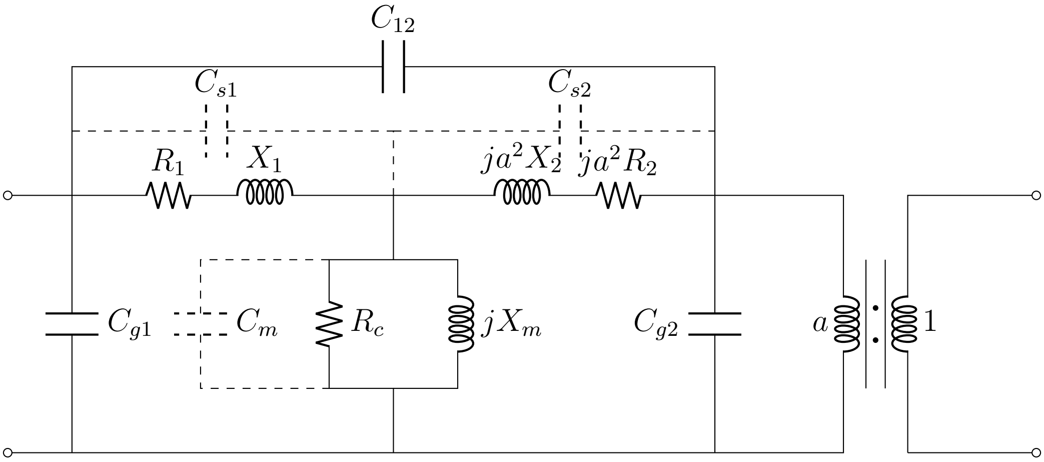

Figure 2.3: The basic transformer model adapted for wideband applications [17, 27].

Douglass [18] proposed a frequency-dependent transformer equivalent-circuit model, where the linear circuit elements of the basic model are replaced by a frequency-dependent non-linear impedance, Z_e, as shown in Fig. 2.4. This model aims to more accurately represent the non-linear hysteric properties of the core.

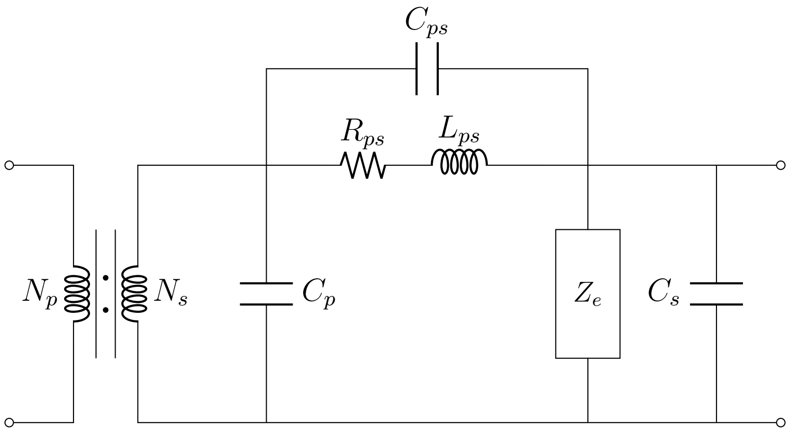

Figure 2.4: The basic transformer model adapted for wideband applications and non-linear core [18].

The following expression was derived for the frequency-dependent impedance Z_e [18],

$$Z_e = k_r\sqrt{f} + jk_x\sqrt{f}, \tag{2.1}$$

where k_r and k_x are constants and f is the frequency in hertz. The primary and secondary leakage inductance and winding resistance are lumped to form L_{ps} and R_{ps}. All circuit elements have been referred to the secondary terminal of the transformer. Douglass investigated the accuracy of the model on the PT48 General Electric Type JVM-3 and PT725 Westinghouse Type PTOM-110 voltage transformers. Douglass reported a good correlation between experimental and modelled frequency responses up to 100kHz for both transformers.

Brozio [19] tested the model presented in Fig. 2.4 on a 16kVA, 22kV/240V distribution transformer. Fig 2.5 shows the measured low-voltage open-circuit input impedance of the test distribution transformer compared to that of the model proposed by Douglass. From this, it is concluded that the model order is too low to represent the minor winding resonances of the input impedance measurements. The model is however able to represent the general trend of the distribution transformer frequency responses. This is illustrated in Fig. 2.5, which shows the measured low-voltage open-circuit input impedance of the 16kVA distribution transformer as compared to the simulated model proposed by Douglass [18].

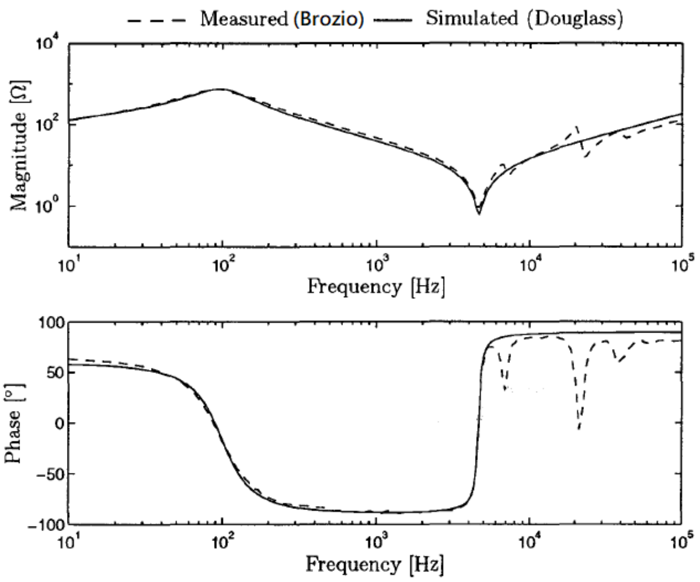

Figure 2.5: Low-voltage open-circuit input impedance of the 16kVA distribution transformer, measured by Brozio, compared to the model proposed by Douglass [19].

2.1.3. Winding-section based transformer models

The modelling approaches discussed in this section use the model of a single transformer winding and then adapt it to include additional windings to model an entire transformer. These winding models cater to the distributed nature of the inductive, resistive, and capacitive elements that constitute each turn of a transformer winding. The equivalent-circuit shown in Fig. 2.6 has been used extensively in literature to model transformer windings [14, 20, 21, 28–31].

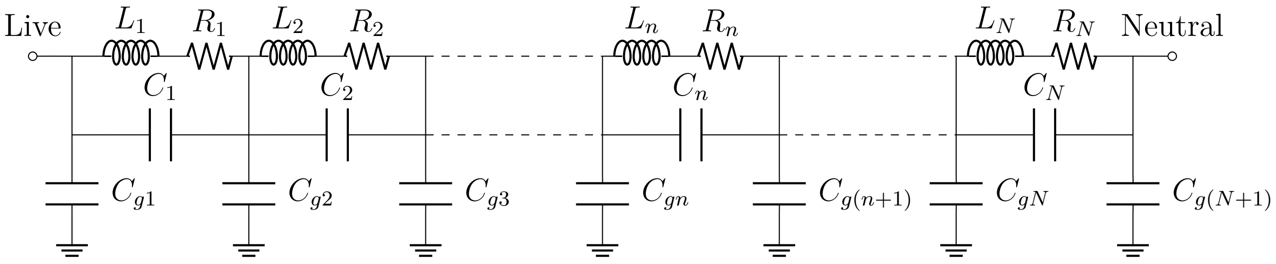

Figure 2.6: A general cascade equivalent-circuit of a transformer winding [19].

In its most physically representative form the circuit describes the transformer winding on a turn-by-turn basis. The n^{th} turn, representing a single section of the equivalent circuit, is mutually coupled to all other turns and consists of series resistive and inductive elements L_n and R_n, whilst provision is also made for the inter-turn capacitance, C_n, as well as the capacitance between each turn and ground, C_{gn}.

Thus, a transformer winding with N turns should ideally be represented by a cascade equivalent circuit with N sections. This method is however impractical and would require large and complex computations to solve for the model parameters.

This model can be simplified by assuming every turn of the winding is identical, thus all N sections could be lumped into a single section to represent the winding. Practical winding turns are, however, not all uniform and are commonly made up of sets of disks or layers. This assumption will, therefore, not capture all the major resonances of the transformer response [32]. Within the winding structure, it is possible to find degrees of uniformity amongst layers or discs that can be lumped together as a single section. In this way, the cascade model can represent all the transformer winding resonances and still be computationally possible to simulate and solve within a reasonable period of time.

The general analytical expression of the input impedance in the Laplace domain for the cascade circuit with N sections when the neutral terminal is open and when the neutral terminal is grounded is respectively given by [28]:

$$Z_i(s) = \frac{n_{2N}s^{2N} + n_{2N-1}s^{2N-1} + ... + n_2s^2 + n_1s + n_0}{d_{2N+1}s^{2N+1} + d_{2N}s^{2N} + ... + d_3s^3 + d_2s^2 + d_1s}, \tag{2.2}$$

and

$$Z_i^{'}(s) = \frac{n^{'}_{2N-1}s^{2N-1} + n^{'}_{2N-2}s^{2N-2} + ... + n^{'}_2s^2 + n^{'}_1s + n^{'}_0}{d^{'}_{2N}s^{2N} + d^{'}_{2N-1}s^{2N-1} + ... + d^{'}_2s^2 + d^{'}_1s + d^{'}_0}. \tag{2.3}$$

The input impedance, $Z_i(s)$, consists of $2N$ numerator coefficients and $2N+1$ denominator coefficients, whilst $Z_i^{'}(s)$ consists of $2N-1$ numerator coefficients and $2N$ denominator coefficients. Mukherjee *et al.* [28] attempted to generalise the analytical driving-point impedance expression in (2.2) and (2.3) in terms of the model's circuit elements. The proposed method is able to synthesize a network to obtain its unique parameters up to six sections. However, the constraints of the method require the winding resistances, self-inductances, inter-turn capacitances, and capacitances from the turns to ground to be assumed identical from section to section. The practical implementation of the method has limitations as the above-mentioned constraints are not always practically guaranteed. For instance, the resistance and self-inductance of each turn within the winding are not necessarily equal due to the turns getting longer as they are wound from layer to layer. The distance from the grounded tank or core to the winding layers are not precisely equal, thus the capacitance from turns to ground could vary.

Chanane *et al.* [14,20,21] used the model in Fig. 2.6 and the same constraints as Mukherjee *et al.* [28] to investigate various methods to solve for the model parameters based on measurements from transformer windings. In all experiments, the input impedance, as well as DC resistance, equivalent inductance, and effective capacitance measurements, were taken and then applied to optimisation techniques to solve for the model parameters.

Particle swarm [33], crow-search [34], grey-wolf [35], genetic algorithm [36] and simulated annealing [37] optimisation algorithms were investigated and produced successful model parameters for the windings under investigation. The model is once again limited in practice due to the constraints imposed on the model.

Keyhani *et al.* [29] developed a methodology to estimate the parameters of the model shown in Fig. 2.6 based on maximum likelihood estimation. In the investigations, Keyhani makes use of an impedance analyser and then transforms the frequency domain data into a time-domain step-response to estimate the parameters of a six-section winding model. The author reported that the optimisation tended to converge to a local minima basin, halting its computations. The author concluded that unique model parameters could only be determined if the initial points were selected close to the final values or if inter-sectional voltage measurements were included in the estimation procedure. Converging to a local minima is a persistent downfall even in modern optimisation algorithms when the search space is complex and contains many local minima [38].

Ragavan *et al.* [39] investigated the use of the model shown in Fig. 2.6 to identify the physical location of changes in a transformer winding. The DC resistance, equivalent inductance, and effective capacitance were measured at the terminals of the transformer, as was done by Chanane *et al.* [14]. An initial voltage distribution constant was obtained from the winding's design details, and subsequently, the input impedance was produced using a swept sine signal. With these measurements Ragavan first determined the number of sections the model topology required to represent the impedance frequency response and then solved for its parameters. Several authors have concluded that determining the required number of sections to represent the frequency response can be done by inspecting the driving-point impedance and selecting N as equal to the number of observed parallel resonances [19, 40, 41]. Ragavan *et al.* [39] highlights the fact that the resonances are not always observable at higher frequencies due to the damping caused by the skin-effect or the misinterpretation of noisy measurements as resonant points.

A two-winding transformer model can be formed by combining two cascade equivalent circuits and introducing lumped inter-winding capacitance between the sections as shown in Fig. 2.7 [8, 12, 42]. This model is particularly appropriate for modelling transformers at higher frequencies where the effects of core losses and core non-linearity have a smaller effect on the transformer responses [8, 43, 44].

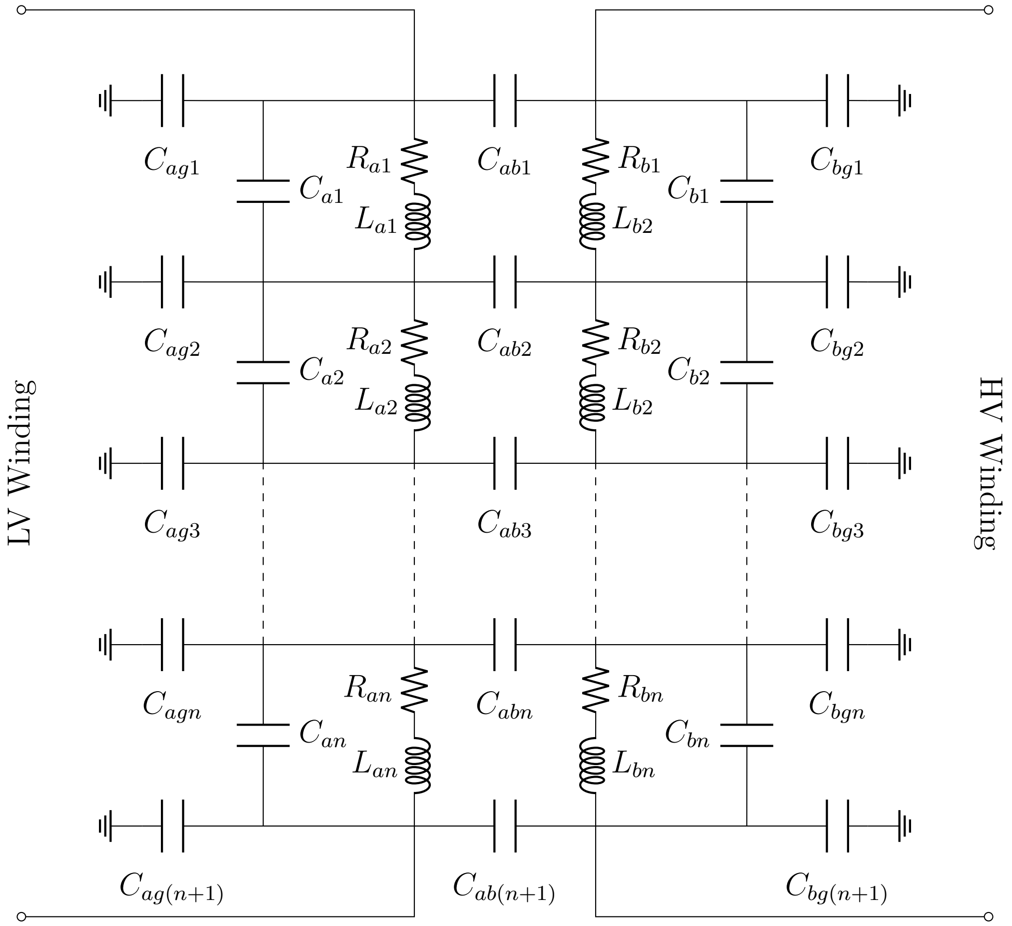

Figure 2.7: Two-winding transformer circuit formed by combining two cascade winding models.

Kheyani *et al.* [8] applied the same methodology as in an earlier contribution [29] to estimate the parameters of the model in Fig. 2.7 by fitting the model response to that of a 15kVA, 7.62kV/240V single-phase distribution transformer. The frequency responses of the physical transformer were reported up to 100kHz and exhibited a low order as only two parallel resonances are observed. Due to this, the transformer model only requires a single low-voltage section and a single high-voltage section with the inclusion of a current-controlled voltage source in each section to model the core losses and magnetizing branch. This model topology gives rise to 8 parameters in the model to be estimated. Keyhani *et al.* [12] investigated the effects of parameter initialisation on the parameter estimation methodology in simulation from a previously known set of two-winding transformer model parameters. The model in this investigation consisted of two sections per winding of the form shown in Fig. 2.7. The authors assumed identical sectional parameters for the two windings, allowing them to create a lumped parameter equivalent model and solve for the parameters using low to mid-frequency data. Once these parameters were identified, the lumped model was separated into sections, and the parameters influencing the mutual coupling between sections were identified using high-frequency data. The authors are unclear as to the frequency bands they use for each step, however, the results are reported up to 1MHz. In their investigation, the model topology in conjunction with the assumptions of identical winding sections results in a total of 16 model parameters to be estimated. The authors report that if sectional voltages of the winding are available, then the parameter estimation procedure is less dependent on the initial choice of parameters.

Brozio *et al.* [11, 19] proposed a new wideband lumped-parameter equivalent-circuit model for two-winding distribution transformers, presented in Fig. 2.8. The authors developed this model such that the parameters can be closely related to the physical elements of the transformer structure. Capacitor C_{a10} is a lumped representation of the Low-Voltage (LV) inter-turn capacitance as well as the capacitance between the LV winding and earth, and C_{ab1} is a lumped representation of the inter-winding capacitance. The core losses are approximated by coupling R_c to the winding inductances L_{a1}-L_{b4} through the inductor L_c. Capacitors C_{b1}-C_{b4} and C_{b12} are lumped inter-turn capacitances whilst C_{b10} is included to represent the capacitance between the HV winding and earth. Lastly, capacitor C_{b34} is a lumped representation of both the inter-turn capacitance and capacitance to earth.

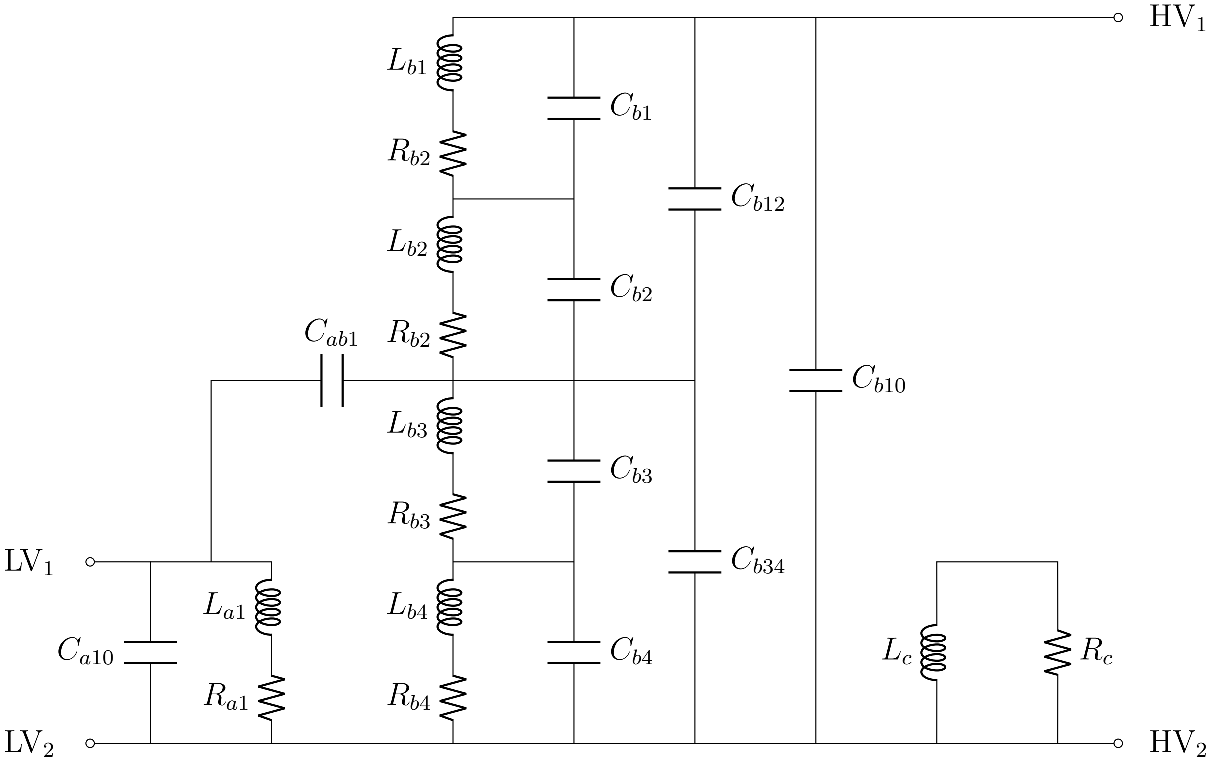

Figure 2.8: Wideband lumped-parameter equivalent-circuit model for two-winding transformers proposed by Brozio [11].

The model order is high enough to represent the frequency response measurements of a 16kVA, 22kV/240V distribution transformer. The self-inductance L_c was fixed in experimental validation as it only serves to couple the core-loss resistance to the winding inductances. The coupling coefficients linking the transformer windings to the core-loss resistance were assumed to be equal for all winding sections, which in practice is not necessarily the case, however computational limitations justified the simplification of the model parameters.

The authors required six measurements to determine the model parameters successfully, namely four input impedance measurements and two voltage transformations. The four input impedances are, High Voltage (HV) winding input impedance with Low Voltage (LV) terminal Open-Circuited (HVOC), HV winding input impedance with LV terminal Short-Circuited (HVSC), LV winding input impedance with HV terminal Open-Circuited (LVOC), and LV winding input impedance with HV terminal Short-Circuited (LVSC). The voltage transformation ratios are taken from both terminals, namely, from the LV terminal to HV terminal (LVHV) and from the HV terminal to LV terminal (HVLV).

Fig. 2.9a presents the measured LVOC input impedance of the transformer and the simulated frequency response of the model topology shown in Fig. 2.8 with linear parameters. The frequency responses closely match above 1kHz.

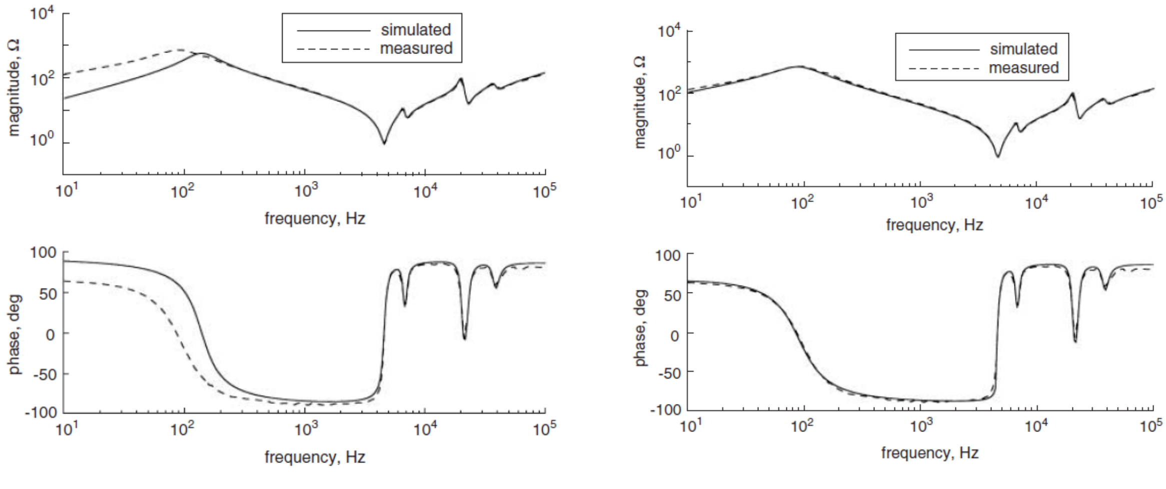

(a) **(b)**

Figure 2.9: Measured LVOC input impedance of the 16kVA distribution transformer compared to the simulated of the **(a)** linear model and **(b)** non-linear model proposed by Brozio [11]

The low-frequency error between the simulated and measured frequency response is attributed by the authors to the non-linear effects of the core that are not taken into account when using linear model parameters [11, 18]. To remedy this, the core resistance R_c is replaced by a frequency-dependent equation [11]:

$$R_c(f) = \frac{a_{Ro} f}{f + b_{Ro}}, \tag{2.4}$$

where a_{Ro} and b_{Ro} are constants that depend on the physical construction and material of the transformer core and f is frequency. During open-circuit conditions the following relationship proposed by Funk and Hantel [45] is used to adjust the linear self-inductances to account for the frequency-dependent magnetising inductance:

$$L_{nonlinear} = a_{Lo} f^{-b_{Lo}} L_{linear}, \tag{2.5}$$

where L_{linear} is the linear inductance parameter and a_{Lo} and b_{Lo} are constants. During short-circuit conditions, the core-flux levels differ. Thus, a new set of constants a_{Ls} and b_{Ls} are derived to adjust the linear inductance parameters to account for the frequency-dependent leakage inductance. The equation [45]:

$$R_{nonlinear} = \frac{R_{linear}}{c_{Rs}} [1 + a_{Rs} (\frac{f}{f_0} - 1)^{b_{Rs}}], \tag{2.6}$$

is used to include the non-linearity of the winding resistance as a result of the skin-effect during short-circuit measurements. The linear and non-linear winding resistances are denoted by R_{linear} and $R_{nonlinear}$, respectively. The constants a_{Rs}, b_{Rs} and c_{Rs} are related to the winding material and f_0 is the frequency at which R_{linear} was measured.

With the inclusion of these nonlinear equations for the model the authors are able to obtain model parameters that results in the model outputs closely matching the transformer measurements over the frequency range of 10Hz to 100kHz. The LVOC comparison is shown in Fig. 2.9b.

2.2. Spectral estimation

This section discusses the various tradeoffs that need to be considered when applying spectral estimation. There are two categories of spectral estimators, namely parametric and non-parametric estimators. Parametric spectral estimators assume a model, determine the parameters of the model and then calculate the Power Spectral Density (PSD) from the model. These techniques offer high-quality estimations, however, are sensitive to modelling errors, high signal-to-noise ratios (SNR), and require *a priori* knowledge of the signal generation process. Non-parametric spectral estimators make no assumptions about the signal generating process and so do not require a signal model. This class of estimators makes use of Discrete Fourier Transform (DFT) techniques to compute a PSD of the signal which offers a significant computational improvement over parametric estimators. As such, the literature review focuses on evaluating four widely accepted non-parametric spectral estimators, namely Periodogram, Blackman-Tukey, Bartlett, and Welch [46, 47].

The PSD, $P_{xx}(f)$, for a stochastic signal, $x(t)$, is defined as the Fourier transform of the autocorrelation function of the signal [48]:

$$P_{xx}(f) = \int_{-\infty}^{\infty} R_{xx}(\tau) e^{-j2\pi f \tau} \, d\tau, \tag{2.7}$$

when the signal is assumed to be ergodic the autocorrelation, R_{xx}, is defined as [46]:

$$R_{xx}(\tau) = \lim_{T\to\infty} \frac{1}{T} \int_{\frac{-T}{2}}^{\frac{T}{2}} x(t+\tau)x(t)\,dt. \tag{2.8}$$

Considering (2.7), the PSD can only be obtained by collecting an infinite amount of continuous data, which in practice is not feasible. However, estimates of the PSD, also known as spectral estimations, can be computed using finite lengths of discrete data. Truncating and digitising the data give rise to spectral leakage and aliasing. Spectral leakage is a phenomenon that distorts the signal measurement such that energy from a given frequency component is spread over adjacent frequency bins. This can cause the obscuring of important frequency peaks at adjacent frequencies. Aliasing is an effect that causes different frequencies to become indistinguishable, this occurs when the sampling frequency is not high enough to capture all of the frequency content within a signal. In practice, aliasing is overcome by applying a low pass filter to the measured signal, and spectral leakage is minimised through an appropriate selection of window functions and signal averaging [49].

The process of windowing a signal is equivalent to convolving the spectrum of the original signal with the spectrum of the window. Even if no window is used, convolution still takes place between the signal and a rectangular window due to the fact that the recorded data is only a snapshot in time of the entire signal [49]. Fig. 2.10 presents the frequency spectrum characteristics of window functions. The side lobes of the window affect the extent to which frequency components leak into adjacent frequency bins, causing a bias in the results of adjacent bins. The spectral resolution is affected by the width of the main lobe, a smaller main lobe allows for two closely spaced frequency components to be detected more effectively. As the main lobe narrows, a window's spectral energy is spread into the side lobes. Thus, the window function should be chosen based on the tradeoff between frequency resolution and spectral leakage [49].

There are many window functions available, of which the most common choices are Rectangular, Hanning (Hann), Hamming, Bartlett, Blackman, and Blackman-Harris [46, 49, 50]. A rectangular window contains the most narrow main lobe width, however, has the highest side lobe amplitude and slow side lobe roll-off rate [46]. Selecting a window function requires a case-by-case approach considering the tradeoff mentioned above. The Hann window is the middle ground between main lobe width and side lobe height and has a high side lobe roll-off rate. According to Cerna *et al.* [49] a Hann window is satisfactory in 95% of cases.

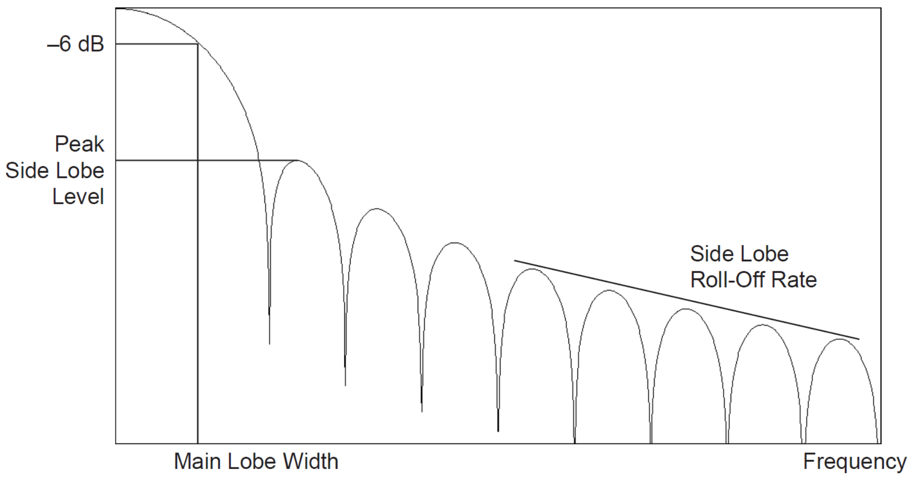

Figure 2.10: Frequency spectrum characteristics of window functions [49].

The most important considerations when choosing an estimator are the variance and bias of the produced spectrum. The variance of the spectrum is defined as the mean squared value minus the square of the mean of the estimated frequency spectrum. A higher variance, therefore, means a more noisy spectral estimation. The bias is the difference between the expected value of the frequency spectrum obtained from the estimator and the true frequency spectrum. Therefore, a perfect estimator has zero variance and bias.

Some common spectral estimators can be summarised as follows [46, 47, 50, 51]:

- **Periodogram:** The periodogram is the most basic nonparametric spectral estimator. Its bias converges to zero as the sample size tends to infinity, however, the variance does not. This makes the periodogram an inconsistent estimator. Despite its shortcomings, its simplicity makes it an important tool for benchmarking other spectral estimators.

- **Blackman-Tukey**: This spectral estimator was developed to address the large variability/variance in the periodogram spectral approach. The Blackman-Tukey spectral estimate can be obtained by computing the autocorrelation up to a limited time horizon. This limited autocorrelation function is then multiplied by a lag window function of the user's choice. The type of lag window is chosen based on the window function tradeoff between frequency resolution and spectral leakage, whilst the size of the window determines the tradeoff between a decreased variance and an increased bias in the spectral estimation.

- **Bartlett:** The Bartlett method is based on averaging periodograms. It splits up the available number of samples into segments using rectangular windows and then averages the periodograms obtained from each segment. This segmentation reduces the resolution of the estimate by the number of windows, however, it also reduces the variance of the spectral estimate by this same order. The compromise between resolution and variance is selected by the number of segmentations in the data sequence.

- **Welch:** The Welch method is based on the Bartlett method. However, the segments are allowed to overlap and can be applied to a variety of window functions prior to applying the periodogram. The segments overlap by a chosen percentage and are windowed based on the user's choice of window function. The goal of allowing overlapped segments is to increase the number of periodograms that are averaged together, thus decreasing variance whilst still maintaining resolution. The ability to choose a window function introduces more control over the bias properties of the estimate and can be used to give less weight to data samples at the overlapped end points of each segment.

Najafi *et al.* [46] shows that for Welch spectral estimation, a 62.5% overlap for the Hann window is optimal and produces accurate spectral estimates in power system identification. These same settings are used by Mwaniki *et al.* [15] to obtain the frequency spectrum of the voltage and current measurements of a complex Thevenin equivalent source under Pseudo-Random Impulse Sequence (PRIS) Perturbation.

2.3. Power system equipment perturbation signals

System identification and parameter estimation typically require excitation of the Device Under Test (DUT) with a perturbation signal containing a wide range of frequencies, i.e. a wideband signal, such that it excites all relevant modes of the system [52]. The PSD is used to determine the spread of power over frequency for a discretised signal of finite temporal length, the PSD is typically determined through spectral estimation techniques [50]. This section discusses the characteristics of a perturbation signal and concludes by describing some perturbation signals commonly used in the characterisation of power systems equipment.

2.3.1. Perturbation signal characteristics

A practical perturbation signal should be able to excite the frequency band of interest such that the excitation energy can negate the effects of environmental noise, digitizer noise and system noise [50, 52].

The two common metrics used to quantify the quality of an excitation signal are the following [5, 53]:

- **Crest factor:** The crest value, $C_r(u)$, of an excitation signal, $u(t)$, is given by the ratio between the peak value, u_{peak}, and the effective rms value, u_{rmse},

$$C_r(u) = \frac{u_{peak}}{u_{rmse}}. \tag{2.9}$$

This metric gives an idea of the compactness of the signal. An impulse waveform, for example, will have a high u_{peak} value and a small u_{rmse} resulting in a high crest factor and will therefore inject much less power into the system than signals with a similar u_{peak} but a larger u_{rmse}. It follows that a well-designed perturbation signal has a small crest factor.

- **Time factor:** The time factor accounts for the power distribution of the signal over the excitation range. In general, if the excitation is unequally distributed across the frequencies of interest with respect to the system noise, some frequency response points will be poorly measured. Ideally, the excitation signal should deliver power consistently over the frequency band of interest to achieve a uniform Signal-to-Noise Ratio (SNR). The time factor indicates the required measurement time per frequency point that is needed to guarantee a minimum SNR with reference to a sine wave. The time factor $T_f(u)$ of a signal $u(t)$ is given by

  $$T_f(u) = 0.5 \cdot (C_r(u))^2 \cdot (\frac{A^{freq}_{rms}}{A^{freq}_{min}})^2, \tag{2.10}$$

  where A^{freq}_{rms} is the rms value of the amplitude spectrum in the frequency band and A^{freq}_{min} is the minimum amplitude in the considered band. The scale factor of 0.5 is to normalise the metric to be 1 for a stepped sine wave. A lower time factor indicates a more optimal perturbation signal.

The remaining sections describe a number of common perturbation signals along with their applications and drawbacks.

2.3.2. Swept sine signal

A swept sine or periodic chirp signal is a sinusoidal signal where the frequency is swept up or down in a single measurement period. The signal is defined by [5]:

$$u(t) = A \cdot sin[(at + b)t] \qquad 0 < t < T_0, \tag{2.11}$$

where

$$a = \frac{\pi(f_2 - f_1)}{T_0} \tag{2.12}$$

and

$$b = 2\pi f_1. \tag{2.13}$$

The parameter T_0 is the measurement period, and parameters f_1 and f_2 are the highest and lowest frequency, respectively, that will be swept through by the sine. Pintelon [5] discusses how the swept sine signal has a relatively low crest factor. The amplitude spectrum is, however, not flat, resulting in certain frequency components with lower SNR. This leads to longer measurement times being required, resulting in a high time factor. It is also important to note that the band of excitation is not limited to the frequencies between f_2 and f_1, the signal produces spectral lines outside of this range thus limiting the controllability of the signal [53]. Swept sine signals have been used extensively in literature as perturbation signals for transformer frequency response analysis and wideband modelling [11, 14, 54].

2.3.3. Pseudo-random binary sequence

The Pseudo-Random Binary Sequence (PRBS) is a deterministic, periodic sequence that switches between two levels. The switching can only occur at multiples of the PRBS clock period T_{clk} and the sequence is generated using a Linear Feedback Shift Register (LFSR). The LFSR sequence is generated using a series of shift registers in conjunction with XOR feedback gates. An n-bit LFSR generates $N = 2^n - 1$ bits for a PRBS sequence before the sequence is repeated, a non-zero seed sequence should be given to the shift registers to generate a pattern. The period of repetition, T, is thus given by the equation:

$$T = T_{clk} \times N. \tag{2.14}$$

Fig. 2.11 shows the PRBS4 sequence generated with a $n = 4$ bit LFSR using a seed sequence of 1111. The entire sequence will contain $N = 2^4 - 1 = 15$ bits before it repeats [5, 55].

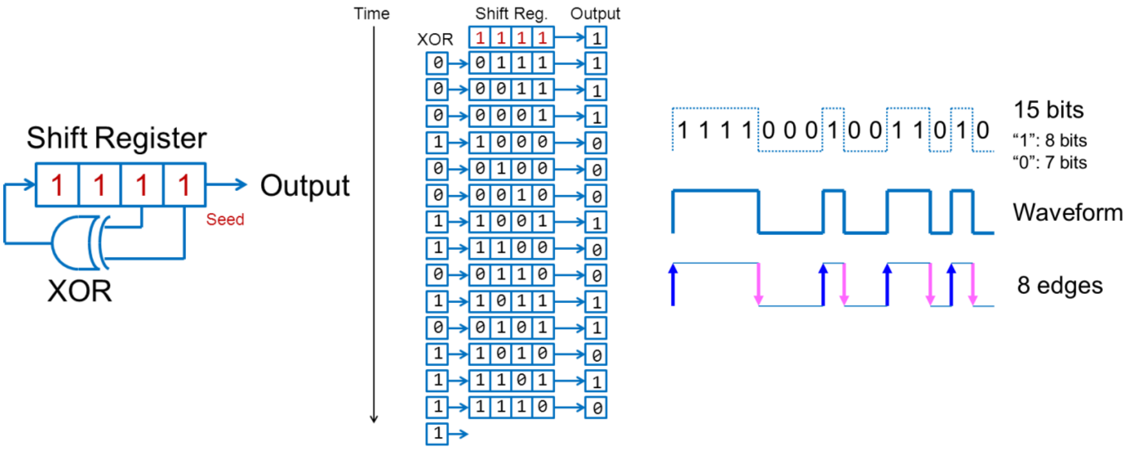

XOR	Shift Reg.	Output
	1 1 1 1	1
0	0 1 1 1	1
0	0 0 1 1	1
0	0 0 0 1	1
1	1 0 0 0	0
0	0 1 0 0	0
0	0 0 1 0	0
1	1 0 0 1	1
1	1 1 0 0	0
0	0 1 1 0	0
1	1 0 1 1	1
0	0 1 0 1	1
1	1 0 1 0	0
1	1 1 0 1	1
1	1 1 1 0	0
1		

Figure 2.11: The generation of a PRBS4 using a linear feedback shift register [55].

Fig. 2.12 shows a general PSD of the PRBS, the spectral power is focused within the frequency band below the PRBS clock frequency $f_{clk} = 1/T_{clk}$ and exhibits an almost uniform frequency spectrum up until the -3dB point of $\frac{1}{3} \times f_{clk}$. This spectral power begins to decay rapidly after the -3dB cut-off frequency up until f_{clk}. Considering the frequency spectrum shown in Fig. 2.12, the spectral power reaches a minimum at multiples of f_{clk} which results in low SNR in the vicinity of these frequencies. This can be remedied in practice by simply choosing higher clock frequencies such that the frequency range of interest is within the main lobe of the excitation signal's PSD. This signal, therefore, provides controllability in focusing the excitation in the frequency range where the modes of the system are prominent [50].

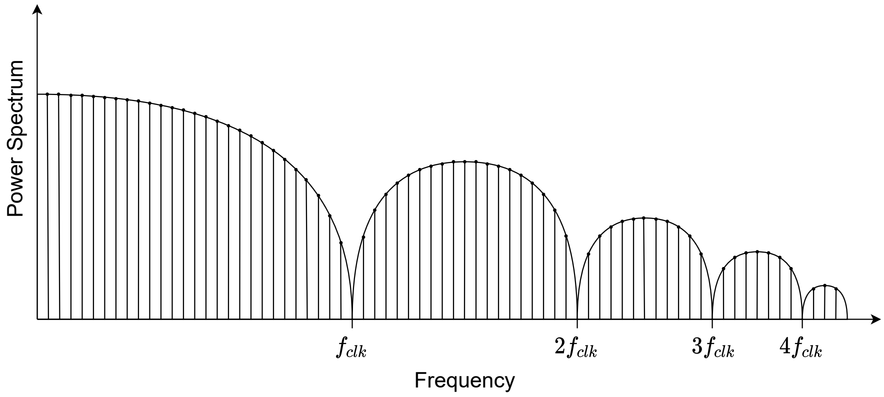

Figure 2.12: General trend of the power spectral density of a PRBS.

The PRBS has been used as a perturbation signal applied to transformers to estimate parameters of various circuit models [13,19,56]. Long unipolar PRBS excitation is not ideal for electromagnetic power system equipment such as transformers or electrical machines, due to the injection of low-frequency components that could result in core saturation, thus driving the DUT towards a biased offset [13]. It is recommended to make use of a bipolar PRBS excitation proposed by Vermeulen *et al.* [13] for electromagnetic equipment.

2.3.4. Pseudo-random impulse sequence

The Pseudo-Random Impulse Sequence (PRIS) perturbation signal was first proposed by Mwaniki *et al.* [15], and is designed for *in situ* system identification in the power system environment. The signal is designed to be able to control the amount of low-frequency content injected into the DUT to overcome the saturation effects of the PRBS.

The ideal time-domain waveform of the PRIS signal is generated by initiating positive impulse waveforms at each positive state transition of a PRBS and a negative impulse waveform for each negative state transition of a PRBS. Fig. 2.13 shows an illustration of a bipolar PRIS signal, denoted by $f^{B}_{PRIS}(t)$, and the corresponding PRBS control signal $f_{PRBS}(t)$.

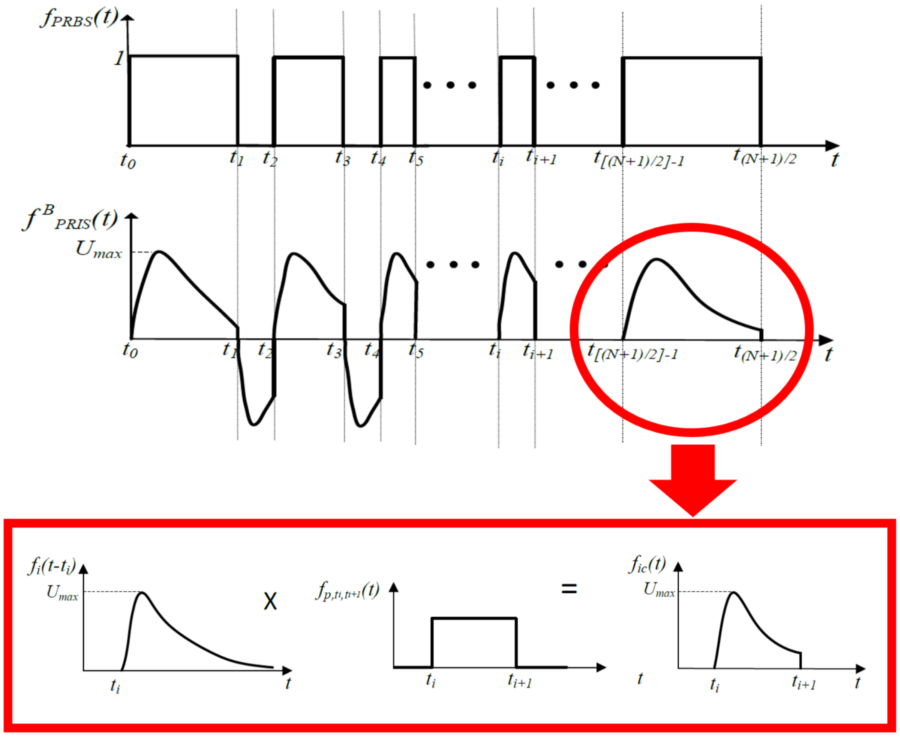

Figure 2.13: The mathematical formulation of a single PRIS impulse by multiplying a time-shifted impulse with a step function strung together to form an ideal PRIS waveform [15].

The time-shifted chopped impulse waveform highlighted in red in Fig. 2.13 is analytically expressed in (2.15) as a multiplication between a time-shifted impulse waveform, $f_i(t-t_i)$, and a unit step window function $f_{p,t_i,t_{i+1}}$.

$$f_{ic}(t-t_i) = f_i(t-t_i) \cdot f_{p,t_i,t_{i+1}}(t) \tag{2.15}$$

The time-shifted impulse waveform is defined by

$$f_i(t-t_i) = U[e^{-(t-t_i)/\tau_1} - e^{-(t-t_i)/\tau_2}], \tag{2.16}$$

where τ_1 and τ_2 denote the time constants of the two exponential functions that form the impulse and U denotes their amplitude. The unit step window function in (2.17) is formed by subtracting the unit step function $u(t-t_i)$ from $u(t-t_{i+1})$, delayed by $t = t_i$ and $t = t_{i+1}$, respectively.

$$f_{p,t_i,t_{i+1}}(t) = u(t-t_i) - u(t-t_{i+1}) \tag{2.17}$$

The PSDs of the PRIS and PRBS waveforms are compared in Fig. 2.14a, the PRBS provides even power at lower frequencies whilst the PRIS waveform provides less excitation at lower frequencies whilst focusing its power at $f_{clk}/3$ [15]. Mwaniki *et al.* [15] investigated the effects of the PRBS clock frequency, f_{clk}, as well as τ_1 and τ_2 on the PRIS power spectrums. The results from these investigations are shown in Figures 2.14b to 2.14d, from which it is clear that the PRIS parameters f_{clk}, τ_1 and τ_2 affect the power spectrum of the excitation signal significantly and thus provide greater controllability than the PRBS.

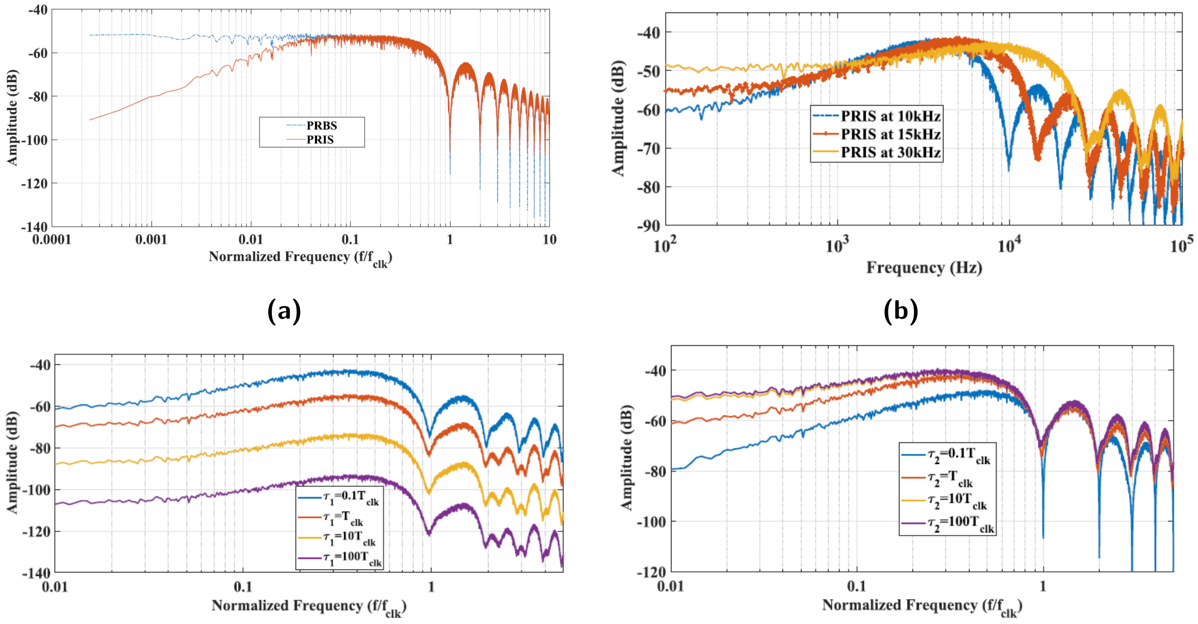

(a) **(b)**

(c) **(d)**

Figure 2.14: Investigations performed to compare **(a)** the PRIS and PRBS power spectrums as well as investigate the effects of **(b)** f_{clk}, **(c)** τ_1 and **(c)** τ_2 on the PRIS power spectrum [15].

The results of the investigation presented in Fig. 2.14b show that the size of the main lobe window increases with f_{clk} and thus also shifts the band of maximum spectral energy to a higher frequency. Fig. 2.14c shows that the impulse rise time constant τ_1 does not affect the overall shape of the spectrum. However, a smaller τ_1 with respect to the clock period, T_{clk}, increases the average spectral energy of the perturbation. Fig. 2.14d shows that the extent of low-frequency excitation is increased by increasing the impulse fall time constant τ_2 with respect to the clock frequency, however, does not have a significant effect around the frequency band of $f_{clk}/3$.

A PRIS perturbation circuit topology for offline perturbation of a target system is shown in Fig. 2.15. The H-Bridge configuration connected to the DC source, V_{DC}, generates a bipolar PRBS voltage that subsequently gets fed through an RLC circuit that governs the time constants τ_1 and τ_2.

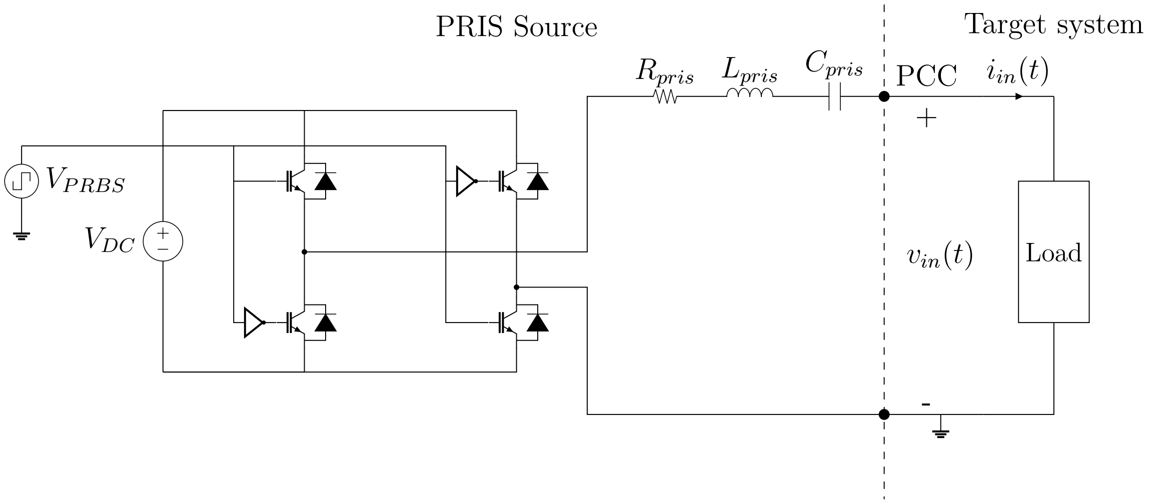

Figure 2.15: Test arrangement to perturb an offline target model with a pseudo-random impulse sequence perturbation.

Practically these time constants can be expressed in terms of the RLC circuit using the relationships:

$$\tau_1 = \frac{1}{|-\frac{R}{2L} - \sqrt{(\frac{R}{2L})^2 - \frac{1}{LC}}|} \tag{2.18}$$

and

$$\tau_2 = \frac{1}{|-\frac{R}{2L} + \sqrt{(\frac{R}{2L})^2 - \frac{1}{LC}}|}, \tag{2.19}$$

where R, L and C represent the three RLC circuit components of the PRIS source denoted by R_{pris}, L_{pris} and C_{pris} in Fig. 2.15, respectively. The PRIS perturbation signal has been used for the *in situ* perturbation of a Capacitive Voltage Transformer (CVT) by Solomon *et al.* [57]. The frequency responses obtained through perturbation are then subsequently used to estimate the parameters of a wideband lumped parameter equivalent-circuit model. The results show an good correlation between the estimated and measured frequency responses. Gerber *et al.* [58] applied offline PRIS perturbations to a ferro-resonance damping circuit.

2.4. Parameter estimation

Once the target system has been excited and the necessary measurements have been taken, a parametric model structure for the target system is chosen based on inspection of the measurements and some educated assumptions. The parameters of the model structure need to be determined before the model can be validated. Generally, this is done by minimising a criterion that measures the goodness of the fit between the outputs measured from the system and the model [5]. An overview of the general parameter estimation procedure is shown in Fig. 2.16.

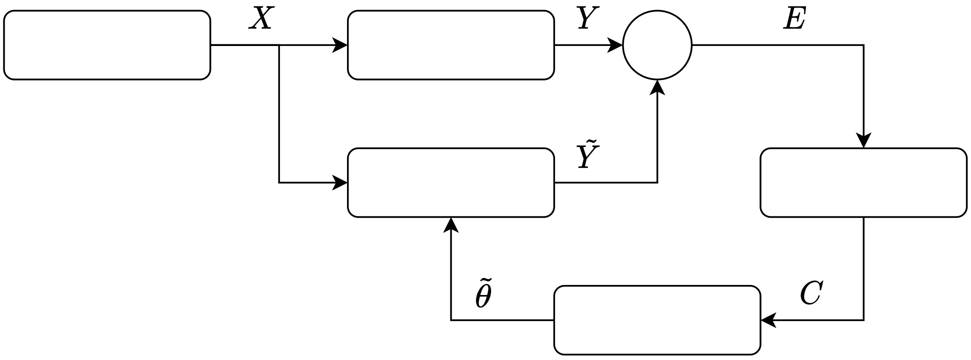

Figure 2.16: General overview of a parameter estimation procedure [59].

The target system and model are both excited and the input data, X, and output data, Y, is recorded. The error, E, is:

$$E = Y - \tilde{Y}, \tag{2.20}$$

where Y denotes the system outputs, and the model outputs are denoted by $\tilde{Y}$. A simple difference calculation can in many cases not be representative of the goodness of the fit between the outputs. A simple example is when the set of errors contains both positive and negative values, the summation of these errors could cause a low error value, however, this is due to the positive and negative errors cancelling each other [60]. Therefore, a cost function is formulated from the error set such that the criterion for an accurate fit between the target system and model can be catered to the characteristics of the output data. Finally, once the cost function has been formulated, the optimisation algorithm uses this criterion to estimate the model parameters, $\tilde{\theta}$, that minimises the cost function value, thus resulting in the model matching the target system.

The rest of this section deals with common cost function formulations and choices for optimisation algorithms that have been developed and documented in literature. The section is concluded by describing the modal decomposition process of empirical mode decomposition.

2.4.1. Cost function formulations

All cost function formulations presented below make use of normalisation by the number of data points in the error set, N. This is a common strategy to ensure that measurements with more data points do not influence the cost function more than measurements with fewer points. This normalised representation is also more intuitive as the cost function value represents a mean error for each data point as opposed to a cumulative error for the entire data set.

A simple way to address the issue of both positive and negative errors is to take the square of the difference, summed over the data set and then normalised:

$$C_{MSE} = \frac{1}{N}\sum_{i=1}^{N}(y_i - \tilde{y}_i)^2, \tag{2.21}$$

where y_i and $\tilde{y}_i$ denotes the i^{th} data point in the target output and model output, respectively. This type of cost function is known as Mean Squared Error (MSE) [61]. An MSE-based cost function formulation places emphasis on larger errors due to the square in the calculation.

If greater emphasis should not be placed on larger errors, there are two alternative approaches. The first is to take the absolute value of the difference as shown in (2.22), this formulation is known as the Mean Absolute Error (MAE). The second is to take the square root of the MSE, this formulation is known as Root Mean Squared Error (RMSE) and is analytically formulated in (2.23).

$$C_{MAE} = \frac{1}{N}\sum_{i=1}^{N}|y_i - \tilde{y}_i| \tag{2.22}$$

$$C_{RMSE} = \sqrt{\frac{1}{N}\sum_{i=1}^{N}(y_i - \tilde{y}_i)^2} \tag{2.23}$$

Cost function formulations based purely on the difference between the outputs do not take into account the range of possible output values in y and $\tilde{y}$. If the range of outputs varies by many orders of magnitude, the differences between points of larger magnitudes outweigh the differences between points of lower magnitudes even if the percentage of the errors are similar. The Mean Absolute Percentage Error (MAPE) in (2.24) attempts to address this by taking the i^{th} absolute difference and dividing it by the i^{th} target data point to obtain a percentage [62].

$$C_{MAPE} = \frac{1}{N}\sum_{i=1}^{N}\frac{|y_i - \tilde{y}_i|}{y_i} \cdot 100\% \tag{2.24}$$

Percentage-based cost function formulations should be avoided if the data is likely to contain zeroes. If a percentage-based cost function formulation is still required, the RMSE can be normalised with respect to either the mean of the target output data, μ_y, or the difference between the maximum and minimum values in the target output data, these formulations are shown in (2.25) and (2.26), respectively [61].

$$C^1_{NRMSE} = \frac{\sqrt{\frac{1}{N}\sum_{i=1}^{N}(y_i - \tilde{y}_i)^2}}{\mu_y} \tag{2.25}$$

$$C^2_{NRMSE} = \frac{\sqrt{\frac{1}{N}\sum_{i=1}^{N}(y_i - \tilde{y}_i)^2}}{max(y) - min(y)} \tag{2.26}$$

The correlation coefficient is a metric used to measure the strength of the relationship between two sets of data. The most popular form of correlation is Pearson correlation which is commonly used in linear regression problems. A value of 1 means a perfect positive relationship while a value of -1 signifies a perfect inverse relationship, and a value of 0 indicates no linear relationship between the two data sets exist. The value that is returned from the correlation coefficient calculation can be transformed into a cost function value for the optimisation to be minimised. The Pearson correlation coefficient, ρ, between two data sets, y and $\tilde{y}$, can be defined as follows [63]:

$$\rho(y, \tilde{y}) = \frac{1}{N-1}\sum_{i=1}^{N}(\frac{y_i - \mu_y}{\sigma_y})(\frac{\tilde{y}_i - \mu_{\tilde{y}}}{\sigma_{\tilde{y}}}), \tag{2.27}$$

where μ_y and σ_y are the mean and standard deviation of y, and $\mu_{\tilde{y}}$ and $\sigma_{\tilde{y}}$ are the mean and standard deviation of $\tilde{y}$, respectively.

2.4.2. Optimisation algorithms

Once the cost function has been defined an optimisation algorithm has to be selected to minimise the cost function, thereby obtaining the optimal parameters of the model that best represents the outputs of the system. The search space within which the optimisation has to find the optimal parameters can in some cases be very complex. This complexity usually increases with the number of parameters the optimisation algorithm needs to solve for [64]. When the search space relies on more than one parameter, it is called a multi-dimensional problem, and the larger this dimensionality becomes, the greater the computational burden [64]. An illustration of a one-dimensional search space, i.e. one model parameter, where the cost function C is denoted by $f(x)$, is shown in Fig. 2.17. The figure shows the locations of both global and local minima. Local minima are points where the cost function is smaller than or equal to the value at nearby points whereas a global minimum is a point where the function value is smaller than or equal to the value at all other feasible points [38]. The aim of optimisation algorithms is to locate the global minimum whilst not mistaking the local minima for the global [65].

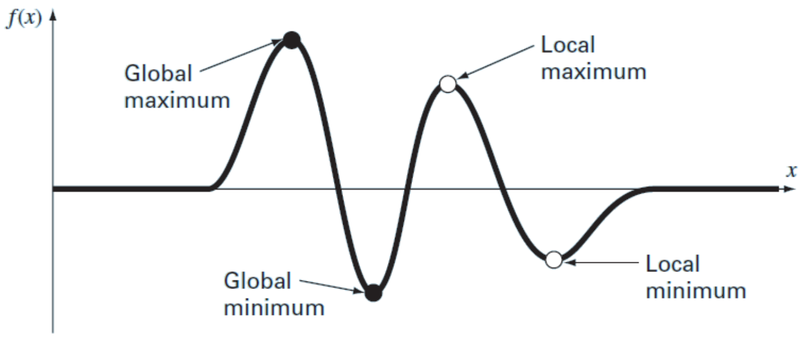

Figure 2.17: One dimensional search space showing global and local extrema [65].

Local optimisation algorithms begin at a starting point and track into the closest minima using gradient-descent-based algorithms such as Newton, Gauss-Newton and trust-region method [60, 66]. Thus, local optimisation solvers are effective for finding local minima. However, their effectiveness in finding the global minimum is highly dependent on the initial starting point. Global optimisation algorithms attempt to solve this by making use of various strategies to find the cost function's global minimum [38]. One strategy is to generate a matrix of starting points that each executes a local optimisation procedure. Another is to inspect the objective function at multiple points at a certain distance, x, from the current point and widen this distance based upon certain criteria. This methodology ensures the algorithm is constantly searching through a wider field of view for the minimum. There are many global optimisation algorithms that also make use of a population of points and compute certain interactions between these points to find the global minimum. These algorithms usually take inspiration from the natural selection found in nature and include degrees of stochasticity, thus this class of optimisation is known as evolutionary metaheuristic algorithms [64]. Metaheuristic algorithms are not proficient in handling equality constraints and are computationally expensive, therefore, these are typically designed to make use of parallel computations to minimise runtimes [64, 67].

2.4.2.1. Fmincon

Fmincon is a local optimisation solver in the MATLAB Optimisation Toolbox [66] and is typically used for problems when constraints can be imposed on some or all of the parameters. These constraints can be implicit constraints relating to the general relationship between certain parameters, for example, if the user knows that one parameter is smaller than another. The constraints can also come in the form of boundary conditions, thus making the search space smaller. *Fmincon* can make use of several optimisation methods, namely, interior-point, trust-region-reflective, sqp, sqp-legacy, and active-set. The interior-point algorithm is best suited to large-scale problems which do not generate full-scale matrices in computations. This can be beneficial when the problem set is large, which is typically the case for real-world problems, to reduce computational burden [66,68].

2.4.2.2. Patternsearch

Patternsearch is classified as a global optimisation routine and forms part of the MATLAB Global Optimisation Toolbox [38], the method evaluates the function at multiple points around the current best function value to choose the direction it needs to move in. The optimisation procedure performs the following tasks from the initial, and every successive point [38]:

- **Evaluate mesh:** The method uses a mesh to determine the distance of the points from the current location it needs to evaluate.
- **Successful poll:** If one of the function evaluations in the mesh is smaller than the current point the optimisation moves to that location, and the mesh size is doubled. The mesh is increased to ensure that the optimisation does not simply continue polling to the closest minimum.
- **Unsuccessful poll:** If none of the points in the mesh are smaller than the current location the mesh size is halved and the mesh is re-evaluated. The mesh is iteratively halved until a point in the mesh is found that is smaller than the current point.

This optimisation, though classified as a global optimisation method still requires an initial point to start with, thus, the choice of initial location plays a role in the final outcome of the algorithm.

2.4.2.3. Globalsearch

Globalsearch generates a multitude of start points based on a scatter-search algorithm. Each of these points then executes the local *fmincon* optimisation routine. This class of optimisation operates on the principle that the probability of approaching the global minimum approaches 1 as the number of start points approaches infinity [67]. Once the initial population of start points has been generated the algorithm loops through the start points performing one of the following [38]:

- **Run local solver:** The local optimisation algorithm, *fmincon*, is initiated. Upon completion, a spherical basin of attraction is generated whereby future start points within this radius are assumed to converge to the same minimum. This basin of attraction is generated with a radius from the start point to the solution of the fmincon solver. This step always executes for the first starting point in the population.
- **Reject start point:** A start point is rejected if the point exists within one of the

basins of attraction of a previous local optimisation run or if the start point cost function value is worse than the output of the initial optimal local basin.

As mentioned previously, local solvers are proficient in handling many constraint equations but typically converge to the closest minima whilst metaheuristic algorithms struggle with equality constraints, however, are proficient in finding global minima. The motivation for using *globalsearch* is it attempts to incorporate the advantages of both whilst avoiding the disadvantages of both [67].

2.4.2.4. Genetic algorithm

Genetic Algorithm (GA) is a metaheuristic optimisation method that is based on natural selection. The genetic algorithm modifies a randomly initialised population of individuals, at each step the algorithm selects individuals from the current population to be parents and then produces children for the next generation. GA can be applied to problems that are discontinuous, non-differentiable, stochastic, and nonlinear [38]. At each generation in the methodology, the algorithm uses three rules: selection, crossover and mutation, to determine which type of child will be produced [38]:

- **Elite children:** The individuals from the previous generation that have the best function values are directly assigned as children and will remain in the next generation.
- **Crossover children:** These children are created from the selection of two parents that contribute a random weighting of their coordinates to the child's location.
- **Mutation children:** Mutation children are created by adding a random vector from a Gaussian distribution to the parent.

The advantage of metaheuristic algorithms such as GA is its overall simplicity and its counterdependence on the presumption of any gradient information about the search space [69]. A large number of computations are required to solve for the locations of the GA population through every iteration, thus this form of optimisation requires large computing power and takes long to converge. It, therefore, makes it an inefficient choice to solve for simple problems where more traditional optimisation methods would suffice.

2.4.2.5. Particle-swarm

Particle-swarm optimisation begins by creating a random set of initial particles within the bounds presented by the user and assigns each particle a random initial velocity. Particle-swarm requires only primitive mathematical operators and is computationally inexpensive [70]. The optimisation is performed by updating each particle in the swarm with its current velocity to obtain its new position, the optimisation executes as follows [38]:

- A particle's new velocity is calculated as a function of a random subset of particles in the swarm, its previous best position, its previous velocity and a weighted inertia variable.

- The particle's position is updated by adding its old position to its calculated velocity. If the particle hits the bounds of the search space the position is adjusted to fall within the bounds.
- If the current particle position is the best function value the particle has experienced thus far, its position, as well as the function value, is stored.
- Similarly, the best function value and position in the entire swarm is updated and stored.
- If the best function value in the swarm is improved the inertia is increased, thereby increasing the particle velocities, and vice versa if the function value has not improved after multiple iterations.

Particle-swarm, in many ways, is similar to genetic algorithm. The genetic algorithm makes use of more stochasticity in its implementation whereas particle-swarm makes use of the concept of increasing velocities of particles to arrive at an optimal solution in a shorter duration [70].

2.4.3. Empirical mode decomposition

A data analysis method known as Empirical Mode Decomposition (EMD) was proposed by Huang *et al.* [71]. The method, at the time, was a novel approach to the adaptive decomposition of non-linear and non-stationary data. The method is investigated in this research in various parameter estimation methodologies. As such, this section provides a brief literature study regarding the decomposition method.

The EMD process generates a collection of Intrinsic Mode Functions (IMFs) that represent the decomposed data. Different from the sine and cosine components of the Fourier transform, IMFs are oscillatory modes whose amplitude and frequency can vary over time [72]. A decomposition is defined as an IMF if it satisfies the following two conditions [71]:

- The number of extrema and the number of zero crossings may differ by no more than one.
- At any point, the average between the envelope defined by the local maxima and the envelope defined by the local minima is zero.

The IMFs are produced through a sifting process. In the first step, all the local maxima and minima of the data sequence, $x(t)$, are identified. From this, a cubic spline is connected through all the local maxima and then similarly for all the local minima. These two envelopes should cover all of the data between them. A mean line $m_1(t)$ is then constructed between the upper and lower envelopes. The first component $h_{11}(t)$ is obtained by taking the difference between the data $x(t)$ and mean line $m_{11}(t)$:

$$h_{11}(t) = x(t) - m_{11}(t). \tag{2.28}$$

Fig. 2.18 shows an illustration of the sifting process. The original data is indicated with a thin solid line, the envelopes are indicated by dashed lines, and the mean by a dark solid line.

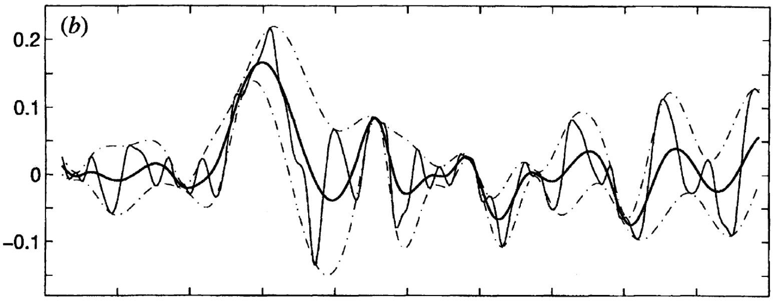

Figure 2.18: An illustration of the sifting process with the data in a thin solid line, the envelopes in dashed lines and the mean line in a thick solid line [71].

The sifting process is then repeated whereby the data, $x(t)$, is replaced by $h_{11}(t)$, new maxima and minima envelopes are calculated and therefore a new mean line $m_{12}(t)$ is generated, the next component, $h_{12}(t)$, is then calculated using:

$$h_{12}(t) = h_{11}(t) - m_{12}(t). \tag{2.29}$$

This process is repeated k times until $h_{1k}(t)$ satisfies the conditions to be an IMF. The sifting can be generally expressed by

$$h_{1k}(t) = h_{1(k-1)}(t) - m_{1k}(t). \tag{2.30}$$

If $h_{1k}(t)$ satisfies the IMF conditions, it is then the first IMF, $c_1(t)$. The first IMF, $c_1(t)$, is then subtracted from the rest of the data to obtain a residual $r_1(t)$. The sifting process is then repeated using $r_1(t)$ as the initial signal until the second IMF, $c_2(t)$, is produced. This procedure can be repeated on all r_js and is generally described by:

$$r_{j-1} - c_j = r_j. \tag{2.31}$$

The decomposition process stops when the component c_j, or residual r_j, becomes smaller than a predetermined value or when residual r_j becomes monotonic from which no more IMFs can be extracted. The original signal is represented as a set of n IMFs and a residue

r_n, mathematically represented by [71]:

$$x(t) = \sum_{j=1}^{n} c_j + r_n \tag{2.32}$$

One of the major drawbacks of the EMD method is the frequent appearance of mode mixing phenomena [73]. Mode mixing is defined as an IMF consisting of signals of widely disparate time scales, or a signal of a similar time scale residing in multiple IMFs and is usually caused by the presence of intermittent signals in the data [73, 74]. Wu *et al.* [73] developed a noise-assisted EMD method, known as Ensemble Empirical Mode Decomposition (EEMD). This method defines the true IMF components as the mean of an ensemble of trials, where each trial consists of the IMF generated by the classical EMD and white noise of finite amplitude. Deering *et al.* [74] proposes the use of a masking signal to prevent mode mixing however this method requires subjective decisions to be made by the user on whether certain components should be separated.

Boundary conditions of the EMD method also need to be carefully addressed. Abnormally high amplitude artefacts can occur toward the boundaries of the IMF components. Various signal extension algorithms have been proposed to minimise these anomalous artefacts such as periodical, symmetric and anti-symmetric [72].

Chapter 3

Pseudo-Random Impulse Sequence Source Hardware Design

This chapter describes the design and assembly of a Pseudo-Random Impulse Sequence perturbation source. The chapter begins with an overview of the source design and all of the various hardware constituents, followed by a description of the PCB designs and functionalities. The chapter concludes with a section presenting the results of the tests performed to validate the source design through the perturbation of a known load.

3.1. Source design overview

The source is designed to meet the following design specifications:

- **Configurable PRBS settings:** The PRBS settings such as the clock frequency, number of repetitions, and order should be configurable and user-friendly.
- **Configurable RLC circuit:** The RLC circuit components should be easily interchangeable. Not all circuit components come in all values, therefore the PCB should facilitate combinations of RLC components to form the desired circuit values.
- **Suitable for high-power environments:** The source should be capable of performing offline and online perturbations and thus needs to withstand large potential differences across the switches as a contingency if the RLC circuit fails.
- **Transportable:** The source should be compact such that it is easy to transport for *in situ* measurements at a testing site.
- **Modular:** If any of the hardware constituents break, it should be easy to remove the respective PCB and replace it with a new one. Similarly, if the hardware or PCB design needs to be upgraded, the whole source should not need to be rebuilt.
- **Protected:** The entire source should be enclosed and protected, both from physical damage as well as electromagnetic interference. The source should also be insulated to protect the operator during high power operation.

A functional block diagram providing an outline of the hardware design is shown in Fig. 3.1. The source consists of five printed circuit boards (PCBs), of which four are shown in the block diagram. The final backplate PCB provides all of the tracks that are used to connect the various PCBs to one another and is, therefore, not shown in the figure.

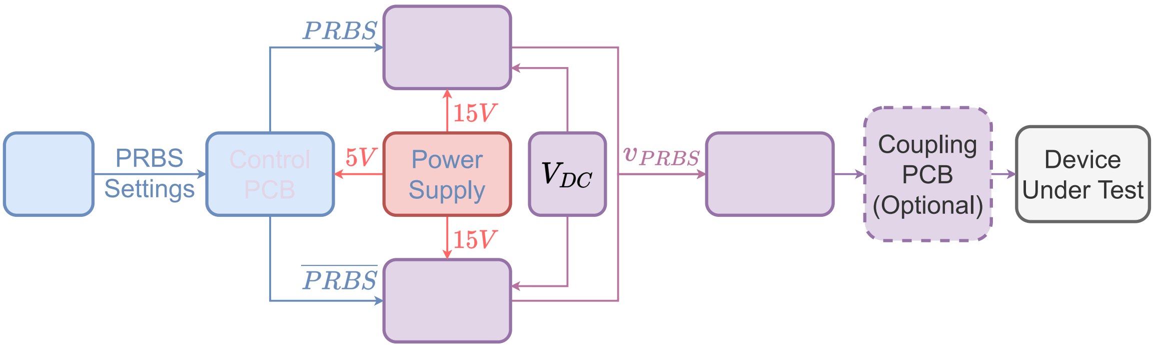

Figure 3.1: Functional block diagram of PRIS source hardware design.

The user is able to configure the PRBS clock frequency, repetitions, and order by flashing data from a Personal Computer (PC) onto the control PCB. The control PCB provides control signals to the two switching PCBs based on the settings issued by the user. The two switching PCBs collectively constitute the H-bridge portion of the PRIS perturbation circuit topology in Fig. 2.15. The resulting voltage waveform is fed through an RLC PCB which houses the circuit elements indicated by R_{pris}, L_{pris} and C_{pris} in Fig. 2.15, then through an optional coupling PCB, and into the device under test. The power supply unit that forms part of the source provides DC power to both the control PCB and switching devices. The DC voltage, denoted as V_{DC} on the PRIS circuit topology shown in Fig. 2.15 as well as shown in Fig. 3.1, is provided by external power supplies. It is important to note that this is a high-level block diagram and does not represent electrical connections made by tracks.

The PCBs are manufactured using the 1.6mm thick FR-4 base material and a HASL (with lead) surface finish. The PCBs slot together in a subrack chassis for modularity and easy transportation. Further detail about each PCB is provided below:

- **Control PCB:** The control circuit board contains headers to connect a Field Programmable Gate Array (FPGA) that is used to generate switching control signals. In conjunction, there are buttons to control the FPGA power and begin the perturbation sequence.
- **Switching PCB 1 and 2:** These PCBs each house two IGBT switches in series and provide a connection between their midpoint, thus each PCB acts as a single leg of the H-Bridge PRIS topology.
- **RLC PCB:** The RLC PCB provides connections for the RLC circuit portion of

the PRIS topology, the PCB is designed such that various series and/or parallel combinations of resistors, inductors, and capacitors can be connected to form the desired circuit values.

- **Coupling PCB:** In the case of *in situ* grid impedance measurements the addition of a coupling capacitor card is designed to protect the source hardware and forms a series connection with the RLC circuit. This circuit is not required in offline perturbation arrangements and as such its design will not be discussed.
- **Backplate PCB:** The backplate facilitates the electrical connections that are required between the various PCBs. These connections can come in the form of control signals or to supply power.

The remainder of this chapter presents the hardware design process followed for each PCB, the subrack choice for a modular design, the FPGA control software and concludes with the source validation.

3.2. Source design

3.2.1. Control PCB design

The switches in the H-Bridge implementation are FF225R17ME4 Infineon IGBT modules that are rated for a collector-emitter voltage of 1700V, a continuous DC collector current of 225A and a total power dissipation of 1.5kW [75]. The IGBT module features direct compatibility with the 2SP0115T dual-channel driver module [76]. This switch can withstand a high collector-emitter voltage difference, so in the case of the RLC circuit failing, the switches are still able to handle the voltage differential between the grid and the DC source. Fig. 3.2 shows a functional block diagram of the Control PCB design.

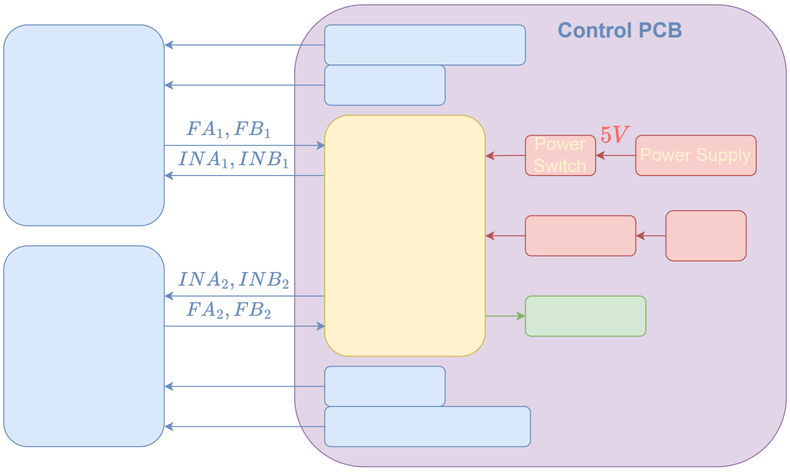

Figure 3.2: Functional block diagram of Control PCB.

The 2SP0115T driver module requires two Pulse-Width Modulated (PWM) signals, INA and INB, a MOD select line, a half-bridge mode blocking time and two fault detection lines, FA and FB [76]. The control PCB dimensions are 220mm x 100mm and were manufactured using 1oz copper. The PCB model is shown in Fig. 3.3 and is used to supply the driver with the necessary control signals.

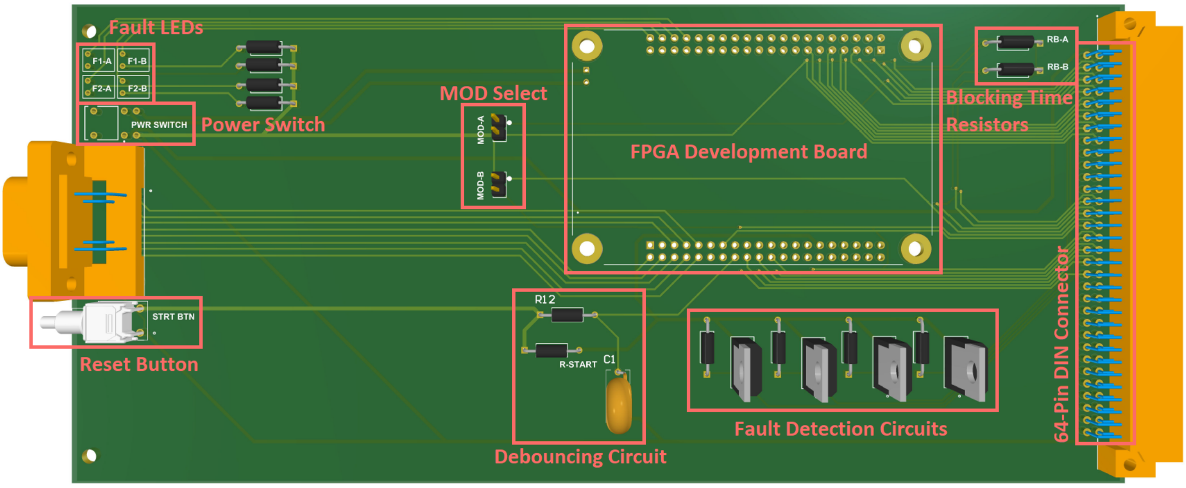

Figure 3.3: Control PCB labelled with its various important constituents.

The various constituents that make up the board are presented in Fig. 3.2 as well as highlighted in red in Fig. 3.3 and discussed below:

- **MOD select:** The MOD select line can either be pulled high or held low to interchange the driver operation between direct mode and half-bridge mode, respectively [76]. The PCB design allows the MOD lines for each driver to be set using a jumper, denoted by MOD-A and MOD-B.

- **FPGA development board:** The FPGA module is connected via female headers to the control circuit board, from here the tracks transmit two sets of control signals to the relevant IGBT/driver pair. Each IGBT driver receives its own INA and INB PWM control signal to ensure each leg of the H-Bridge switches in compliment. The FPGA used is a DE0-Nano development board, the board is chosen due to its affordability, compact size, and user-friendly software [77].

- **Fault detection circuits and fault LEDs:** There are two fault lines per driver that get pulled low when a fault is detected. The recommended circuit of a Schottky diode in parallel with a 150kΩ pull-up resistor is implemented for each of the four fault lines [76]. In the case of a fault, the FPGA board detects the low fault line and sets a GPIO pin to high, which in turn powers a Light Emitting Diode (LED) to signal the user that a fault has occurred.

- **Blocking time resistors:** In half-bridge mode, a blocking resistor, R_b, needs to be chosen. The blocking time between the complementary switching of the two IGBTs in series, is set using the following formula [76]:

$$R_b[k\Omega] = \frac{7650 + 150 \cdot T_b[ms]}{99 - T_b[ms]} - 6.8 \qquad 20ms < T_b < 90ms \tag{3.1}$$

The blocking time, T_b, is set to a minimum of 9μs by selecting $R_b = 0\Omega$.

- **Reset button and debouncing circuit:** A pin on the FPGA is programmed to reset the development board when the reset line gets pulled low. A push button along with an RC debouncing circuit is, therefore, included in the design as shown in Fig 3.4.

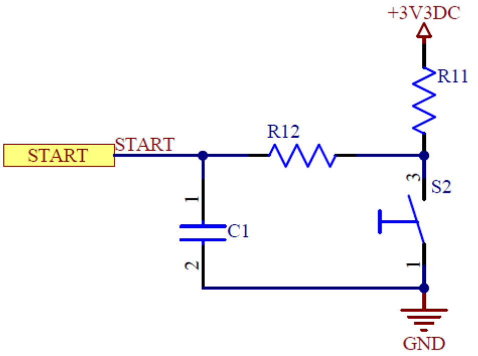

Figure 3.4: Reset button and debouncing circuit schematic diagram.

This reset pin serves as the startup initiation for a PRIS perturbation cycle. The debouncing circuit uses $R_{12} = 10k\Omega$ and $R_{11} = 100k\Omega$ resistors, along with $C_1 = 0.1\mu F$, this yields a RC time constant of $\tau = R_{12} \times C_1 = 1ms$.

- **Power switch:** The FPGA is supplied by a 5V power supply rail. When new code needs to be flashed onto the FPGA the USB port provides power to the FPGA. A switch is, therefore, added to disconnect the 5V supply to prevent any grounding errors when new code is being uploaded.
- **64-Pin DIN connector:** The 64-Pin DIN connector is connected to the back of the control PCB and serves as the connection to the backplate PCB. This is where all of the IGBT control signals are routed, as well as where the 5V supply to power the FPGA is obtained from.

Table 3.1 provides a list of the components required to assemble the control PCB and the schematic diagram is available in Appendix A.

Table 3.1: Control PCB parts list.

Part Name	Part Description
64-Pin DIN Male	ERNI, DIN 41612 64 Way 2.54mm Pitch, Type B, 2 Row, Right Angle DIN 41612 Connector, Plug
Power Switch	GT22MABE Toggle Switch DPST Through Hole, Right Angle
Reset Button	Switch Push SPST-NO 0.4VA 20V
FPGA	DE0-NANO EVAL BOARD

3.2.2. Switching PCB

The switching PCB was designed as part of another research project, consequently, this subsection will only provide a brief overview of the board and its constituents. The switching PCB dimensions are 220mm x 100mm and manufactured using 1oz copper. The switching card houses a single IGBT and driver pair, this is achieved through a cutout in the centre of the board that allows the relatively large driver to be mounted onto the PCB.

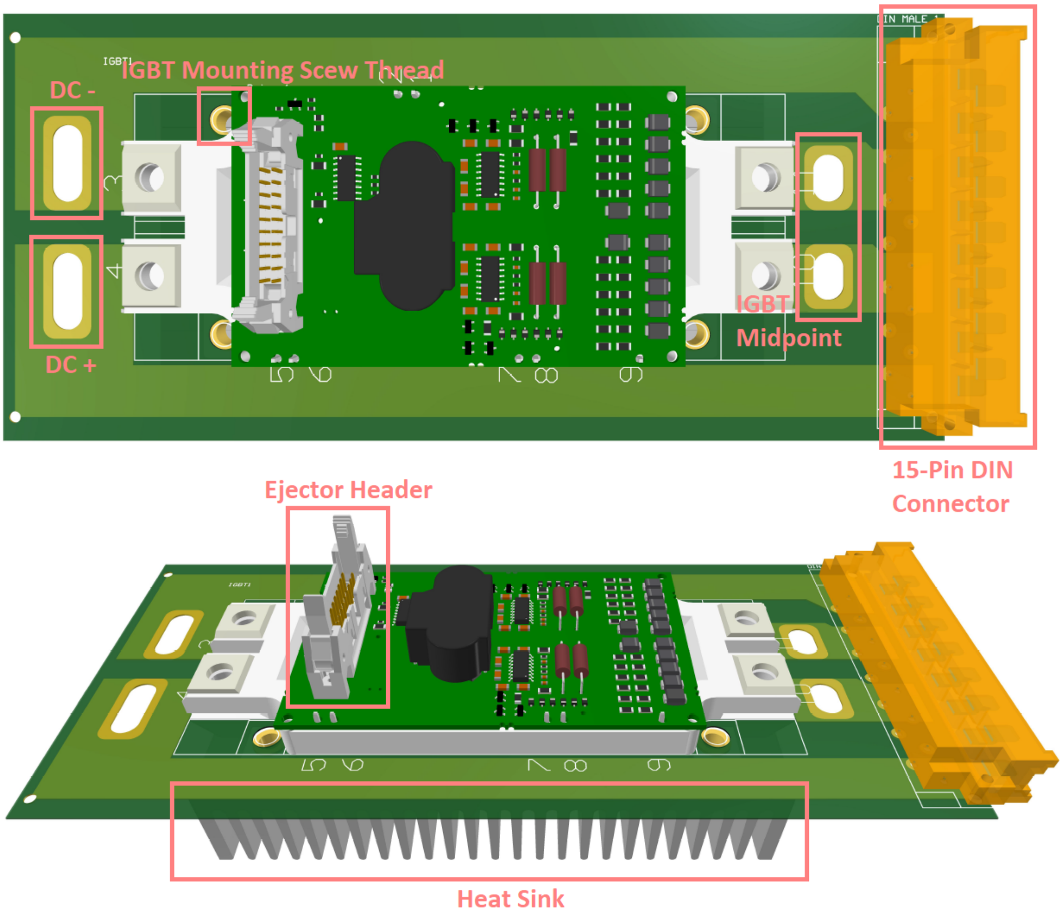

Figure 3.5: Switching PCB labelled with its various important constituents.

The constituents that make up the board are indicated in Fig. 3.5 and are as follows:

- **IGBT mounting screw thread:** There are four screw threads on the IGBT module that are used to mount it to the PCB.
- **DC-, DC+ & IGBT midpoint:** The IGBT module's internal connection topology is shown in Fig. 3.6. The positive and negative terminals, i.e. pins 4 and 3, are connected to the DC voltage supply using the vias located at DC+ and DC-, respectively. The midpoint output voltage, i.e. pins 10/11, is connected to the backplate via three pins on the 15-Pin DIN connector. Three pins were used to increase the current carrying capacity to 45A [78].

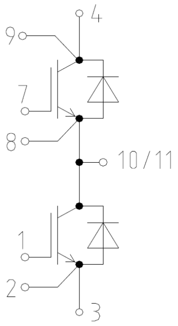

Figure 3.6: Internal connection topology of a single IGBT module [75].

- **15-Pin DIN connector:** The DIN connector serves as the connection point for the DC voltage to supply the IGBT switches, and the midpoint voltage of the H-Bridge leg.
- **Ejector header:** The control signals that are generated by the FPGA for switching operation are connected to the driver module via the ejector header. As such the control signals are not routed through the DIN connector but instead come directly from an ejector header soldered to the backplate via a ribbon cable. The ribbon cable is a 28 American Wire Gauge (AWG) twisted pair flat cable recommended by the IGBT driver datasheet [76, 79].

Table 3.2 provides details of the components that were ordered to assemble the switching PCB. The switching PCB schematic diagram adopted from a work in progress is presented in Appendix D.

Table 3.2: Switching PCB parts list.

Part Name	Part Description
DIN 15-PIN Power Male	HARTING, DIN 41612 15 Way 5.08mm Pitch, Right Angle Rectangular Connector, Plug
2SP0115T	IGBT Driver, controls 2 IGBTs
FF225R17-ME4	IGBT, includes 2 IGBTs
Heat Sink	75x150x27mm 1,4K/W

3.2.3. RLC PCB

The RLC PCB was designed as part of another research project, consequently, this subsection will only provide a brief overview of the board and its constituents. The RLC circuit board dimensions are 220mm x 100mm and were manufactured using 2oz copper. Fig. 3.7 shows a circuit diagram of the design topology whilst Fig. 3.8 shows the connection points for the capacitors, resistors, and inductors that make up the PRIS RLC PCB.

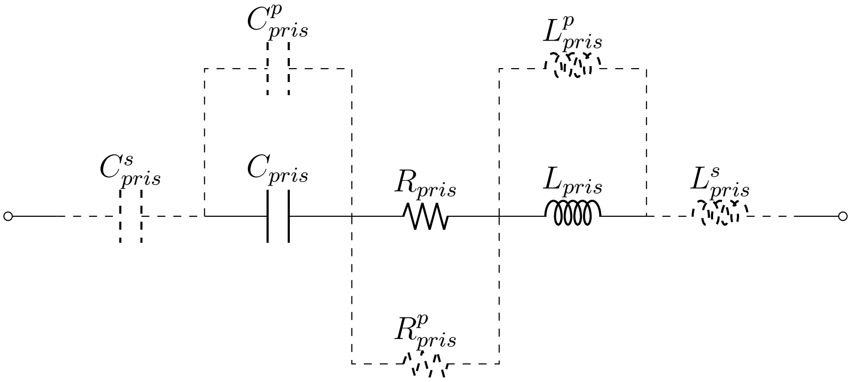

Figure 3.7: Circuit diagram of RLC PCB design.

The capacitor and inductor connections have the capability to accommodate an additional series component, C^s_{pris} and L^s_{pris}, as well as additional parallel components, C^p_{pris} and L^p_{pris}. The resistance connections can accommodate an additional parallel resistor, R^p_{pris}. The smallest track width of 21.34mm spread over two layers is located on the RLC PCB. This limits the total current that can be used to perturb a DUT to 25A if the track temperature is allowed to increase to 45°C [80]. The details of the RLC circuit DIN connector and spade terminals are presented in Table. 3.3. The schematic diagram adopted from a work in progress is available in Appendix C.

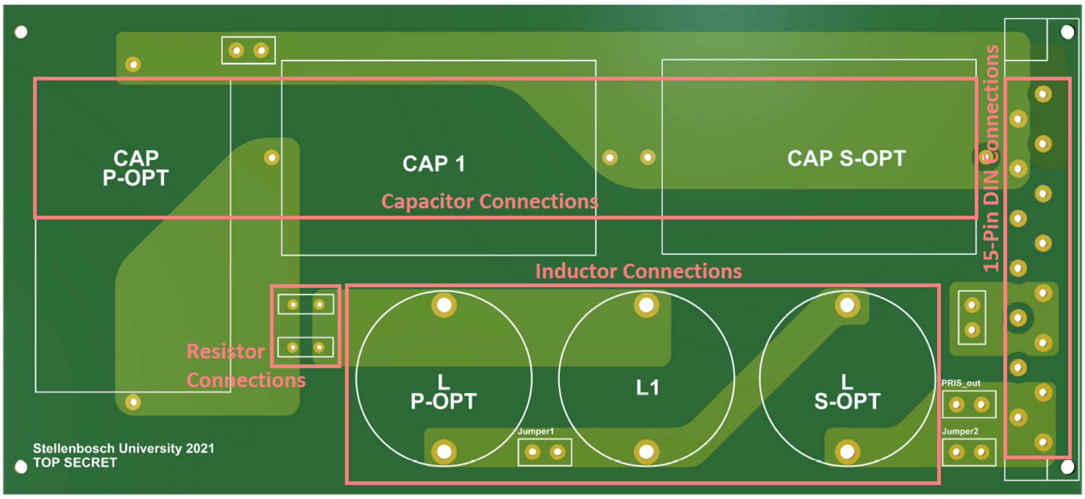

Figure 3.8: RLC PCB labelled with its various important constituents.

Table 3.3: RLC PCB parts list.

Part Name	Part Description
15-PIN Power DIN Male	HARTING, DIN 41612 15 Way 5.08mm Pitch, Right Angle Rectangular Connector, Plug
Spade Terminal	TE Connectivity, FASTON .250 Grey Uninsulated Spade Connector, 6.35 x 0.83mm Tab Size

3.2.4. Backplate PCB design

The backplate PCB serves as a means for all the other PCBs to connect to one another in a modular way. This circuit board contains tracks that transmit both control signals as well as supply power to the FPGA and IGBT/driver modules. The EPLAX Bivolt PK60B 60W is a power supply compatible with 19" subrack systems and has dual 5V and 15V outputs to supply the FPGA and IGBT drivers [81]. The backplate dimensions are 370.8mm x 128.7mm and were manufactured using 2oz copper. A model of the PCB is shown in Fig. 3.9. The design opted for spade connectors and copper cables to connect the H-Bridge legs to the RLC card as opposed to copper tracks to ensure the design is modular, in this way, if the RLC circuit board needed to be redesigned the backplate could remain unchanged. The smallest track clearance of 4.26mm is located on the Backplate PCB, this limits the voltage insulation between tracks to 1.62kV [82]. A detailed schematic diagram is provided in Appendix B.

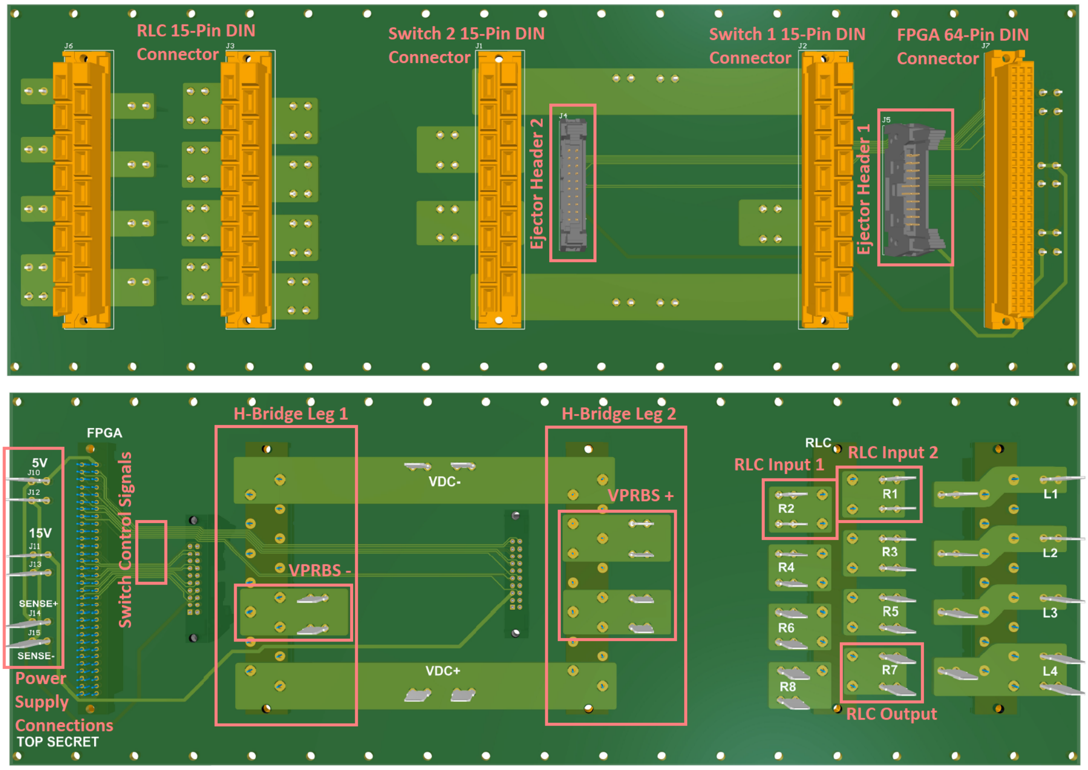

Figure 3.9: Backplate PCB labelled with its various important constituents.

The constituents that make up the backplate design are indicated and labelled in red on Fig. 3.9 and are discussed below:

- **DIN connectors:** Female 15-Pin and 64-Pin DIN connectors are used to electrically and structurally connect the backplate to the PCBs described in the previous subsections.

- **Power supply connections:** The power supply is a separate unit and thus is connected to the backplate, and subsequently all other related PCBs, with spade terminals and copper cables. There are connections for the 5V and 15V live and neutral terminals to power the FPGA and IGBT/driver modules, respectively. The EPLAX Bivolt PK60B has an optional sensing circuit to compensate for voltage drops during transmission. The compensation is not necessary as the cable size and distance are not significant enough for voltage drops to be a concern.

- **Ejector headers and switch control signal:** As shown in Fig. 3.5, the ejector header for connecting the IGBT driver control signals is located perpendicular to the IGBT PCB. Due to limited space, the control signals from the FPGA are not routed through the switch PCB 15-Pin DIN connector but are alternatively routed to a set of ejector headers soldered to the backplate. A ribbon cable is used to connect the control lines from the ejector header on the backplate with the ejector header located on the IGBT driver module.

- **H-Bridge legs and VPRBS:** Each H-Bridge leg consists of two IGBTs in series. The centre point of each leg is indicated as VPRBS+/VPRBS-, VPRBS+ has two copper pours to allow for more connections. The two pours are connected internally within the IGBT module. The VDC- and VDC+ connections are indicated on the PCB to indicate the orientation of the IGBT modules.
- **RLC input 1:** If no additional series capacitor is included in the RLC circuit, then the VPRBS+ terminal should be connected to one of these terminals using copper cables terminated with female spade connectors.
- **RLC input 2:** These terminals should be used as input to the RLC PCB if an additional series capacitor is included in the RLC circuit.
- **RLC output:** This terminal is the output terminal of the RLC circuit PCB, and is the connection point for the DUT.

Table 3.4 below provides a comprehensive list of the components required to assemble the backplate design.

Table 3.4: Backplate parts list.

Part Name	Part Description
Spade Connector	RS PRO Yellow Insulated Spade Connector 6.35 x 0.8mm Tab Size, 4mm^2 to 6mm^2
Spade Terminal	TE, FASTON .250 Grey Uninsulated Spade Connector, 6.35 x 0.83mm Tab Size
Ejector Header	Amphenol ICC, Quickie, 20 Way 2 Row, Straight PCB Header
15-Pin Power DIN Female	HARTING, DIN 41612 15 Way, 10.16mm Pitch Straight, Connector, Socket
64-Pin DIN Female	Harting 64 Way 2.54mm Pitch, Type B Class C2, 2 Row, Straight DIN 41612 Connector, Socket

3.2.5. Subrack design

All PCBs were manufactured to the Eurocard standard. This standardisation allows the circuit board to be used in any equally standardised mounting system. The mounting system used in the design is a 19” KM6-II subrack. The overall design works much like one would file documents in a filing cabinet. The backplate is mounted to the rear of the subrack, and the various PCBs are slotted in on guides to connect to the backplate. This allows the PCBs to easily be inserted and removed from the subrack.

The Eurocard standard unit of length is Horizontal Pitch (HP) which equates to 5.08mm. The guides used to slot in the various PCBs can be attached to the subrack chassis in increments of 1HP. The DIN connectors found on the backplate in Fig. 3.9, therefore, are placed apart from one another in multiples of 5.08mm to allow for the PCB design to be compatible with the subrack standard [83]. The Verotec KM6-II subrack used for the design is 84HP in width with a depth of 240mm and a standardised height of 3U, which translates to a 100mm PCB height. A pair of backplane spacers and one-part guides should be ordered as recommended in the catalogue [84]. Table 3.5 provides a full breakdown of all the components purchased for the subrack chassis.

Table 3.5: Subrack parts list.

Part Name	Part Description
KM6-II Subrack	3U height, 240mm depth, 84HP (84 x 5.08mm)
Backplate Spacers	Insulated spacing between backplane and tapped stripped (for screws)
One Part Guides	Guides for inserting 1.6mm x 220mm PCBs

3.2.6. FPGA control software

The FPGA software was programmed in VHDL as part of another parallel running research project. The software allows the user to select the order, length, number of repetitions, and clock frequency of the PRBS control signals that are sent to the H-Bridge switches. The seed for the PRBS generation is set as ones for any PRBS order chosen by the user. Appendix E provides a screenshot of the Graphical User Interface (GUI) developed in Python that can be used to set the PRBS generation parameters and subsequently flashed onto the FPGA development board.

3.3. Source design validation

A 3D model of the source is shown in Fig. 3.10, the source consists of the five PCBs discussed above and a power supply unit that fit together to form a modular design topology. The subrack is 244mm x 483mm x 132mm so as to make it easy for a single person to transport and carry. The RLC card is easily configurable to meet the operator's RLC circuit choice. Verotec offers cases compatible with the KM6-II subrack, the case protects the internal circuit from physical damage as well as provides Electromagnetic Compatibility (EMC) and Radio Frequency Interference (RFI) protection [85].

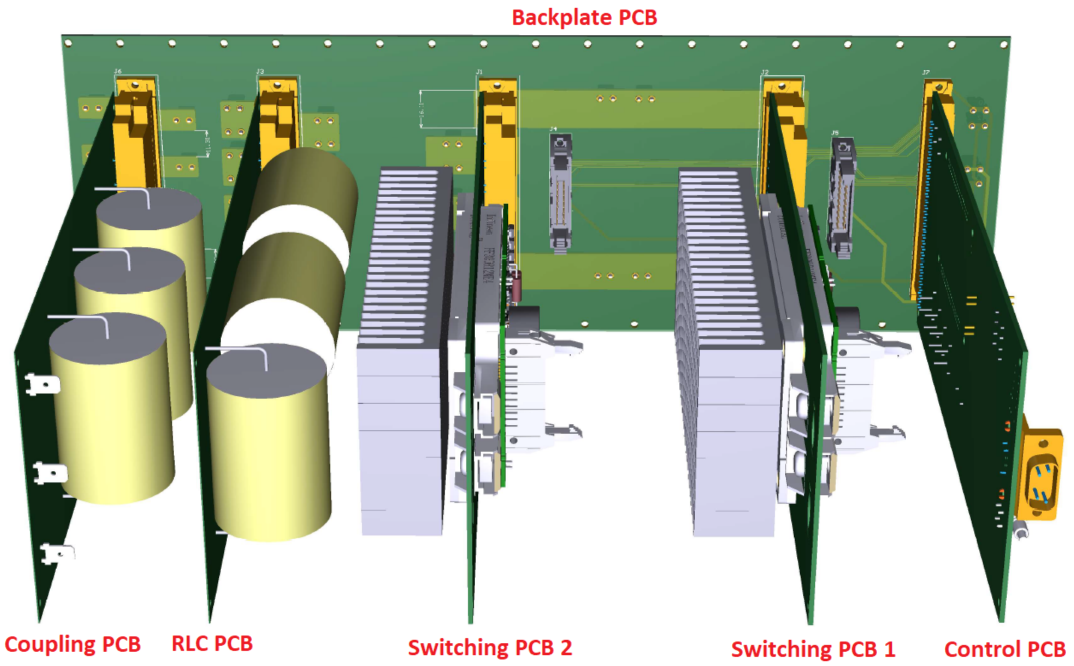

Figure 3.10: Three-dimensional overview of the source design generated in Altium Designer.

A 15Ω resistive load is perturbed experimentally by the PRIS source. Fig. 3.11 presents the results of the source validation whereby the practical measurements of the input voltage and current, $v_{in}(t)$ and $i_{in}(t)$, are compared to a simulation of the same topology. The RLC circuit parameters are chosen as 57.1Ω, $1mH$, and $4\mu F$, respectively. Four cycles of a 4^{th} order PRBS at a clock frequency of 10kHz are shown in the figure. It is clear that the PRBS state transitions occur at the same instances as in simulation, which validates the correct operation of the switching legs. The RLC circuit functions correctly as the waveforms have similar time constants with slight variation in amplitude.

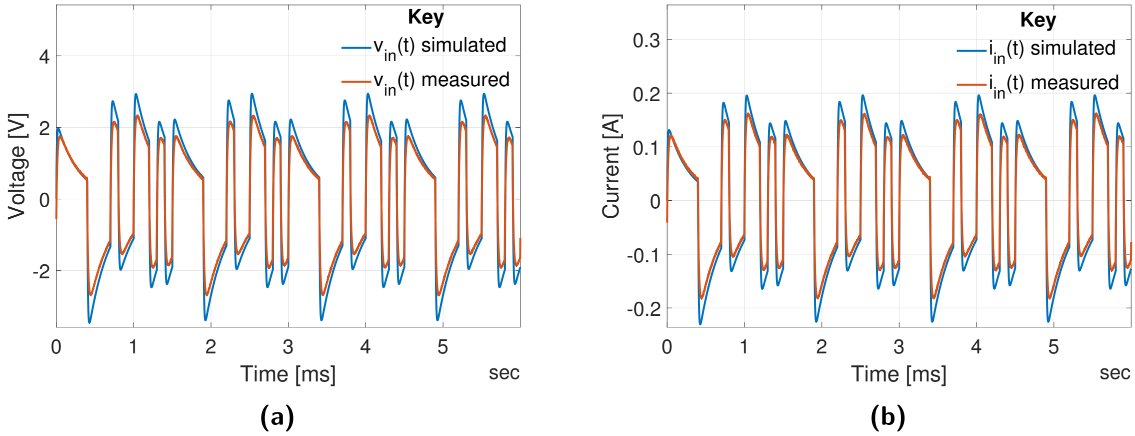

Figure 3.11: Practically measured and simulated perturbation input **(a)** voltage and **(b)** current of a 15Ω load under PRIS perturbation.

The resistances of the tracks and cables within the arrangement are measured and included in the simulation, the inclusion of the line resistances raises the total resistance to 61.2Ω. The capacitance and inductance of the components are measured using an LCR meter to be 1.024mH and 3.707μF, respectively whilst the load is measured to be 15.3Ω. The circuit parameters are adjusted in simulation to reflect these measurements. The resulting simulation compared to the practical measurements in Fig. 3.12 shows the results match more closely after the inclusion. The remaining error could be accounted for through losses as well as the parasitic inductance and capacitance of the IGBTs that are not taken into account in the simulation.

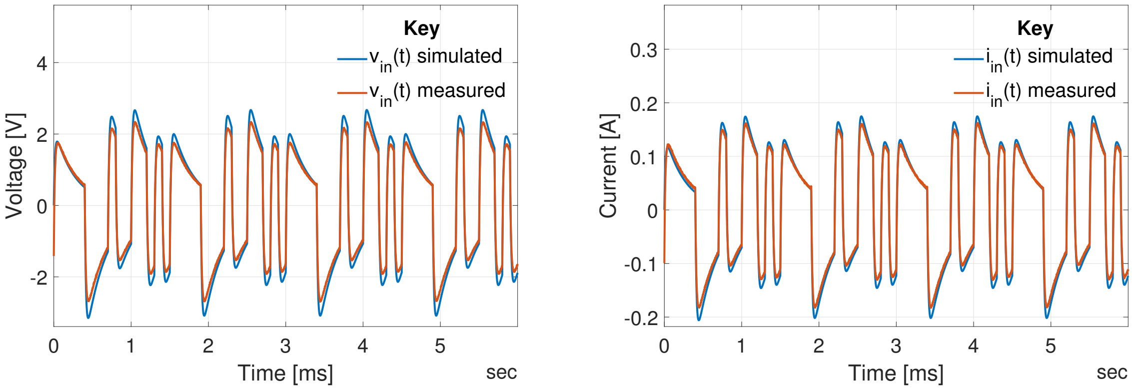

(a) **(b)**

Figure 3.12: Practically measured and simulated perturbation input **(a)** voltage and **(b)** current of a 15.3Ω load under PRIS perturbation, with measured resistances, inductance and capacitance.

Chapter 4

Parameter Estimation of Simulated Cascaded Transformer Winding Models

This chapter focuses on the use of the PRIS perturbation source to obtain the wideband frequency response measurements of two cascaded transformer winding models in simulation. These responses are then subsequently applied to various parameter estimation techniques. The chapter serves as an introduction to the implementation of PRIS perturbation in the context of transformer-based circuit models as well as an investigative study into various parameter estimation techniques to solve for the parameter values of the winding models.

4.1. Two-section transformer winding model

This section focuses on the implementation through simulation of the PRIS source in an offline perturbation arrangement of a two-section transformer winding model. Analytical expressions of the Laplace-domain input impedance and voltage ratios that represent the model are derived and these expressions are then used to validate the frequency responses obtained through PRIS perturbation of the target model. A frequency domain parameter estimation methodology is applied to solve the model parameters. The purpose of this investigation is to perform a perturbation and parameter estimation methodology in a simplified and controlled environment prior to the practical implementation, allowing each step in the methodology to be verified.

4.1.1. Analytical derivation of model frequency responses

An analytical expression for the input impedance of a passive circuit model can be derived by formulating mesh current equations for each loop in the model and re-arranging them to set up a matrix equation in the general form below:

$$\mathbf{ZI} = \mathbf{V} \tag{4.1}$$

where

$$\mathbf{Z} = \begin{bmatrix} Z_{11} & Z_{12} & \dots & Z_{1n} \\ Z_{21} & Z_{22} & \dots & Z_{2n} \\ \vdots & \vdots & \ddots & \vdots \\ Z_{n1} & Z_{n2} & \dots & Z_{nn} \end{bmatrix}, \tag{4.2}$$

$$\mathbf{I} = \begin{bmatrix} I_1 \\ I_2 \\ \vdots \\ I_{in} \end{bmatrix} \tag{4.3}$$

and

$$\mathbf{V} = \begin{bmatrix} 0 \\ 0 \\ \vdots \\ V_{in} \end{bmatrix}. \tag{4.4}$$

The Laplace-domain input impedance transfer function can now be determined by using

$$Z_{in}(s) = \frac{V_{in}(s)}{I_{in}(s)} = \frac{\Delta_Z}{\Delta_{(n,n)}}, \tag{4.5}$$

where Δ_Z is the determinant and $\Delta_{(n,n)}$ is the (n,n)-th cofactor of $\mathbf{Z}$.

This methodology can be applied to the simplified two-section transformer winding model shown in Fig. 4.1. The inductors, L_i and L_j, are mutually coupled to form a mutual inductance, M_{ij}, that is defined mathematically by the general relationship:

$$M_{ij} = k_{ij}\sqrt{L_i L_j} \quad 0 < k_{ij} < 1, \tag{4.6}$$

where k_{ij} refers to the coupling coefficient between inductors L_i and L_j. It is expected in practical transformers for the lumped inter-turn or inter-layer capacitances, C_1 and C_2, to be larger than capacitances between winding sections and ground, thus winding to ground capacitances are omitted in this initial case study [19].

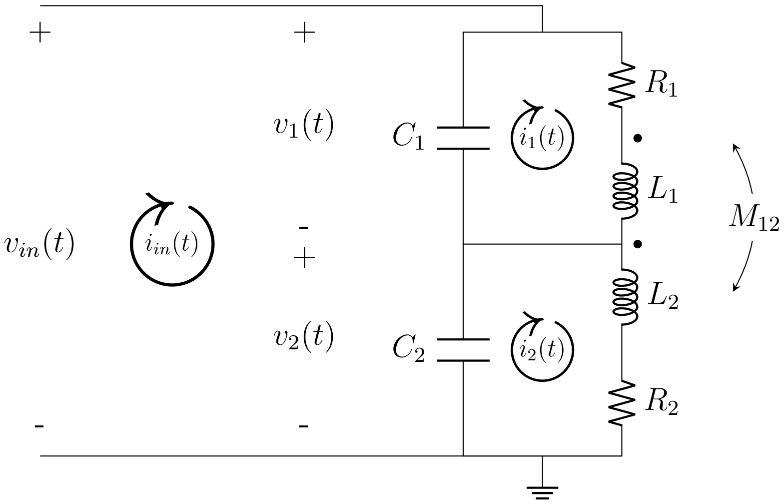

Figure 4.1: Cascaded two-section lumped parameter transformer winding model [19].

The mesh currents defined by $i_1(t)$, $i_2(t)$ and $i_{in}(t)$ are used to form the matrix equation:

$$\begin{bmatrix} sL_1 + \frac{1}{sC_1} + R_1 & sM_{12} & \frac{1}{sC_1} \\ sM_{12} & sL_2 + \frac{1}{sC_2} + R_2 & \frac{1}{sC_2} \\ \frac{1}{sC_1} & \frac{1}{sC_2} & \frac{1}{sC_1} + \frac{1}{sC_2} \end{bmatrix} \begin{bmatrix} I_1(s) \\ I_2(s) \\ I_{in}(s) \end{bmatrix} = \begin{bmatrix} 0 \\ 0 \\ V_{in}(s) \end{bmatrix}, \tag{4.7}$$

where $I_1(s)$, $I_2(s)$, $I_{in}(s)$ and $V_{in}(s)$ are Laplace transforms of the associated time-domain signals.

The impedance matrix, $\mathbf{Z}$, is then subsequently used to calculate three frequency response transfer functions to represent the circuit. An input impedance transfer function, $Z_{in}(s)$, and two voltage ratio transfer functions, $R_{1,in}(s)$ and $R_{2,in}(s)$, these transfer function are in the form defined in (4.8),(4.9) and (4.10), respectively.

$$Z_{in}(s) = \frac{V_1(s)}{V_{in}(s)} = \frac{\alpha_1 s^3 + \alpha_2 s^2 + \alpha_3 s + \alpha_4}{\beta_1 s^4 + \beta_2 s^3 + \beta_3 s^2 + \beta_4 s + \beta_5} \tag{4.8}$$

$$R_{1,in}(s) = \frac{V_1(s)}{V_{in}(s)} = \frac{\alpha_1 s^3 + \alpha_2 s^2 + \alpha_3 s + \alpha_4}{\beta_1 s^3 + \beta_2 s^2 + \beta_3 s + \beta_4} \tag{4.9}$$

$$R_{2,in}(s) = \frac{V_2(s)}{V_{in}(s)} = \frac{\lambda_1 s^3 + \lambda_2 s^2 + \lambda_3 s + \lambda_4}{\beta_1 s^3 + \beta_2 s^2 + \beta_3 s + \beta_4} \tag{4.10}$$

The input impedance, $Z_{in}(s)$, is calculated using (4.5) and the voltage ratios are determined by assuming an input step voltage of 1V, this assumption allows for the determination of the currents $I_1(s)$, $I_2(s)$ and $I_{in}(s)$ and subsequently the voltages $V_1(s)$ and $V_2(s)$ using the following equations:

$$R_{1,in}(s) = \frac{V_1(s)}{V_{in}(s)} = \frac{V_1(s)}{1} = -I_1(s)\cdot(\frac{1}{sC_1}), \tag{4.11}$$

$$R_{2,in}(s) = \frac{V_2(s)}{V_{in}(s)} = \frac{V_2(s)}{1} = -I_2(s)\cdot(\frac{1}{sC_2}). \tag{4.12}$$

The associated transfer function coefficients are defined in terms of the circuit elements and are listed in Table. 4.1.

Table 4.1: Transfer function coefficients for $Z_{in}(s)$,$R_{1,in}(s)$ and $R_{2,in}(s)$.

Coefficient	$Z_{in}(s)$	$R_{1,in}(s)$ and $R_{2,in}(s)$
α_1	$(C_1+C_2)(L_1L_2-M_{12}^2)$	$(C_2)(L_1L_2-M_{12}^2)$
α_2	$(C_1+C_2)(L_1R_2+L_2R_1)$	$(C_2)(L_1R_2+L_2R_1)$
α_3	$L_1+L_2+2M_{12}+R_1R_2(C_1+C_2)$	$L_1+M_{12}+R_1R_2C_2$
α_4	R_1+R_2	R_1
λ_1		$(C_1)(L_1L_2-M_{12}^2)$
λ_2		$(C_1)(L_1R_2+L_2R_1)$
λ_3		$L_2+M_{12}+R_1R_2C_1$
λ_4		R_2
β_1	$(C_1C_2)(L_1L_2-M_{12}^2)$	$(C_1+C_2)(L_1L_2-M_{12}^2)$
β_2	$(C_1C_2)(L_1R_2+L_2R_1)$	$(C_1+C_2)(L_1R_2+L_2R_1)$
β_3	$(C_1L_1+C_2L_2+C_1C_2R_1R_2)$	$R_1R_2(C_1+C_2)+L_1+L_2+2M_{12}$
β_4	$C_1R_1+C_2R_2$	R_1+R_2
β_5	1	0

4.1.2. Simulated model perturbation and validation of frequency responses

The frequency-domain transfer function, $H_{xy}(f)$, for a linear time-invariant system can be calculated using the formula [86]

$$H_{xy}(f) = \frac{Y(f)}{X(f)}, \tag{4.13}$$

where $Y(f)$ and $X(f)$ are the DFTs of the input and output signal, respectively. This method is rudimentary as the accuracy of the resulting transfer function is highly influenced by the system noise level [86]. An alternative approach uses the power spectrum of the input and output signals in conjunction with spectral estimation techniques to improve the SNR. The resulting transfer function for a single-input single-output system thus becomes [86, 87]:

$$H_{xy}(f) = \frac{P_{xy}(f)}{P_{xx}(f)}, \tag{4.14}$$

where $P_{xy}(f)$ is the cross power spectral density of signal $x(t)$ and $y(t)$, while $P_{xx}(f)$ is the PSD of signal $x(t)$. The MATLAB Signal Processing Toolbox [87] makes use of the *tfestimate* function to determine the frequency domain transfer function using (4.14). The PSDs $P_{xx}(f)$ and $P_{xy}(f)$ are determined using the *pwelch* spectral estimator with a window function, window size and percentage overlap as specified by the user. As discussed in Chapter 2, a larger window size results in improved spectral resolution at the cost of decreasing the number of windows that can be averaged. In this context there is no need for significant averaging as the simulation environment does not contain any additional noise. Thus, for the remainder of this chapter a window size of half the entire data length is applied. As motivated in Chapter 2, a 62.5 % overlap in combination with a Hann window function is suitable in most cases of power system identification and is thus chosen.

The offline perturbation arrangement implemented in MATLAB Simulink is shown in Fig. 4.2. The model parameter values in Table 4.2 are used by Brozio [19] to investigate and explain the resonant behaviour of an isolated winding. These parameters are used in the remainder of the investigation to compare the frequency responses obtained through simulated perturbation with that obtained from the analytical expressions.

Table 4.2: Parameter values for the model shown in Fig. 4.1.

$R_1[\Omega]$	$R_2[\Omega]$	$C_1[nF]$	$C_2[nF]$	$L_1[H]$	$L_2[H]$	$M_{12}[H]$
10	10	1	1	10	100	30

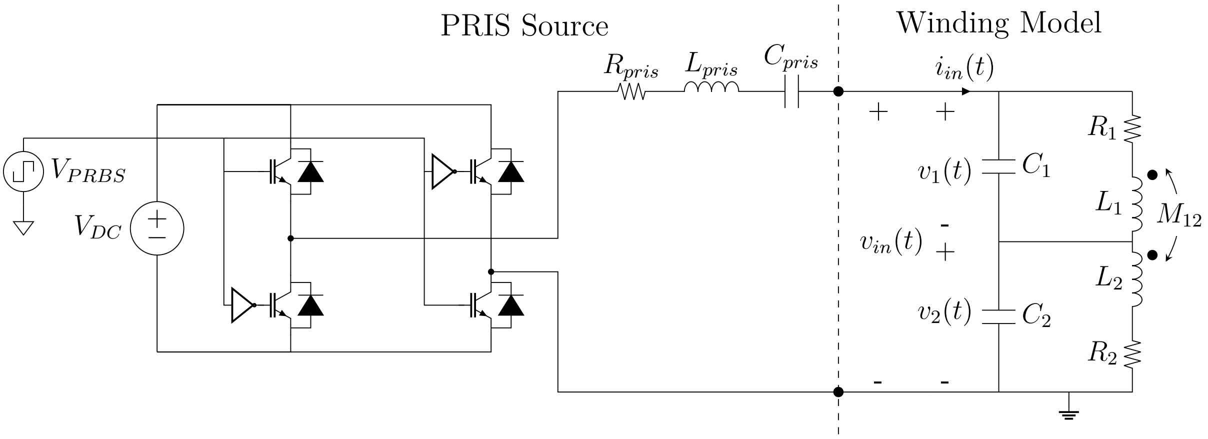

Figure 4.2: Test arrangement to perturb the two-section winding model [88].

It stands to reason that in an offline perturbation arrangement, the transformer winding model is placed in series with the PRIS source's RLC circuit. The impedance of the winding in series with the RLC circuit influences the perturbation current $i_{in}(t)$, the current will, therefore, not be the ideal train of impulses as depicted in Fig. 2.13. If it is necessary for the perturbation current to exhibit the exact spectral properties of the ideal signal, then the RLC circuit needs to be the dominant influence on the current. This can be achieved by selecting the RLC circuit parameters such that its impedance magnitude is much greater than the input impedance magnitude of the DUT. The disadvantage of this approach is that most of the perturbation energy is dissipated in the RLC circuit resulting in a low SNR of measurements taken across the DUT. This presents a tradeoff between choosing a set of RLC circuit parameters that have a high impedance compared to the input impedance of the DUT, allowing the RLC circuit to fully control the PSD of the perturbation, and taking away perturbation energy from the device under test thus decreasing the SNR.

An iterative approach is applied for RLC selection to emulate an application whereby very little *a priori* knowledge is known of the DUT. The selection of the τ_1 and τ_2 parameters of the perturbation is documented by Mwaniki [15], where the author presents the effects of the time constants on the resulting perturbation power spectrum. A specific choice of time constants can be achieved by an infinite combination of RLC values. In offline perturbation arrangements, the RLC component selection is coupled with the criterion for a specific RLC impedance magnitude that is comparable to the input impedance of the DUT.

Figures 4.3, 4.5 and 4.6 presents simulated power spectral densities of the input voltage and current, $V_{in}(\omega)$ and $I_{in}(\omega)$, and input impedances, $Z_{in}(\omega)$, for various choices of RLC parameters. In all three investigations, the RLC combinations produce the same impulse τ_1 and τ_2 time constants, but the RLC circuit impedance magnitudes vary between small, similar, and large compared to the winding model input impedance. The RLC circuit impedance magnitude, $Z_{rlc}(\omega)$, is calculated analytically and presented by dashed lines. The impedance magnitude is scaled by α using the following relationships:

$$R_{pris(new)} = R_{pris(base)} \cdot \alpha, \tag{4.15}$$

$$L_{pris(new)} = L_{pris(base)} \cdot \alpha, \text{ and} \tag{4.16}$$

$$C_{pris(new)} = C_{pris(base)} \cdot \frac{1}{\alpha}, \tag{4.17}$$

where $R_{pris(base)} = 31.8\Omega$, $L_{pris(base)} = 253mH$ and $C_{pris(base)} = 10\mu F$. Figures 4.3a and 4.3b show the simulated current and voltage power spectral densities along with the resulting input impedance frequency response when $\alpha = 1$ and the RLC circuit impedance magnitude is much lower than the magnitude of the winding model input impedance. The voltage power spectral density measured at the winding model terminals is essentially a PRBS power spectrum. Due to the voltage PSD being controlled by the H-Bridge switching, the majority of the resonant behaviour of the winding model is reflected in the PSD of the current.

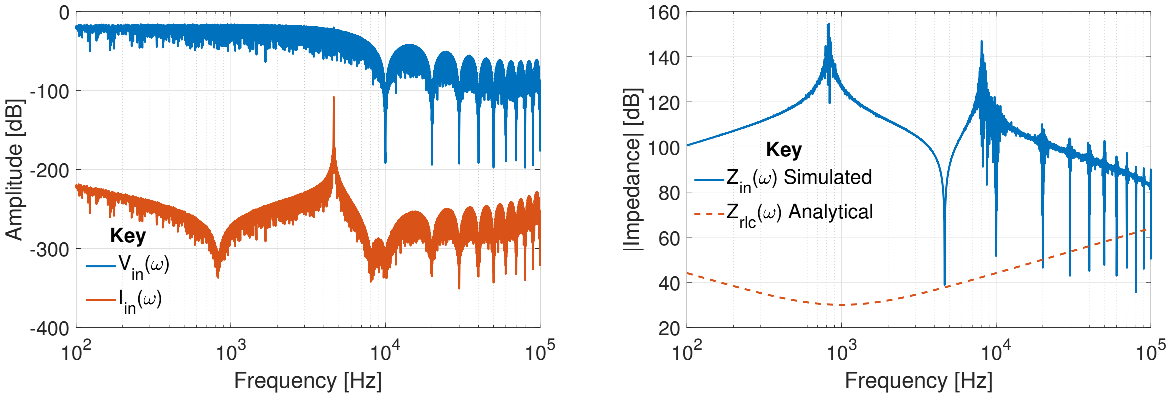

(a) **(b)**

Figure 4.3: **(a)** Power spectral densities and **(b)** input impedance for a comparably low RLC impedance magnitude compared to the DUT input impedance.

The current waveform with fast rise times is shown in Fig. 4.4. The fast switching that occurs at the PRBS switching instances causes the capacitive nature of the winding to dominate the current waveform in cases when the RLC circuit impedance magnitude is comparably low to the input impedance of the winding model. The fast current rise times as a result of the winding capacitance are difficult to sample thereby causing aliasing in the frequency response measurements.

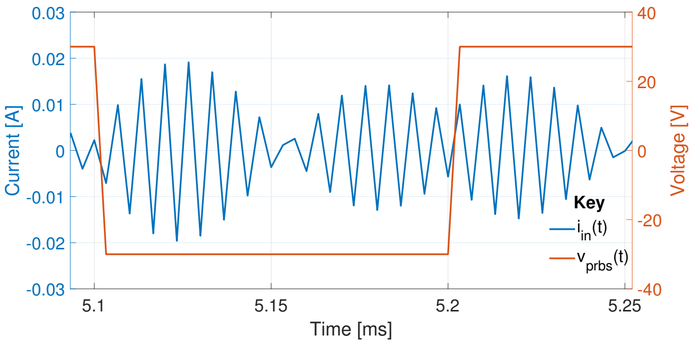

Figure 4.4: Insufficient sampling of the input current, $i_{in}(t)$, due to the fast rise times at the PRBS switching instances with a low RLC impedance.

Figures 4.5a and 4.5b show the simulated current and voltage PSDs along with the resulting input impedance frequency response obtained when $\alpha = 1000$ and the RLC impedance magnitude is similar to the magnitude of the winding model input impedance. The aliasing has been mitigated and the results show a frequency response devoid of variance. In this case, the winding model and RLC circuit have an approximately equitable influence on the perturbation current thus the current PSD does not resemble the ideal PRIS spectrum. The resonant behavior of the winding model is also reflected in both the current and voltage PSDs.

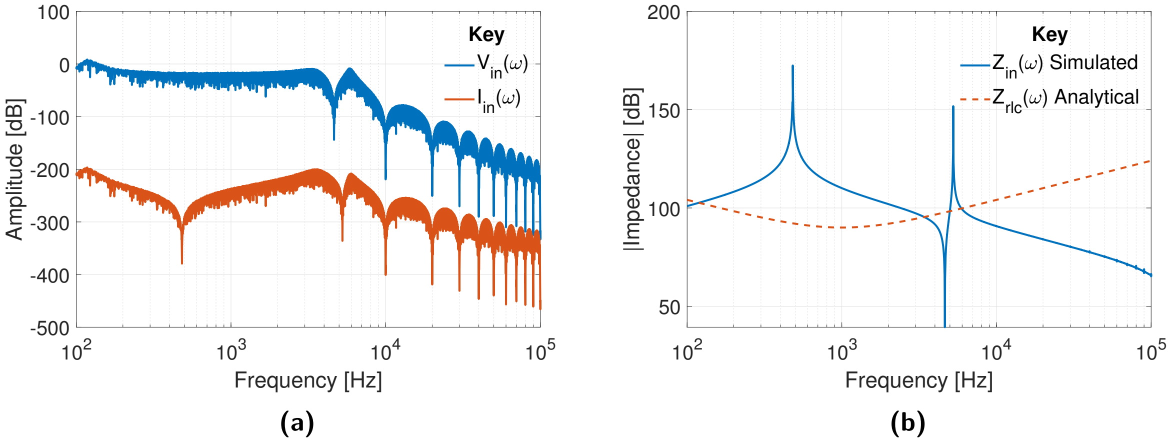

Figure 4.5: **(a)** Power spectral densities and **(b)** input impedance for a comparably similar RLC impedance magnitude compared to the DUT input impedance.

Figures 4.6a and 4.6b show the PSDs and input impedance obtained when $\alpha = 10^6$ and the RLC circuit impedance magnitude is much larger than the magnitude of the winding model input impedance. In this case, the current PSD is indicative of the ideal PRIS PSD, which is to be expected as the RLC circuit is dominating the control of the perturbation current. The resonances that result from the winding model are thus reflected in the voltage PSD. The disadvantage of this methodology is the current perturbation energy is greatly reduced, which in practical measurements could cause SNR limitations.

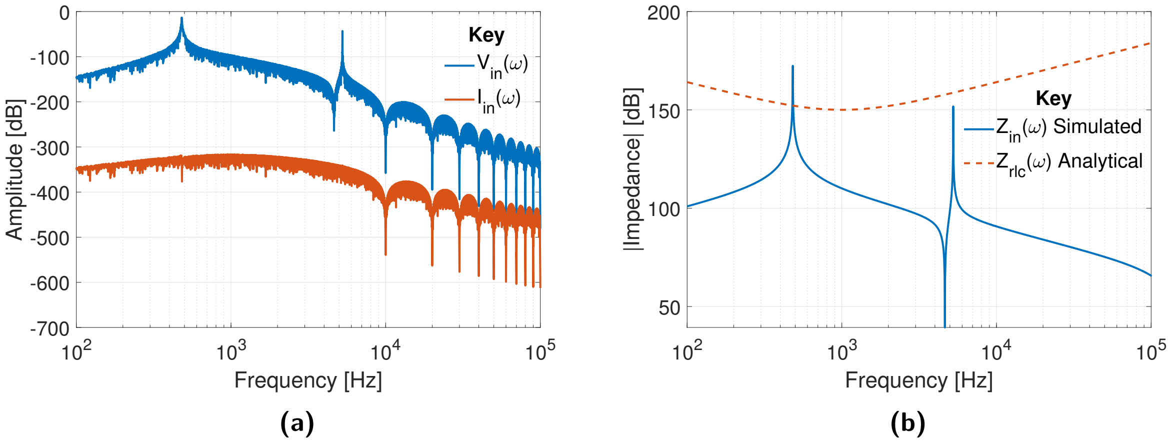

Figure 4.6: **(a)** Power spectral densities and **(b)** input impedance for a comparably high RLC impedance magnitude compared to the DUT input impedance.

The final PRIS perturbation arrangement uses a 30V DC voltage switching with a PRBS clock frequency of $f_{clk} = 10$kHz. The RLC circuit parameters are chosen to maintain a similar impedance magnitude compared to the winding model resulting in a $R_{pris} = 31.8k\Omega$, $L_{pris} = 2.53H$ and $C_{pris} = 10nF$. The winding is perturbed in simulation for 300ms with a sampling frequency, $f_s = 300kHz$. Fig. 4.7 presents a comparison of $Z_{in}(\omega), R_{1,in}(\omega)$ and $R_{2,in}(\omega)$ obtained through the simulated PRIS perturbation and analytical expressions in (4.8) to (4.10), respectively. From these results, it is clear that the offline PRIS perturbation arrangement is able to obtain the input impedance and voltage ratio frequency response.

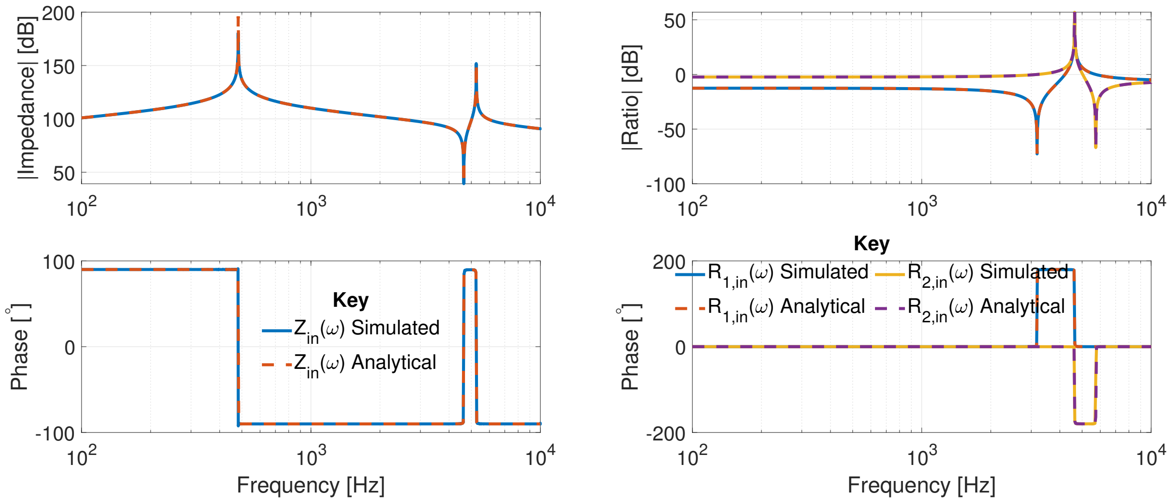

(a) **(b)**

Figure 4.7: Comparison between the magnitude and phase responses obtained analytically and through simulated PRIS perturbation of the **(a)** input impedance and **(b)** voltage ratios [88].

4.1.3. Parameter estimation methodology

Fig. 4.8 shows a block diagram of the parameter estimation methodology adopted in this investigation. The methodology adopted to solve for the model parameters makes use of the three frequency responses in the previous section.

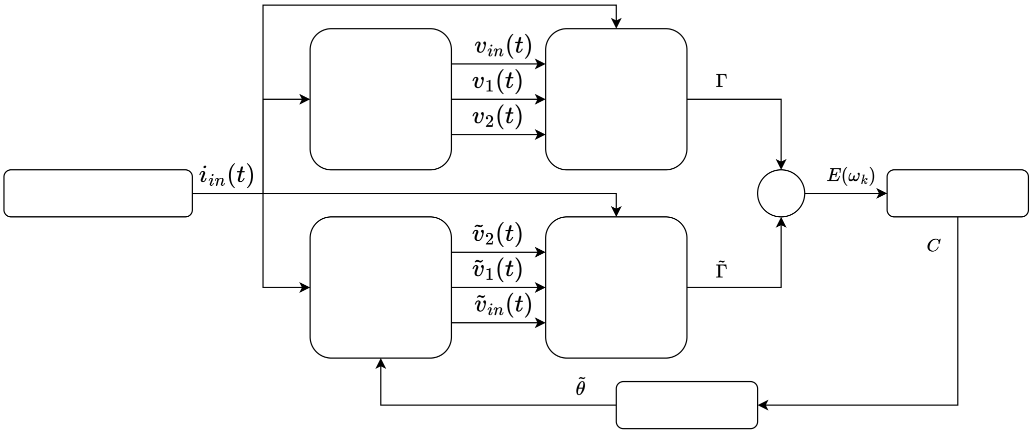

Figure 4.8: Overview of frequency domain parameter estimation methodology.

The PRIS perturbation source is applied to the target model and the estimated model in simulation. From the time-domain signals the set of frequency responses of the relevant transfer functions for both the target and estimate models, denoted by Γ and $\tilde{\Gamma}$, are determined. A set of errors, $E(\omega_k)$, are defined as the difference between the frequency response sets and subsequently used in a cost function formulation, C. The estimated model parameters, $\tilde{\theta}$, are iteratively updated by the optimisation algorithm until the cost function is minimised. Various case studies that make use of different combinations of the three frequency responses in Γ and $\tilde{\Gamma}$, are considered. The set of transfer function frequency responses can be expressed mathematically in the form

$$\Gamma = \{\gamma_r | r = 1, 2 ... N_r\}, \tag{4.18}$$

where γ_r is the r^{th} transfer function in the set Γ. Table 4.3 summarises the different definitions adopted for Γ based on the various parameter estimation case studies.

Table 4.3: Cost functions applied to parameter estimation case studies [88].

Cost Function	N_r	Transfer Function Set
A	1	$\Gamma = \{Z_{in}(w)\}$
B	2	$\Gamma = \{Z_{in}(w), R_{2,in}(w)\}$
C	3	$\Gamma = \{Z_{in}(w), R_{2,in}(w), R_{1,in}(w)\}$

The set of errors, $E(\omega_k)$, between the magnitudes of the frequency response of the target and estimated models are determined on a point-by-point basis for each frequency sample ω_k, such that

$$E(\omega_k) = \{\epsilon_r(\omega_k) | r = 1, 2, 3 ... N_r\}, \tag{4.19}$$

where

$$\epsilon_r(\omega_k) = \log_{10} |\gamma_r(\omega_k)| - \log_{10} |\tilde{\gamma_r}(\omega_k)|. \tag{4.20}$$

The magnitudes of the frequency response transfer functions vary over several decades, therefore the errors are defined in terms of the logarithms of the magnitudes. The cost function, C, is defined by the relationship

$$C = \sum_{r=1}^{N_r} \left[\sum_{k=1}^{N_k} (\epsilon_r(\omega_k))^2 \right]. \tag{4.21}$$

The sample frequencies ω_k are distributed logarithmically up to N_k samples, such that the contributions from $\epsilon_r(\omega_k)$ to the cost function are distributed equitably across the frequency range of interest.

The target circuit presented in Fig. 4.1 has seven parameters to be estimated, which translates to a complex multi-dimension optimisation problem. To simplify the optimisation, it is useful to implement constraints on the parameter values. The following constraints are adopted in this investigation:

- The winding sections are typically of the same physical dimensions as assumed by Chanane [14] and Keyhani [8]. Therefore, the model is simplified using the assumptions $C_1 = C_2$ and $R_1 = R_2$.
- The coupling coefficient k_{12}, which is always bounded between zero and one, rather than mutual inductance, M_{12}, is estimated.

These constraints give rise to the following vector of parameters to be estimated:

$$\theta = [R_1, C_1, L_1, L_2, k_{12}]. \tag{4.22}$$

Table 4.4 summarises the boundary constraints adopted for the various parameters, the lower and upper bounds of the parameters aside from the coupling coefficient are chosen as a tenth of and ten times the target parameter values, respectively. These bounds are relatively conservative, in parameter estimation of practical measurements the bounds will need to be increased as the target parameters will be unknown. The coupling of most well-designed transformers are expected to be near unity, but is not practically able to reach unity, thus the bounds are chosen to reflect this assumption [89].

Table 4.4: Parameter boundary constraints [88].

Parameters	$R_1[\Omega]$	$C_1[nF]$	$L_1[H]$	$L_2[H]$	k_{12}
Lower Bound	1	0.1	1	10	0.9
Upper Bound	100	10	100	1000	0.99997

The *globalsearch* optimisation algorithm provided the most accurate model parameter estimates in this investigation, although it is relatively slow compared to some of the metaheuristic-based optimisation algorithms. The parameter estimation case studies can be summarised as follows:

- **Case study 1:** The parameter values are estimated using only the input impedance frequency response, $Z_{in}(\omega)$.
- **Case study 2:** The parameter values are estimated using the input impedance, $Z_{in}(\omega)$, in conjunction with the voltage ratio $R_{2,in}(\omega)$.
- **Case study 3:** The parameter values are estimated using both voltage ratios, i.e. $R_{1,in}(\omega)$ and $R_{2,in}(\omega)$, together with the input impedance $Z_{in}(\omega)$.
- **Case study 4:** Case study 2 is repeated with a decreased sampling frequency of $f_s = 100$kHz and a smaller simulation measurement window of 50ms.

- **Case study 5:** Case study 2 is repeated, however the set of frequency response from the estimated model, $\tilde{\Gamma}$, are obtained from the analytical transfer function expressions as opposed to through the simulation of the PRIS perturbation.

4.1.4. Parameter estimation results

Table 4.5 summarises the results obtained for the case studies listed above. The percentage error for the n^{th} model parameter is calculated using the relationship

$$Error(n) = \left|\frac{\theta(n) - \theta(\tilde{n})}{\theta(n)}\right| \times 100 \quad [\%], \tag{4.23}$$

where $\tilde{\theta}$ denotes the set of final parameter estimates and θ denote the set of target model parameters listed in Table 4.2.

Table 4.5: Parameter estimation results.

		R_1		C_1		L_1		L_2		M_{12}			
Case Study	Cost Function	Value [Ω]	Error [%]	Value [nF]	Error [%]	Value [H]	Error [%]	Value [H]	Error [%]	Value [H]	Error [%]	C	Runtime [mins]
1	A	9.9973	0.027	1.0000	0.000	100.000	900.0	10.000	90.00	29.9999	0.000	1.792×10^{-6}	5877
2	B	10.0391	0.391	1.0000	0.000	9.9999	0.001	100.00	0.000	29.9998	0.001	4.820×10^{-5}	1860
3	C	10.0006	0.006	1.0000	0.000	10.0000	0.000	100.00	0.000	29.9999	0.000	2.809×10^{-5}	3199
4	B	14.9172	49.17	0.8162	18.38	10.0336	0.336	125.34	25.34	33.3094	11.03	1.831×10^{3}	2101
5	B	55.6582	456.6	1.0049	0.491	9.9574	0.426	99.587	0.413	29.8749	1.404	3.383×10^{2}	9

The cost function in case study 1 is low, indicating good correlation between the target and estimate impedance frequency response. However, the parameters L_1 and L_2 are swapped around, this speaks to an important concept addressed by Keyhani [8] whereby in some cases it is not possible to obtain a unique solution to the problem. Even though the estimated input impedance, $\tilde{Z}_{in}(\omega)$, is similar to the target model's input impedance, $Z_{in}(\omega)$, the individual model parameters are incorrect. Fig. 4.9 shows the input impedance frequency responses when the parameter L_1 and L_2 switch values, the frequency response remained the same meaning that it is not possible to obtain unique values for these parameters using only the measurement of $Z_{in}(\omega)$.

The inclusion of an extra measurement in case study 2 allowed for a unique solution to be obtained with a percentage error of below 1%. The inclusion of a third measurement in case study 3 improved the R_1 estimation error at the cost of a much longer runtime.

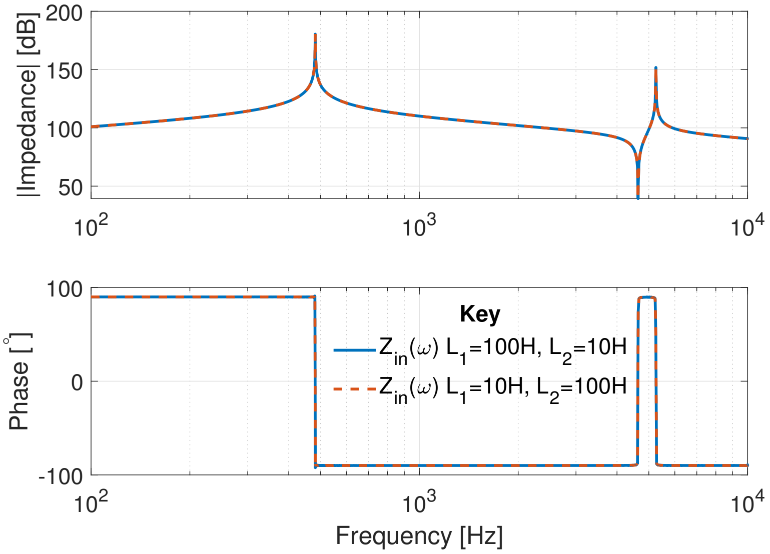

Figure 4.9: Magnitude and phase responses obtained when self-inductance's of L_1 and L_2 are switched.

In an attempt to improve the runtime of case study 2 the sampling frequency and simulation measurement window is reduced in case study 4. The high variance and aliasing affected the resultant frequency responses during perturbation and a desirable solution for the parameters could not be found. Thus, for accurate parameter estimation using simulated frequency responses from the estimated model a requirement is a high quality simulation with sufficiently long measurement times and a high sampling frequency. This requirement causes the parameter estimations of case studies 1-4 to take between one and three days to complete.

The parameter estimation procedure in case study 5 is able to obtain the general shape of the target frequency responses using the analytical transfer function expressions. The damping resulting from resistors R_1 and R_2 is low thereby not affecting the overall frequency response to a large degree, which in turn makes it challenging for the simulated frequency responses of the target model to obtain the resistive parameters. Thus even though the resistance error is large, the error is only visible close to the resonant peaks of the frequency responses. This decline in parameter estimation accuracy comes with a significant improvement in runtime, which presents an advantage in cases where more complex model topologies with more intensive simulations and larger parameter sets need to be solved.

4.2. Three-section transformer winding model

This section focuses on investigating the use of empirical mode decomposition strategies to improve the parameter estimation accuracy and computational times achieved from classical frequency and time-domain methodologies. The model under investigation is changed to a more complex three-section transformer winding model arrangement. The simulations performed in this section only make use of terminal voltage and current measurements to emulate a practical arrangement where internal connections to the transformer are not accessible.

4.2.1. Analytical derivation of model frequency response

The investigation targets the model shown in Fig. 4.10 identified by Chanane *et al.* [14] for a fully interleaved continuous-disc winding with 5 discs, consisting of 30 turns per disc, of copper conductor with a cross-sectional area of $10mm^2$. The winding features an insulated core with the insulation thickness and duct spacing corresponding to a 30kV rating.

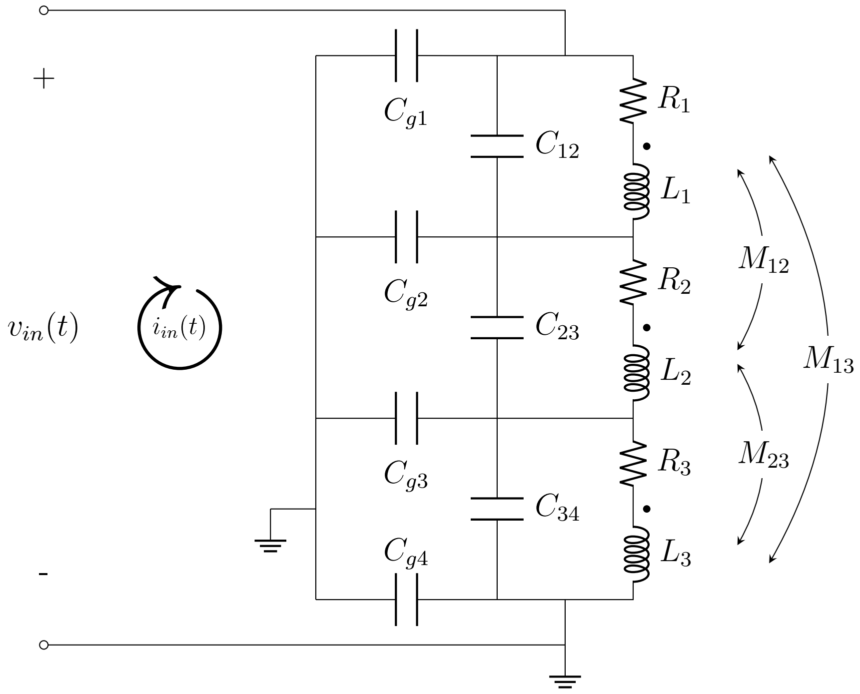

Figure 4.10: Three-section lumped parameter transformer winding model [14].

The model has a total of 16 parameters to be estimated. These can, however, be reduced by applying the following assumptions as Chanane *et al.* [14, 20, 21]:

- The winding sections have the same physical dimensions such that $R_1{=}R_2{=}R_3{=}R_s$ and $L_1{=}L_2{=}L_3{=}L_s$.
- The dimensions between sections are also assumed to be similar, and thus $C_{12}{=}C_{23}{=}C_{34}{=}C_s$.
- The capacitances from the individual sections to ground are equal, aside from the sections closest to the grounded core and tank, which is assumed to be half the ground capacitance, so $C_{g1}{=}C_{g4}{=}\frac{C_g}{2}$ and $C_{g2}{=}C_{g3}{=}C_g$.

The purpose of this section is to investigate various modal decomposition strategies to aid in the parameter estimation procedure, not to report on the practical implications of assuming transformer winding symmetry. Thus, the above assumptions are maintained for all investigations to follow in this section.

The impedance matrix, **Z**, is derived using the mesh currents as described in Section 4.1.1. This yields the 7x7 impedance matrix

$$\mathbf{Z} = \begin{bmatrix} Z_{11} & sM_{12} & sM_{13} & \frac{-1}{sC_{12}} & 0 & 0 & 0 \\ sM_{12} & Z_{22} & sM_{23} & 0 & \frac{-1}{sC_{23}} & 0 & 0 \\ sM_{13} & sM_{23} & Z_{33} & 0 & 0 & \frac{-1}{sC_{34}} & 0 \\ \frac{-1}{sC_{12}} & 0 & 0 & Z_{44} & \frac{-1}{sC_{g2}} & 0 & \frac{-1}{sC_{g1}} \\ 0 & \frac{-1}{sC_{23}} & 0 & \frac{-1}{sC_{g2}} & Z_{55} & \frac{-1}{sC_{g3}} & 0 \\ 0 & 0 & \frac{-1}{sC_{34}} & 0 & \frac{-1}{sC_{g3}} & Z_{66} & 0 \\ 0 & 0 & 0 & \frac{-1}{sC_{g1}} & 0 & 0 & Z_{77} \end{bmatrix}, \tag{4.24}$$

where the diagonal terms in the matrix are defined in Table 4.6.

Table 4.6: Diagonal entries of 4.24.

Diagonal	Value	Diagonal	Value
Z_{11}	$R_1 + sL_1 + \frac{1}{sC_{12}}$	Z_{55}	$\frac{1}{sC_{23}} + \frac{1}{sC_{g2}} + \frac{1}{C_{g3}}$
Z_{22}	$R_2 + sL_2 + \frac{1}{sC_{23}}$	Z_{66}	$\frac{1}{sC_{34}} + \frac{1}{sC_{g3}}$
Z_{33}	$R_3 + sL_3 + \frac{1}{sC_{34}}$	Z_{77}	$\frac{1}{sC_{g1}}$
Z_{44}	$\frac{1}{sC_{12}} + \frac{1}{sC_{g1}} + \frac{1}{sC_{g2}}$		

The input impedance $Z_{in}(s)$ of the three-section model can be derived from the impedance matrix **Z**, using the relationship in (4.5). The resulting analytical expression for the input impedance transfer function can be expressed as

$$Z_{in}(s) = \frac{\alpha_1 s^5 + \alpha_2 s^4 + \alpha_3 s^3 + \alpha_4 s^2 + \alpha_5 s + \alpha_6}{\beta_1 s^6 + \beta_2 s^5 + \beta_3 s^4 + \beta_4 s^3 + \beta_5 s^2 + \beta_6 s + \beta_7}. \tag{4.25}$$

The coefficients of the numerator and denominator are defined in terms of the model parameters in Appendix F. The analytical transfer function is derived without including the constraints introduced by the assumptions.

4.2.2. Simulated model perturbation and validation of frequency response

Various parameter estimation techniques are investigated in this section. These techniques make use of either the input impedance frequency response, voltage time-domain waveform or decomposed voltage time-domain waveform. Therefore, the terminal voltage and current waveforms under perturbation and the frequency-domain input impedance are reported.

The model parameters obtained by Chanane [14] are summarised in Table 4.7 and represent the target parameters for the various parameter estimation approaches to follow.

Table 4.7: Parameter values for the winding model in Fig. 4.10.

$R_s[\Omega]$	$C_s[pF]$	$C_g[nF]$	$L_s[\mu H]$	K_{12}	K_{13}	K_{23}
0.083	970	1.6	181	0.8792	0.8729	0.8564

The three-section winding model is perturbed at its terminals in MATLAB Simulink using the same PRIS arrangement presented in Fig. 4.2. The parameters for the PRIS circuit topology are chosen to be $R_{pris} = 150\Omega$, $L_{pris} = 4mH$, $C_{pris} = 1uF$ and $V_{dc} = 100V$. These parameters provide an RLC circuit that is both practically implementable and gives rise to an impedance response of a similar magnitude to the model. The PRIS signal is generated using a clock frequency, f_{clk}, of 100kHz and a 12^{th} order PRBS for frequency response simulations and a 6^{th} order PRBS for time-domain simulations.

Fig. 4.11 shows the voltage and current waveforms, $v_{in}(t)$ and $i_{in}(t)$, simulated at the terminals of the winding model for a single PRBS6 period. The voltage and current waveforms are subsequently used in the *tfestimate* MATLAB function to produce the winding model input impedance frequency response presented in Fig. 4.12. Fig. 4.12 also presents the input impedance frequency response obtained through the analytical expression in (4.25), the good correlation between the two responses validates the success of the PRIS perturbation.

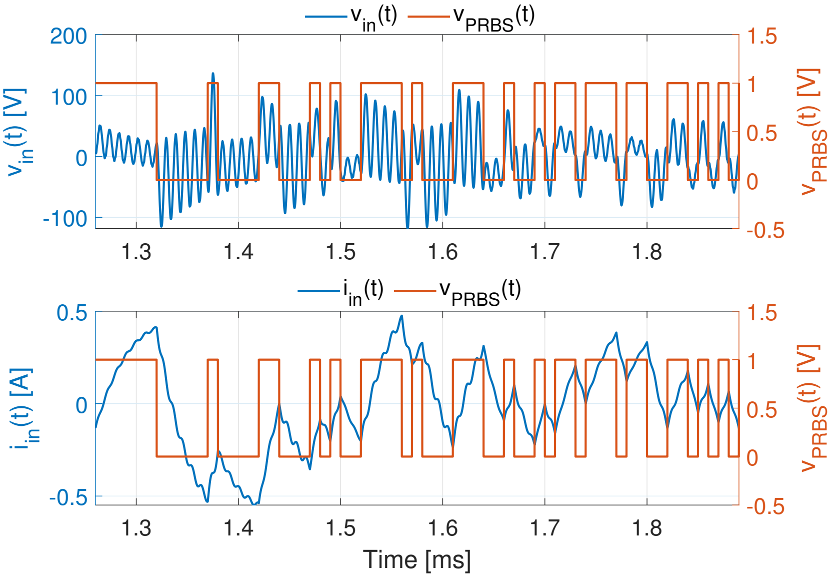

Figure 4.11: Extract of the simulated input voltage and current waveforms of the three-section model in Fig. 4.10 under PRIS perturbation [90].

The DUT responds during the rising and falling edges of the PRIS impulses, as such long PRIS signals with many state transitions are not necessary to capture the system's dynamics during time-domain simulations. Longer perturbations are required for the frequency-domain input impedance simulations so as to improve the frequency resolution. The frequency resolution for a Hanning window is equal to its main lobe width, which can be calculated as follows [91]:

$$f_{res} = \frac{4}{M}, \tag{4.26}$$

where M is the window length in seconds. Thus a 12^{th} order PRBS in conjunction with a Hanning window size of half the time-domain data results in a frequency resolution of 152.59Hz. This frequency resolution is acceptable due to the relatively high locations of the winding resonances on the frequency spectrum. The high location of the winding resonances has the inverse effect of requiring a high PRBS clock frequency of 100kHz to focus the PRIS spectral energy at a high enough frequency to sufficiently perturb the frequency range of the resonances.

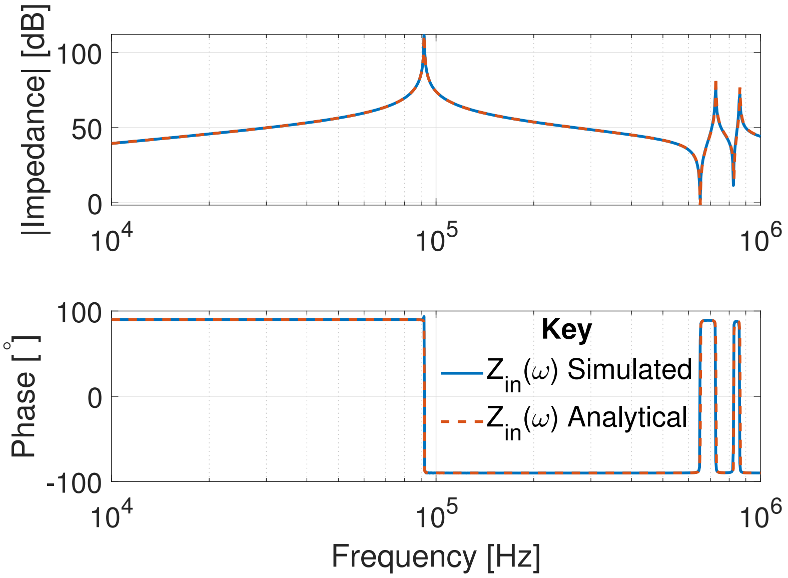

Figure 4.12: Target system magnitude and phase responses obtained analytically and through simulated perturbation [90].

Empirical mode decomposition is applied to the voltage waveform of Fig. 4.11 to produce a set of voltage IMFs to be used in parameter estimation strategies. Fig 4.13 presents the IMFs and residual that form the set of waveforms used to represent the target model.

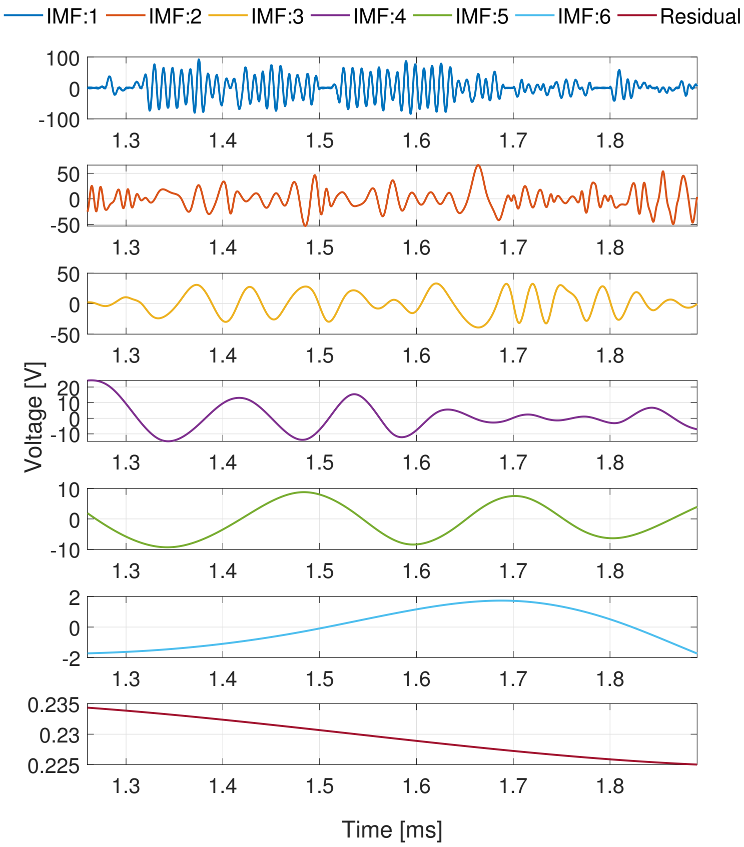

Figure 4.13: Target system voltage intrinsic mode functions [90].

4.2.3. Estimated model simulation arrangement

The cost function formulations compare various measurements taken from the target and estimate model to one another. These measurements are sampled, thus, the cost functions are formulated by applying a point-by-point comparison between the measurements. During frequency-domain estimation, the frequency vectors of the target and estimated input impedances are easily synchronised by supplying the *tfestimate* with the same frequency vector. However, in the case of time-domain estimation, the sampled waveforms that are produced by the target and estimate models need to be synchronised in a different manner. This synchronisation problem will also be encountered in practice, thus the solution adopted pays careful attention to ensure its practical feasibility.

To ensure the sampling of the target measurements and estimate measurements occur at the same instances the target model's current waveform under perturbation is used as the perturbation input to the estimated model. The current waveform injected into the estimated model is thus now a discretised version of the continuous waveform generated during the perturbation of the target model. This discrepancy between the current injected into the target model, and the current injected into the estimate model results in a difference between the resulting voltage waveforms, $v_{in}(t)$, of the target and estimate even when the parameters are identical. This difference in the voltage waveforms is shown in Fig. 4.14. The results reported in Fig. 4.14 are produced by sampling the target system perturbation current, $i_{in}(t)$, at 11MHz. The difference between the voltage waveforms can be reduced by increasing the sampling frequency. However, the increased sampling slows down simulation runtimes presenting a tradeoff between a more accurate waveform and faster runtimes.

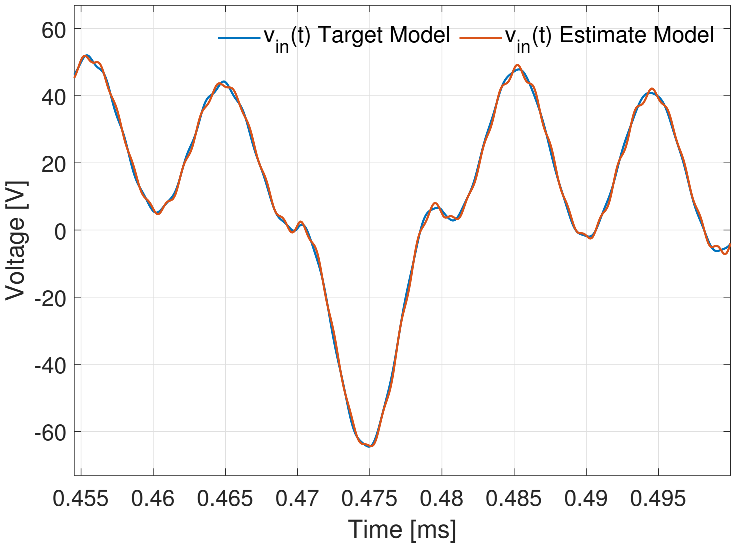

Figure 4.14: Discrepancy between the voltage of the target and estimate models when the estimate model is perturbed by the target model's discretised input current $i_{in}(t)$.

4.2.4. Parameter estimation methodology

The parameter estimation approach targets the parameter vector, θ, given in (4.27), where the parameters are normalised by applying the scaling factors, θ_{scale}, given in (4.28). Scaling the parameters to similar values results in the step sizes in all dimensions being relatively similar for the optimisation algorithm, if the step sizes differ by orders of magnitude between dimensions, it makes it challenging for the algorithm to solve. Table 4.8 summarises the bounds of the search space adopted in the investigation. The upper bounds of the parameters, aside from coupling coefficients, are chosen to be an order of magnitude larger than the lower bounds. The bounds are large to assume little *a priori* information about the parameter values. It is desired for manufacturers to construct efficient transformers with coupling coefficients as close to unity as possible, thus a standard engineering tolerance of 10% is used for the width of the coupling coefficient bounds. The lower bound is selected as 0.85 to allow for the target coupling coefficient values of Table. 4.7 to remain within the search space.

$$\theta = [R_s, C_s, C_g, L_s, k_{12}, k_{13}, k_{23}] \tag{4.27}$$

$$\theta_{scale} = [10^{-3}, 10^{-12}, 10^{-9}, 10^{-6}, 10^{-2}, 10^{-2}, 10^{-2}] \tag{4.28}$$

Table 4.8: Parameter boundary constraints after the scaling factors have been applied.

Parameters	R_s	C_s	C_g	L_s	k_{12}	k_{13}	k_{23}
Lower Bound	1	1	1	1	85	85	85
Upper Bound	1000	1000	1000	1000	95	95	95

In comparison to the two-section winding case study, the three-section winding model has an increased number of model parameters. The bounds of the search space have also increased ten-fold, and measurements are only taken at the winding terminals. All of these alterations to the problem definition compound to create a more complex optimisation problem.

Figures 4.15 to 4.17 present the three parameter estimation methodologies implemented in this investigation. The frequency-domain parameter estimation methodology implemented to solve for the two-section winding case study is once again used in this investigation. However, the available frequency response is limited to only the input impedance $Z_{in}(\omega)$ and is presented in Fig. 4.15. The classical time-domain approach to parameter estimation, whereby the measured voltage waveforms from the target and estimated models are compared and used in a cost function formulation, is presented in Fig. 4.16.

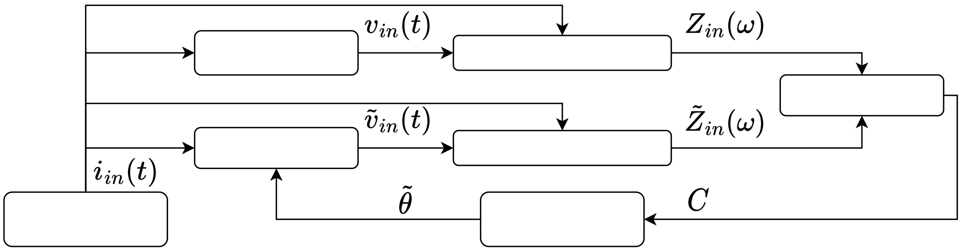

Figure 4.15: Classical frequency-domain parameter estimation methodology applied in the investigation.

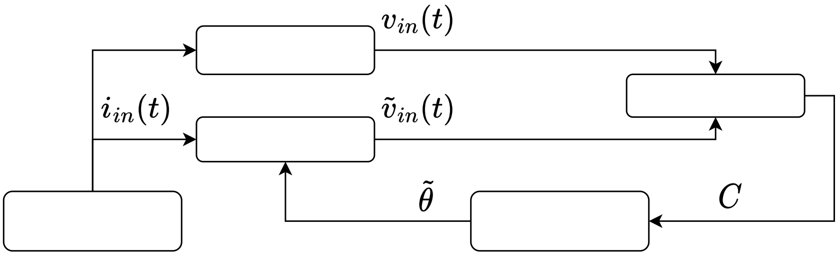

Figure 4.16: Classical time-domain parameter estimation methodology applied in the investigation [90].

Fig. 4.17 presents the proposed approach whereby the time-domain voltage waveforms first undergo a modal decomposition stage. Two implementations of modal decomposition are investigated. The first applied standard EMD to the target and estimated model voltage waveforms, and formulates the cost function in terms of the resulting IMFs and residuals. The second uses a decomposition method proposed in this study known as Inferred EMD (IEMD) to represent the estimated model, from which the cost function is derived.

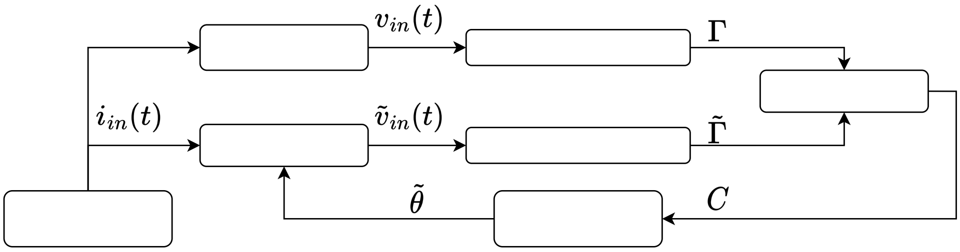

Figure 4.17: Time-domain modal decomposition parameter estimation methodologies applied in the investigation [90].

Cost functions constructed in terms of both Root Mean Squared Error (RMSE) and correlation coefficient (ρ) metrics are implemented for all approaches. Metaheuristic-based algorithms that generate a population of start points are used based on the assumption that limited *a priori* knowledge is available on the model parameters to be estimated. As such they perform well under conditions where the search space is widely bounded and complex. For completeness, both the Genetic Algorithm (GA) as well as Particle-Swarm Optimisation (PSO) are explored as possible candidates for the methodologies. The algorithms run 250 search iterations, with a population of 1000 points obtained using a default random seed. Upon completion of the global optimisation procedure, the optimisation results are refined using a local solver, *fmincon*.

4.2.5. Cost function formulations

4.2.5.1. Frequency-domain approach

For the frequency-domain parameter estimation, the RMSE-based cost function, C^z_{rmse}, is calculated as

$$C^z_{rmse} = \sqrt{\frac{1}{N_k}\sum_{k=1}^{N_k}(\epsilon(\omega_k))^2}, \tag{4.29}$$

where

$$\epsilon(\omega_k) = \log_{10}|Z_i(\omega_k)| - \log_{10}|\tilde{Z}_i(\omega_k)|,\ \ k = 1, 2, ..., N_k. \tag{4.30}$$

The errors, $\epsilon(\omega_k)$, between the input impedance frequency responses of the target system, $Z_i(\omega)$ and estimated model, $\tilde{Z}_i(\omega)$ are calculated on a point-by-point basis for each frequency sample w_k across all N_k samples. The sample frequencies ω_k are distributed logarithmically such that the contributions from $\epsilon(\omega_k)$ to the cost function are distributed equitably across the frequency range of interest.

The correlation coefficient metric is used to compute the correlation-based cost function, C_ρ^z, given by

$$C_\rho^z = -\rho\{Z_i(\omega), \tilde{Z}_i(\omega)\} + 1. \tag{4.31}$$

The correlation coefficient, ρ, between $Z_i(\omega)$ and $\tilde{Z}_i(\omega)$ is transformed such that the value of zero represents a perfect match in frequency responses and can thus be minimised.

4.2.5.2. Time-domain approach

The time-domain target voltage waveform is defined by $v_{in}(t)$ as shown in Fig. 4.11. The cost function, C_{rmse}^v, using the RMSE metric is calculated as

$$C_{rmse}^v = \sqrt{\frac{1}{N_k}\sum_{k=1}^{N_k}(\epsilon(t_k))^2}, \tag{4.32}$$

where

$$\epsilon(t_k) = v_{in}(t_k) - \tilde{v}_{in}(t_k), \ k = 1, 2, ..., N_k. \tag{4.33}$$

The errors, $\epsilon(t_k)$, between the voltage waveform of the target system $v_{in}(t)$, and the estimated model, $\tilde{v}_{in}(t)$ is calculated on a point-by-point basis for each time sample t_k up to N_k samples.

Similar to (4.31), the correlation-based cost function, C_ρ^v, is defined in terms of the correlation between the target and estimated voltage waveforms as

$$C_\rho^v = -\rho\{v_{in}(t), \tilde{v}_{in}(t)\} + 1. \tag{4.34}$$

4.2.5.3. Empirical mode decomposition approach

The voltage waveforms associated with the target system and estimated model, denoted by $v(t)$ and $\tilde{v}(t)$ respectively, can be expressed in terms of IMFs, governed by the relationships

$$v(t) = \sum_{i=1}^{N_i} v_i^m(t) + v^r(t) \tag{4.35}$$

and

$$\tilde{v}(t) = \sum_{i=1}^{\tilde{N}_i} \tilde{v}_i^m(t) + \tilde{v}^r(t), \tag{4.36}$$

where $v_i^m(t)$ and $\tilde{v}_i^m(t)$ denote the i^{th} IMFs, N_i and $\tilde{N}_i$ denotes the total number of IMFs, and $v^r(t)$ and $\tilde{v}^r(t)$ denote the residuals, of the target system and estimated model, respectively. The IMFs and residual are placed in sets, for the target and estimate denoted as Γ and $\tilde{\Gamma}$, respectively, and are shown in (4.37) and (4.38). The r^{th} waveform in the target and estimate set is denoted by $\gamma_r(t)$ and $\tilde{\gamma}_r(t)$, whilst the set sizes are denoted as N_r and $\tilde{N}_r$, respectively.

$$\begin{aligned}\Gamma &= \{v_1^m(t),\ v_2^m(t)\ ...\ v_{N_i}^m(t),\ v^r(t)\} \\ &= \{\gamma_r(t)|r = 1, 2...N_r\}\end{aligned} \tag{4.37}$$

$$\begin{aligned}\tilde{\Gamma} &= \{\tilde{v}_1^m(t),\ \tilde{v}_2^m(t)\ ...\ ,\ \tilde{v}_{\tilde{N}_i}^m(t),\ \tilde{v}^r(t)\} \\ &= \{\tilde{\gamma}_r(t)|r = 1, 2...\tilde{N}_r\}\end{aligned} \tag{4.38}$$

The number of IMFs produced through the EMD procedure is dependent on the dynamics within the signal being decomposed, as such the length of the sets, Γ and $\tilde{\Gamma}$, are not guaranteed to be equal. The set with fewer waveforms is padded with zeros such that the sets are of equal length and can be directly compared on a point-by-point basis. The Normalised RMSE (NRMSE) cost function, C_{nrmse}^m, for the Empirical Mode Decomposition approach is calculated as

$$C_{nrmse}^m = \sum_{r=1}^{N_r} \frac{1}{\psi_r} \sqrt{\frac{1}{N_k} \sum_{k=1}^{N_k} (\epsilon_r(t_k))^2}, \tag{4.39}$$

where the errors, $\epsilon_r(t_k)$, is defined in (4.40) as the difference between the r^{th} waveforms in sets Γ and $\tilde{\Gamma}$ at sample time t_k.

$$\epsilon_r(t_k) = \gamma_r(t_k) - \tilde{\gamma}_r(t_k) \tag{4.40}$$

The respective errors are then normalised by applying a normalisation constant, ψ_r, that is defined as the difference between the maximum and minimum amplitude of the r^{th} target IMF waveform, as shown in (4.41)

$$\psi_r = \max\{\gamma_r(t)\} - \min\{\gamma_r(t)\} \tag{4.41}$$

This normalisation is required to counter the cost function biasing towards waveforms with higher amplitude as the measurement set consists of waveforms with varying amplitudes. The normalisation constant is omitted in cases when the target data set is padded as it results in a $\psi_r = 0$.

In the case of the correlation-based cost function the larger set between the target and estimated sets is truncated to the length of the shorter set, denoted by N_s, as correlation coefficient metrics do not allow for padded zero waveforms. Due to this truncation a variance occurs in the number of IMFs from iteration to iteration in the optimisation procedure thus the result is normalised by N_s. The cost function, C_ρ^m, is thus defined as

$$C_\rho^m = \frac{1}{N_s}\sum_{r=1}^{N_s}[-\rho\{\gamma_r(t), \tilde{\gamma}_r(t)\} + 1]. \tag{4.42}$$

4.2.5.4. Inferred empirical mode decomposition approach

In this method, the IMFs produced by the estimated waveforms are never computed. Instead, a set of inferred IMFs (iIMFs) is produced to represent the estimated model. The target set, Γ, remains the same as in (4.37). The r^{th} iIMF, $\tilde{v}_r^i(t)$, is defined in (4.43) for the estimated waveform, $\tilde{v}(t)$, and is produced by subtracting waveforms 1 to $r-1$ and waveforms $r+1$ to N_r in Γ from $\tilde{v}(t)$.

$$\tilde{v}_r^i(t) = \tilde{v}(t) - \sum_{k=1}^{r-1}\gamma_k(t) - \sum_{k=r+1}^{N_r}\gamma_k(t) \tag{4.43}$$

The estimated set, while in the same form as in (4.38), consists of the iIMFs of the estimated voltage waveform as described in (4.43). The number of iIMFs produced is always the same as the number of target IMFs, thus, the length of $\tilde{\Gamma}$ becomes N_r and is redefined in (4.44).

$$\begin{aligned}\tilde{\Gamma} &= \{\tilde{v}_1^i(t), \tilde{v}_2^i(t)\ ...\ \tilde{v}_{N_r}^i(t)\} \\ &= \{\tilde{\gamma}_r(t) | r = 1, 2...N_r\}\end{aligned} \tag{4.44}$$

This formulation is based on the property that EMD produces IMFs that add up to the original signal. If all target IMFs aside from the n^{th} are subtracted from the estimated model's voltage waveform, the resulting waveform is the n^{th} iIMF. If the estimate model is correct, then the remaining waveform, $\tilde{v}_r^n(t)$, equals the n^{th} target IMF. The cost function for the NRMSE-based metric is calculated as

$$C_{nrmse}^i = \sum_{r=1}^{N_r}\frac{1}{\psi_r}\sqrt{\frac{1}{N_k}\sum_{k=1}^{N_k}(\epsilon_r(t_k))^2}, \tag{4.45}$$

where the errors, $\epsilon_r(t_k)$, and normalisation constants, ψ_r, are defined as in (4.40) and (4.41), respectively.

The correlation-based cost function in the context of the Inferred EMD (IEMD) approach does not require truncation of the IMFs nor normalisation. The cost function, C^i_ρ, is thus reduced to the form

$$C^i_\rho = \sum_{r=1}^{N_r} [-\rho\{\gamma_r(t), \tilde{\gamma}_r(t)\} + 1]. \tag{4.46}$$

Fig. 4.18 presents a typical set of iIMFs within the context of the parameter estimation presented in this section. The iIMFs are colour coded, whilst the set of target waveforms in Fig. 4.13 are indicated in black. This decomposition approach creates a set of iIMFs that each contains the error dynamics within the estimated signal while also containing the corresponding target IMF dynamics that are present in the estimated waveform.

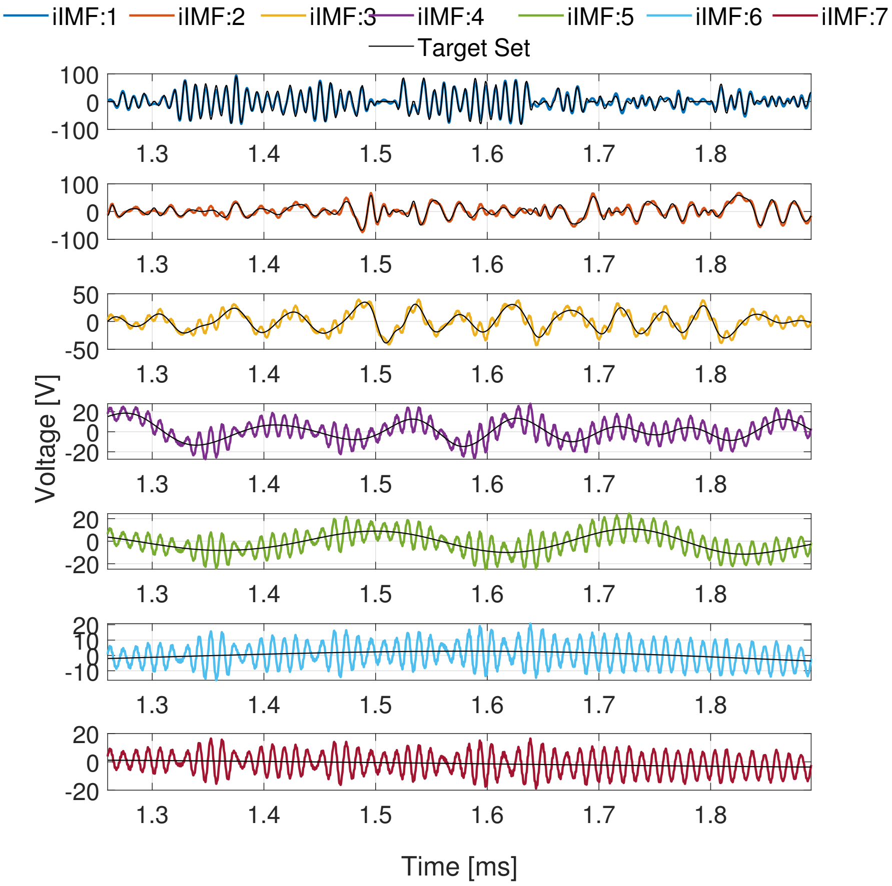

Figure 4.18: A typical set of iIMFs as well as the set of target IMFs produced from the model target parameters.

4.2.6. Results

The results of the parameter estimation simulations are presented in Tables 4.9 and 4.10 for the RMSE- and correlation-based cost functions, respectively. The parameter estimation approaches that yielded five or more parameters within 10% of the target parameter values are highlighted in green.

Table 4.9: Parameter estimation results for RMSE-based cost function formulations.

	Frequency Approach Errors [%]		Time Approach Errors [%]		EMD Approach Errors [%]		IEMD Approach Errors [%]	
Model Parameter	Genetic Algorithm	Particle Swarm	Genetic Algorithm	Particle Swarm	Genetic Algorithm	Particle Swarm	Genetic Algorithm	Particle Swarm
R_s	-299.2	-242.5	91.85	1.14	-977.6	36.90	34.56	1.14
C_s	-2.69	-3.09	95.31	-1.91	66.44	-3.03	38.53	-1.91
C_g	-3.61	0.67	-1512	-0.59	-519.1	-59.55	-761.1	-0.59
L_s	5.68	2.55	94.61	1.73	77.94	33.47	89.68	1.73
K_{12}	-8.83	-8.83	-5.06	-4.78	-4.82	-5.03	-8.79	-4.78
K_{13}	0.04	0.03	-4.92	-3.15	2.15	2.50	-8.83	-3.15
K_{23}	-4.70	-5.29	-6.45	0.53	-2.01	-0.50	-1.52	0.53
C	2.6098	2.5917	32.543	1.0859	1.0854	0.5516	49.695	0.5067
Runtime	15.71	29.89	4.51	12.33	3.26	5.92	6.42	8.33

Table 4.10: Parameter estimation results for correlation-based cost function formulations.

	Frequency Method Errors [%]		Time Method Errors [%]		EMD Method Errors [%]		IEMD Method Errors [%]	
Model Parameter	Genetic Algorithm	Particle Swarm	Genetic Algorithm	Particle Swarm	Genetic Algorithm	Particle Swarm	Genetic Algorithm	Particle Swarm
R_s	93.36	45.23	-14.26	83.13	-543.24	-941.4	98.79	-84.61
C_s	36.21	-0.50	12.30	47.17	74.29	25.25	43.58	21.58
C_g	-6890	37.50	-66.13	-723.1	-155.5	37.50	-46257	-3.74
L_s	-321.1	-40.25	36.26	86.26	58.679	-51.22	-452.49	-0.91
K_{12}	-0.824	-3.73	-1.298	-4.85	-8.605	0.42	-2.957	0.67
K_{13}	-6.534	-8.80	-6.792	-5.45	-3.876	-3.10	-6.1796	1.88
K_{23}	-6.758	-6.70	-2.9295	-8.03	-4.442	-0.41	-10.935	0.74
$C(\times10^{-3})$	14.94	0.452	0.426	0.422	629	38.41	6016	390
Runtime	13.87	11.81	0.714	4.31	2.46	1.76	2.43	8.87

To aid in the analysis of the results, a visual representation of the search spaces are presented in Figures 4.19 to 4.22. The figures are created by incrementally moving the parameter away from its target value by 0.2%. For legibility purposes Figures 4.19 to 4.22 only show the cost function as R_s, C_s, C_g and L_s are varied. The search spaces shown are one-dimensional meaning that each parameter is varied individually whilst all others are kept at their target value. Therefore, there are intricacies within the search space that can not be seen.

Figures 4.19a and 4.19b present the search spaces produced by the frequency-domain RMSE- and correlation-based cost functions, respectively. The frequency-domain RMSE-based optimisation obtained errors below 10% for all parameters aside from R_s. The R_s parameter does not influence the cost function significantly, as seen in Fig. 4.19a, as it predominantly affects the damping at the resonant points of the frequency response. The correlation-based cost function formulation performed poorly in comparison with the RMSE-based cost function formulation, with several parameters converging to errors above 10%. This can be attributed to the increased stochasticity of the search space in Fig. 4.19b in comparison to Fig. 4.19a. The variance in runtimes between the simulations is as a result of both the optimisation algorithm, the search space as well as the device hardware. There is no guarantee that the simulations were executed on similar hardware, as the simulations were performed on Stellenbosch University's High-Performance Computing cluster (HPC) where the node assignment is done randomly. It is observed that the runtimes of frequency-domain parameter estimation are, on average, longer compared to the average runtimes of time-domain and modal decomposition approaches. This is attributed to the need for longer simulation times to obtain high frequency resolution over a wide frequency band.

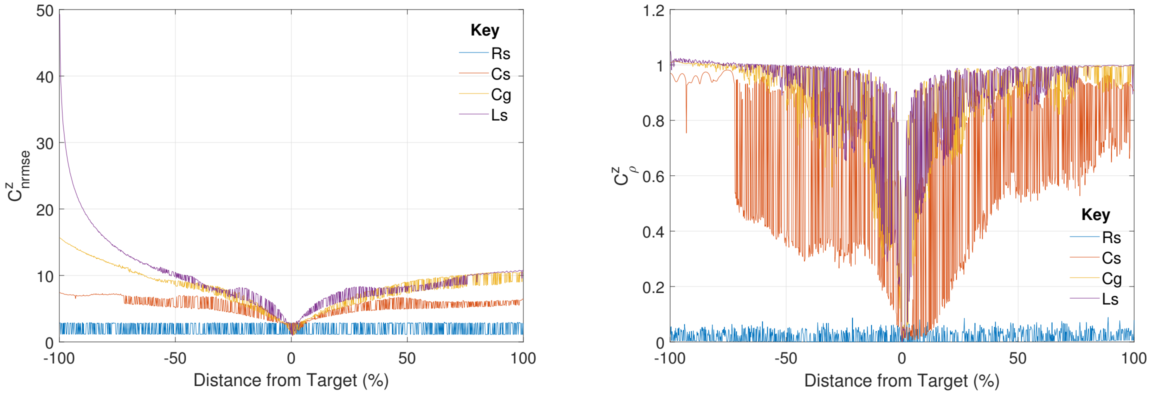

(a) **(b)**

Figure 4.19: (a) C^z_{rmse} and (b) C^z_{ρ} versus distance from target parameter.

From Tables 4.9 and 4.10 it is clear that neither correlation nor NRMSE-based cost functions using the EMD approach are able to obtain parameters as accurately as the classical time domain-approach. This is attributed to the content within each IMF being completely dependent on the dynamics present in the original signal. EMD does not guarantee the presence of specific modes within a specific IMF. Although the presence of certain modes within the estimated waveform may be correct, it cannot be predicted into which of the IMFs these will be decomposed. This characteristic makes the optimisation challenging when only comparing the n^{th} IMF of the target with the n^{th} IMF of the estimated waveforms. The EMD approach is sensitive to minor changes in the time-domain waveforms making the search space stochastic, as shown in Fig. 4.20.

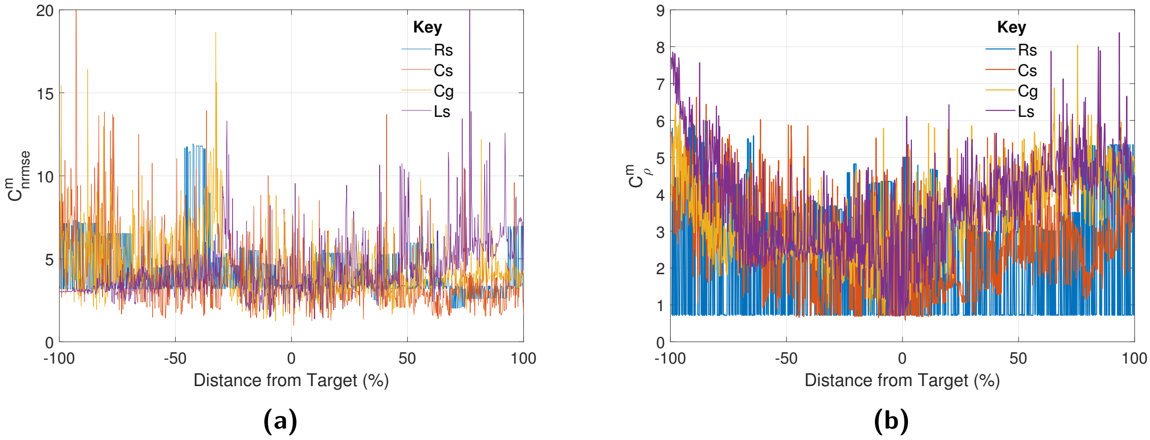

(a) **(b)**

Figure 4.20: (a) C^{m}_{nrmse} and (b) C^{m}_{ρ} versus distance from target parameter.

The RMSE-based cost functions for both classical time-domain and IEMD converged to the same parameter values in the optimisation algorithm. This is attributed to RMSE-based cost function formulations producing similar multi-dimensional search spaces, as shown in Figures 4.21a and 4.22a. This, in many respects, is a welcome result, as traditional EMD decomposes a time-domain waveform into a set of IMFs that sum up to the original signal, IEMD is able to decompose the error between the two voltage waveforms into sets that, when summed make up the original search space. In this way, there are now possibilities to explore the iIMFs individually to investigate their ability to improve the parameter estimation results further. The superior results obtained through the time-domain and IEMD approaches when compared to the EMD approach can be attributed to the overall downward trend as parameter values arrive closer to the target in Figures 4.21 and 4.22 as opposed to the stochastic search spaces shown in Fig. 4.20.

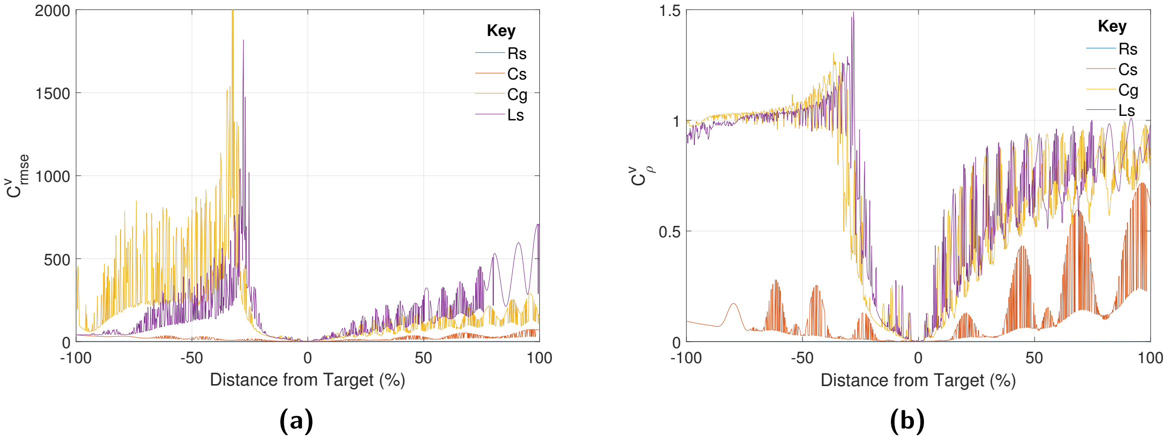

(a) **(b)**

Figure 4.21: (a) C^{v}_{nrmse} and (b) C^{v}_{ρ} versus distance from target parameter.

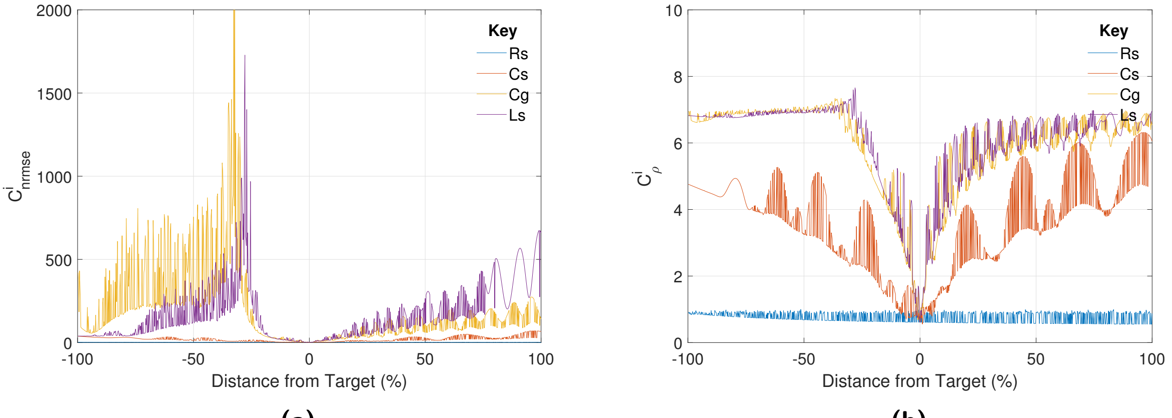

(a) **(b)**

Figure 4.22: (a) C^i_{nrmse} and (b) C^i_ρ versus distance from target parameter.

In all cases, it is evident that PSO outperforms GA at the cost of longer runtimes. Thus for future experiments, PSO is the optimisation algorithm of choice.

In the case of characterising and solving the parameters of a practical transformer, the number of parameters increases rapidly in comparison to a single winding. Simulink provides accuracy in mimicking the practical arrangement employed by the user in obtaining the measurements from the transformer, however, the computational overhead of using Simulink within a parameter estimation procedure to solve for the transformer model parameters is high. If the runtimes of the current optimisation procedures are extrapolated to problems whereby a full transformer model needs to be solved, it is clear that the computational intensity is simply too high to obtain accurate results within a reasonable time period. Thus for larger problems, the optimal choice of parameter estimation methodology is still the evaluation of the analytical impedance transfer functions, which would improve runtimes significantly.

Chapter 5

Perturbation and Parameter Estimation of a Practical High-Voltage Transformer

This chapter describes the perturbation, modelling and parameter estimation of a 7.5kVA, 230V/100kV high-voltage test transformer. The chapter begins by describing the practical perturbation arrangement, the data acquisition equipment used to measure the transformer waveforms and presents the resulting frequency responses obtained through various open-circuit and short-circuit tests. It continues by presenting the results of three case studies investigated to determine an accurate model for the observed responses.

5.1. Experimental perturbation of a high-voltage transformer

This section describes the methodology applied for obtaining practical measurements of a 7.5kVA, 230V/100kV high-voltage test transformer. Satisfactory measurements are classified as frequency response measurements with as little influence from noise as possible. This noise could be the result of insufficient sampling rates of the measurement equipment, insufficient perturbation at some frequency bands or an incorrect spectral estimation methodology.

5.1.1. Data acquisition arrangement and measurement equipment

Due to the requirements imposed by wideband excitation signals of power system equipment, the measurement and data acquisition instrumentation should be capable of measuring high voltages at high sampling rates with accurate resolution. The following commercially available equipment is chosen:

- **Voltage measurements:** The voltage signals are measured using a GW Instek GDP-025 differential high voltage probe [92] capable of measuring differential voltages of $1400V_{pp}$ with a bandwidth of 25MHz, and a PINTECH N1000A differential probe [93] capable of measuring $1400V_{pp}$ up to 40MHz.

- **Data acquisition:** The NI 9223 C-series voltage input module from National Instruments is a measurement module capable of measuring four voltage inputs at a sampling rate of 1MS/s with simultaneous Analogue-to-Digital Conversion (ADC) using 16-bit resolution [94]. The voltage input module is compatible with the NI cDAQ-9178 chassis to interface with the host computer via USB to stream and store the measured signals [95].
- **Low pass filter:** Two Thorlabs EF502 100kHz Low-Pass Filters (LPFs) are used to attenuate signals above 100kHz that could cause aliasing in the signal's frequency response. The filters are designed for a 1dB passband up to 100kHz and falls to a 30dB rejection at 199kHz [96]. The LPFs have Coaxial BNC feedthrough connections allowing it to be installed between the measurement probe and NI 9223 voltage input module.

During preliminary testing it was found that the current probe vertical resolution was insufficient to measure the low current levels during perturbation of the high-voltage winding. Two solutions were investigated to improve the vertical resolution. The first solution increased the number of turns through the current probe to three and the second investigated measuring the voltage across the resistor in the RLC circuit. The LVOC and HVOC input impedance frequency responses obtained using both measurement approaches are presented in Fig. 5.1. It is clear in Fig. 5.1a that in the case of measurements on the low-voltage winding the current probe performs just as well as voltage measurements over the sense resistor. However, in the case of measurements on the high-voltage winding such as the one in Fig. 5.1b, the measured currents are too small for the vertical resolution of the current probe and thus introduces drastic measurement errors. As such, all subsequent current measurements are obtained by measuring the voltage over the resistor in the RLC circuit, denoted as $v_{sense}(t)$, as opposed to using a current probe.

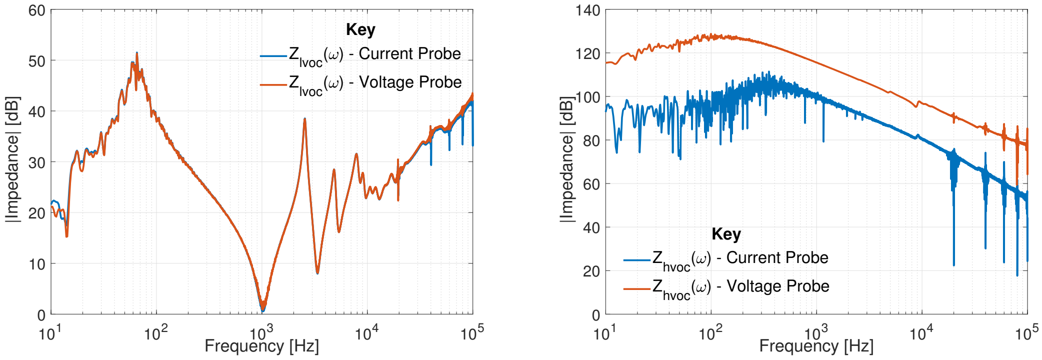

(a) **(b)**

Figure 5.1: Comparison between using a current probe and voltage probe to measure the input current during perturbation to obtain the frequency responses of the **(a)** LVOC and **(b)** HVOC input impedances.

Two different perturbation arrangements, with three measurements from each are performed to form a total of six measurements used in the parameter estimation procedure. It is concluded in Chapter 4 that, in general, maintaining a PRIS source RLC impedance similar to the transformer input impedance provides a good starting point for an iterative RLC selection approach. Mwaniki *et al.* [50] present this same reasoning and emphasise that the design of an optimum PRIS source for system identification is highly dependent on the characteristics of the target system. Knowledge of the HV transformer's characteristics is limited to its transformation ratio and power rating, there is no information available with regards to its internal mechanical structure or winding topology. Thus, various RLC components were ordered to iteratively determine a suitable combination that provides the clearest frequency response results for frequencies up to 100kHz. Due to the large transformation ratio of approximately 1:435 of the HV transformer, it is expected for the HV winding to contain significantly more turns than the LV winding. It is, therefore, also expected for the associated frequency responses and impedance magnitudes to vary significantly between perturbation of the LV and HV windings. The measurement approach and iterative RLC procedure for the perturbation of the LV and HV terminals are performed separately and presented in the following two sections.

5.1.2. Perturbation of the low-voltage terminal

Fig. 5.2 shows the practical arrangement for perturbing the transformer low-voltage terminal. Throughout the iterative RLC selection procedure, a DC voltage of 30V from a single DC bench power supply in conjunction with a single PRBS16 sequence switching at 20kHz is used. The RLC circuit components that produces the clearest set of frequency responses is a combination of $R^{lv}_{pris} = 56\Omega$, $L^{lv}_{pris} = 500\mu H$ and $C^{lv}_{pris} = 4\mu F$. This results in an overdamped RLC series resonant frequency at 3558.8kHz with an impulse rise time constant of $\tau_1 = 9.3\mu s$ and fall time constant $\tau_2 = 214.7\mu s$. As the majority of LV resonances are located between 1kHz and 10kHz the series resonance location of the RLC circuit is also placed within this region.

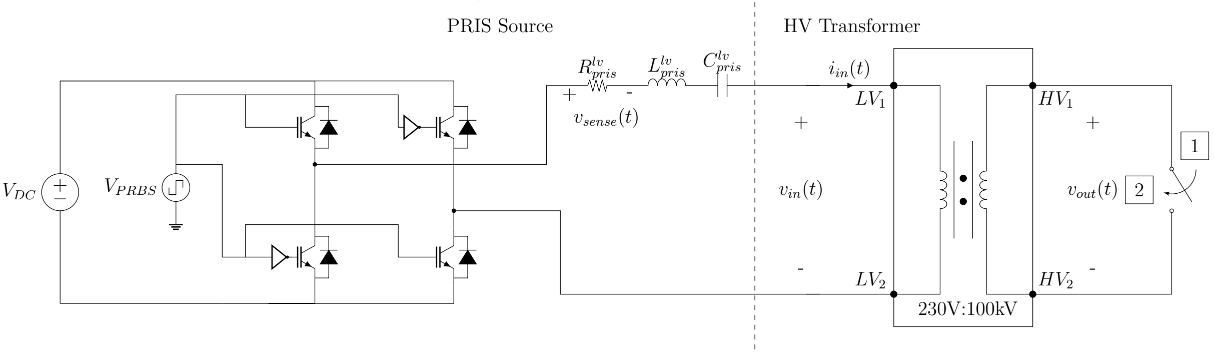

Figure 5.2: PRIS arrangement for perturbing the low-voltage terminal of the practical transformer.

Three frequency responses are obtained using the perturbation arrangement shown in Fig. 5.2, the measurement for each response is detailed below:

1. **LVOC:** This experiment measures the input impedance frequency response, $Z_{lvoc}(\omega)$ from input current, $i_{in}(t)$, and input voltage, $v_{in}(t)$, whilst the switch on the HV side is open, i.e. in position 1. The resulting input impedance is shown in Fig. 5.3a.
2. **LVSC:** This experiment measures the input impedance frequency response, $Z_{lvsc}(\omega)$, from input current, $i_{in}(t)$, and input voltage, $v_{in}(t)$, whilst the switch on the HV side is closed, i.e. in position 2. The resulting input impedance is shown in Fig. 5.3b.
3. **LVHV:** This experiment measures the low-voltage to high-voltage transformation ratio frequency response, $R_{lvhv}(\omega)$, from input voltage, $v_{in}(t)$, and output voltage $v_{out}(t)$, whilst the switch located on the HV side is open. Due to the high transformation ratio of the transformer under investigation the DC voltage is reduced to 10V during the transformation ratio measurements to ensure that $v_{out}(t)$ remains within the $1400V_{pp}$ rating of the GW Instek differential probe [92]. The transformation ratio frequency response is depicted in Fig. 5.3c.

In conjunction with the measured responses, Fig. 5.3 shows the impedance frequency response of the RLC circuit, $Z_{rlc}(\omega)$, derived analytically. The choice of an RLC impedance frequency response that is slightly higher than the associated frequency responses of the transformer provides the clearest results.

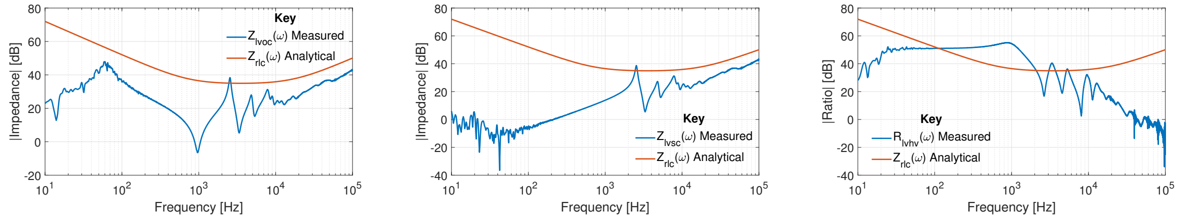

(a) **(b)** **(c)**

Figure 5.3: **(a)** $Z_{lvoc}(\omega)$ and **(b)** $Z_{lvsc}(\omega)$ input impedances as well as the **(c)** $R_{lvhv}(\omega)$ obtained using a 20kHz clock frequency.

It is expected for $Z_{lvsc}(\omega)$ and $R_{lvhv}(\omega)$ to exhibit a resistive frequency response below 50Hz, however, in both cases, the responses are unclear due to large variance and noisy results. This can be attributed to insufficient low-frequency perturbation and can be remedied by lowering the PRBS clock frequency to 2kHz thus focusing the perturbation energy to $\frac{f_{clk}}{3} = 666.67$Hz. The PRBS order is reduced to a PRBS13 to maintain consistent frequency resolution. A combination methodology is applied to all frequency responses whereby the measurements from 2kHz and 20kHz clock frequency perturbations are combined to form the synthesised frequency response. An illustration of the combination methodology is shown in Fig. 5.4 whereby the measurements from the 2kHz and 20kHz clock frequency perturbations are combined to form the synthesised $Z_{lvsc}(\omega)$ and $R_{lvhv}(\omega)$ measurements. The final combined frequency responses with minimal noise over the entire frequency range are presented in Fig. 5.5.

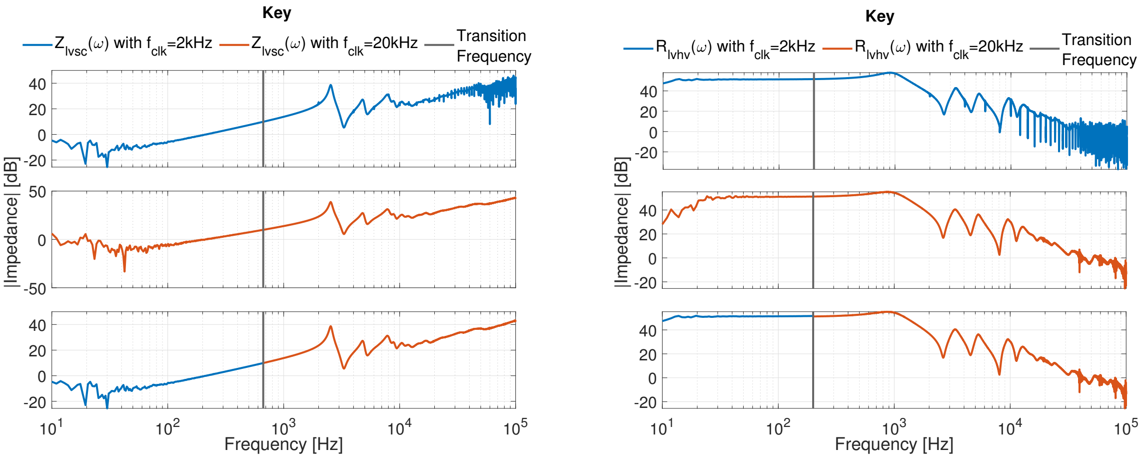

(a) **(b)**

Figure 5.4: Illustration of **(a)** $Z_{lvsc}(\omega)$ and **(b)** $R_{lvhv}(\omega)$ obtained through the combination of 2kHz and 20kHz clock frequency perturbations

The region from 10Hz to 666Hz of $Z_{lvoc}(\omega)$ and $Z_{lvsc}(\omega)$ are measured using the 2kHz clock frequency and are presented in Figures 5.5a and 5.5b. In the case of $R_{lvhv}(\omega)$ in Fig. 5.5c the response measured using the 2kHz clock frequency perturbation make up the portion from 10Hz to 200Hz. Selecting a 200Hz transition frequency for the voltage transformation frequency response results in the smallest discontinuity at the point of transition between the two sets of frequency response measurements.

The LVOC impedance, $Z_{lvoc}(\omega)$, in Fig. 5.5a has a prominent parallel-series resonant pair at approximately 50Hz and 1kHz followed by four additional minor parallel-series resonant pairs up to 10kHz, the four minor parallel-series resonant pairs can also be seen in $Z_{lvsc}(\omega)$ in Fig. 5.5b. Due to the larger number of turns on the HV winding, it is expected that its total self-inductance would be significantly larger than compared to that of the LV winding. Similarly, the larger surface area of the HV winding results in a larger inter-turn capacitance. The resonant frequencies of the HV winding are, therefore, expected to be located at lower frequencies than the locations of the resonant frequencies caused by the LV winding. Consequently, it is possible that the measurements from the LV terminal are presenting the resonant behaviour of the HV winding as seen from the LV terminals as opposed to resonances caused by the LV winding itself.

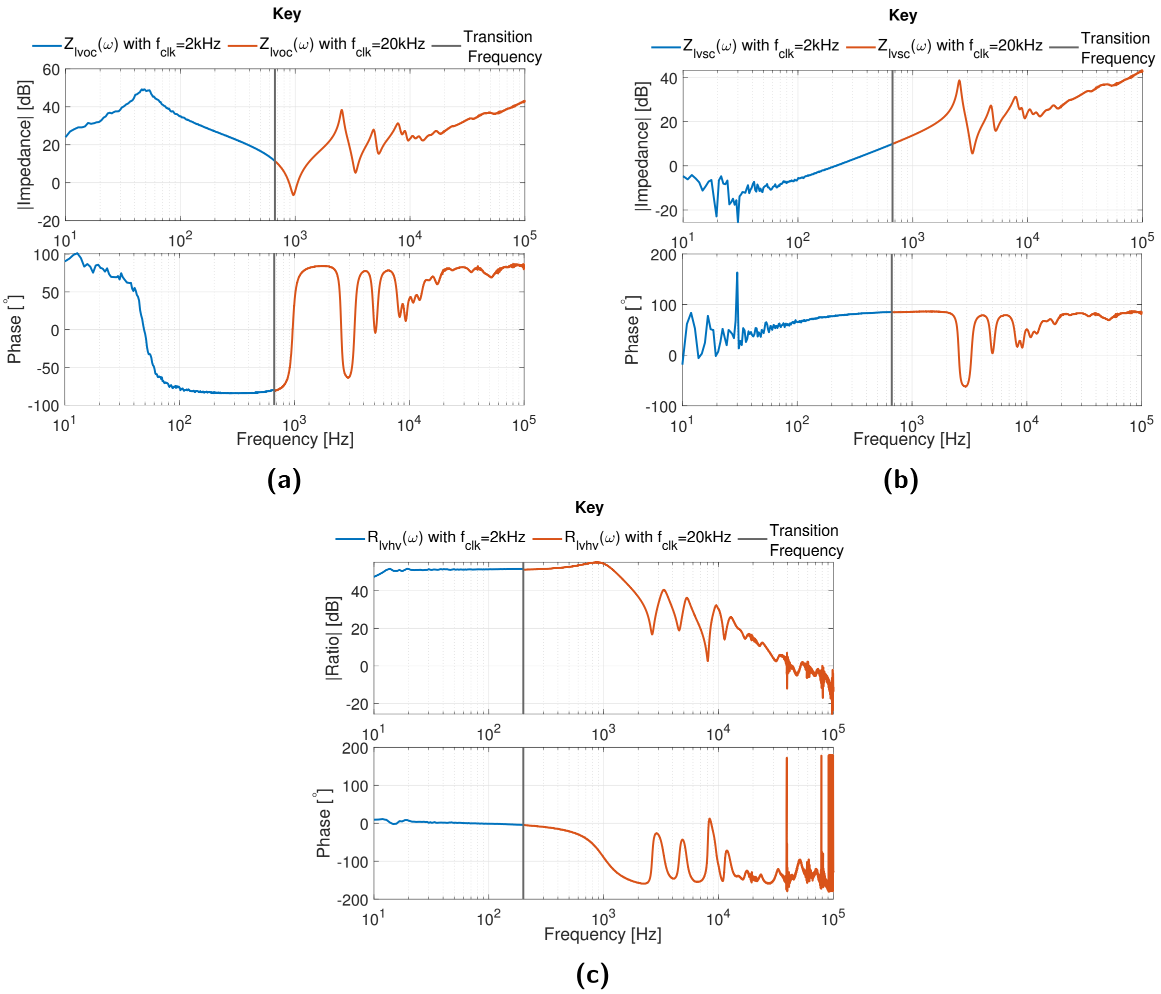

Figure 5.5: Magnitude and phase responses of **(a)** $Z_{lvoc}(\omega)$, **(b)** $Z_{lvsc}(\omega)$ and **(c)** $R_{lvhv}(\omega)$ obtained through the combination of 2kHz and 20kHz clock frequency perturbations.

5.1.3. Perturbation of the high-voltage terminal

Due to the relatively low magnitude of the input impedance as seen from the LV winding, RLC circuit components that produce impedance magnitudes similar to the responses of the transformer are readily available. The high-voltage input impedance is, however, orders of magnitude larger compared to the low-voltage side. Therefore, the set of RLC components needs to be large to have an impedance magnitude comparable to the HV winding. Such large components are, in many cases, either not practical or are not readily accessible. As such the RLC circuit design for the perturbations of the HV terminal needs to be selected with care as the dominant influence on the perturbation waveform will be the HV winding rather than the RLC circuit. The practical arrangement for perturbing the transformer high-voltage terminal is shown in Fig. 5.6.

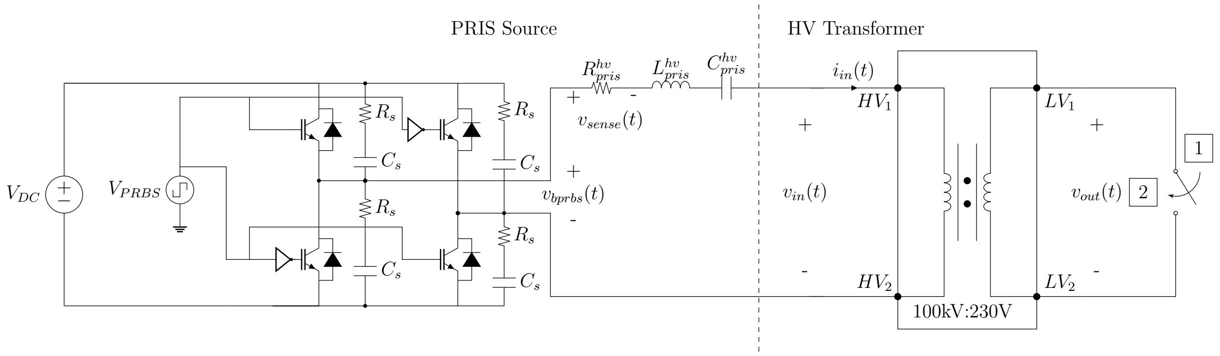

Figure 5.6: PRIS arrangement for perturbing the high-voltage terminal of the practical transformer.

The fast switching that occurs at the PRBS state transitions causes the capacitive nature of the winding to dominate the current waveform. This capacitance, in turn, produces very fast current rise times, making the accurate sampling of the waveforms particularly challenging with the data acquisition equipment available. This same phenomenon is addressed in Section 4.1.2 by increasing the impedance magnitude so that it is comparable to the input impedance magnitude of the DUT. However, in this context forming an RLC impedance magnitude that is comparable to the HV winding is not possible. Thus, only the inductive component of the RLC circuit was increased such that the voltage and current waveform dynamics are slowed to the point where the signals can be sampled accurately by the data acquisition system. Fig. 5.7 compares voltage and current signals from a high-voltage short-circuit perturbation with a varying RLC inductor, L^{hv}_{pris}. The perturbation in Fig. 5.7a makes use of a $15mH$ inductor and the perturbation in Fig. 5.7b uses a $60mH$ inductor. Both investigations use a R_{pris} of $25k\Omega$, a C_{pris} of $100nF$ and a V_{DC} of 120V. It is clear that the addition of more inductance to the RLC design decreases the voltage and current rise times allowing for more accurate waveform samples which in turn limits the effect of aliasing in the frequency domain.

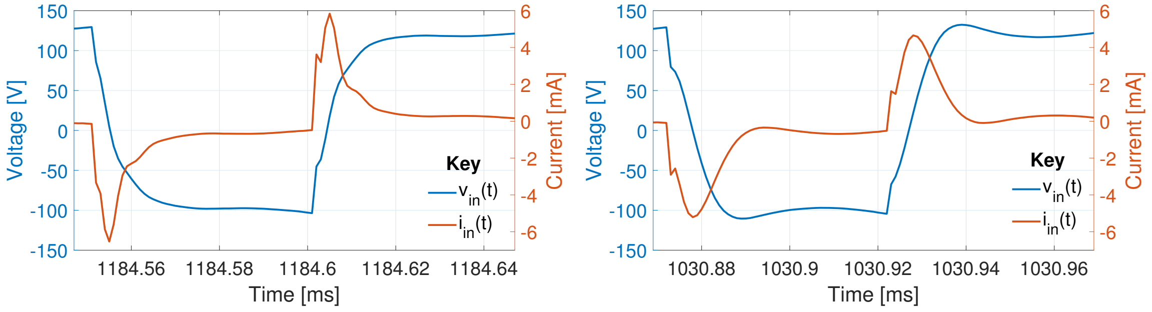

(a) **(b)**

Figure 5.7: Effect on the voltage and current rise times using a L^{hv}_{pris} of **(a)** $15mH$ and **(b)** $60mH$.

In both sets of measurements in Fig. 5.7, there is a jagged artefact that occurs during the rise time of the current signals. This can be attributed to ringing on the bipolar PRBS voltage, $v_{bprbs}(t)$, that is generated between the two centre points of the switching legs. A snubber circuit limits the rate of rise of currents through the IGBTs during switch on [97]. The snubber topology places an RC snubber across each IGBT switch in the PRIS source as shown in Fig. 5.6.

The natural ringing frequency, f_r, present across each switch in the arrangement without the inclusion of snubbers can be expressed as

$$f_r = \frac{1}{2\pi\sqrt{L_p C_p}}, \tag{5.1}$$

where L_p and C_p is the effective parasitic inductance and capacitance, respectively [98]. With the inclusion of snubber capacitor, C_s, the new ringing frequency, f_{r2}, becomes

$$f_{r2} = \frac{1}{2\pi\sqrt{L_p(C_p + C_s)}}. \tag{5.2}$$

From (5.1) and (5.2) it is possible to derive an expression for the parasitic inductance [98]:

$$L_p = \frac{1}{4\pi^2(f_{r2} - f_r)^2 C_s}. \tag{5.3}$$

From the measurement of f_r and f_{r2}, and the calculation of L_p it is possible to calculate C_p using (5.1). Finally, for optimal damping the snubber resistor, R_s, should be $R_s = \frac{1}{2}\sqrt{\frac{L_p}{C_p}}$ [98]. The initial ringing frequency of $v_{bprbs}(t)$ is measured to be $f_r = 2.2936$MHz as shown in Fig. 5.8a. The snubber design uses a $C_s = 10nF$ to reduce the ringing to $f_{r2} = 482.63$kHz resulting in a theoretical R_s of 50.1Ω for optimal damping. Due to component sizing limitations the final design uses $R_s = 55\Omega$. The bipolar PRBS voltage after the inclusion of RC snubbers is shown in Fig. 5.8b.

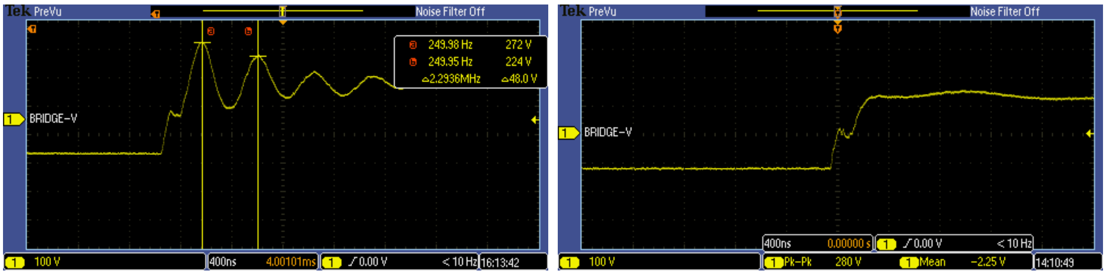

(a) **(b)**

Figure 5.8: The switch ringing of $v_{bprbs}(t)$ **(a)** before and **(b)** after the inclusion of an RC snubber.

The perturbation arrangement presented in Fig. 5.6 has a DC voltage of 120V to improve the SNR and final RLC parameters of $R^{hv}_{pris} = 29.7k\Omega$, $L^{hv}_{pris} = 30mH$ and $C^{hv}_{pris} = 100nF$. The following frequency responses are obtained to represent the results of perturbing the high-voltage terminal:

4. **HVOC:** This experiment measures the input impedance frequency response, $Z_{hvoc}(\omega)$ from input current, $i_{in}(t)$, and input voltage, $v_{in}(t)$, whilst the switch on the LV side is open. The resulting input impedance is obtained by combining 2kHz and 20kHz PRBS clock frequency perturbations and shown in Fig. 5.9a.

5. **HVSC:** This experiment measures the input impedance frequency response, $Z_{hvsc}(\omega)$, from input current, $i_{in}(t)$, and input voltage, $v_{in}(t)$, whilst the switch on the LV side is closed. The resulting input impedance is obtained by combining 2kHz and 20kHz PRBS clock frequency perturbations and shown in Fig. 5.9b.

6. **HVLV:** This experiment measures the high-voltage to low-voltage transformation ratio frequency response, $R_{hvlv}(\omega)$, from input voltage, $v_{in}(t)$, and output voltage $v_{out}(t)$, whilst the switch located on the LV side is open. The resulting voltage transformation ratio is obtained by combining 2kHz and 20kHz PRBS clock frequency perturbations and shown in Fig. 5.9c.

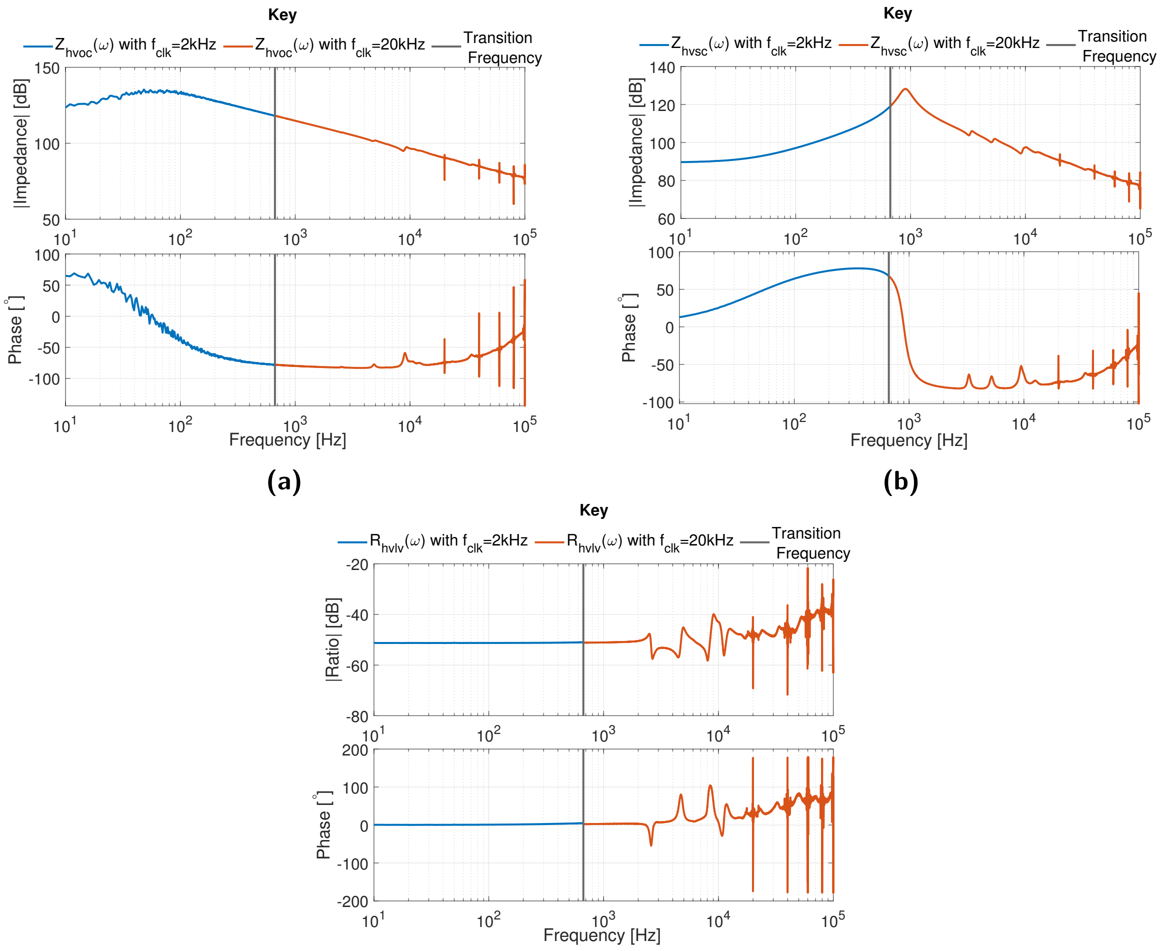

(a) **(b)**

(c)

Figure 5.9: Magnitude and phase responses of **(a)** $Z_{hvoc}(\omega)$, **(b)** $Z_{hvsc}(\omega)$ and **(c)** $R_{hvlv}(\omega)$ obtained through the combination of 2kHz and 20kHz clock frequency perturbations.

The HVOC input impedance, $Z_{hvoc}(\omega)$, exhibits a main parallel resonance at approximately 70Hz followed by two highly damped series-parallel resonant pairs at approximately 5kHz and 9khz. These two resonance pairs are also visible in the LVOC input impedance of Fig. 5.5a as parallel-series pairs. The main parallel resonance of $Z_{hvsc}(\omega)$ at 1kHz is followed by three clearly visible series-parallel resonant pairs below 10kHz and then two highly damped resonance pairs at approximately 12 kHz and 34kHz. Praminik *et al.* [40] and Ragavan *et al.* [41] suggest a starting point for identifying the number of sections to represent a winding to be the number of observed parallel resonances. The main parallel resonance and five series-parallel pairs suggest a minimum of six high-voltage winding sections to represent the HV winding up to 100kHz.

5.2. Case studies for a high-voltage transformer model

This section presents the characterisation and parameter estimation of the high-voltage transformer applying the six measurements presented in the previous section. This section presents three case studies that adapt the wideband equivalent-circuit model developed by Brozio [19] in various ways to obtain an equivalent-circuit model that best represents the transformer measurements. The section begins by presenting the parameter estimation methodology that is applied to the case studies. The models are then introduced along with their respective analytical impedance matrices, the most successful parameter estimation results obtained for each model are presented and discussed.

5.2.1. Parameter estimation methodology

Noise is observed in the practical measurements above frequencies of 20kHz in the transformation ratios, as is visible in Figures 5.5c and 5.9c, as well as the high-voltage input impedance measurements in Figures 5.9a and 5.9b. The frequency range used for the parameter estimation is, therefore, limited to between 10Hz and 10kHz for all case studies. It is expected for the response of the LVSC input impedance measurement below 50Hz to be dominated by the low-voltage winding resistance. However, noise on the measurement data could cause the estimator to misconstrue the noise for a series resonant point, thus the data below 50Hz for the LVSC measurement is omitted in the parameter estimation methodology.

The parameter estimation methodology is visually represented in Fig. 5.10. The HV transformer perturbation leg of the figure is described in the previous section and the resulting set of four input impedances and two voltage transformation ratio frequency responses are:

$$\Gamma = [Z_{lvoc}(\omega), Z_{lvsc}(\omega), Z_{hvoc}(\omega), Z_{hvsc}(\omega), R_{lvhv}(\omega), R_{hvlv}(\omega)]. \tag{5.4}$$

The corresponding set of estimate frequency responses from the transformer model is defined as

$$\tilde{\Gamma} = [\tilde{Z}_{lvoc}(\omega), \tilde{Z}_{lvsc}(\omega), \tilde{Z}_{hvoc}(\omega), \tilde{Z}_{hvsc}(\omega), \tilde{R}_{lvhv}(\omega), \tilde{R}_{hvlv}(\omega)], \tag{5.5}$$

where the responses are obtained from the analytically derived impedance matrices of the model under investigation. The number of frequency responses in both Γ and $\tilde{\Gamma}$ is denoted as N_r. More generally, the sets of practical and estimated responses can respectively, be described as

$$\Gamma = [\gamma_r(\omega) | r = 1, 2, 3 \ldots N_r] \tag{5.6}$$

and

$$\tilde{\Gamma} = [\tilde{\gamma}_r(\omega) | r = 1, 2, 3 \ldots N_r]. \tag{5.7}$$

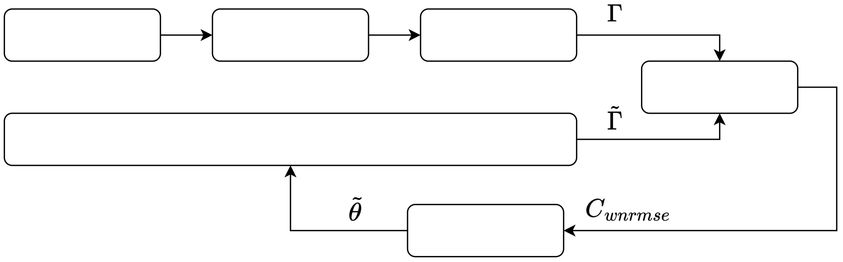

Figure 5.10: Parameter estimation methodology applied to the model case studies.

The cost function, C_{wnrmse}, is formulated by calculating the Weighted Normalised Root Mean Squared Error (WNRMSE) between each frequency response and then summed over all entries in the sets Γ and $\tilde{\Gamma}$. The cost function is formulated as

$$C_{wnrmse} = \sum_{r=1}^{N_r} \frac{1}{\psi_r} \sqrt{\frac{1}{N_k} \sum_{k=1}^{N_k} \lambda_r(\omega_k)(\epsilon_r(\omega_k))^2}, \tag{5.8}$$

where the errors, $\epsilon_r(\omega_k)$, are defined as the point-by-point difference between the logarithm of the r^{th} frequency response magnitude in the sets Γ and $\tilde{\Gamma}$. The error is formulated as

$$\epsilon_r(w_k) = \log_{10} |\gamma_r(\omega_k)| - \log_{10} |\tilde{\gamma}_r(\omega_k)|, \tag{5.9}$$

where ω_k represents the k^{th} index of a logspaced frequency vector, consisting of N_k samples.

Provision is made for the option to weigh the errors based on their location in the frequency band. The weighting vector, λ_r, multiplies the errors with a weighting factor, Λ. The mathematical formulation of the weighting vector is

$$\lambda_r(\omega) = \Lambda \cdot (u(\omega - \omega_{k,low}) - u(\omega - \omega_{k,high})), \tag{5.10}$$

where the constant Λ is multiplied by a unit step window function between the frequencies $f_{k,low}$ and $f_{k,high}$, where $\omega = 2\pi f$. The indices, k, low and $k, high$, are chosen such that the resonant frequencies observed in the measured frequency responses are within the range between $f_{k,low}$ and $f_{k,high}$. Table 5.1 summarises the lower and upper bounds of the frequencies chosen in the weighting vector.

Table 5.1: Bounding frequencies of λ_r based on the resonant points in the measured frequency response data, Γ.

Weighting Vector	$f_{k,low}$ [kHz]	$f_{k,high}$ [kHz]
λ_1	0.8	10
λ_2	2	10
λ_3	2	10
λ_4	0.8	10
λ_5	2	10
λ_6	2	10

The respective errors are normalised by applying the normalisation constant

$$\psi_r = \max\{\gamma_r(\omega)\} - \min\{\gamma_r(\omega)\}, \tag{5.11}$$

where $\max\{\gamma_r(\omega)\}$ and $\min\{\gamma_r(\omega)\}$ are the maximum and minimum magnitude of the r^{th} measured frequency response, respectively. This normalisation is required to prevent the cost function biasing towards frequency responses with higher magnitudes.

The particle-swarm optimisation algorithm is used in all the case studies. Upon completion of the particle-swarm optimisation the hybrid functionality of the optimisation method is enabled, which executes the local *fmincon* solver with the interior-point algorithm to refine the results. The parameter estimation is performed twenty times by incrementally increasing the weighting factor, Λ, from one to twenty. For each weighting factor the methodology follows a two-step approach:

1. **Seed iterations:** The particle-swarm optimisation is executed, the start-points are generated randomly based on the Mersenne Twister pseudo-random number generator with a seed set from 1 to 5. This effectively results in performing a PSO beginning at five unique sets of start points.
2. **Final seed:** Once all five parameter estimations are completed the model parameters

that obtained the lowest cost function are stored and used as the starting point for a *fmincon* optimisation execution.

Once all weighting factors have undergone this methodology, the parameter values that provide the most accurate frequency response are regarded as the final parameters. Due to the difference in weighting factor between parameter estimation attempts the cost function values will naturally increase with an increasing weighting factor. Therefore comparing the C_{wnrmse} resulting from cost functions using different weighting factors does not provide an indication of the best performing parameter estimation. Therefore, once the two step approach has been completed the estimated model parameters are used to plot the respective frequency responses and visually compared to the measurements to select the best result. The swarm size and the number of iterations executed by the particle-swarm algorithm and the *fmincon* solver are specific to the case study and are reported within the respective sections.

Due to the large number of model parameters to be estimated the search space has a complex and large number of dimensions that needs to be traversed by the optimisation algorithm. It is favourable to execute multiple PSOs with smaller populations beginning at different points and then subsequently comparing the different convergence results as opposed to one larger PSO that provides only a single convergence result. The default number of iterations for PSO is $200 \times n_{vars}$, where n_{vars} are the number of parameters to be estimated [38]. The model topologies in the case studies to follow are large resulting in between 30 and 45 parameters, which would cause each optimisation to take dozens of hours. To decrease the runtimes the number of iterations is decreased and instead followed by the less complex *fmincon* local optimisation procedure.

5.2.2. Analytical frequency response derivation methodology

Four analytical input impedance transfer functions and two analytical voltage transformation ratio transfer functions need to be computed for each model. The methodology used to derive the transfer functions is the same for each model. This section provides a general overview of the methodology, whilst the relevant case study will provide the validation of the derived analytical frequency responses. The analytical frequency responses are all computed in terms of the relevant model parameters such that they can be used within the parameter estimation procedure to compute the model's frequency responses based on the model parameters obtained from iteration to iteration.

The four input impedance transfer functions of the model, i.e. $\tilde{Z}_{lvoc}(\omega)$, $\tilde{Z}_{lvsc}(\omega)$, $\tilde{Z}_{hvoc}(\omega)$ and $\tilde{Z}_{hvsc}(\omega)$, are obtained by determining the impedance matrix, $\mathbf{Z}$, for each measurement case through mesh current equations. The mesh current equations differ from response to response due to the location of the input voltage as well as the addition of either an open-circuit or short-circuit at the terminals. Each input impedance transfer function can be obtained by applying the general equation:

$$Z_{in}(s) = \frac{V_{in}(s)}{I_{in}(s)} = \frac{\Delta_Z}{\Delta_{(n,n)}}, \tag{5.12}$$

where Δ_Z is the determinant and $\Delta_{(n,n)}$ is the (n,n)-th cofactor of the $n \times n$ impedance matrix $\mathbf{Z}$.

The two voltage transformation ratio transfer functions, i.e. $\tilde{R}_{lvhv}(\omega)$ and $\tilde{R}_{hvlv}(\omega)$, can be obtained by assuming a 1V input voltage. This simplifies the transformation ratio to the following

$$R(s) = \frac{V_o(s)}{V_{in}(s)} = \frac{V_o(s)}{1}. \tag{5.13}$$

Therefore, the frequency-dependent transformation ratio, $R(s)$, is derived by obtaining $V_o(s)$. With the assumption of a 1V input voltage it is possible to calculate the resulting current column vector $\mathbf{I}$ using $\mathbf{ZI} = \mathbf{V}$. The LVOC impedance matrix is used for calculating $\tilde{R}_{lvhv}(\omega)$ and the HVOC impedance matrix is used for calculating $\tilde{R}_{hvlv}(\omega)$. The output voltage $V_o(s)$ is calculated by mutiplying the corresponding mesh current with the impedance of the circuit elements across $V_o(s)$.

Performing a calculation of the determinant of large matrices in terms of model parameters requires long computations. Therefore, to quicken the computations, and by extension the parameter estimation runtimes, the model parameters are first substituted into the impedance matrices prior to calculating the respective frequency responses.

5.2.3. Case Study 1: Wideband lumped-parameter transformer model

This case study investigates the model shown in Fig. 5.11 as proposed by Brozio [11]. The impedance matrices are derived in terms of the model parameters and are presented in Appendix G.

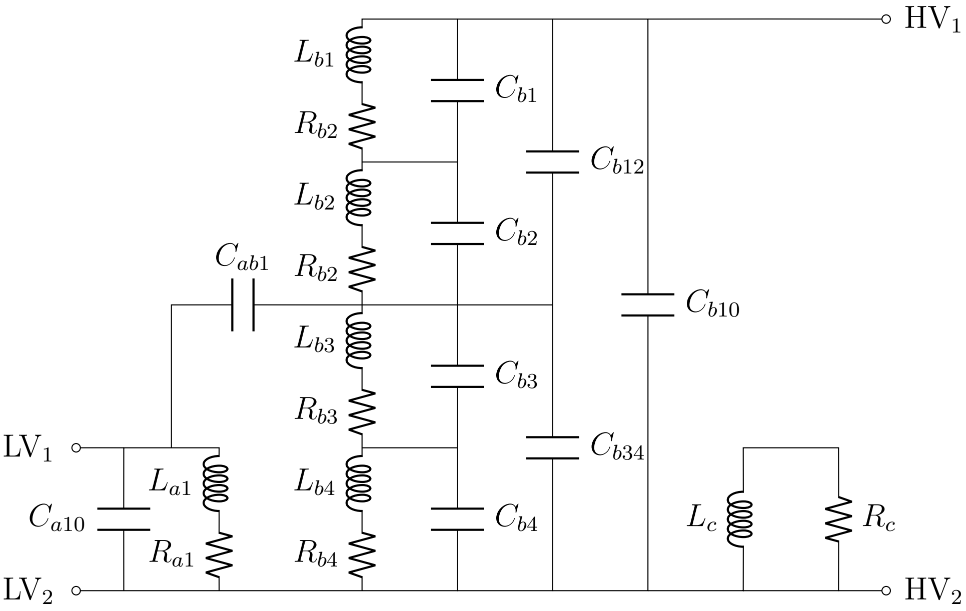

Figure 5.11: Wideband lumped-parameter transformer model as proposed by Brozio [11].

The analytical impedance matrices are derived through the methodology presented in Section 5.2.2. Random variables are chosen for the model parameters and the model is perturbed in simulation using PRIS perturbation. The resulting frequency responses are compared to the derived analytical expressions. Fig. 5.12 shows that the two methodologies yielded similar frequency responses for all tests, thereby validating the analytically derived impedance matrices.

The model structure of Fig. 5.11 has a total of 36 parameters to be estimated however some simplifications are made by Brozio [11] to reduce the number of parameters. To simplify the modelling of core losses all flux components, including leakage flux, that are linked by the lumped winding inductances are assumed to be confined to the core and, therefore, contribute to the core losses. The coupling coefficient between each winding section self-inductance and L_c is assumed to be equal and approximated by a tight coupling approaching unity. A coupling coefficient, K_c, of 0.9999 is selected. Lastly, L_c is made a constant as it only serves to couple the core-loss resistance, R_c, to the winding inductances. Brozio [11] chose an arbitrary value of 37.5H, which placed the value of R_c within a numerically convenient range. The above assumptions reduces the number of model parameters to be estimated to 30.

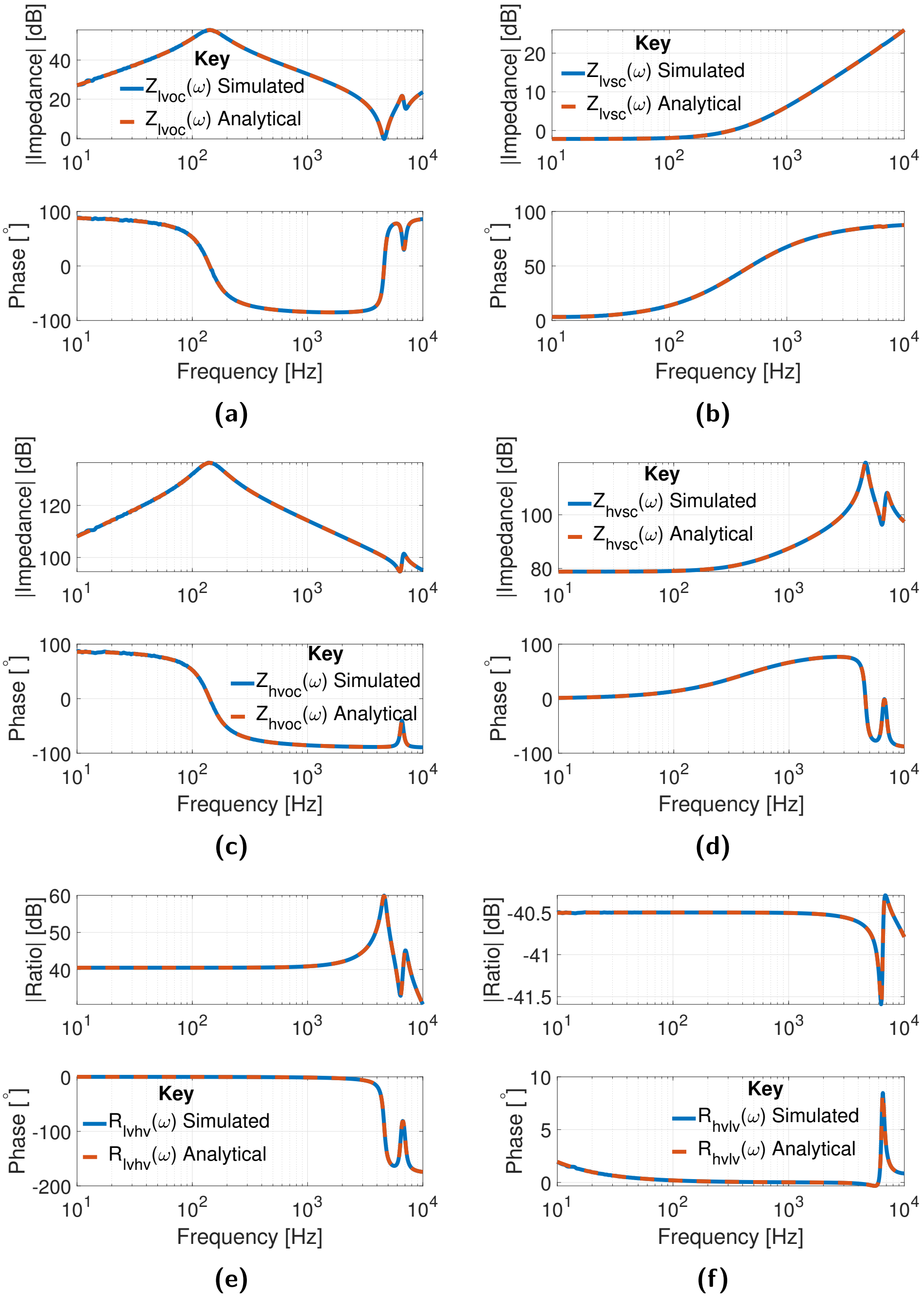

Figure 5.12: Magnitude and phase responses of **(a)**$Z_{lvoc}(\omega)$, **(b)**$Z_{lvsc}(\omega)$, **(c)**$Z_{hvoc}(\omega)$, **(d)**$Z_{hvsc}(\omega)$, **(e)**$R_{lvhv}(\omega)$ and **(f)**$R_{hvlv}(\omega)$ obtained analytically and through simulated PRIS perturbation of the model presented in Fig. 5.11 for a random set of parameters.

The parameter simplification and assumptions are altered for this case study by freely allowing parameters R_c and L_c to be estimated. The assumption that all flux components pass through the core is not possible as leakage components would not contribute to the core losses. The assumption that there is tight and equal coupling between each winding section self-inductance and the inductance L_c is removed, and each coupling coefficient is estimated individually. Due to the resistive elements within the winding sections influencing the resulting frequency response the least when compared to the inductive and capacitive elements, all high-voltage windings resistances are assumed to be equal, resulting in $R_b = R_{b1} = R_{b2} = R_{b3} = R_{b4}$. Applying these assumptions result in an optimisation problem with 33 parameters to be estimated.

The self-inductances of the high-voltage winding are defined collectively in the subvector given by:

$$\mathbf{L}_b = \begin{bmatrix} L_{b1} & L_{b2} & L_{b3} & L_{b4} \end{bmatrix}, \tag{5.14}$$

these parameters can be grouped together as they are scaled by the same factor and are assigned the same upper and lower bounds. Similarly, parameter subvectors for the capacitance and coupling coefficient parameters are respectively given by:

$$\mathbf{C}_{sg} = \begin{bmatrix} C_{a10} & C_{b1} & C_{b2} & C_{b3} & C_{b4} & C_{b12} & C_{b34} & C_{b10} & C_{ab1} \end{bmatrix} \tag{5.15}$$

and

$$\begin{aligned} \mathbf{K}_{abc} =[&K_{a1b1} \quad K_{a1b2} \quad K_{a1b3} \quad K_{a1b4} \quad K_{b1b2} \quad K_{b1b3} \quad K_{b1b4} \quad K_{b2b3} \\ &K_{b2b4} \quad K_{b3b4} \quad K_{a1c} \quad K_{b1c} \quad K_{b2c} \quad K_{b3c} \quad K_{b4c}]. \end{aligned} \tag{5.16}$$

Table 5.2 presents the scaling factors for each model parameter as well as the lower and upper bounds set in the optimisation procedure. Wide lower and upper bounds are set for the parameter estimation procedure to increase the likelihood of the global minimum being located within the search space. The core-loss resistance, R_c, is expected to be larger than the winding resistance so the bounds are adjusted to reflect this expectation. If parameters upon completion of the optimisation are estimated on the bounds of the search space the bounds are re-defined, and the optimisation repeated.

Table 5.2: Parameter scaling factors and bounds.

Parameter	Scaling Factor	Lower Bound	Upper Bound	Units
R_{a1}	10^{-3}	1	1000	$m\Omega$
R_b	10^{2}	1	1000	$k\Omega$
R_c	10^{2}	500	1500	$k\Omega$
$\mathbf{C}_{sg}$	10^{-12}	1	1000	pF
L_{a1}	10^{-2}	1	1000	mH
$\mathbf{L}_b$	10^{1}	1	1000	H
L_c	10^{0}	1	1000	H
$\mathbf{K}_{abc}$	10^{-2}	99	99.99	

Table 5.3 presents the cost function values obtained by the hybrid particle-swarm optimisation algorithm for the methodology described in Section 5.2.1. The first optimisation step contains a swarm size of 50 executing for 200 iterations, followed by *fmincon* executing

for 5000 iterations. The second optimisation step increases the *fmincon* iterations to 20000. The green cells represent the best cost function per weighting factor after the first optimisation step and represent the model parameters that will be used as start points for the second step. The results in italics represent the cost function values obtained as a result of the second parameter estimation step. The results from each optimisation procedure are visually inspected to identify the best result. The best result, highlighted in blue, is obtained with a weighting factor of $\Lambda = 17$ using the fifth seed iteration.

Table 5.3: The cost function value, C_{wnrmse}, from the parameter estimation of the model presented Fig. 5.11 for varying weighting factors and random seed initialisations.

Λ	Seed Iterations					*Final Seed*	Λ	Seed Iterations					*Final Seed*
	1	2	3	4	5			1	2	3	4	5	
1	0.557	1.101	1.049	0.791	0.913	*0.460*	**11**	3.503	2.332	4.473	1.590	3.214	*1.130*
2	0.778	1.892	1.198	1.020	1.420	*0.560*	**12**	1.738	1.789	1.797	4.482	4.130	*1.187*
3	1.545	2.390	1.514	3.516	1.505	*1.229*	**13**	5.064	4.700	4.337	3.986	2.205	*1.289*
4	0.973	2.099	0.994	2.498	1.564	*0.684*	**14**	4.664	3.492	4.093	1.907	4.400	*1.292*
5	1.144	1.111	1.955	1.054	1.969	*0.986*	**15**	4.189	4.464	6.148	5.078	5.624	*4.077*
6	2.770	2.372	2.133	2.170	2.617	*2.083*	**16**	4.804	7.550	6.851	4.926	1.630	*1.433*
7	2.567	2.932	2.485	2.618	1.277	*0.862*	**17**	5.650	6.134	5.395	5.989	4.147	*1.491*
8	2.672	2.847	2.892	2.188	3.111	*1.544*	**18**	5.230	5.530	5.969	6.391	2.860	*1.578*
9	2.915	3.817	3.354	3.515	3.203	*0.650*	**19**	1.829	7.399	4.493	4.920	5.948	*1.668*
10	2.670	2.893	3.354	1.406	2.967	*1.063*	**20**	3.012	6.101	6.387	2.505	5.643	*1.690*

The model parameters that produced the best estimate in frequency responses are presented in Table. 5.4. The resulting magnitude and phase responses are plotted in orange in Fig. 5.13, whilst the transformer frequency response measurements are presented in blue.

Table 5.4: Final parameter estimates of the model presented in Fig. 5.11.

Parameter	Value	Parameter	Value	Parameter	Value	Parameter	Value
$R_{a1}\ [mH]$	117.3	$C_{b3}\ [pF]$	441.4	$L_c\ [H]$	308.6	K_{b2b3}	0.9981
$R_b\ [k\Omega]$	4.475	$C_{b4}\ [pF]$	188.2	K_{a1b1}	0.9947	K_{b2b4}	0.9976
$R_c\ [k\Omega]$	73.29	$C_{ab1}\ [pF]$	54.7	K_{a1b2}	0.9969	K_{b3b4}	0.9983
$C_{a10}\ [pF]$	177.9	$L_{a1}\ [mH]$	255.7	K_{a1b3}	0.9989	K_{a1c}	0.9924
$C_{b10}\ [pF]$	85.25	$L_{b1}\ [H]$	879	K_{a1b4}	0.9981	K_{b1c}	0.9921
$C_{b12}\ [pF]$	604.7	$L_{b2}\ [H]$	904.6	K_{b1b2}	0.9943	K_{b2c}	0.9933
$C_{b34}\ [pF]$	95.67	$L_{b3}\ [H]$	2916	K_{b1b3}	0.9952	K_{b3c}	0.9943
$C_{b1}\ [pF]$	199.7	$L_{b4}\ [H]$	3972	K_{b1b4}	0.9985	K_{b4c}	0.9939
$C_{b2}\ [pF]$	143.4						

Although the noisy LVSC measurements below 50Hz are excluded from the parameter estimation the model is still able to obtain a low-frequency estimate that closely matches the measurements. The damping of the resonant points does not perfectly match that of the measurements. The damping is especially incorrect at resonant points that are located below 1kHz. This is due to the core resistance and winding inductance parameters not including any frequency-dependent non-linearities in the estimation procedure. Similar results are reported by Brozio [19] when linear circuit elements were used to model the distribution transformer.

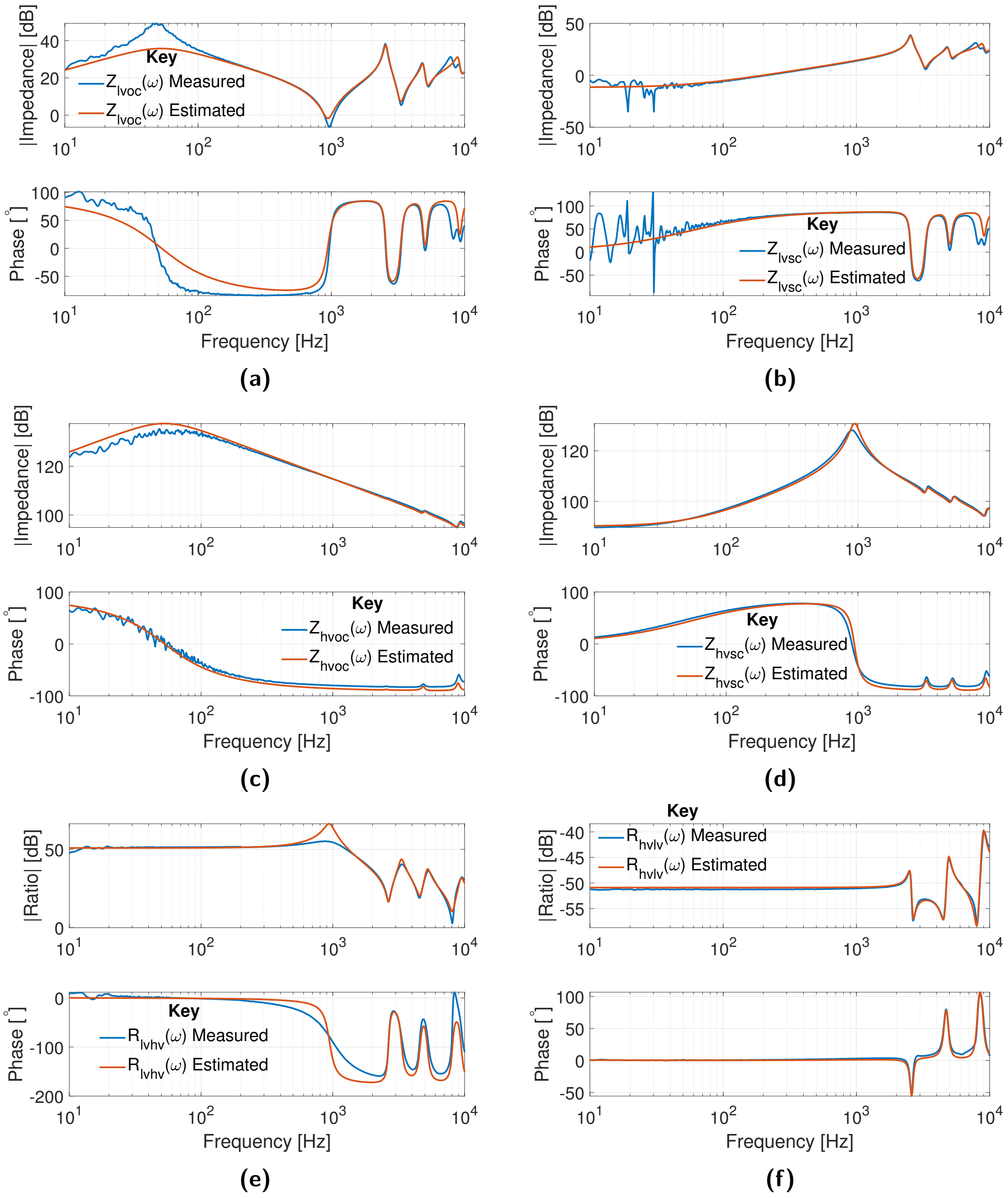

(a) **(b)**

(c) **(d)**

(e) **(f)**

Figure 5.13: Comparison between the measured and estimated magnitude and phase responses of **(a)**$Z_{lvoc}(\omega)$, **(b)**$Z_{lvsc}(\omega)$, **(c)**$Z_{hvoc}(\omega)$, **(d)**$Z_{hvsc}(\omega)$, **(e)**$R_{lvhv}(\omega)$ and **(f)**$R_{hvlv}(\omega)$ of the model presented in Fig. 5.11.

The model is able to produce the same number of resonant points for all measurements, aside from the minor series-parallel pair at approximately 9kHz in the LVOC and LVSC input impedances. This suggests that the order is not high enough to produce any more resonant points. The lower model order is to be expected as the distribution transformer that the model was developed for only exhibits four parallel-series resonant pairs in the LVOC measurement and two parallel-series pairs in the LVSC measurement. Whereas, the HV transformer under investigation has five resonant pairs in the LVOC and four in the LVSC measurements.

5.2.4. Case Study 2: Wideband lumped-parameter transformer model with additional inter-winding capacitance

Due to the higher transformation ratio of the HV test transformer compared to the distribution transformer investigated by Brozio, it is hypothesized that the number of turns on the HV winding is where the major discrepancy lies between Brozio's model in Fig. 5.11 and the HV test transformer currently under investigation. A solution would be to add additional sections to the HV winding, which would increase the number of parameters significantly, resulting in a larger and more complex search space to optimise within. An alternative approach is investigated in this case study that includes only one additional lumped inter-winding capacitance, C_{ab2}, to the model. This is done to more accurately model the distributed nature of the capacitive coupling between the LV and HV winding due to the larger number of turns on the HV winding.

For the first attempt the additional capacitance is added to couple the upper terminals of the LV and HV winding directly to one another as shown in Fig. 5.14. The impedance matrices of this model are derived and presented in Appendix H. The analytical expressions are subsequently derived from a random set of model parameters using the methodology descibed in Section 5.2.2 and the resulting analytical frequency responses are validated by the same procedure as in the previous case study. The frequency responses yielded analytically and through simulated PRIS perturbation show excellent correlation and are presented in Appendix I.

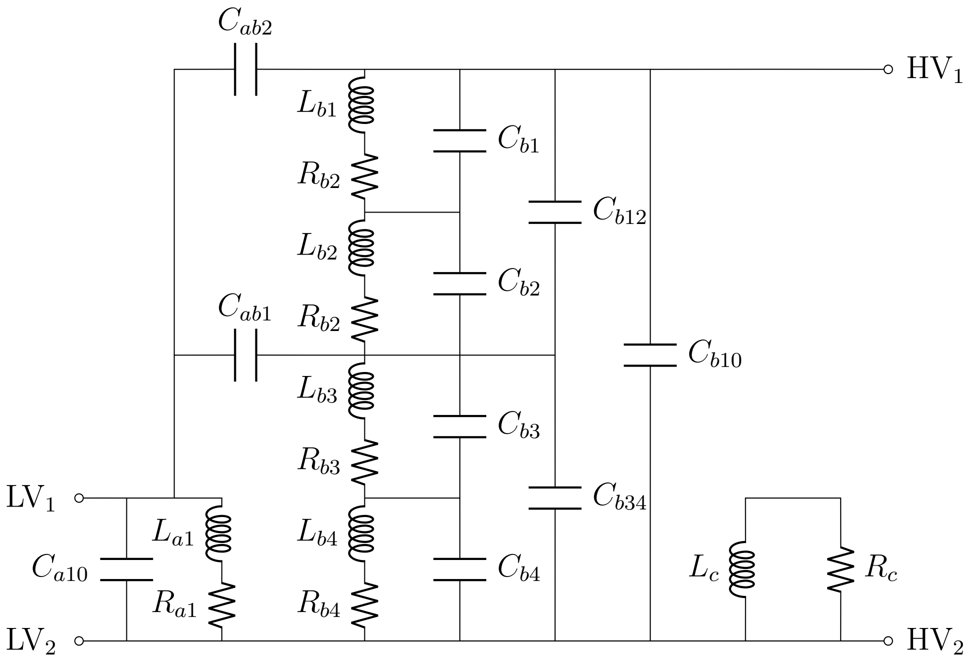

Figure 5.14: Wideband lumped-parameter transformer model with additional inter-winding capacitance placed between the upper transformer winding terminals.

The capacitance subvector of this model is redefined in (5.17) to include the additional inter-winding capacitance, C_{ab2}. All other parameter subvectors remain as presented in Case Study 1.

$$\mathbf{C}_{sg} = \begin{bmatrix} C_{a10} & C_{b1} & C_{b2} & C_{b3} & C_{b4} & C_{b12} & C_{b34} & C_{b10} & C_{ab1} & C_{ab2} \end{bmatrix} \tag{5.17}$$

The assumptions, scaling factors and bounds for the respective model parameters and subvectors remain the same as for the previous case study, as presented in Table. 5.2.

The cost function values obtained from the parameter estimation methodology are presented in Table. 5.5. The first step in the optimisation makes use of a swarm size of 50 running for 200 iterations followed by *fmincon* for 5000 iterations. The second step allows *fmincon* to execute for maximum of 20000 iterations. The parameter estimation settings are not altered from Case Study 1, as the addition of one parameter would only increase the size of the search space by a single dimension. The seed that obtained the lowest C_{wnrmse} values for each weighting factor is highlighted in green. The results obtained from the second step are presented in italics. The most successful overall result, identified through visual inspection, is highlighted in blue.

Table 5.5: The cost function value, C_{wnrmse}, from the parameter estimation of the model presented in Fig. 5.14 for varying weighting factors and random seed initialisations.

Λ	Seed Iterations					*Final Seed*	Λ	Seed Iterations					*Final Seed*
	1	2	3	4	5			1	2	3	4	5	
1	1.412	0.724	0.726	0.958	1.031	*0.489*	**11**	3.427	4.222	2.301	3.471	1.437	*1.114*
2	1.278	1.483	1.459	1.058	1.131	*0.851*	**12**	5.890	4.275	4.128	6.607	1.483	*1.283*
3	1.480	0.947	1.639	0.914	0.799	*0.605*	**13**	2.873	4.314	3.931	1.343	1.488	*1.251*
4	1.165	1.997	1.823	1.787	1.822	*0.674*	**14**	4.425	4.520	2.270	1.973	1.814	*1.345*
5	2.007	0.832	2.071	2.129	2.066	*0.736*	**15**	4.427	4.872	1.705	6.079	1.630	*1.609*
6	2.322	2.328	2.333	2.579	2.176	*0.864*	**16**	7.832	6.151	1.985	6.180	5.070	*1.466*
7	2.988	2.284	3.429	2.536	1.190	*0.903*	**17**	5.368	3.286	5.100	2.779	5.409	*2.577*
8	2.446	2.944	2.180	2.599	2.430	*1.164*	**18**	5.346	9.325	8.459	5.373	2.582	*1.582*
9	2.677	1.354	3.883	4.189	2.728	*1.017*	**19**	5.516	5.819	5.397	5.743	4.023	*2.510*
10	2.89	3.560	2.075	3.070	3.078	*1.105*	**20**	2.875	6.104	2.566	6.530	6.563	*1.669*

Table. 5.6 presents the best set of model parameters whilst Fig. 5.15 shows the resulting frequency responses that these parameters produce, in orange, compared to the transformer measurements, in blue. The estimated frequency responses in Fig. 5.15 are of the same order as the previous case study with no significant improvement achieved by adding the extra inter-winding capacitance. The LV input impedance series-parallel resonance at approximately 9kHz is still not able to be matched by the model, which indicates that the model order has not increased within the frequency range below 10kHz.

Table 5.6: Final parameter estimates of the model presented in Fig. 5.14.

Parameter	Value	Parameter	Value	Parameter	Value	Parameter	Value
R_{a1} $[mH]$	168.9	C_{b3} $[pF]$	128.4	L_c $[H]$	226.7	K_{b2b3}	0.9939
R_b $[k\Omega]$	3.554	C_{b4} $[pF]$	150.7	K_{a1b1}	0.9968	K_{b2b4}	0.9974
R_c $[k\Omega]$	67.42	C_{ab1} $[pF]$	156.9	K_{a1b2}	0.9942	K_{b3b4}	0.9984
C_{a10} $[pF]$	133.1	C_{ab2} $[pF]$	52.09	K_{a1b3}	0.9988	K_{a1c}	0.9929
C_{b10} $[pF]$	9.912	L_{a1} $[mH]$	242.8	K_{a1b4}	0.9982	K_{b1c}	0.9949
C_{b12} $[pF]$	247.9	L_{b1} $[H]$	1377	K_{b1b2}	0.9974	K_{b2c}	0.9924
C_{b34} $[pF]$	118.7	L_{b2} $[H]$	289.5	K_{b1b3}	0.9981	K_{b3c}	0.9946
C_{b1} $[pF]$	849.3	L_{b3} $[H]$	2872	K_{b1b4}	0.9990	K_{b4c}	0.9951
C_{b2} $[pF]$	794.3	L_{b4} $[H]$	3897				

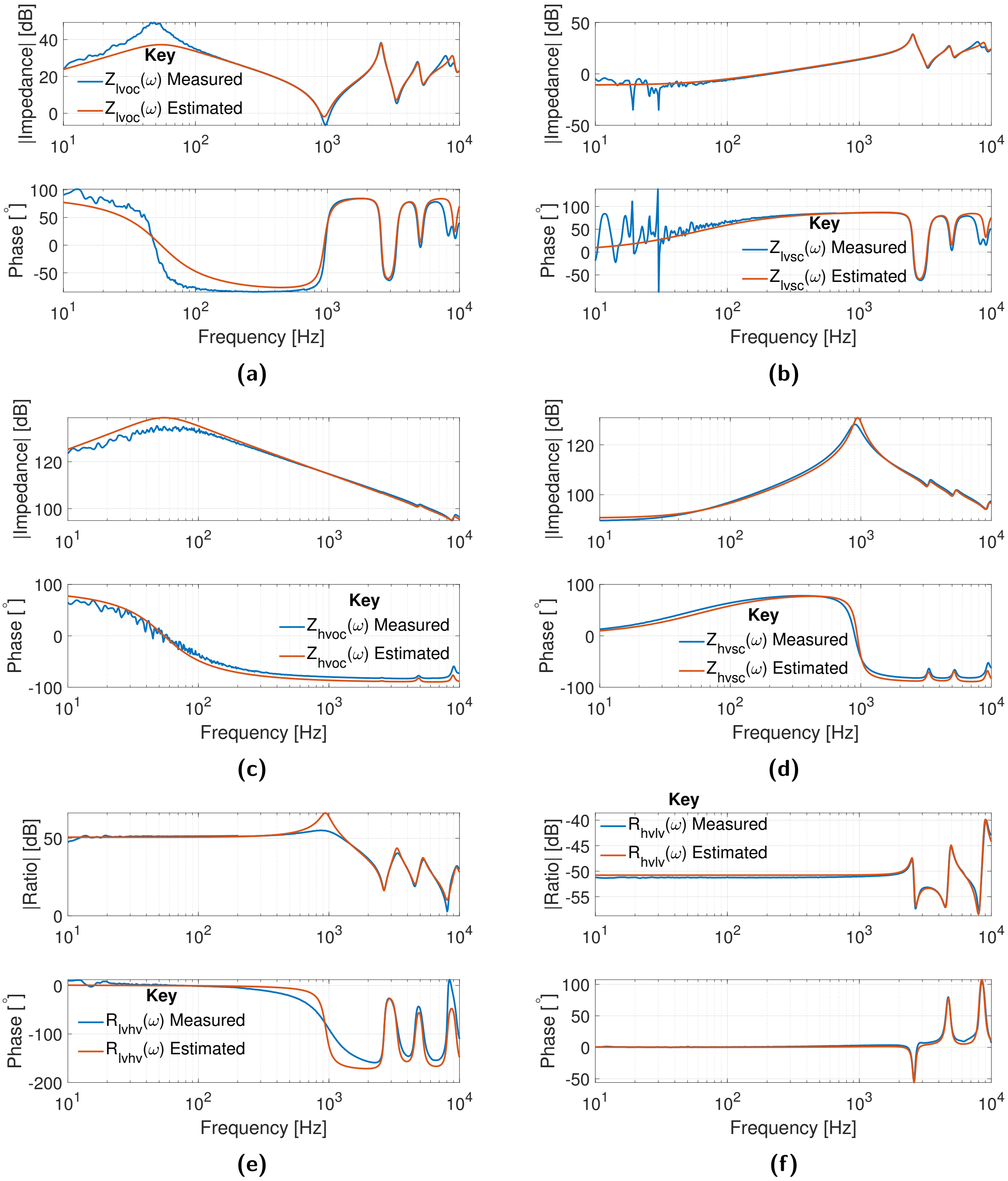

(a) **(b)** **(c)** **(d)** **(e)** **(f)**

Figure 5.15: Comparison between the measured and estimated magnitude and phase responses of **(a)**$Z_{lvoc}(\omega)$, **(b)**$Z_{lvsc}(\omega)$, **(c)**$Z_{hvoc}(\omega)$, **(d)**$Z_{hvsc}(\omega)$, **(e)**$R_{lvhv}(\omega)$ and **(f)**$R_{hvlv}(\omega)$ of the model presented in Fig. 5.14.

The second attempt adjusts the location of the two inter-winding capacitances such that the capacitances are tapped into the HV winding symmetrically as shown in Fig. 5.16. This is done to mimic the symmetry in the HV winding of the model in Fig. 5.11. The four impedance matrices are derived and presented in Appendix J. The model implements the same random set of parameters as used in the previous validation. The resultant frequency responses obtained from analytical expressions are compared to the frequency responses obtained through simulated PRIS perturbation in Appendix K. The two methods yielded similar frequency responses for all tests, thereby validating the analytically derived impedance matrices.

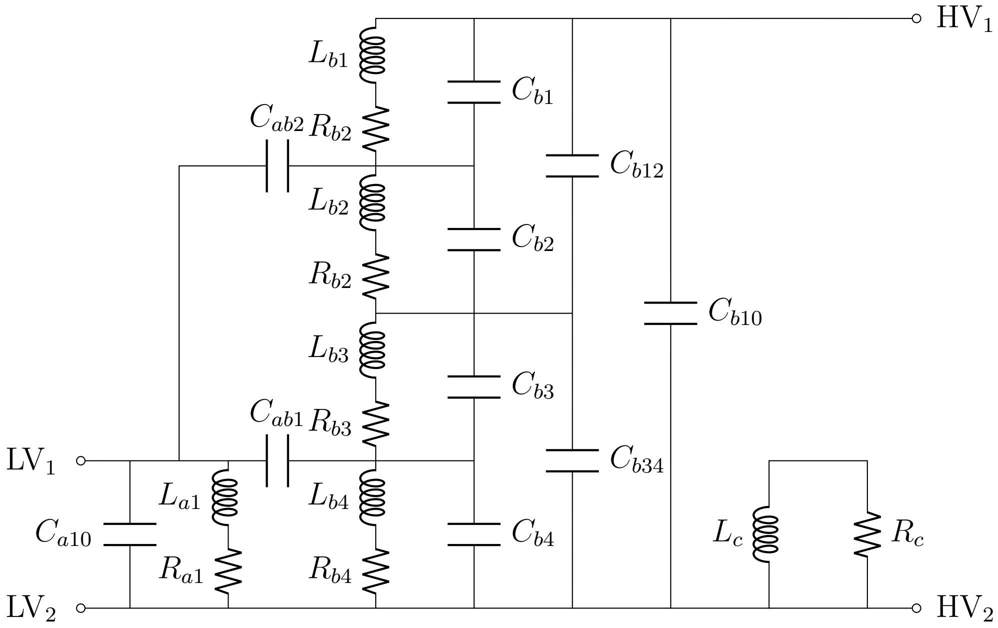

Figure 5.16: Wideband lumped-parameter transformer model with the inter-winding capacitances connected symmetrically to the high-voltage winding.

The value of R_c is estimated in the previous two model parameter estimations to be below $100k\Omega$ and as such the bounds are adjusted to match the bounds of R_b. The remaining assumptions, scaling factors and bounds for the model parameters and subvectors remain as in the previous case study and are presented in Table. 5.7.

Table 5.7: Parameter scaling factors and bounds.

Parameter	Scaling Factor	Lower Bound	Upper Bound	Units
R_{a1}	10^{-3}	1	1000	$m\Omega$
R_b	10^{2}	1	1000	$k\Omega$
R_c	10^{2}	1	1000	$k\Omega$
$\mathbf{C}_{sg}$	10^{-12}	1	1000	pF
L_{a1}	10^{-2}	1	1000	mH
$\mathbf{L}_b$	10^{1}	1	1000	H
L_c	10^{0}	1	1000	H
$\mathbf{K}_{abc}$	10^{-2}	99	99.99	

The cost function values for the parameter estimations of the model in Fig. 5.16 are presented in Table. 5.8. The optimisation swarm size and iterations are set to the same values as the previous model due to the number of model parameters remaining unchanged. Once again the best result identified through visual inspection is highlighted in blue.

Table 5.8: The cost function value, C_{wnrmse}, from the parameter estimation of the model presented in Fig. 5.16 for varying weighting factors and random seed initialisations.

Λ	Seed Iterations					*Final Seed*	Λ	Seed Iterations					*Final Seed*
	1	2	3	4	5			1	2	3	4	5	
1	0.767	0.713	1.036	1.107	0.472	*0.711*	**11**	5.092	4.288	4.4307	3.735	3.632	*1.068*
2	0.724	1.625	1.151	1.514	0.641	*0.542*	**12**	5.974	3.665	1.833	4.161	1.565	*1.238*
3	1.798	1.552	1.759	2.147	2.151	*1.277*	**13**	1.881	1.438	4.357	4.563	4.413	*1.288*
4	1.667	1.901	2.045	2.437	1.808	*1.491*	**14**	5.294	1.710	4.758	4.553	2.913	*1.360*
5	2.301	2.372	2.295	2.327	1.000	*0.736*	**15**	4.767	4.215	3.577	2.148	4.595	*1.408*
6	1.784	3.359	3.033	0.919	2.327	*0.806*	**16**	5.936	5.158	2.288	6.932	5.869	*1.487*
7	2.942	2.845	2.436	3.344	2.590	*2.321*	**17**	4.480	5.162	2.382	5.387	5.659	*1.582*
8	3.120	2.972	1.472	1.047	2.693	*0.934*	**18**	3.434	2.013	6.545	4.141	1.709	*1.579*
9	3.241	3.096	3.405	3.773	3.031	*2.885*	**19**	4.071	5.688	2.045	2.117	5.201	*1.619*
10	3.193	3.185	3.530	4.229	1.595	*1.068*	**20**	5.906	6.699	5.639	2.126	5.230	*1.705*

The parameters estimated for the model are presented in Table. 5.9 and are used to generate the estimated frequency responses in Fig. 5.17. The relocation of the inter-winding capacitances to reflect a symmetrical coupling to the HV winding did not improve the results. It is found in both attempts within this case study that the inter-winding capacitance had no effect on the frequency response order below 10kHz. This result aligns with the conclusions drawn by Brozio [19] and Bak-Jenson [99] that the inter-winding capacitance only affects frequencies above 500kHz.

Table 5.9: Final parameter estimates of the model presented in Fig. 5.16.

Parameter	Value	Parameter	Value	Parameter	Value	Parameter	Value
R_{a1} $[mH]$	143.4	C_{b3} $[pF]$	658.9	L_c $[H]$	80.90	K_{b2b3}	0.9968
R_b $[k\Omega]$	3.888	C_{b4} $[pF]$	15.26	K_{a1b1}	0.9988	K_{b2b4}	0.9982
R_c $[k\Omega]$	20.92	C_{ab1} $[pF]$	31.27	K_{a1b2}	0.9976	K_{b3b4}	0.9965
C_{a10} $[pF]$	87.03	C_{ab2} $[pF]$	19.47	K_{a1b3}	0.9955	K_{a1c}	0.9927
C_{b10} $[pF]$	35.40	L_{a1} $[mH]$	239.6	K_{a1b4}	0.9974	K_{b1c}	0.9948
C_{b12} $[pF]$	466.0	L_{b1} $[H]$	2753	K_{b1b2}	0.9971	K_{b2c}	0.9927
C_{b34} $[pF]$	375.5	L_{b2} $[H]$	424.3	K_{b1b3}	0.9970	K_{b3c}	0.9935
C_{b1} $[pF]$	237.2	L_{b3} $[H]$	360.5	K_{b1b4}	0.9981	K_{b4c}	0.9944
C_{b2} $[pF]$	110.0	L_{b4} $[H]$	6315				

The parameters of both L_c and R_c are estimated to be much lower in this experiment, however, the estimated frequency responses remain relatively similar to the previous case study. If one compares the relation between R_c and L_c from all the parameter estimation case studies they seem to be proportional, i.e. both either increase or decrease. This is indicative of the reasoning provided by Brozio [19], whereby L_c was kept constant and the resistance, R_c, was included as a parameter. This suggests that fixing the inductance L_c within a range of the values obtained in the above case studies could aid in improving the parameter estimation results.

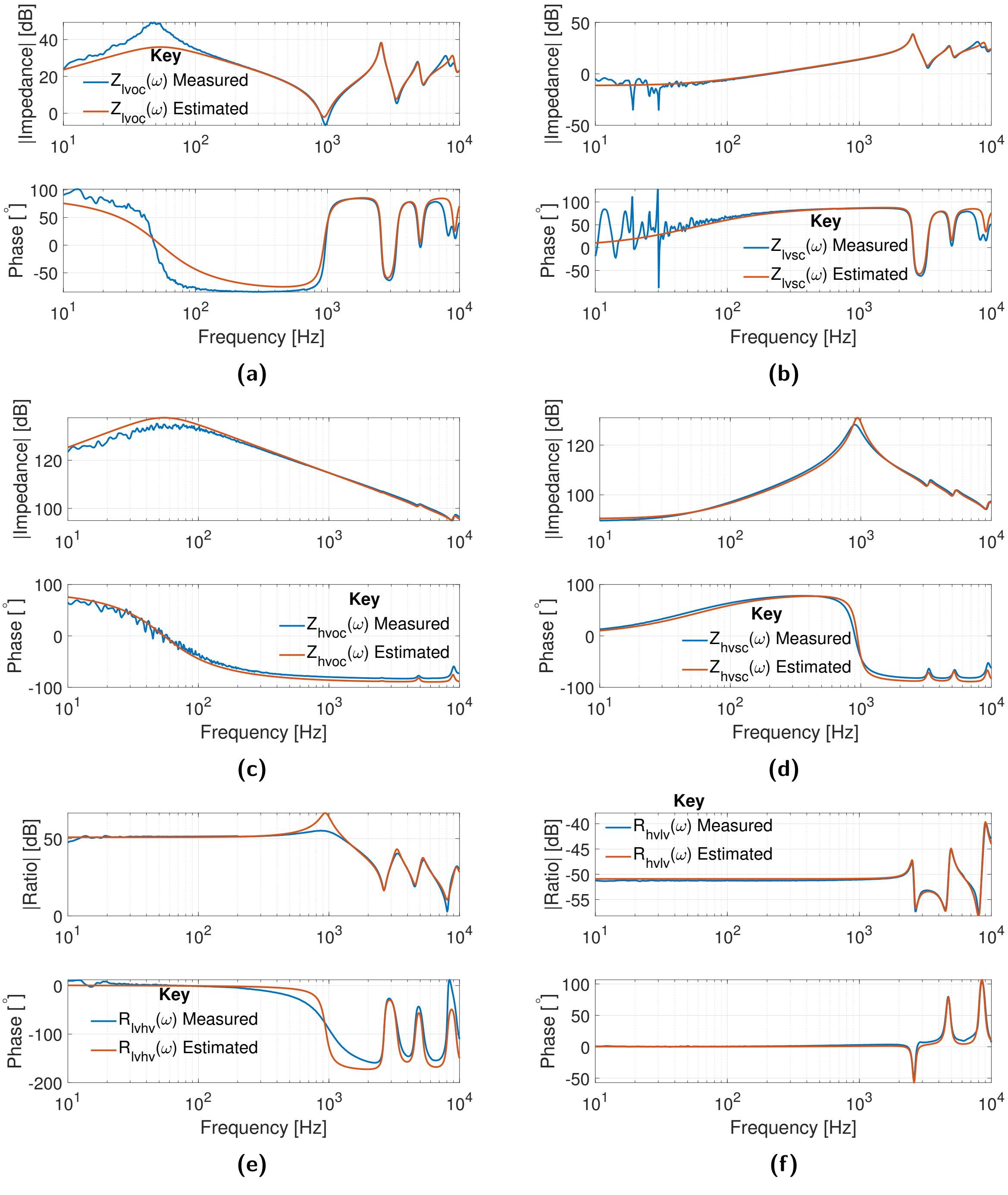

Figure 5.17: Comparison between the measured and estimated magnitude and phase responses of **(a)**$Z_{lvoc}(\omega)$, **(b)**$Z_{lvsc}(\omega)$, **(c)**$Z_{hvoc}(\omega)$, **(d)**$Z_{hvsc}(\omega)$, **(e)**$R_{lvhv}(\omega)$ and **(f)**$R_{hvlv}(\omega)$ of the model presented in Fig. 5.16.

In Case Study 1 and Case Study 2, the second optimisation step was also performed by *fmincon* for a maximum of 50000 iterations. Most of the results had, however, already converged by 20000 iterations. The slight improvement after 50000 iterations in the resulting estimated frequency responses does not warrant the increased runtime.

5.2.5. Case Study 3: Wideband lumped-parameter transformer model with additional high-voltage winding sections

The previous case study shows that using an additional inter-winding capacitance to model the larger high-voltage winding is not sufficient to add additional orders in the low-voltage input impedance frequency responses for the frequency range below 10kHz. The model adopted in this case study adapts the wideband lumped-parameter transformer model in Fig. 5.11 by adding two sections to the high-voltage winding. Two sections are added so as to maintain the symmetrical location of the inter-winding capacitance, C_{ab1}, as seen from the high-voltage winding. The choice of a six-section high-voltage winding is further motivated by the six observed parallel resonances in $Z_{hvsc}(\omega)$. The derived analytical impedance matrices are presented in Appendix L and subsequently validated using the same methodology as presented in the previous two case studies. The results of the validation confirming that the derived impedance matrices are correct, are presented in Appendix M.

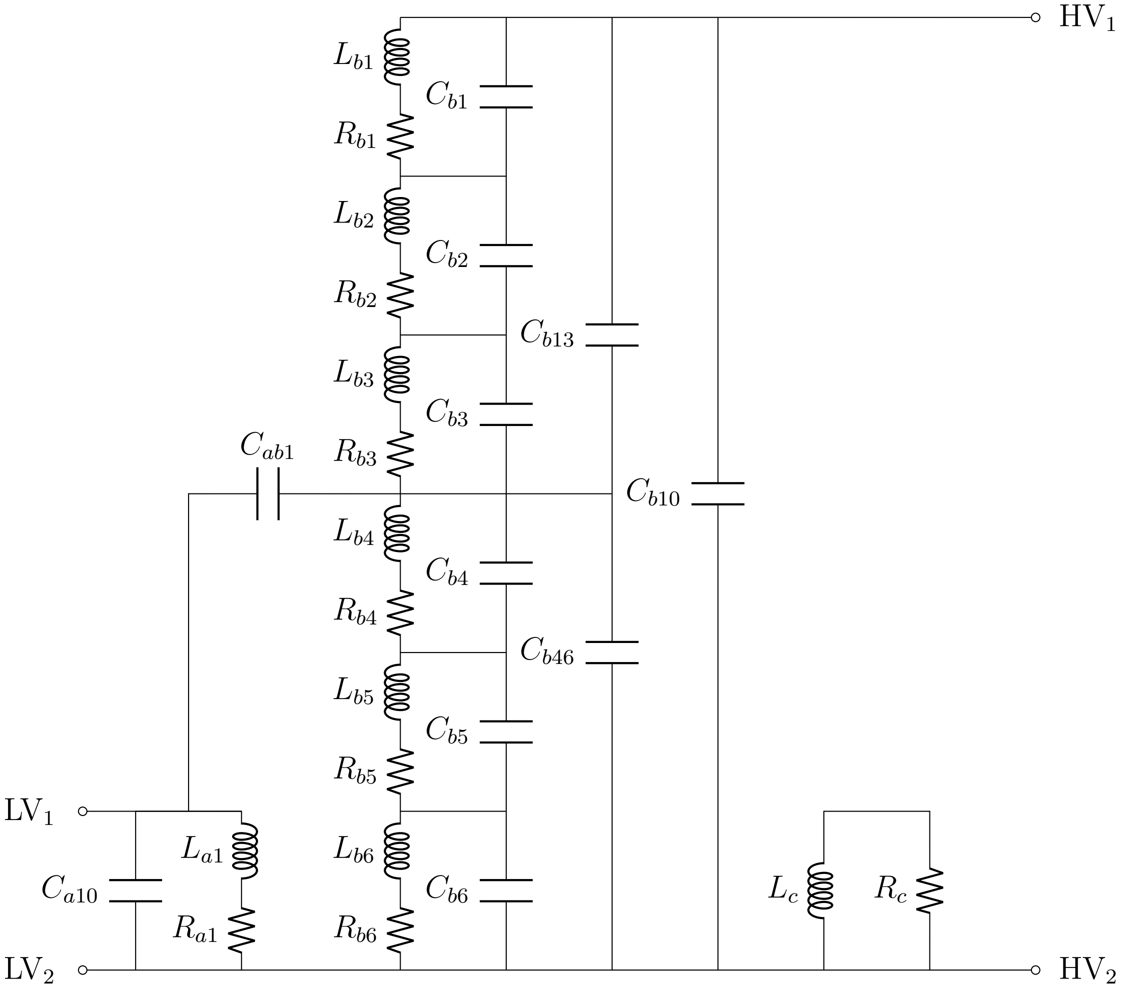

Figure 5.18: Wideband lumped-parameter transformer model with two additional high-voltage winding sections.

The addition of the two sections to the high-voltage winding introduces 19 new parameters to be estimated. Of which 13 are additional coupling coefficients linking the new sections to the original low-voltage section, high-voltage sections and core-loss section. Due to the large number of additional parameters, further assumptions are introduced to decrease the dimensionality of the problem. All the high-voltage winding resistances are, again, assumed to be equal and are replaced with the parameter $R_b = R_{b1} = R_{b2} = R_{b3} = R_{b4} = R_{b5} = R_{b6}$. The self-inductance and capacitance parameters remain separate and are respectively summarised in the subvectors given by:

$$\mathbf{L}_b = \begin{bmatrix} L_{b1} & L_{b2} & L_{b3} & L_{b4} & L_{b5} & L_{b6} \end{bmatrix}, \tag{5.18}$$

and

$$\begin{aligned}\mathbf{C}_{sg} =& [C_{a10} \quad C_{b1} \quad C_{b2} \quad C_{b3} \quad C_{b4} \quad C_{b5} \\ & C_{b6} \quad C_{b13} \quad C_{b46} \quad C_{b10} \quad C_{ab1}].\end{aligned} \tag{5.19}$$

To reduce the number of coupling coefficients to be estimated, the leakage flux associated with each lumped winding inductance is assumed to be constant and so the coupling coefficients linking the winding inductances to L_c are assumed to be equal. The coupling value is not fixed and still remains a parameter to be estimated, the simplification, therefore, becomes $K_c = K_{a1c} = K_{b1c} = K_{b2c} = K_{b3c} = K_{b4c} = K_{b5c} = K_{b6c}$. The subvector of coupling coefficient parameters is given by:

$$\begin{aligned}\mathbf{K}_{abc} =& [K_{a1b1} \quad K_{a1b2} \quad K_{a1b3} \quad K_{a1b4} \quad K_{a1b5} \quad K_{a1b6} \quad K_{b1b2} \\ & K_{b1b3} \quad K_{b1b4} \quad K_{b1b5} \quad K_{b1b6} \quad K_{b2b3} \quad K_{b2b4} \quad K_{b2b5} \quad K_{b2b5} \\ & K_{b2b6} \quad K_{b3b4} \quad K_{b3b5} \quad K_{b3b6} \quad K_{b4b5} \quad K_{b4b6} \quad K_{b5b6} \quad K_c].\end{aligned} \tag{5.20}$$

Table 5.10 presents the scaling factors and bounds for the 43 model parameters to be estimated in the optimisation procedure. The inductor, L_c, serves to couple the core-loss resistance to the transformer winding inductances, as such, the parameter is kept constant to reduce the number of parameters to be estimated. The value of 100H places the inductor and R_c in a similar range of values as estimated in the previous case studies.

Table 5.10: Parameter scaling factors and bounds.

Parameter	Scaling Factor	Lower Bound	Upper Bound	Units
R_{a1}	10^{-3}	1	1000	$m\Omega$
R_b	10^{2}	1	1000	$k\Omega$
R_c	10^{2}	1	1000	$k\Omega$
$\mathbf{C}_{sg}$	10^{-12}	1	1000	pF
L_{a1}	10^{-2}	1	1000	mH
$\mathbf{L}_b$	10^{1}	1	1000	H
$\mathbf{K}_{abc}$	10^{-2}	99	99.99	

Due to the significant increase in the number of parameters to be estimated, the PSO iterations are increased to 500. The PSO swarm size are increased in two separate investigations to 200 and 300. Significant improvement is obtained through a swarm size of 300, and as such, the results using the swarm size of 300 is reported. The maximum number of iterations of the hybrid *fmincon* within the first step remains set to 5000. Initially, the second step limited *fmincon* to 20000 iterations, however, a large number of estimations do not converge by the end of the iterations. The second step limits are, therefore, raised to 50000 iterations. The best result is highlighted in blue in Table. 5.11 and the estimated model parameters are listed in Table. 5.12.

Table 5.11: The cost function value, C_{wnrmse}, from the parameter estimation of the model presented in Fig. 5.18 for varying weighting factors and random seed initialisations.

Λ	Seed Iterations					*Final Seed*	Λ	Seed Iterations					*Final Seed*
	1	2	3	4	5			1	2	3	4	5	
1	0.623	0.644	0.423	0.718	0.767	*0.439*	**11**	4.322	4.118	4.639	4.053	4.132	*3.862*
2	1.099	1.034	0.552	1.156	0.583	*0.417*	**12**	4.401	4.752	4.771	4.796	4.579	*0.772*
3	2.349	0.696	1.569	1.692	1.817	*0.527*	**13**	4.964	1.944	2.676	1.836	5.572	*0.871*
4	0.747	1.822	2.036	1.922	1.135	*0.514*	**14**	3.779	2.043	6.051	7.220	5.373	*0.897*
5	0.842	2.733	0.948	0.821	1.039	*0.550*	**15**	2.152	5.460	6.046	5.482	5.477	*0.846*
6	2.511	1.647	0.988	2.518	1.350	*0.557*	**16**	4.812	6.329	1.556	5.834	1.467	*0.926*
7	3.598	3.442	3.665	2.859	1.527	*0.755*	**17**	1.980	5.984	5.838	4.276	2.043	*0.909*
8	1.003	3.292	3.205	1.152	1.605	*0.651*	**18**	6.403	2.016	6.487	6.539	4.890	*1.013*
9	0.928	4.268	5.064	1.228	3.627	*0.674*	**19**	6.403	8.070	7.017	7.419	5.290	*1.231*
10	1.176	4.045	4.310	3.677	1.502	*0.646*	**20**	7.271	3.253	7.034	7.418	2.183	*2.182*

The parameters estimated for the model are presented in Table. 5.12 and are used to generate the estimated frequency responses in Fig. 5.19. The estimated frequency responses show improvement in matching the measured frequency response when compared to the previous case studies in the frequency band above 1kHz. With the inclusion of additional sections to the high-voltage winding the order of the LV input impedance responses increased and can accurately estimate the minor series-parallel resonance at approximately 9kHz.

Table 5.12: Final parameter estimates of the model presented in Fig. 5.18.

Parameter	Value	Parameter	Value	Parameter	Value	Parameter	Value
R_{a1} $[mH]$	38.88	C_{b5} $[pF]$	288.4	K_{a1b1}	0.9965	K_{b2b3}	0.9928
R_b $[k\Omega]$	4.993	C_{b6} $[pF]$	424.8	K_{a1b2}	0.9956	K_{b2b4}	0.9959
R_c $[k\Omega]$	28.97	C_{ab1} $[pF]$	502.2	K_{a1b3}	0.9981	K_{b2b5}	0.9975
C_{a10} $[pF]$	569.7	L_{a1} $[mH]$	193.7	K_{a1b4}	0.9952	K_{b2b6}	0.9983
C_{b10} $[pF]$	78.13	L_{b1} $[H]$	263.3	K_{a1b5}	0.9959	K_{b3b4}	0.9953
C_{b13} $[pF]$	112.5	L_{b2} $[H]$	2984	K_{a1b6}	0.9960	K_{b3b5}	0.9945
C_{b46} $[pF]$	548.6	L_{b3} $[H]$	916.8	K_{b1b2}	0.9959	K_{b3b6}	0.9922
C_{b1} $[pF]$	209.7	L_{b4} $[H]$	144.4	K_{b1b3}	0.9941	K_{b4b5}	0.9944
C_{b2} $[pF]$	117.1	L_{b5} $[H]$	619.8	K_{b1b4}	0.9948	K_{b4b6}	0.9920
C_{b3} $[pF]$	508.3	L_{b6} $[H]$	286.4	K_{b1b5}	0.9970	K_{b5b6}	0.9932
C_{b4} $[pF]$	335.9			K_{b1b6}	0.9944	K_c	0.9979

The open-circuit input impedance measurements at low-frequencies are dominated by the core losses, and magnetising inductance. As discussed in Chapter 2, Brozio [19] found that by representing R_c and the winding self-inductances by frequency-dependent elements, the resonance at approximately 50Hz could be obtained for both the LVOC and HVOC measurements. Due to the considered model in Fig. 5.18 excluding these non-linearities, the combination of the estimated R_c and the linear self-inductances is able to estimate the damping of the parallel resonance at approximately 50Hz of only the HVOC measurement but not the LVOC measurement.

The winding resistance and leakage inductances of the windings dominate the short-circuit input impedance measurements. Due to the skin-effect, Brozio [19] included a frequency-dependent equation for the winding resistances. As the core forms part of the leakage flux paths a frequency-dependent equation is also used for the winding self-inductances when estimating the model parameters for short-circuit measurements. It is reported by Brozio [19] that the leakage inductance is not a strong function of frequency which explains the slight shift in the location of the first parallel resonance in the estimated HVSC input impedance frequency response. The combination of parameters can estimate the LVSC input impedance's measurement as well as the overall shape of HVSC impedance measurement accurately.

It is clear in both the open-circuit and short-circuit estimated frequency responses that due to the omission of frequency-dependent parameters, the input impedances at low-frequencies could only be estimated for either $Z_{lvoc}(\omega)$ or $Z_{hvoc}(\omega)$, and similarly for either $Z_{lvsc}(\omega)$ or $Z_{hvsc}(\omega)$, but not both. Due to $Z_{hvoc}(\omega)$ and $Z_{lvsc}(\omega)$ exhibiting low order responses below 1kHz, those responses are estimated correctly, as opposed to the more complex resonant behaviour below 1kHz in the measurements of $Z_{lvoc}(\omega)$ and $Z_{hvsc}(\omega)$.

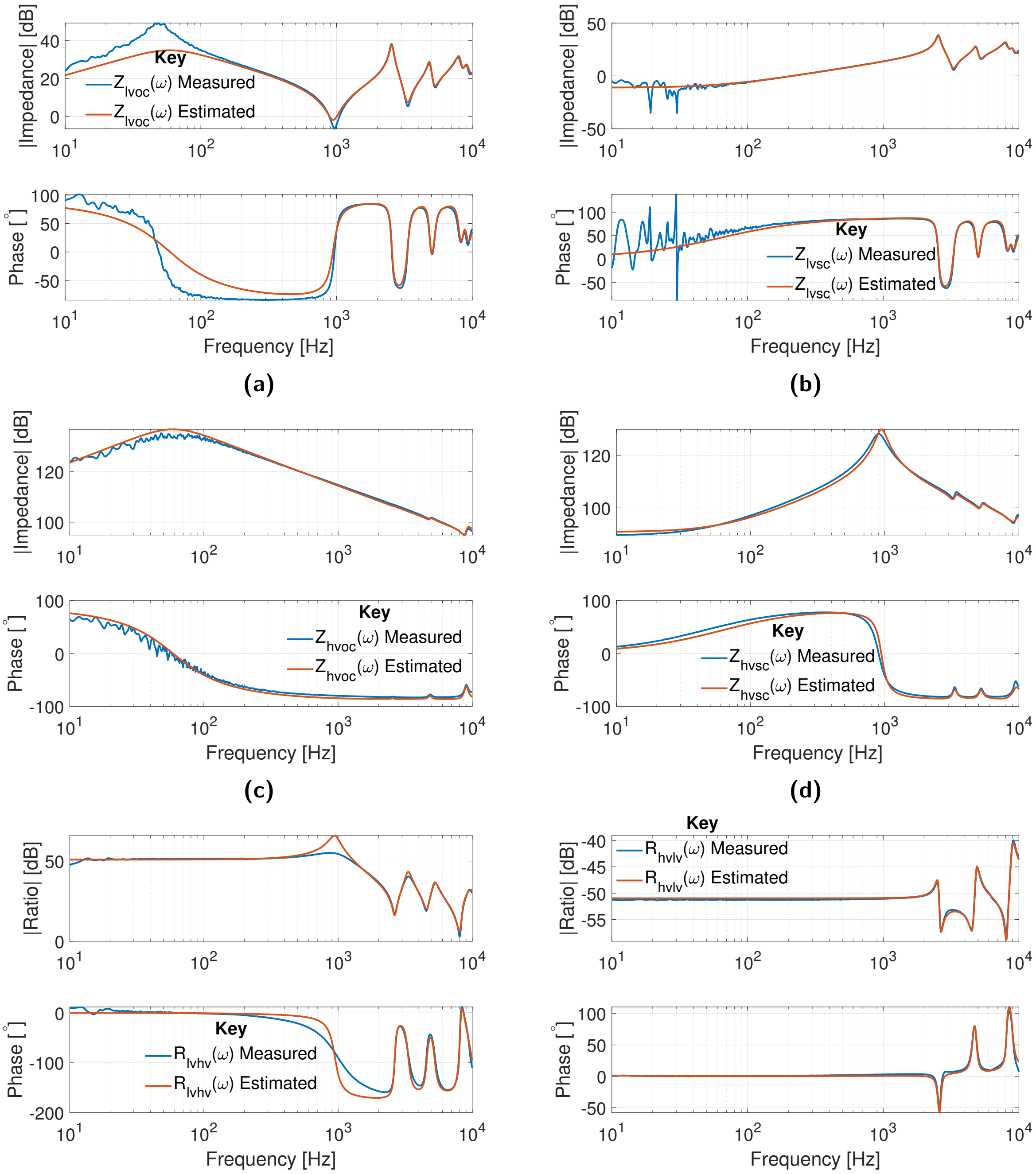

(a) **(b)**

(c) **(d)**

(e) **(f)**

Figure 5.19: Comparison between the measured and estimated magnitude and phase responses of **(a)**$Z_{lvoc}(\omega)$, **(b)**$Z_{lvsc}(\omega)$, **(c)**$Z_{hvoc}(\omega)$, **(d)**$Z_{hvsc}(\omega)$, **(e)**$R_{lvhv}(\omega)$ and **(f)**$R_{hvlv}(\omega)$ of the model presented in Fig. 5.18.

Chapter 6

Conclusions and Recommendations

This chapter summarises the findings and conclusions of the research conducted. The conclusions are presented with reference to the original research objectives and, as such, are categorised accordingly. The chapter is concluded with a summary of possible further areas of research.

6.1. Simulated perturbation

The PRIS perturbation arrangement is applied to a two-section transformer winding model as well as a three-section transformer winding model in simulation. The analytical transfer functions of the two-section transformer winding model's input impedance, and voltage ratios between the winding sections and input voltage, are derived. The frequency responses obtained through simulated perturbation and through the analytical expressions are used to verify the sufficient perturbation of the winding model. Similarly, the analytical transfer function of the input impedance for the three-section transformer winding model is derived, and presents frequency responses similar to the results obtained through a simulated PRIS perturbation of the model. These simulations validate the use of a PRIS perturbation signal in an offline perturbation arrangement of transformer winding models.

An investigation in simulation is conducted into the effects of the impedance magnitude of the PRIS RLC circuit in an offline perturbation arrangement. It is concluded that selecting a PRIS RLC circuit impedance magnitude of similar order to the input impedance magnitude of the DUT provides an acceptable tradeoff between controllability of the resulting perturbation current waveform and sufficient perturbation energy to the DUT to ensure an acceptable SNR. Selecting an RLC circuit combination with an impedance magnitude significantly larger than the input impedance magnitude of the DUT results in improved control over the perturbation current spectral properties. However, significantly decreases the spectral magnitude of the perturbation. Selecting an RLC impedance magnitude significantly smaller than the input impedance magnitude of the DUT results in a voltage perturbation that resembles the spectral properties of the PRBS, which is undesirable within the context of transformer winding models. If the winding model is perturbed using a PRIS RLC circuit with an impedance magnitude significantly smaller than the input impedance magnitude of the winding model, the capacitive nature of the winding input impedance dominates the responses of the current waveforms at the PRBS state transitions. This results in fast current rise times that are challenging to sample accurately.

6.2. Parameter estimation approaches

The frequency responses obtained through simulated perturbation of the two-section winding model are applied in a parameter estimation methodology. Various parameter estimation case studies are investigated, whereby different combinations of the input impedance and two voltage ratios are included in the cost function formulation. The parameter estimation methodology makes use of the *globalsearch* optimisation algorithm to obtain parameter estimates within 0.006% of the target values when all three frequency responses are included. These responses rely on being able to access the internal windings of the transformer, which in many practical testing arrangements is not possible. When the simulated perturbation arrangement is used to obtain the estimated model frequency responses during optimisation the runtimes are in the order of 1-3 days, even for a conservative set of five parameters. The final case study investigates the use of the analytical transfer function in the parameter estimation methodology as an alternative. The parameter estimation errors worsened to within 2% of the target values for all parameters aside from the resistance estimation, the resistance is estimated with a 460% error. It is concluded that compared to the inductive and capacitive parameters, the resistive parameters affect the frequency response the least, as such even with the large error in estimated resistance the general frequency response shape is still estimated accurately. The final case study optimisation took 9 minutes to complete, which provides a significant improvement over case studies where the simulated perturbation arrangement is used in optimisation. Therefore, the methodology provides an advantage in cases where more complex model topologies with larger parameter sets need to be estimated.

The frequency-domain, time-domain, and decomposed time-domain measurements obtained through simulated perturbation of the three-section winding model are subsequently used in various parameter estimation approaches cost function formulations and optimisation algorithms. The hybrid particle-swarm optimisation algorithm in conjunction with an RMSE-based cost function formulation achieved the parameter values with the lowest error percentages for all parameter estimation approaches, as such, the discussion to follow focuses on the results obtained through this methodology. The parameter estimation results obtained through the use of the frequency-domain input impedance produced parameter estimates within 10% of the target values for all parameters aside from the winding resistance. Making use of EMD to decompose both the target and estimate voltage waveforms achieved the set of parameters with the worst error percentages. This can be related to the dependence of the resulting IMFs on the dynamics within the original signal which, in turn, makes it difficult to predict into which IMFs certain modes will be decomposed. Additionally, the EMD is sensitive to minor changes in the time-domain waveforms making the search space stochastic, resulting in the optimisation algorithm converging to local minima. A form of decomposition presented in this work, named Inferred Empirical Mode Decomposition (IEMD), improves the results obtained from EMD. The methodology produces a set of inferred Intrinsic Mode Functions (iIMFs) that are decompositions of the estimated model's terminal voltage waveform. The overall best result of within 5% of the target values for all parameters is obtained through the IEMD approach and classical time-domain.

From the investigations into various parameter estimation approaches, it is concluded that the optimal approach to implement in the characterisation and parameter estimation of a two-winding transformer is a hybrid particle-swarm optimisation algorithm using a frequency-domain approach. The optimisation makes use of the analytical transfer functions of the input impedances and voltage transformation ratios as measured from the terminals of the transformer model. This is due to the computational simplicity of calculating the analytical frequency responses and the efficient runtimes that result.

6.3. PRIS source hardware design

The PRIS source is designed and built to conform to the following specifications:

- **Configurable PRBS settings:** The source is designed such that an FPGA provides the gating signals to the IGBT switches within the H-Bridge configuration. The FPGA was programmed such that it can be configured from a PC to control the PRBS order, clock frequency and number of repetitions. The FPGA is powered through the power supply on the subrack during operation, however, it can be disconnected during programming to ensure a common ground on the FPGA board.
- **Configurable RLC circuit:** The RLC PCB design provides connections for series and/or parallel combinations of capacitors and inductors as well as parallel combinations of resistances. This design is adopted such that the desired RLC circuit values can be created for a specific perturbation use case.
- **Suitable for high-power environments:** The PCB track width allows for a 25A current and the track clearance enables insulation up to 1.62 kV. The IGBT switches are rated for a 1.6kV collector-emitter voltage in the event that the RLC circuit fails.
- **Transportable:** The entire source is housed in a KM6-II subrack that is 244mm x

483mm x 132mm in size. This makes the source compact enough to be carried by a single person between testing sites.

- **Modular:** The Eurocard standard in conjunction with the KM6-II subrack enables a modular design topology whereby each PCB contributes a specific function to the overall source design. A backplate PCB facilitates the interconnection of the various PCBs. These PCBs can be individually removed from the subrack housing with ease and replaced when necessary.
- **Protected:** The KM6-II subrack is compatible with various cases that can be ordered to offer physical protection as well as provides electromagnetic compatibility and protection against radio frequency interference.

The source design is validated by comparing the voltage and current time-domain waveforms during the perturbation of a 15.3Ω load in a practical arrangement and simulation. The validation makes use of a 4^{th} order PRBS switching at 10kHz in conjunction with RLC circuit parameters of 57.1Ω, 1.024mH, and 3.707μF. The results show that the PRBS switching and H-Bridge configuration work correctly as the state-transitions occur at the same instances. The voltage and current waveforms show a close correlation with slight discrepancies in the amplitudes. The remaining discrepancies can be accounted for by the parasitic inductance and capacitance of the IGBTs that are not taken into account in the simulation.

6.4. Practical perturbation

The PRIS source presented in Chapter 3 is used to perturb a 7.5kVA, 230V/100kV high-voltage test transformer. The measurement instrumentation is presented, and an investigation into the optimal current measurement arrangement found that using a voltage probe over the resistor in the RLC circuit provided improved vertical resolution over the current probe. This improved vertical resolution aided in obtaining accurate current measurements during the perturbation of the high-voltage terminal. The transformer underwent six measurement arrangements, whereby four input impedances, namely, $Z_{lvoc}(\omega)$, $Z_{lvsc}(\omega)$, $Z_{hvoc}(\omega)$, and $Z_{hvsc}(\omega)$, and two voltage transformation ratios, namely, $R_{lvhv}(\omega)$ and $R_{hvlv}(\omega)$, were measured. Each of the six perturbations mentioned above is performed using a 2kHz and 20kHz clock frequency to improve low-frequency accuracy. The two measurements are synthesised to form the resultant frequency responses.

Due to the relatively low impedance magnitude of the LV winding, the iterative RLC selection procedure yielded a set of RLC components of similar magnitude and sensible time constants that are readily available. The resulting measurements of $Z_{lvsc}(\omega)$, $Z_{lvoc}(\omega)$, and $R_{lvhv}(\omega)$ have minimal variance up until approximately 40kHz. The resulting set of

RLC circuit components required to match the HV winding input impedance magnitude are large and, therefore, not practical or readily accessible. As such the resulting RLC circuit impedance when performing perturbations on the HV terminal remains relatively low in magnitude in comparison to the HV winding. Due to the reduced influence of the RLC circuit on the resulting perturbation current, the PRBS state transitions resulted in fast current rise times, which are challenging to sample. This can be remedied by increasing the inductive component in the RLC circuit until the current waveform is able to be sampled more effectively by the available measurement equipment. A further challenge presented itself in the form of switch ringing on the H-Bridge voltage waveform, in turn causing aliased artefacts of the ringing to manifest in the sampled current waveform. The inclusion of an RC snubber circuit placed across each IGBT reduces the effects of ringing. The resulting measurements of $Z_{hvoc}(\omega)$, $Z_{hvsc}(\omega)$, and $R_{hvlv}(\omega)$ are affected by slight aliasing and insufficient perturbation at multiples of the clock frequency, as such the effects of noise distort the measurements from 20kHz.

6.5. Characterisation and parameter estimation of a high-voltage transformer

Due to the limited information available on the HV test transformer, an iterative approach is applied to determine a suitable model that is able to reproduce the frequency response measurements. The equivalent-circuit model for a two-winding distribution transformer developed by Brozio [11] is adapted in various ways in three case studies. The distribution transformer investigated by Brozio [11] has a lower transformation ratio than the HV transformer under investigation, resulting in a significant difference in the number of turns on the HV winding between the two transformers.

The initial case study implements the model topology as developed by Brozio [11] but does not make the assumption that all flux components are tightly coupled and confined to the core. Due to the winding resistance influencing the frequency response the least when compared to the inductive and capacitive components, all sections that make up the HV winding are assumed to have equal resistance. The resultant frequency response obtained through parameter estimation shows that the model order is high enough to represent the measurements from the HV input impedances and transformation ratios up to 10kHz. However, the minor series-parallel resonant pair at 9kHz in the LVOC and LVSC input impedances could not be matched. The HV winding resonances are expected to be located at lower frequencies than the LV winding due to the increased self-inductance and inter-turn capacitance as a result of the higher number of turns on the HV winding. Therefore, the minor resonance at 9kHz is a result of the order of the HV winding not being high enough.

The second case study investigated the inclusion of an additional inter-winding capacitance to more accurately model the increased distribution of the capacitive coupling between the windings due to the more significant number of turns on the HV winding. This case study is attempted with the aim of increasing the model order whilst only increasing the number of model parameters by one. It is concluded that the additional capacitance does not increase the model order in the region of 10Hz to 10kHz.

To model the increased number of turns of the HV test transformer under investigation compared to the distribution transformer, the final case study includes two additional sections to the HV winding. Two sections are added to maintain symmetry with respect to the inter-winding capacitance being located at the centre point of the HV winding as well as due to the six observed parallel resonances in the HVSC input impedance frequency response. The model topology and estimated parameters are able to match the minor resonance at 9kHz in the LVOC and LVSC input impedance measurements, and there is strong agreement between the measured and estimated frequency responses above 1kHz. The mismatch in the low-frequency portion of the LVOC input impedance can be attributed to the lack of any frequency-dependent effects of hysteresis of the core-loss resistance as well as the frequency-dependent effects of magnetising inductance on the winding self-inductances included in the model. The mismatch in the HVSC input impedance can be attributed to excluding a frequency-dependent component to account for the skin-effect in the winding resistances as well as excluding the frequency-dependence of leakage inductance on the winding self-inductances.

6.6. Recommendations for future work

This study revealed several areas for further investigation:

- **Hardware design to include RC snubber:** The RC snubber designed during perturbation of the HV terminal had to be soldered to the back of the backplate PCB as there was no PCB included in the design to cater for an RC snubber. The RLC PCB design can be adjusted to include an optional connection for an RC snubber network.
- **Further investigation into modal decomposition methods:** The practical implementation of a parameter estimation methodology based on modal decomposition was not performed as part of this project, there is scope to investigate its viability. Further research into the IEMD methodology, for example, to include weighting vectors into the set of iIMFs to improve parameter estimation results can be explored. Finally, an investigation into the performance of other modal decomposition methods such as EEMD or Iterative Filtering (IF) when compared to EMD and IEMD is another avenue of possible investigation.

- **Extension of HV transformer parameter estimation:** The topologies used for the HV test in this study assumed linear equivalent-circuit parameters. Further work can consider adapting the core-loss resistance, winding self-inductances and winding resistances to include frequency-dependent circuit elements with the objective of improving the frequency-domain estimations below 1kHz. Using data acquisition equipment with higher sampling rates would also allow the opportunity to model the HV test transformer for frequencies above 10kHz.

Bibliography

[1] V. Smil, "A brief history of transformers (not the robot kind)," 2021. [Online]. Available: https://www.wired.com/story/brief-history-transformers-not-robots/

[2] C. Global, "What is the purpose of power transformer?" 2021, north Baixiang, Yueqing, Zhejiang, 325603, P.R.China. [Online]. Available: https://chintglobal.com/blog/power-transformer-purpose/

[3] Electrical4U, "High voltage transformers: What is it? (testing and voltage regulation)," 2021. [Online]. Available: https://www.electrical4u.com/high-voltage-transformer/#:~:text=High%20voltage%20transformers%20are%20normally,insulation%20under%20test%20breaks%20down.

[4] B. Peterson, J. Rens, M. G. Botha, and J. Desmet, "On harmonic emission assessment: A discriminative approach," *SAIEE Africa Research Journal*, vol. 108, 12 2017.

[5] R. Pintelon and J. Schoukens, *System Identification - A Frequency Domain Approach*, 2^{nd} ed. Hoboken, New Jersey, USA: John Wiley & Sons, 2012.

[6] J. C. Bekker and H. J. Vermeulen, "Parameter estimation of a doubly-fed induction generator in a wind generation topology," in *2012 47th International Universities Power Engineering Conference (UPEC)*, 2012, pp. 1–6.

[7] H. J. Vermeulen, J. M. Strauss, and V. Shikoana, "Online estimation of synchronous generator parameters using PRBS perturbations," *IEEE Transactions on Power Systems*, vol. 17, no. 3, pp. 694–700, 2002.

[8] A. Keyhani, S. Chua, and S. Sebo, "Maximum likelihood estimation of transformer high frequency parameters from test data," *IEEE Transactions on Power Delivery*, vol. 6, no. 2, pp. 858–865, 1991.

[9] B. Miao, R. Zane, and D. Maksimovic, "System identification of power converters with digital control through cross-correlation methods," *IEEE Transactions on Power Electronics*, vol. 20, no. 5, pp. 1093–1099, 2005.

[10] L. Ljung, *System Identification: Theory for the User*, 2^{nd} ed. Upper Saddle River, New Jersey, USA: Prentice-Hall, 1999.

[11] C. C. Brozio and H. J. Vermeulen, “Wideband equivalent circuit modelling and parameter estimation methodology for two-winding transformers,” *IEE Proceedings - Generation, Transmission and Distribution*, vol. 150, pp. 487–492(5), July 2003.

[12] A. Keyhani, H. Tsai, S. Pillutla, and A. Abur, “Identification of high frequency transformer model parameters,” *Electric Power Systems Research*, vol. 42, no. 2, pp. 127–133, 1997.

[13] H. J. Vermeulen, R. G. Koch, and W. T. Rawlins, “Broadband modelling of magnetic voltage transformers through application of parameter estimation techniques,” 6^{th} *International Symposium on High Voltage Engineering*, vol. PAS-6, no. 50.12, 1989.

[14] A. Chanane, O. Bouchhida, and H. Houassine, “Investigation of the transformer winding high-frequency parameters identification using particle swarm optimisation method,” *IET Electric Power Applications*, vol. 10, no. 9, pp. 923–931, 2016.

[15] F. M. Mwaniki and H. J. Vermeulen, “Characterization and application of a pseudo-random impulse sequence for parameter estimation applications,” *IEEE Transactions on Instrumentation and Measurement*, vol. 69, no. 6, pp. 3917–3927, 2020.

[16] C. González and J. Pleite, “Transformer modeling approaches for frequency response analysis,” in *The XIX International Conference on Electrical Machines - ICEM 2010*, 2010, pp. 1–6.

[17] G. Aponte, H. Cadavid, J. C. Burgos, and E. Gomez, “A methodology for obtaining by measurements the transformer physical-circuital model parameters,” *Przeglad Elektrotechniczny*, vol. 88, no. 9 A, pp. 12–15, 2012.

[18] D. A. Douglass, “Potential transformer accuracy at 60Hz voltages above and below rating and at frequencies above 60Hz,” *IEEE Transactions on Power Apparatus and Systems*, vol. PAS-100, no. 3, pp. 1370–1375, 1981.

[19] C. C. Brozio, “Wideband modelling and parameter estimation of two-winding transformers,” Ph.D. dissertation, Department of Electrical and Electronic Engineering, University of Stellenbosch, South Africa, 1999.

[20] A. Chanane, H. Houassine, and O. Bouchhida, “Enhanced modelling of the transformer winding high frequency parameters identification from measured frequency response analysis,” *IET Generation, Transmission & Distribution*, vol. 13, no. 8, pp. 1339–1345, 2019.

[21] A. Chanane and M. Belazzoug, “On accuracy of a mutually coupled ladder network model high-frequency parameters identification for a transformer winding using gray wolf optimizer method,” *Compel*, vol. 40, no. 1, 2021-02-26.

[22] J. D. Glover, T. J. Overbye, and M. S. Sarma, *Power System Analysis & Design*, 6th ed. 20 Channel Center Street, Boston, USA: Cengage Learning, 2016.

[23] A. Fitzgerald, C. Kingsley, and S. D. Umans, *Electric Machinery*, 7th ed. 2 Penn Plaza, New York, Boston, USA: McGraw-Hill, 2014.

[24] D. A. Bradley, P. S. Bodger, and P. R. Hyland, "Harmonic response tests on voltage transducers for the New Zealand power system," *IEEE Transactions on Power Apparatus and Systems*, vol. PAS-104, no. 7, pp. 1750–1756, 1985.

[25] G. Olivier, R. P. Bouchard, Y. Gervais, and D. Mukhedkar, "Frequency response of HV test transformers and the associated measurement problems," *IEEE Transactions on Power Apparatus and Systems*, vol. PAS-99, no. 1, pp. 141–146, 1980.

[26] J. Luszcz and I. Moson, "Modelling of voltage transformer performance in power system harmonic frequency range," in *2008 International School on Nonsinusoidal Currents and Compensation*, 2008, pp. 1–4.

[27] G. R. Slemon, *Magnetoelectric devices: transducers, transformers, and machines*, 2nd ed. Hoboken, New Jersey, USA: John Wiley & Sons, 1966.

[28] P. Mukherjee and L. Satish, "Construction of equivalent circuit of a transformer winding from driving-point impedance function – analytical approach," *IET Electric Power Applications*, vol. 6, pp. 172–180(8), March 2012.

[29] A. Keyhani, H. Tsai, and A. Abur, "Maximum likelihood estimation of high frequency machine and transformer winding parameters," *IEEE Transactions on Power Delivery*, vol. 5, no. 1, pp. 212–219, 1990.

[30] R. Degeneff, "A general method for determining resonances in transformer windings," *IEEE Transactions on Power Apparatus and Systems*, vol. 96, no. 2, pp. 423–430, 1977.

[31] J. N. Ahour, S. Seyedtabaii, and G. B. Gharehpetian, "Valuable tips for transformer ladder network parameters estimation," in *2016 24th Iranian Conference on Electrical Engineering (ICEE)*, 2016, pp. 632–637.

[32] P. Vaessen and E. Hanique, "A new frequency response analysis method for power transformers," *IEEE Transactions on Power Delivery*, vol. 7, no. 1, pp. 384–391, 1992.

[33] R. Eberhart and J. Kennedy, "A new optimizer using particle swarm theory," in *MHS'95. Proceedings of the Sixth International Symposium on Micro Machine and Human Science*, 1995, pp. 39–43.

[34] A. Askarzadeh, “A novel metaheuristic method for solving constrained engineering optimization problems: Crow search algorithm,” *Computers & Structures*, vol. 169, pp. 1–12, 2016.

[35] S. Mirjalili, S. M. Mirjalili, and A. Lewis, “Grey wolf optimizer,” *Advances in Engineering Software*, vol. 69, pp. 46–61, 2014.

[36] K. Man, K. Tang, and S. Kwong, “Genetic algorithms: concepts and applications [in engineering design],” *IEEE Transactions on Industrial Electronics*, vol. 43, no. 5, pp. 519–534, 1996.

[37] S. Kirkpatrick, C. D. Gelatt, and M. P. Vecchi, “Optimization by simulated annealing,” *Science*, vol. 220, no. 4598, pp. 671–680, 1983.

[38] “MATLAB Global Optimization Toolbox,” R2020a, the MathWorks, Natick, MA, USA.

[39] K. Ragavan and L. Satish, “Localization of changes in a model winding based on terminal measurements: Experimental study,” *IEEE Transactions on Power Delivery*, vol. 22, no. 3, pp. 1557–1565, 2007.

[40] S. Pramanik and L. Satish, “Estimation of series capacitance of a transformer winding based on frequency-response data: An indirect measurement approach,” *IEEE Transactions on Power Delivery*, vol. 26, no. 4, pp. 2870–2878, 2011.

[41] K. Ragavan and L. Satish, “Construction of physically realizable driving-point function from measured frequency response data on a model winding,” *IEEE Transactions on Power Delivery*, vol. 23, no. 2, pp. 760–767, 2008.

[42] A. Abu-Siada, M. I. Mosaad, D. Kim, and M. F. El-Naggar, “Estimating power transformer high frequency model parameters using frequency response analysis,” *IEEE Transactions on Power Delivery*, vol. 35, no. 3, pp. 1267–1277, 2020.

[43] A. Morched, L. Marti, and J. Ottevangers, “A high frequency transformer model for the EMTP,” *IEEE Transactions on Power Delivery*, vol. 8, no. 3, pp. 1615–1626, 1993.

[44] S. Javadi, B. Vahidi, and S. H. Hosseinian, “Three phase transformer modeling with consideration the core effect,” in *2008 International Conference on Electrical Machines and Systems*, 2008, pp. 4375–4378.

[45] G. Funk and T. Hantel, “Frequenzabhängigkeit der betriebsmittel von drehstromnetzen,” 1987.

[46] B. Najafi and H. Hakim, "A comparative study of non-parametric spectral estimators for application in machine vibration analysis," *Mechanical Systems and Signal Processing*, vol. 6, no. 6, pp. 551–574, 1992.

[47] K. Angelopoulos and G. O. Glentis, "Nonparametric spectral estimation - an overview," in *25th Pan-Hellenic Conference on Informatics*, ser. PCI 2021. New York, NY, USA: Association for Computing Machinery, 2021, p. 118–123.

[48] R. B. Blackman and J. W. Tukey, "The measurement of power spectra from the point of view of communications engineering — part i," *The Bell System Technical Journal*, vol. 37, no. 1, pp. 185–282, 1958.

[49] M. Cerna and F. H. Harvey, "The fundamentals of FFT-based signal analysis and measurement," National Instruments, Austin, TX 78759-3504, Tech. Rep., 2000. [Online]. Available: https://www.sjsu.edu/people/burford.furman/docs/me120/FFT_tutorial_NI.pdf

[50] F. M. Mwaniki, "Modelling and performance evaluation of a pseudo-random impulse sequence for in situ parameter estimation in energy applications," Ph.D. dissertation, Department of Electrical and Electronic Engineering, University of Stellenbosch, South Africa, 2020.

[51] P. Stoica and R. Moses, *Spectral Analysis and Signals*, 1^{st} ed. Upper Saddle River, New Jersey, USA: Prentice Hall, 2005.

[52] K. R. Godfrey, "Comparison of perturbation signals for linear system identification in the frequency domain," *IEE Proceedings - Control Theory and Applications*, vol. 146, pp. 535–548(13), November 1999.

[53] J. Schoukens, R. Pintelon, E. van der Ouderaa, and J. Renneboog, "Survey of excitation signals for FFT based signal analyzers," *IEEE Transactions on Instrumentation and Measurement*, vol. 37, no. 3, pp. 342–352, 1988.

[54] E. Gomez-Luna, G. Aponte Mayor, C. Gonzalez-Garcia, and J. Pleite Guerra, "Current status and future trends in frequency-response analysis with a transformer in service," *IEEE Transactions on Power Delivery*, vol. 28, no. 2, pp. 1024–1031, 2013.

[55] H. Okawara, "DSP-based testing – fundamentals 50 PRBS (Pseudo Random Binary Sequence)," Advantest Corporation, Chiyoda City, Tokyo, Japan, Tech. Rep., 2013 [Online]. [Online]. Available: https://www3.advantest.com/documents/11348/3e95df23-22f5-441e-8598-f1d99c2382cb

[56] B. Bak-Jensen and L. Ostergaard, "Estimation of the model parameters in equivalent circuit models of potential transformers," in *IEEE Power Engineering Society. 1999 Winter Meeting (Cat. No.99CH36233)*, vol. 2, 1999, pp. 1053–1058 vol.2.

[57] A. Solomon, F. M. Mwaniki, and H. J. Vermeulen, "Application of pseudo-random impulse perturbation for characterizing capacitor voltage transformer frequency responses," *2020 6th IEEE International Energy Conference (ENERGYCon)*, pp. 744–748, 2020.

[58] I. P. Gerber, F. M. Mwaniki, and H. J. Vermeulen, "Parameter estimation of a ferroresonance damping circuit using pseudo-random impulse sequence perturbations," in *2021 56th International Universities Power Engineering Conference (UPEC)*, 2021, pp. 1–6.

[59] J. C. Bekker and H. J. Vermeulen, "Implementation of a wind turbine system as a native C-code MATLAB model for parameter estimation application," in *2011 46th International Universities' Power Engineering Conference (UPEC)*, 2011, pp. 1–6.

[60] J. C. Bekker, "Efficient modelling of a wind turbine system for parameter estimation applications," M.Eng. thesis, Department of Electrical and Electronic Engineering, University of Stellenbosch, South Africa, 2012.

[61] Jedox, "Error metrics: How to evaluate your forecasts," 2022. [Online]. Available: https://www.jedox.com/en/blog/error-metrics-how-to-evaluate-forecasts/#:~:text=An%20error%20metric%20is%20a,the%20model%20executes%20its%20tasks

[62] K. Rink, "Time series forecast error metrics you should know," Towards Data Science, Oct. 21 2021. [Online]. Available: https://towardsdatascience.com/time-series-forecast-error-metrics-you-should-know-cc88b8c67f27

[63] "MATLAB Data Import and Analysis Toolbox," R2020a, the MathWorks, Natick, MA, USA.

[64] M. N. Omidvar, X. Li, and X. Yao, "A review of population-based metaheuristics for large-scale black-box global optimization: Part a," *IEEE Transactions on Evolutionary Computation*, pp. 1–1, 2021.

[65] S. C. Chapra, *Applied numerical methods with MATLAB for engineers and scientists*, 3rd ed. 3 Apple Hill Drive, Massachusetts, USA: McGraw-Hill, 2012.

[66] "MATLAB Optimization Toolbox," R2020a, the MathWorks, Natick, MA, USA.

[67] Z. Ugray, L. Lasdon, J. Plummer, F. Glover, J. Kelly, and R. Martí, "Scatter search and local NLP solvers: A multistart framework for global optimization," *INFORMS Journal on Computing*, vol. 19, no. 3, pp. 328–340, 2007.

[68] E. Muñoz, E. Capón-García, J. M. Laínez-Aguirre, A. Espuña, and L. Puigjaner, "Integration of methods for optimization in a knowledge management framework," in *24th European Symposium on Computer Aided Process Engineering*, ser. Computer

Aided Chemical Engineering, J. J. Klemeš, P. S. Varbanov, and P. Y. Liew, Eds. Elsevier, 2014, vol. 33, pp. 859–864.

[69] D. Reid, “Genetic algorithms in constrained optimization,” *Mathematical and Computer Modelling*, vol. 23, no. 5, pp. 87–111, 1996. [Online]. Available: https://www.sciencedirect.com/science/article/pii/0895717796000143

[70] J. Kennedy and R. Eberhart, “Particle swarm optimization,” in *Proceedings of ICNN’95 - International Conference on Neural Networks*, vol. 4, 1995, pp. 1942–1948 vol.4.

[71] N. E. Huang, Z. Shen, S. R. Long, M. C. Wu, H. H. Shih, Q. Zheng, N. Yen, C. C. Tung, and H. H. Liu, “The empirical mode decomposition and the hilbert spectrum for nonlinear and non-stationary time series analysis,” *Proceedings of the Royal Society of London. Series A: Mathematical, Physical and Engineering Sciences*, vol. 454, pp. 903 – 995, 1998.

[72] A. Stallone, A. Cicone, and M. Materassi, “New insights and best practices for the successful use of empirical mode decomposition, iterative filtering and derived algorithms,” *Scientific Reports*, vol. 10, 2020.

[73] Z. WU and N. E. HUANG, “Ensemble empirical mode decomposition: A noise-assisted data analysis method,” *Advances in Adaptive Data Analysis*, vol. 01, no. 01, pp. 1–41, 2009.

[74] R. Deering and J. F. Kaiser, “The use of a masking signal to improve empirical mode decomposition,” *Proceedings. (ICASSP ’05). IEEE International Conference on Acoustics, Speech, and Signal Processing, 2005.*, vol. 4, pp. iv/485–iv/488 Vol. 4, 2005.

[75] *Technical Information IGBT-Module FF225R17ME4*, Infineon, Neubiberg, Germany, 2014. [Online]. Available: https://www.infineon.com/dgdl/Infineon-FF225R17ME4-DS-v02_04-EN.pdf?fileId=db3a30431ddc9372011e1c4df9f53c3d

[76] *2SP0115T Preliminary Description & Application Manual*, CT-Concept Technologie GmbH, 2504 Biel-Benne, Switzerland, 2014. [Online]. Available: https://www.power.com/sites/default/files/documents/2SP0115T2A0-FF225R17ME4.pdf

[77] *Deo-Nano User Manual*, Terasic Inc., Hsinchu County, Taiwan, 2021. [Online]. Available: https://www.terasic.com.tw/cgi-bin/page/archive.pl?Language=English&CategoryNo=139&No=593&PartNo=4#contents

[78] *Harting Connectors DIN 41612*, Harting, Espelkamp, Germany. [Online]. Available: https://docs.rs-online.com/8d4e/0900766b81628e26.pdf

[79] *3M™ Twisted Pair Flat Cable*, 3M Interconnect Solutions, Austin, Texas, USA, 2008. [Online]. Available: https://multimedia.3m.com/mws/media/22068O/3mtm-twisted-pair-flat-cable-050-28awg-1700-series-ts0115.pdf

[80] 4pcb, "Pcb trace width calculator," 2014. [Online]. Available: https://www.4pcb.com/trace-width-calculator.html

[81] *Bivolt PK60B Plug-In Power Supply*, Eplax GmbH., Fritz-Thiele-Straße 12, D-28279 Bremen. [Online]. Available: https://docs.rs-online.com/634b/A700000007822752.pdf

[82] L. Rozenblat, "Calculating spacing between pcb traces for various voltage levels," 2014. [Online]. Available: https://www.smps.us/pcbtracespacing.html

[83] R. Components, "A complete guide to eurocards," RS Components. [Online]. Available: https://za.rs-online.com/web/generalDisplay.html?id=ideas-and-advice/eurocards-pcb-guide

[84] *Verotec Electronics Packaging*, Verotec Electronics Enclosures, Curdridge, Southampton, Hampshire, United Kingdom. [Online]. Available: https://www.verotec.co.uk/web_book/KM6_RF_Subracks/KM6_II_Subracks.pdf

[85] *Verotec Electronics Packaging*, Verotec Cases, Curdridge, Southampton, Hampshire, United Kingdom. [Online]. Available: https://www.verotec.co.uk/tech-downloads/Section%205%20-%20Verotec%20Cases.pdf

[86] A. Girgis and R. McManis, "Frequency domain techniques for modeling distribution or transmission networks using capacitor switching induced transients," *IEEE Transactions on Power Delivery*, vol. 4, no. 3, pp. 1882–1890, 1989.

[87] "MATLAB Signal Processing Toolbox," R2020a, the MathWorks, Natick, MA, USA.

[88] D. M. Banks, J. C. Bekker, and H. J. Vermeulen, "Parameter estimation of a two-section transformer winding model using pseudo-random impulse sequence perturbation," in *2021 56th International Universities Power Engineering Conference (UPEC)*, 2021, pp. 1–6.

[89] F. Wang, R. Ren, X. Yin, N. Yu, and Y. Yang, "A transformer with high coupling coefficient and small area based on TSV," *Integration*, vol. 81, pp. 211–220, 2021.

[90] D. M. Banks, J. C. Bekker, and H. J. Vermeulen, "Parameter estimation of a three-section winding model using intrinsic mode functions," in *2022 IEEE International Conference on Environment and Electrical Engineering and 2022 IEEE Industrial and Commercial Power Systems Europe (EEEIC / I&CPS Europe)*, 2022, pp. 1–6.

[91] J. E. Greenberg and N. T. Smith, “Overview of spectral analysis,” 2001, 77 Massachusetts Avenue, Cambridge, MA, USA. [Online]. Available: http://web.mit.edu/ruggles/SpectralAnalysis/reference.html#overview

[92] *High Voltage Differential Probe*, GW Instek, New Taipei City, Taiwan. [Online]. Available: https://www.gwinstek.com/en-global/products/downloadSeriesDownNew/493/1598

[93] *N1000A(50MHz,1500Vp-p) differential probe - 1% accuracy*, PINTECH, Queen’s Road Central, Hong Kong. [Online]. Available: https://www.pintech.com.cn/en/sys-pd/15.html?fromColId=104

[94] *NI 9223 Specifications*, National Instruments, Austin, Texas, United States. [Online]. Available: https://www.ni.com/docs/en-US/bundle/ni-9223-specs/page/specifications.html

[95] *Specifications NI cDAQ™-9178, NI CompactDAQ Eight-Slot USB Chassis*, National Instruments, Austin, Texas, United States. [Online]. Available: https://www.amplicon.com/actions/viewDoc.cfm?doc=NI_CompactDAQ-cDAQ-9178.pdf

[96] *EEF502 100 kHz Low-Pass Filter*, Thorlabs, Newton, New Jersey, United States. [Online]. Available: https://www.thorlabs.com/drawings/153695d4bcf60672-38221B11-FE90-5845-6B137D0AE8688944/EF502-SpecSheet.pdf

[97] N. Mohan, T. M. Underland, and W. P. Robbins, *Power Electronics*, 3rd ed. Hoboken, New Jersey, USA: John Wiley & Sons, 2003.

[98] *Minimizing Switching Ringing at TPS53355 and TPS53353 Family Devices*, Texas Instruments, Dallas, Texas, United States. [Online]. Available: https://www.ti.com/lit/an/slua831a/slua831a.pdf?ts=1645612405368&ref_url=https%253A%252F%252Fwww.google.com%252F#:~:text=The%20addition%20of%20RC%20snubber,to%20ground%20pins%20as%20possible.

[99] J. Bak-Jenson, B. Bak-Jenson, S. Mikkelsen, and C. Jensen, “Parametric identification in potential transformer modelling,” *IEEE Transactions on Power Delivery*, vol. 7, no. 1, pp. 70–76, 1992.

Appendix A

Control PCB Schematic Diagram

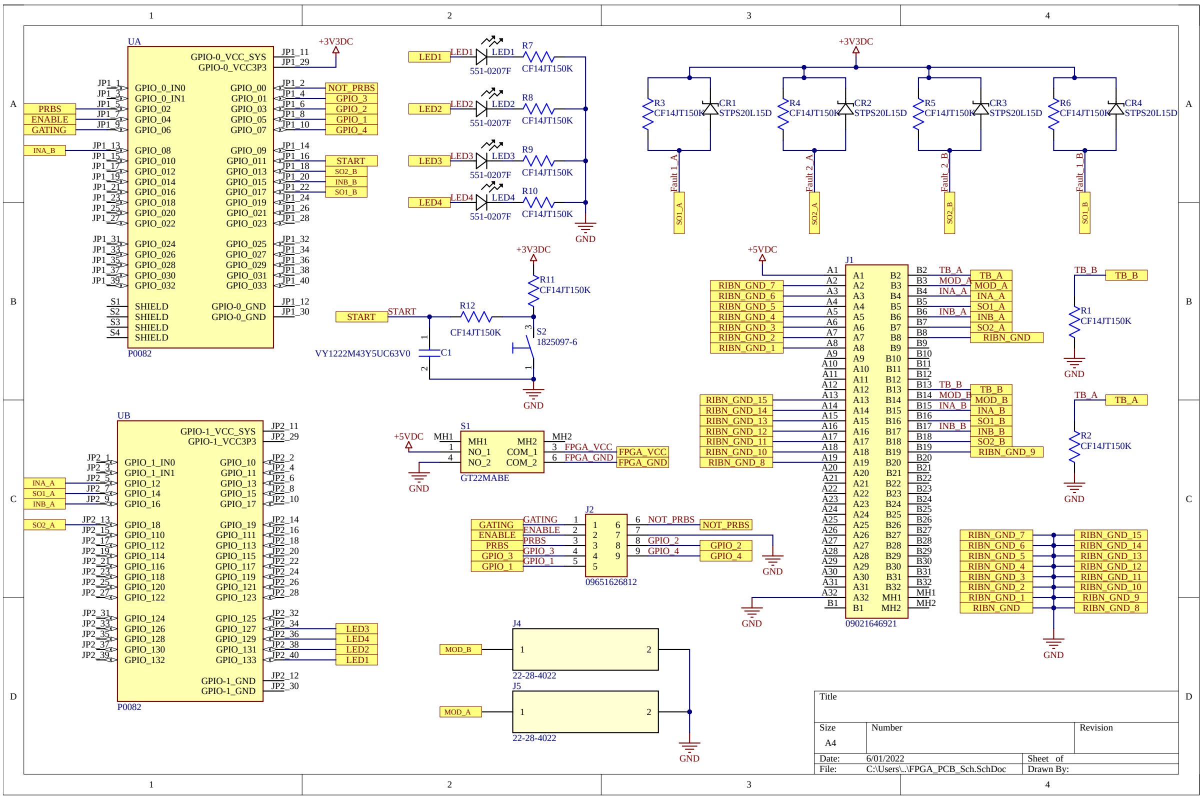

Figure A.1: Control PCB schematic diagram

Appendix B

Backplate PCB Schematic Diagram

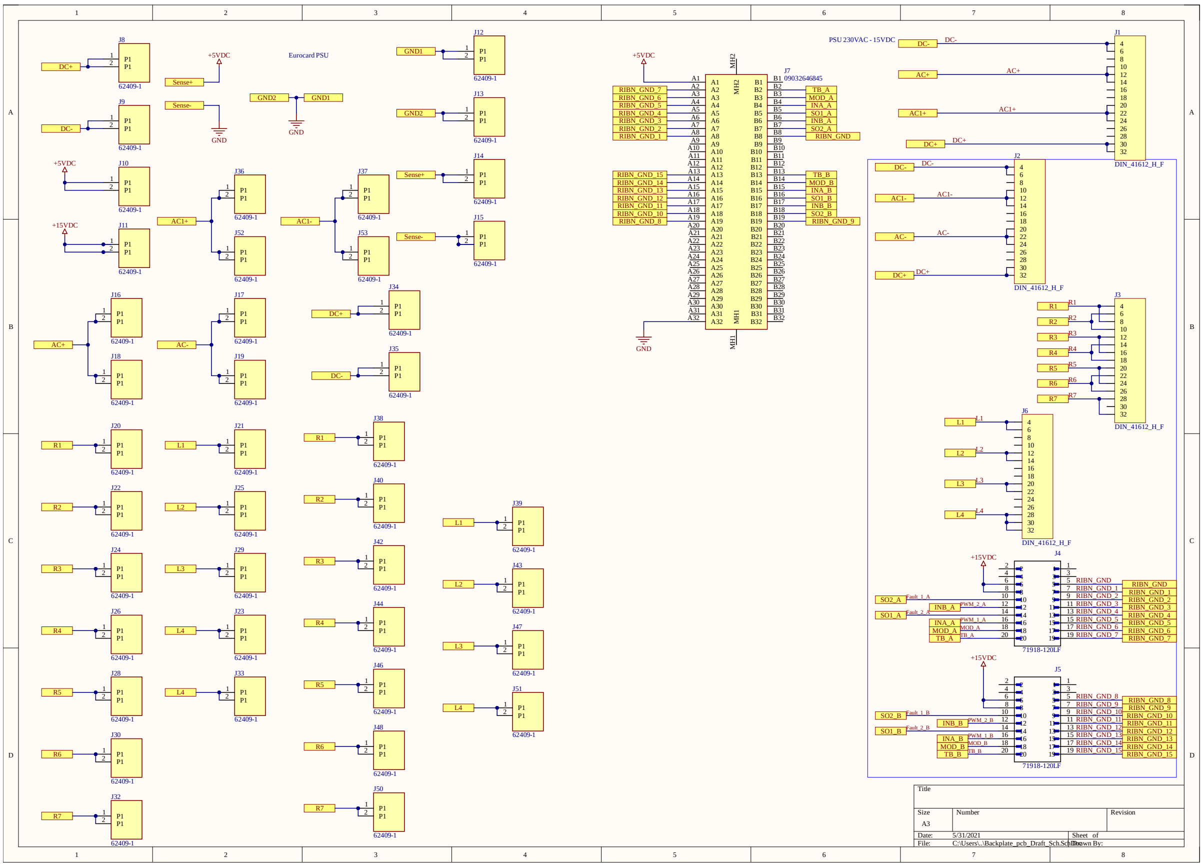

Figure B.1: Backplate PCB schematic diagram

Appendix C

RLC PCB Schematic Diagram

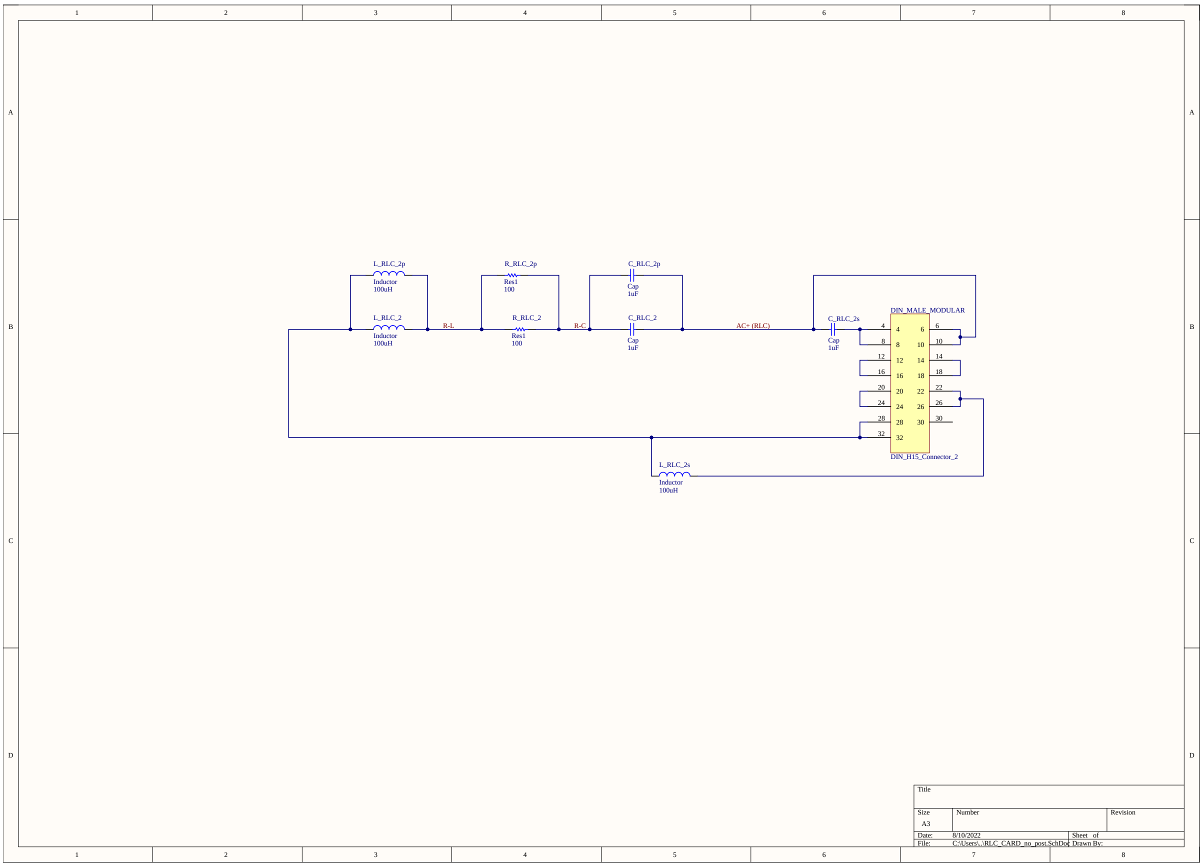

Figure C.1: RLC PCB schematic diagram adopted from a work in progress

Appendix D

Switching PCB Schematic Diagram

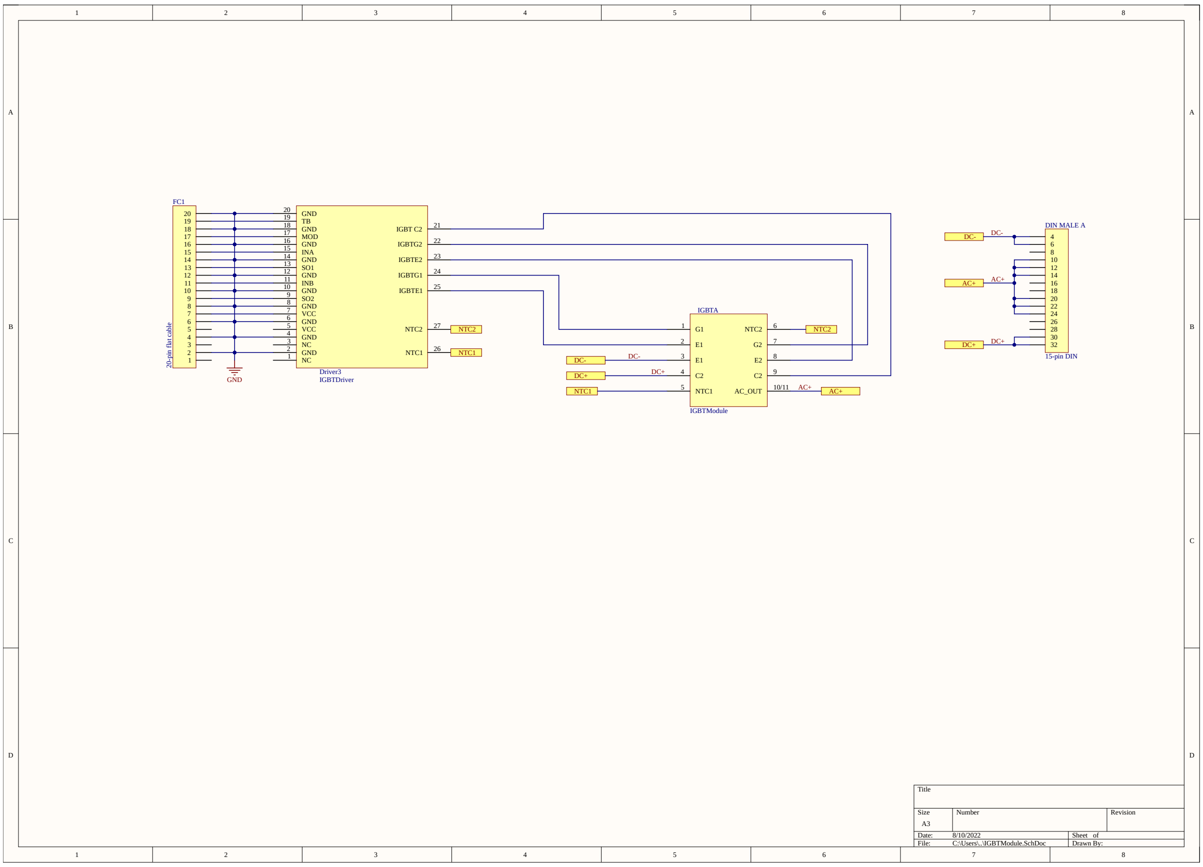

Figure D.1: Switching PCB schematic diagram adopted from a work in progress

Appendix E

FPGA Software Graphical User Interface

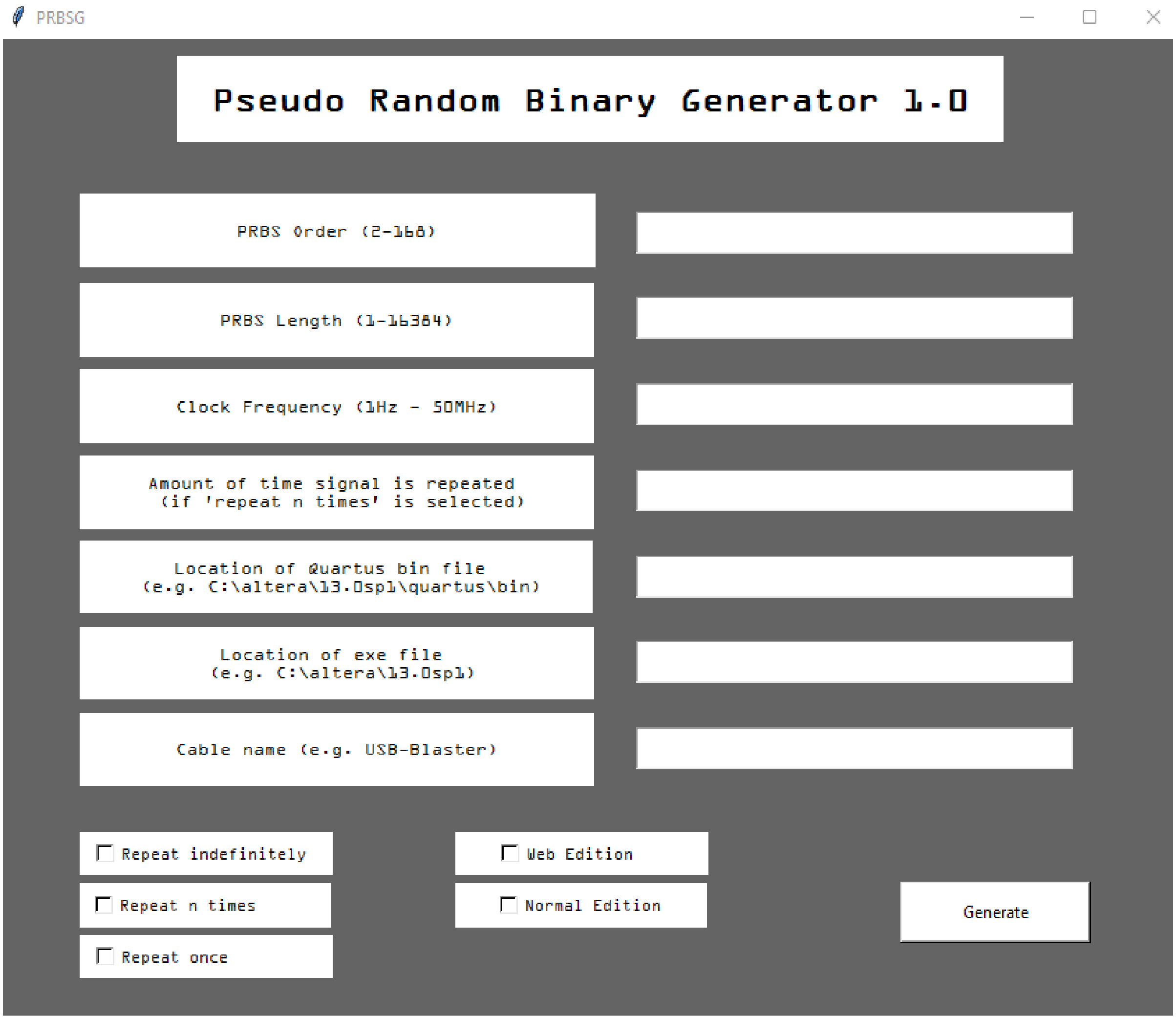

Figure E.1: Graphical user interface developed in python to set various PRBS generation parameters on the FPGA adopted from a work in progress

Appendix F

Three-Section Transformer Winding Analytical Input Impedance Coefficients

Table F.1: Transfer function numerator coefficients for $Z_{in}(s)$.

Coefficient	Value
α_1	$(C_{12}C_{23} + C_{12}C_{34} + C_{23}C_{34} + C_{12}C_{g3} + C_{23}C_{g3} + C_{23}C_{g2} + C_{34}C_{g2} + C_{g3}C_{g2})$ $(L_1L_2L_3 + 2M_{12}M_{13}M_{23} - L_2M_{13}^2 - L_3M_{12}^2 - L_1M_{23}^2)$
α_2	$-1(M_{12}^2R_3 + M_{13}^2R_2 + M_{23}^2R_1)(C_{12}C_{23} + C_{12}C_{34} + C_{23}C_{34}$ $+C_{12}C_{g3} + C_{23}C_{g3} + C_{23}C_{g2} + C_{34}C_{g2} + C_{g1}C_{g2})$
α_3	$(C_{12} + C_{g2})(L_1L_2 + L_1L_3 + 2L_1M_{23} - M_{12}^2 - M_{13}^2 - 2M_{12}M_{13})$ $+(C_{34} + C_{g3})(L_1L_3 + L_2L_2 + 2L_3M_{12} - M_{12} - M_{13}^2 - M_{23}^2 - 2M_{13}M_{23})$ $+C_{23}(L_1L_2 + L_2L_3 + 2L_2M_{13} - M_{12}^2 - M_{23}^2 - 2M_{12}M_{23})$ $+(L_1R_2R_3 + L_2R_1R_3 + L_3R_1R_2)(C_{12}C_{23} + C_{12}C_{34}+$ $C_{23}C_{34} + C_{12}C_{g3} + C_2C_{g3} + C_2C_{g2} + C_{34}C_{g2} + C_{g3}C_{g2})$
α_4	$(C_{12} + C_{23} + C_{g2})(L_1R_2 + L_2R_1) + (C_{12} + C_{23} + C_{g3})(L_1R_3 + L_3R_1)+$ $(C_{23} + C_{34} + C_{g3})(L_2R_3 + L_3R_2) + R_1R_2R_3(C_{12}C_{23} + C_{12}C_{34} + C_{23}C_{34}$ $+C_{12}C_{g3} + C_{23}C_{g3} + C_{23}C_{g1} + C_{34}C_{g1} + C_{g3}C_{g2}) + 2M_{23}R_1(C_{12} + C_{g2})$ $+2M_{12}R_3(C_{34}C_{g3}) + 2C_{23}M_{13}R_2$
α_5	$L_1 + L_2 + L_3 + 2M_{12} + 2M_{13} + 2M_{23} + R_1(R_2 + R_3)(C_{12} + C_{g2})$ $+R_3(R_1 + R_2)(C_{34} + C_{g3}) + C_{g2}R_1(R_2 + R_3)$
α_6	$R_1 + R_2 + R_3$

Table F.2: Transfer function denominator coefficients for $Z_{in}(s)$.

Coefficient	Value
β_1	$(-L_3M_{12}^2 + 2M_{12}M_{13}M_{23} - L_2M_{13}^2 - L_1M_{23}^2 + L_1L_2L_3)(C_{12}C_{23}C_{34} + C_{12}C_{23}C_{g3} + C_{12}C_{23}C_{g2} + C_{12}C_{23}C_{g1} + C_{12}C_{34}C_{g2} + C_{12}C_{34}C_{g1} + C_{23}C_{34}C_{g1} + C_{12}C_{g3}C_{g2} + C_{12}C_{g3}C_{g1} + C_{23}C_{g3}C_{g1} + C_{23}C_{g2}C_{g1} + C_{34}C_{g2}C_{g1} + C_{g3}C_{g2}C_{g1})$
β_2	$(-R_3M_{12}^2 - R_2M_{13}^2 - R_1M_{23}^2 + L_1L_2R_3 + L_1 + L_3R_2 + L_2L_3R_1)(C_{12}C_{23}C_{34} + C_{12}C_{23}C_{g3} + C_{12}C_{23}C_{g2} + C_{12}C_{23}C_{g1} + C_{12}C_{34}C_{g2} + C_{12}C_{34}C_{g1} + C_{23}C_{34}C_{g1} + C_{12}C_{g3}C_{g2} + C_{12}C_{g3}C_{g1} + C_{23}C_{g3}C_{g1} + C_{23}C_{g2}C_{g1} + C_{34}C_{g2}C_{g1} + C_{g3}C_{g2}C_{g1})$
β_3	$-M_{12}^2(C_{12}C_{23} + C_{12}C_{g2} + C_{12}C_{g1} + C_{23}C_{g1} + C_{g2}C_{g1}) - M_{13}^2(C_{12}C_{34} + C_{12}C_{g3} + C_{12}C_{g2} + C_{12}C_{g1} + C_{34}C_{g1} + C_{g3}C_{g1} + C_{g2}C_{g1}) - M_{23}^2(C_{23}C_{34} + C_{23}C_{g3} + C_{23}C_{g2} + C_{23}C_{g1} + C_{34}C_{g2} + C_{34}C_{g1} + C_{g3}C_{g2} + C_{g3}C_{g1}) + L_1L_2(C_{12}C_{23} + C_{12}C_{g2} + C_{12}C_{g1} + C_{23}C_{g1} + C_{g2}C_{g1}) + L_1L_3(C_{12}C_{34} + C_{12}C_{g3} + C_{12}C_{g2} + C_{12}C_{g1} + C_{34}C_{g1} + C_{g3}C_{g1} + C_{g2}C_{g1}) + L_2L_3(C_{23}C_{34} + C_{23}C_{g3} + C_{23}C_{g2} + C_{23}C_{g1} + C_{34}C_{g2} + C_{34}C_{g1} + C_{g3}C_{g2} + C_{g3}C_{g1}) + 2C_{g1}(C_{23}L_2M_{13} + C_{34}L_3M_{12} + C_{12}L_1M_{23} + C_{g3}L_3M_{12} - C_{12}M_{12}M_{13} - C_{23}M_{12}M_{23} - C_{34}M_{13}M_{23} - C_{g3}M_{13}M_{23}) + 2C_{g2}(C_{12}L_1M_{23} - C_{12}M_{12}M_{13} - C_{g1}M_{12}M_{13} + C_{g1}L_1M_{23}) + (L_1R_2R_3 + L_2R_1R_3 + L_3R_1R_2)(C_{12}C_{23}C_{34} + C_{12}C_{23}C_{g3} + C_{12}C_{23}C_{g2} + C_{12}C_{23}C_{g1} + C_{12}C_{34}C_{g2} + C_{12}C_{34}C_{g1} + C_{12}C_{g3}C_{g2} + C_{12}C_{g3}C_{g1} + C_{23}C_{g3}C_{g1} + C_{23}C_{g2}C_{g1} + C_{34}C_{g2}C_{g1} + C_{g3}C_{g2}C_{g1})$
β_4	$(L_1R_2 + L_2R_1)(C_{12}C_{23} + C_{12}C_{g2} + C_{12}C_{g1} + C_{23}C_{g1} + C_{g2}C_{g1}) + (L_1R_2 + L_3R_1)(C_{12}C_{34} + C_{12}C_{g3} + C_{12}C_{g2} + C_{12}C_{g1} + C_{34}C_{g1} + C_{g3}C_{g1} + C_{g2}C_{g1}) (L_2R_3 + L_3R_2)(C_{23}C_{34} + C_{23}C_{g3} + C_{23}C_{g2} + C_{23}C_{g1} + C_{34}C_{g2} + C_{34}C_{g1} + C_{g3}C_{g2} + C_{g3}C_{g1}) + 2M_{23}R_1(C_{12}C_{g2} + C_{12}C_{g1} + C_{g2}C_{g1}) + 2C_{g1}(C_{23}M_{13}R_2 + C_{34}M_{12}R_3 + C_{g3}M_{12}R_3) + R_1R_2R_3(C_{12}C_{23}C_{34} + C_{12}C_{23}C_{g3} + C_{12}C_{23}C_{g2} + C_{12}C_{23}C_{g1} + C_{12}C_{34}C_{g2} + C_{12}C_{34}C_{g1} + C_{23}C_{34}C_{g1} + C_{12}C_{g3}C_{g2} + C_{12}C_{g3}C_{g1} + C_{23}C_{g3}C_{g1} + C_{23}C_{g2}C_{g1} + C_{34}C_{g2}C_{g1} + C_{g3}C_{g2}C_{g1})$
β_5	$L_1(C_{12} + C_{g1}) + L_2(C_{23} + C_{g2} + C_{g1}) + L_3(C_{34} + C_{g3} + C_{g2} + C_{g1}) + 2C_{g1}(M_{12} + M_{13} + M_{23}) + 2C_{g2}M_{23} + R_1R_2(C_{12}C_{23} + C_{12}C_{g2} + C_{12}C_{g1} + C_{23}C_{g1} + C_{g2}C_{g1}) + R_1R_3(C_{12}C_{34} + C_{12}C_{g3} + C_{12}C_{g2} + C_{12}C_{g1} + C_{34}C_{g1} + C_{g3}C_{g1} + C_{g2}C_{g1}) + R_2R_3(C_{23}C_{34} + C_{23}C_{g3} + C_{23}C_{g2} + C_{23}C_{g1} + C_{34}C_{g1} + C_{g3}C_{g2} + C_{g3}C_{g1})$
β_6	$C_{12}R_1 + C_{23}R_2 + C_{34}R_3 + C_{g3}R_3 + C_{g2}(R_2 + R_3) + C_{g1}(R_1 + R_2 + R_3)$
β_7	1

Appendix G

Case Study 1: Impedance Matrices

$$Z^1_{lvoc} = \begin{bmatrix} \frac{1}{sC_{a10}} + R_{a1} + sL_{a1} & -R_{a1} - sL_{a1} + sM_{a1b3} + sM_{a1b4} \\ -R_{a1} - sL_{a1} + sM_{a1b3} + sM_{a1b4} & \frac{1}{sC_{ab1}} + R_{a1} + sL_{a1} - sM_{a1b3} - sM_{a1b4} + R_{b4} + sL_{b4} - sM_{a1b4} + sM_{b34} + R_{b3} + sL_{b3} - sM_{a1b3} + sM_{b34} \\ -sM_{a1b1} & -sM_{b13} - sM_{b14} + sM_{a1b1} \\ -sM_{a1b2} & -sM_{b23} - s_{Mb24} + sM_{a1b2} \\ -sM_{a1b3} & -R_{b3} - sL_{b3} - sM_{b34} + sM_{a1b3} \\ -sM_{a1b4} & -R_{b4} - sL_{b4} - sM_{b34} + sM_{a1b4} \\ 0 & 0 \\ 0 & 0 \\ 0 & 0 \\ -sM_{a1bc} & sM_{a1bc} - sM_{b3bc} - sM_{b4bc} \\ \frac{1}{sC_{a10}} & 0 \end{bmatrix} \tag{G.1}$$

$$Z^2_{lvoc} = \begin{bmatrix} -sM_{a1b1} & -sM_{a1b2} & -sM_{a1b3} & -sM_{a1b4} & 0 \\ sM_{a1b1} - sM_{b14} - sM_{b13} & sM_{a1b2} - sM_{b24} - sM_{b23} & sM_{a1b3} - sM_{b34} - sL_{b3} - R_{b3} & sM_{a1b4} - R_{b4} - sL_{b4} - sM_{b34} & 0 \\ R_{b1} + \frac{1}{sC_{b1}} + sL_{b1} & sM_{b12} & sM_{b13} & sM_{b14} & \frac{-1}{sC_{b1}} \\ sM_{b12} & R_{b2} + \frac{1}{sC_{b2}} + sL_{b2} & sM_{b23} & sM_{b24} & \frac{-1}{sC_{b2}} \\ sM_{b13} & sM_{b23} & R_{b3} + \frac{1}{sC_{b3}} + sL_{b3} & sM_{b34} & 0 \\ sM_{b14} & sM_{b24} & sM_{b34} & R_{b4} + \frac{1}{sC_{b4}} + sL_{b4} & 0 \\ \frac{-1}{sC_{b1}} & \frac{-1}{sC_{b2}} & 0 & 0 & \frac{1}{sC_{b1}} + \frac{1}{sC_{b2}} + \frac{1}{sC_{b12}} \\ 0 & 0 & \frac{-1}{sC_{b3}} & \frac{-1}{sC_{b4}} & 0 \\ 0 & 0 & 0 & 0 & \frac{-1}{sC_{b12}} \\ sM_{b1bc} & sM_{b2bc} & sM_{b3bc} & sM_{b4bc} & 0 \\ 0 & 0 & 0 & 0 & 0 \end{bmatrix} \tag{G.2}$$

$$Z^3_{lvoc} = \begin{bmatrix} 0 & 0 & -sM_{a1bc} & \frac{-1}{sC_{a10}} \\ 0 & 0 & sM_{a1bc} - sM_{b4bc} - sM_{b3bc} & 0 \\ 0 & 0 & sM_{b1bc} & 0 \\ 0 & 0 & sM_{b2bc} & 0 \\ \frac{-1}{sC_{b3}} & 0 & sM_{b3bc} & 0 \\ \frac{-1}{sC_{b4}} & 0 & sM_{b4bc} & 0 \\ 0 & \frac{-1}{sC_{b12}} & 0 & 0 \\ \frac{1}{sC_{b3}} + \frac{1}{sC_{b4}} + \frac{1}{sC_{b34}} & \frac{-1}{sC_{b34}} & 0 & 0 \\ \frac{-1}{sC_{b34}} & \frac{1}{sC_{b12}} + \frac{1}{sC_{b34}} + \frac{1}{sC_{b10}} & 0 & 0 \\ 0 & 0 & R_c + sL_c & 0 \\ 0 & 0 & 0 & \frac{-1}{sC_{a10}} \end{bmatrix} \tag{G.3}$$

$$Z_{lvoc} = \begin{bmatrix} Z^1_{lvoc} & Z^2_{lvoc} & Z^3_{lvoc} \end{bmatrix} \tag{G.4}$$

$$Z^1_{lvsc} = \begin{bmatrix} \frac{1}{sC_{a10}} + R_{a1} + sL_{a1} & -R_{a1} - sL_{a1} + sM_{a1b3} + sM_{a1b4} \\ -R_{a1} - sL_{a1} + sM_{a1b3} + sM_{a1b4} & \frac{1}{sC_{ab1}} + R_{a1} + sL_{a1} - sM_{a1b3} - sM_{a1b4} + R_{b4} + sL_{b4} - sM_{a1b4} + sM_{b34} + R_{b3} + sL_{b3} - sM_{a1b3} + sM_{b34} \\ -sM_{a1b1} & -sM_{b13} - sM_{b14} + sM_{a1b1} \\ -sM_{a1b2} & -sM_{b23} - s_{Mb24} + sM_{a1b2} \\ -sM_{a1b3} & -R_{b3} - sL_{b3} - sM_{b34} + sM_{a1b3} \\ -sM_{a1b4} & -R_{b4} - sL_{b4} - sM_{b34} + sM_{a1b4} \\ 0 & 0 \\ 0 & 0 \\ 0 & 0 \\ -sM_{a1bc} & sM_{a1bc} - sM_{b3bc} - sM_{b4bc} \\ sM_{a1bc} & -s_{Ma1bc} + sM_{b3bc} + s_{Mb4bc} \\ \frac{1}{sC_{a10}} & 0 \end{bmatrix} \tag{G.5}$$

$$Z^2_{lvsc} = \begin{bmatrix} -sM_{a1b1} & -sM_{a1b2} & -sM_{a1b3} & -sM_{a1b4} & 0 \\ sM_{a1b1} - sM_{b14} - sM_{b13} & sM_{a1b2} - sM_{b24} - sM_{b23} & sM_{a1b3} - sM_{b34} - sL_{b3} - R_{b3} & sM_{a1b4} - R_{b4} - sL_{b4} - sM_{b34} & 0 \\ R_{b1} + \frac{1}{sC_{b1}} + sL_{b1} & sM_{b12} & sM_{b13} & sM_{b14} & \frac{-1}{sC_{b1}} \\ sM_{b12} & R_{b2} + \frac{1}{sC_{b2}} + sL_{b2} & sM_{b23} & sM_{b24} & \frac{-1}{sC_{b2}} \\ sM_{b13} & sM_{b23} & R_{b3} + \frac{1}{sC_{b3}} + sL_{b3} & sM_{b34} & 0 \\ sM_{b14} & sM_{b24} & sM_{b34} & R_{b4} + \frac{1}{sC_{b4}} + sL_{b4} & 0 \\ \frac{-1}{sC_{b1}} & \frac{-1}{sC_{b2}} & 0 & 0 & \frac{1}{sC_{b1}} + \frac{1}{sC_{b2}} + \frac{1}{sC_{b12}} \\ 0 & 0 & \frac{-1}{sC_{b3}} & \frac{-1}{sC_{b4}} & 0 \\ 0 & 0 & 0 & 0 & \frac{-1}{sC_{b12}} \\ sM_{b1bc} & sM_{b2bc} & sM_{b3bc} & sM_{b4bc} & 0 \\ -sM_{b1bc} & -sM_{b2bc} & -sM_{b3bc} & -sM_{b4bc} & 0 \\ 0 & 0 & 0 & 0 & 0 \end{bmatrix} \tag{G.6}$$

$$Z^3_{lvsc} = \begin{bmatrix} 0 & 0 & -sM_{a1bc} & sM_{a1bc} & \frac{-1}{sC_{a10}} \\ 0 & 0 & sM_{a1bc} - sM_{b4bc} - sM_{b3bc} & -sM_{a1bc} + sM_{b4bc} + sM_{b3bc} & 0 \\ 0 & 0 & sM_{b1bc} & -sM_{b1bc} & 0 \\ 0 & 0 & sM_{b2bc} & -sM_{b2bc} & 0 \\ \frac{-1}{sC_{b3}} & 0 & sM_{b3bc} & -sM_{b3bc} & 0 \\ \frac{-1}{sC_{b4}} & 0 & sM_{b4bc} & -sM_{b4bc} & 0 \\ 0 & \frac{-1}{sC_{b12}} & 0 & 0 & 0 \\ \frac{1}{sC_{b3}} + \frac{1}{sC_{b4}} + \frac{1}{sC_{b34}} & \frac{-1}{sC_{b34}} & 0 & 0 & 0 \\ \frac{-1}{sC_{b34}} & \frac{1}{sC_{b12}} + \frac{1}{sC_{b34}} + \frac{1}{sC_{b10}} & 0 & \frac{-1}{sC_{b10}} & 0 \\ 0 & 0 & R_c + sL_c & -R_c - sL_c & 0 \\ 0 & \frac{-1}{sC_{b10}} & -R_c - sL_c & \frac{1}{sC_{b10}} + R_c + sL_c & 0 \\ 0 & 0 & 0 & 0 & \frac{-1}{sC_{a10}} \end{bmatrix} \tag{G.7}$$

$$Z_{lvsc} = \begin{bmatrix} Z^1_{lvsc} & Z^2_{lvsc} & Z^3_{lvsc} \end{bmatrix} \tag{G.8}$$

$$Z^1_{hvoc} = \begin{bmatrix} \frac{1}{sC_{a10}} + R_{a1} + sL_{a1} & -R_{a1} - sL_{a1} + sM_{a1b3} + sM_{a1b4} \\ -R_{a1} - sL_{a1} + sM_{a1b4} + sM_{a1b3} & \frac{1}{sC_{ab1}} + R_{a1} + sL_{a1} - sM_{a1b3} - sM_{a1b4} + R_{b4} + sL_{b4} - sM_{a1b4} + sM_{b34} + R_{b3} + sL_{b3} - sM_{a1b3} + sM_{b34} \\ -sM_{a1b1} & -sM_{b13} - sM_{b14} + sM_{a1b1} \\ -sM_{a1b2} & -sM_{b23} - sM_{b24} + sM_{a1b2} \\ -sM_{a1b3} & -R_{b3} - sL_{b3} - sM_{b34} + sM_{a1b3} \\ -sM_{a1b4} & -R_{b4} - sL_{b4} - sM_{b34} + sM_{a1b4} \\ 0 & 0 \\ 0 & 0 \\ 0 & 0 \\ -sM_{a1bc} & sM_{a1bc} - sM_{b3bc} - sM_{b4bc} \\ sM_{a1bc} & -sM_{a1bc} + sM_{b3bc} + sM_{b4bc} \end{bmatrix} \tag{G.9}$$

$$Z^2_{hvoc} = \begin{bmatrix} -sM_{a1b1} & -sM_{a1b2} & -sM_{a1b3} & -sM_{a1b4} & 0 \\ sM_{a1b1} - sM_{b14} - sM_{b13} & sM_{a1b2} - sM_{b24} - sM_{b23} & sM_{a1b3} - sM_{b34} - sL_{b3} - R_{b3} & sM_{a1b4} - R_{b4} - sL_{b4} - sM_{b34} & 0 \\ R_{b1} + \frac{1}{sC_{b1}} + sL_{b1} & sM_{b12} & sM_{b13} & sM_{b14} & \frac{-1}{sC_{b1}} \\ sM_{b12} & R_{b2} + \frac{1}{sC_{b2}} + sL_{b2} & sM_{b23} & sM_{b24} & \frac{-1}{sC_{b2}} \\ sM_{b13} & sM_{b23} & R_{b3} + \frac{1}{sC_{b3}} + sL_{b3} & sM_{b34} & 0 \\ sM_{b14} & sM_{b24} & sM_{b34} & R_{b4} + \frac{1}{sC_{b4}} + sL_{b4} & 0 \\ \frac{-1}{sC_{b1}} & \frac{-1}{sC_{b2}} & 0 & 0 & \frac{1}{sC_{b1}} + \frac{1}{s_{Cb2}} + \frac{1}{sC_{b12}} \\ 0 & 0 & \frac{-1}{sC_{b3}} & \frac{-1}{sC_{b4}} & 0 \\ 0 & 0 & 0 & 0 & \frac{-1}{sC_{b12}} \\ sM_{b1bc} & sM_{b2bc} & sM_{b3bc} & sM_{b4bc} & 0 \\ -sM_{b1bc} & -sM_{b2bc} & -sM_{b3bc} & -sM_{b4bc} & 0 \end{bmatrix} \tag{G.10}$$

$$Z^3_{hvoc} = \begin{bmatrix} 0 & 0 & -sM_{a1bc} & sM_{a1bc} \\ 0 & 0 & sM_{a1bc} - sM_{b4bc} - sM_{b3bc} & -sM_{a1bc} + sM_{b4bc} + sM_{b3bc} \\ 0 & 0 & sM_{b1bc} & -sM_{b1bc} \\ 0 & 0 & sM_{b2bc} & -sM_{b2bc} \\ \frac{-1}{sC_{b3}} & 0 & sM_{b3bc} & -sM_{b3bc} \\ \frac{-1}{sC_{b4}} & 0 & sM_{b4bc} & -sM_{b4bc} \\ 0 & \frac{-1}{sC_{b12}} & 0 & 0 \\ \frac{1}{sC_{b3}} + \frac{1}{sC_{b4}} + \frac{1}{sC_{b34}} & \frac{-1}{sC_{b34}} & 0 & 0 \\ \frac{-1}{sC_{b34}} & \frac{1}{sC_{b12}} + \frac{1}{sC_{b34}} + \frac{1}{sC_{b10}} & 0 & \frac{-1}{sC_{b10}} \\ 0 & 0 & R_c + sL_c & -R_c - sL_c \\ 0 & \frac{-1}{sC_{b10}} & -R_c - sL_c & \frac{1}{sC_{b10}} + R_c + sL_c \end{bmatrix} \tag{G.11}$$

$$Z_{hvoc} = \begin{bmatrix} Z^1_{hvoc} & Z^2_{hvoc} & Z^3_{hvoc} \end{bmatrix} \tag{G.12}$$

$$Z_{hvsc}^{1} = \begin{bmatrix} \frac{1}{sC_{a10}} + R_{a1} + sL_{a1} & -R_{a1} - sL_{a1} + sM_{a1b3} + sM_{a1b4} \\ -R_{a1} - sL_{a1} + sM_{a1b4} + sM_{a1b3} & \frac{1}{sC_{ab1}} + R_{a1} + sL_{a1} - sM_{a1b3} - sM_{a1b4} + R_{b4} + sL_{b4} - sM_{a1b4} + sM_{b34} + R_{b3} + sL_{b3} - sM_{a1b3} + sM_{b34} \\ -sM_{a1b1} & -sM_{b13} - sM_{b14} + sM_{a1b1} \\ -sM_{a1b2} & -sM_{b23} - sM_{b24} + sM_{a1b2} \\ -sM_{a1b3} & -R_{b3} - sL_{b3} - sM_{b34} + sM_{a1b3} \\ -sM_{a1b4} & -R_{b4} - sL_{b4} - sM_{b34} + sM_{a1b4} \\ 0 & 0 \\ 0 & 0 \\ 0 & 0 \\ -sM_{a1bc} & sM_{a1bc} - sM_{b3bc} - sM_{b4bc} \\ \frac{-1}{sC_{a10}} & 0 \\ sM_{a1bc} & -sM_{a1bc} + sM_{b3bc} + sM_{b4bc} \end{bmatrix} \tag{G.13}$$

$$Z_{hvsc}^{2} = \begin{bmatrix} -sM_{a1b1} & -sM_{a1b2} & -sM_{a1b3} & -sM_{a1b4} & 0 \\ sM_{a1b1} - sM_{b14} - sM_{b13} & sM_{a1b2} - sM_{b24} - sM_{b23} & sM_{a1b3} - sM_{b34} - sL_{b3} - R_{b3} & sM_{a1b4} - R_{b4} - sL_{b4} - sM_{b34} & 0 \\ R_{b1} + \frac{1}{sC_{b1}} + sL_{b1} & sM_{b12} & sM_{b13} & sM_{b14} & \frac{-1}{sC_{b1}} \\ sM_{b12} & R_{b2} + \frac{1}{sC_{b2}} + sL_{b2} & sM_{b23} & sM_{b24} & \frac{-1}{sC_{b2}} \\ sM_{b13} & sM_{b23} & R_{b3} + \frac{1}{sC_{b3}} + sL_{b3} & sM_{b34} & 0 \\ sM_{b14} & sM_{b24} & sM_{b34} & R_{b4} + \frac{1}{sC_{b4}} + sL_{b4} & 0 \\ \frac{-1}{sC_{b1}} & \frac{-1}{sC_{b2}} & 0 & 0 & \frac{1}{sC_{b1}} + \frac{1}{s_{Cb2}} + \frac{1}{sC_{b12}} \\ 0 & 0 & \frac{-1}{sC_{b3}} & \frac{-1}{sC_{b4}} & 0 \\ 0 & 0 & 0 & 0 & \frac{-1}{sC_{b12}} \\ sM_{b1bc} & sM_{b2bc} & sM_{b3bc} & sM_{b4bc} & 0 \\ 0 & 0 & 0 & 0 & 0 \\ -sM_{b1bc} & -sM_{b2bc} & -sM_{b3bc} & -sM_{b4bc} & 0 \end{bmatrix} \tag{G.14}$$

$$Z_{hvsc}^{3} = \begin{bmatrix} 0 & 0 & -sM_{a1bc} & \frac{-1}{sC_{a10}} & sM_{a1bc} \\ 0 & 0 & sM_{a1bc} - sM_{b4bc} - sM_{b3bc} & 0 & -sM_{a1bc} + sM_{b4bc} + sM_{b3bc} \\ 0 & 0 & sM_{b1bc} & 0 & -sM_{b1bc} \\ 0 & 0 & sM_{b2bc} & 0 & -sM_{b2bc} \\ \frac{-1}{sC_{b3}} & 0 & sM_{b3bc} & 0 & -sM_{b3bc} \\ \frac{-1}{sC_{b4}} & 0 & sM_{b4bc} & 0 & -sM_{b4bc} \\ 0 & \frac{-1}{sC_{b12}} & 0 & 0 & 0 \\ \frac{1}{sC_{b3}} + \frac{1}{sC_{b4}} + \frac{1}{sC_{b34}} & \frac{-1}{sC_{b34}} & 0 & 0 & 0 \\ \frac{-1}{sC_{b34}} & \frac{1}{sC_{b12}} + \frac{1}{sC_{b34}} + \frac{1}{sC_{b10}} & 0 & 0 & \frac{-1}{sC_{b10}} \\ 0 & 0 & R_c + sL_c & 0 & -R_c - sL_c \\ 0 & 0 & 0 & \frac{1}{sC_{a10}} & 0 \\ 0 & \frac{-1}{sC_{b10}} & -R_c - sL_c & 0 & \frac{1}{sC_{b10}} + R_c + sL_c \end{bmatrix} \tag{G.15}$$

$$Z_{hvsc} = \begin{bmatrix} Z_{hvsc}^{1} & Z_{hvsc}^{2} & Z_{hvsc}^{3} \end{bmatrix} \tag{G.16}$$

Appendix H

Case Study 2: Attempt 1 Impedance Matrices

$$Z_{lvsc}^{1} = \begin{bmatrix} \frac{1}{sC_{a10}} + R_{a1} + sL_{a1} & -R_{a1} - sL_{a1} + sM_{a1b3} + sM_{a1b4} \\ -R_{a1} - sL_{a1} + sM_{a1b4} + sM_{a1b3} & \frac{1}{sC_{ab1}} + R_{a1} + sL_{a1} - sM_{a1b3} - sM_{a1b4} + R_{b4} + sL_{b4} - sM_{a1b4} + sM_{b34} + R_{b3} + sL_{b3} - sM_{a1b3} + sM_{b34} \\ sM_{a1b1} + sM_{a1b2} & \frac{-1}{sC_{ab1}} - sM_{a1b1} + sM_{b13} + sM_{b14} - sM_{a1b2} + sM_{b23} + sM_{b24} \\ -sM_{a1b1} & -sM_{b13} - sM_{b14} + sM_{a1b1} \\ -sM_{a1b2} & -sM_{b23} - sM_{b24} + sM_{a1b2} \\ -sM_{a1b3} & -R_{b3} - sL_{b3} - sM_{b34} + sM_{a1b3} \\ -sM_{a1b4} & -R_{b4} - sL_{b4} - sM_{b34} + sM_{a1b4} \\ 0 & 0 \\ 0 & 0 \\ 0 & 0 \\ -sM_{a1bc} & sM_{a1bc} - sM_{b3bc} - sM_{b4bc} \\ sM_{a1bc} & -sM_{a1bc} + sM_{b3bc} + sM_{b4bc} \\ \frac{1}{sC_{a10}} & 0 \end{bmatrix} \tag{H.1}$$

$$Z_{lvsc}^{2} = \begin{bmatrix} sM_{a1b1} + sM_{a1b2} & -sM_{a1b1} & -sM_{a1b2} & -sM_{a1b3} & -sM_{a1b4} \\ \frac{-1}{sC_{ab1}} - sM_{a1b1} - sM_{a1b2} + sM_{b13} + sM_{b23} + sM_{b14} + sM_{b24} & sM_{a1b1} - sM_{b14} - sM_{b13} & sM_{a1b2} - sM_{b24} - sM_{b23} & sM_{a1b3} - sM_{b34} - sL_{b3} - R_{b3} & sM_{a1b4} - R_{b4} - sL_{b4} - sM_{b34} \\ \frac{1}{sC_{ab1}} + \frac{1}{sC_{ab2}} + R_{b1} + sL_{b1} + sM_{b12} + R_{b2} + sL_{b2} + sM_{b12} & -R_{b1} - sL_{b1} - sM_{b12} & -sM_{b12} - R_{b2} - sL_{b2} & -sM_{b13} - sM_{b23} & -sM_{b14} - sM_{b24} \\ -R_{b1} - sL_{b1} - sM_{b12} & R_{b1} + \frac{1}{sC_{b1}} + sL_{b1} & sM_{b12} & sM_{b13} & sM_{b14} \\ -R_{b2} - sL_{b2} - sM_{b12} & sM_{b12} & R_{b2} + \frac{1}{sC_{b2}} + sL_{b2} & sM_{b23} & sM_{b24} \\ -sM_{b13} - sM_{b23} & sM_{b13} & sM_{b23} & R_{b3} + \frac{1}{sC_{b3}} + sL_{b3} & sM_{b34} \\ -sM_{b14} - sM_{b24} & sM_{b14} & sM_{b24} & sM_{b34} & R_{b4} + \frac{1}{sC_{b4}} + sL_{b4} \\ 0 & \frac{-1}{sC_{b1}} & \frac{-1}{sC_{b2}} & 0 & 0 \\ 0 & 0 & 0 & \frac{-1}{sC_{b3}} & \frac{-1}{sC_{b4}} \\ 0 & 0 & 0 & 0 & 0 \\ -sM_{b1bc} - sM_{b2bc} & sM_{b1bc} & sM_{b2bc} & sM_{b3bc} & sM_{b4bc} \\ sM_{b1bc} + sM_{b2bc} & -sM_{b1bc} & -sM_{b2bc} & -sM_{b3bc} & -sM_{b4bc} \\ 0 & 0 & 0 & 0 & 0 \end{bmatrix} \tag{H.2}$$

$$Z_{lvsc}^{3} = \begin{bmatrix} 0 & 0 & 0 & -sM_{a1bc} & sM_{a1bc} & \frac{-1}{sC_{a10}} \\ 0 & 0 & 0 & sM_{a1bc} - sM_{b4bc} - sM_{b3bc} & -sM_{a1bc} + sM_{b3bc} + sM_{b4bc} & 0 \\ 0 & 0 & 0 & -sM_{b1bc} - sM_{b2bc} & sM_{b1bc} + sM_{b2bc} & 0 \\ \frac{-1}{sC_{b1}} & 0 & 0 & sM_{b1bc} & -sM_{b1bc} & 0 \\ \frac{-1}{sC_{b2}} & 0 & 0 & sM_{b2bc} & -sM_{b2bc} & 0 \\ 0 & \frac{-1}{sC_{b3}} & 0 & sM_{b3bc} & -sM_{b3bc} & 0 \\ 0 & \frac{-1}{sC_{b4}} & 0 & sM_{b4bc} & -sM_{b4bc} & 0 \\ \frac{1}{sC_{b1}} + \frac{1}{sC_{b2}} + \frac{1}{sC_{b12}} & 0 & \frac{-1}{sC_{b12}} & 0 & 0 & 0 \\ 0 & \frac{1}{sC_{b3}} + \frac{1}{sC_{b4}} + \frac{1}{sC_{b34}} & \frac{-1}{sC_{b34}} & 0 & 0 & 0 \\ \frac{-1}{sC_{b12}} & \frac{-1}{sC_{b34}} & \frac{1}{sC_{b12}} + \frac{1}{sC_{b34}} + \frac{1}{sC_{b10}} & 0 & \frac{-1}{sC_{b10}} & 0 \\ 0 & 0 & 0 & R_c + sL_c & -R_c - sL_c & 0 \\ 0 & 0 & \frac{-1}{sC_{b10}} & -R_c - sL_c & \frac{1}{sC_{b10}} + R_c + sL_c & 0 \\ 0 & 0 & 0 & 0 & 0 & \frac{-1}{sC_{a10}} \end{bmatrix} \tag{H.3}$$

$$Z_{lvsc} = \begin{bmatrix} Z_{lvsc}^{1} & Z_{lvsc}^{2} & Z_{lvsc}^{3} \end{bmatrix} \tag{H.4}$$

$$Z^1_{lvoc} = \begin{bmatrix} \frac{1}{sC_{a10}} + R_{a1} + sL_{a1} & -R_{a1} - sL_{a1} + sM_{a1b3} + sM_{a1b4} \\ -R_{a1} - sL_{a1} + sM_{a1b4} + sM_{a1b3} & \frac{1}{sC_{ab1}} + R_{a1} + sL_{a1} - sM_{a1b3} - sM_{a1b4} + R_{b4} + sL_{b4} - sM_{a1b4} + sM_{b34} + R_{b3} + sL_{b3} - sM_{a1b3} + sM_{b34} \\ sM_{a1b1} + sM_{a1b2} & \frac{-1}{sC_{ab1}} - sM_{a1b1} + sM_{b13} + sM_{b14} - sM_{a1b2} + sM_{b23} + sM_{b24} \\ -sM_{a1b1} & -sM_{b13} - sM_{b14} + sM_{a1b1} \\ -sM_{a1b2} & -sM_{b23} - sM_{b24} + sM_{a1b2} \\ -sM_{a1b3} & -R_{b3} - sL_{b3} - sM_{b34} + sM_{a1b3} \\ -sM_{a1b4} & -R_{b4} - sL_{b4} - sM_{b34} + sM_{a1b4} \\ 0 & 0 \\ 0 & 0 \\ 0 & 0 \\ -sM_{a1bc} & sM_{a1bc} - sM_{b3bc} - sM_{b4bc} \\ \frac{1}{sC_{a10}} & 0 \end{bmatrix} \tag{H.5}$$

$$Z^2_{lvoc} = \begin{bmatrix} sM_{a1b1} + sM_{a1b2} & -sM_{a1b1} & -sM_{a1b2} & -sM_{a1b3} & -sM_{a1b4} \\ \frac{-1}{sC_{ab1}} - sM_{a1b1} - sM_{a1b2} + sM_{b13} + sM_{b23} + sM_{b14} + sM_{b24} & sM_{a1b1} - sM_{b14} - sM_{b13} & sM_{a1b2} - sM_{b24} - sM_{b23} & sM_{a1b3} - sM_{b34} - sL_{b3} - R_{b3} & sM_{a1b4} - R_{b4} - sL_{b4} - sM_{b34} \\ \frac{1}{sC_{ab1}} + \frac{1}{sC_{ab2}} + R_{b1} + sL_{b1} + sM_{b12} + R_{b2} + sL_{b2} + sM_{b12} & -R_{b1} - sL_{b1} - sM_{b12} & -sM_{b12} - R_{b2} - sL_{b2} & -sM_{b13} - sM_{b23} & -sM_{b14} - sM_{b24} \\ -R_{b1} - sL_{b1} - sM_{b12} & R_{b1} + \frac{1}{sC_{b1}} + sL_{b1} & sM_{b12} & sM_{b13} & sM_{b14} \\ -R_{b2} - sL_{b2} - sM_{b12} & sM_{b12} & R_{b2} + \frac{1}{sC_{b2}} + sL_{b2} & sM_{b23} & sM_{b24} \\ -sM_{b13} - sM_{b23} & sM_{b13} & sM_{b23} & R_{b3} + \frac{1}{sC_{b3}} + sL_{b3} & sM_{b34} \\ -sM_{b14} - sM_{b24} & sM_{b14} & sM_{b24} & sM_{b34} & R_{b4} + \frac{1}{sC_{b4}} + sL_{b4} \\ 0 & \frac{-1}{sC_{b1}} & \frac{-1}{sC_{b2}} & 0 & 0 \\ 0 & 0 & 0 & \frac{-1}{sC_{b3}} & \frac{-1}{sC_{b4}} \\ 0 & 0 & 0 & 0 & 0 \\ -sM_{b1bc} - sM_{b2bc} & sM_{b1bc} & sM_{b2bc} & sM_{b3bc} & sM_{b4bc} \\ 0 & 0 & 0 & 0 & 0 \end{bmatrix} \tag{H.6}$$

$$Z^3_{lvoc} = \begin{bmatrix} 0 & 0 & 0 & -sM_{a1bc} & \frac{-1}{sC_{a10}} \\ 0 & 0 & 0 & sM_{a1bc} - sM_{b4bc} - sM_{b3bc} & 0 \\ 0 & 0 & 0 & -sM_{b1bc} - sM_{b2bc} & 0 \\ \frac{-1}{sC_{b1}} & 0 & 0 & sM_{b1bc} & 0 \\ \frac{-1}{sC_{b2}} & 0 & 0 & sM_{b2bc} & 0 \\ 0 & \frac{-1}{sC_{b3}} & 0 & sM_{b3bc} & 0 \\ 0 & \frac{-1}{sC_{b4}} & 0 & sM_{b4bc} & 0 \\ \frac{1}{sC_{b1}} + \frac{1}{sC_{b2}} + \frac{1}{sC_{b12}} & 0 & \frac{-1}{sC_{b12}} & 0 & 0 \\ 0 & \frac{1}{sC_{b3}} + \frac{1}{sC_{b4}} + \frac{1}{sC_{b34}} & \frac{-1}{sC_{b34}} & 0 & 0 \\ \frac{-1}{sC_{b12}} & \frac{-1}{sC_{b34}} & \frac{1}{sC_{b12}} + \frac{1}{sC_{b34}} + \frac{1}{sC_{b10}} & 0 & 0 \\ 0 & 0 & 0 & R_c + sL_c & 0 \\ 0 & 0 & 0 & 0 & \frac{-1}{sC_{a10}} \end{bmatrix} \tag{H.7}$$

$$Z_{lvoc} = \begin{bmatrix} Z^1_{lvoc} & Z^2_{lvoc} & Z^3_{lvoc} \end{bmatrix} \tag{H.8}$$

$$Z^1_{hvsc} = \begin{bmatrix} \frac{1}{sC_{a10}} + R_{a1} + sL_{a1} & -R_{a1} - sL_{a1} + sM_{a1b3} + sM_{a1b4} \\ -R_{a1} - sL_{a1} + sM_{a1b4} + sM_{a1b3} & \frac{1}{sC_{ab1}} + R_{a1} + sL_{a1} - sM_{a1b3} - sM_{a1b4} + R_{b4} + sL_{b4} - sM_{a1b4} + sM_{b34} + R_{b3} + sL_{b3} - sM_{a1b3} + sM_{b34} \\ sM_{a1b1} + sM_{a1b2} & \frac{-1}{sC_{ab1}} - sM_{a1b1} + sM_{b13} + sM_{b14} - sM_{a1b2} + sM_{b23} + sM_{b24} \\ -sM_{a1b1} & -sM_{b13} - sM_{b14} + sM_{a1b1} \\ -sM_{a1b2} & -sM_{b23} - sM_{b24} + sM_{a1b2} \\ -sM_{a1b3} & -R_{b3} - sL_{b3} - sM_{b34} + sM_{a1b3} \\ -sM_{a1b4} & -R_{b4} - sL_{b4} - sM_{b34} + sM_{a1b4} \\ 0 & 0 \\ 0 & 0 \\ 0 & 0 \\ -sM_{a1bc} & sM_{a1bc} - sM_{b3bc} - sM_{b4bc} \\ \frac{1}{sC_{a10}} & 0 \\ sM_{a1bc} & -sM_{a1bc} + sM_{b3bc} + sM_{b4bc} \end{bmatrix} \tag{H.9}$$

$$Z^2_{hvsc} = \begin{bmatrix} sM_{a1b1} + sM_{a1b2} & -sM_{a1b1} & -sM_{a1b2} & -sM_{a1b3} & -sM_{a1b4} \\ \frac{-1}{sC_{ab1}} - sM_{a1b1} - sM_{a1b2} + sM_{b13} + sM_{b23} + sM_{b14} + sM_{b24} & sM_{a1b1} - sM_{b14} - sM_{b13} & sM_{a1b2} - sM_{b24} - sM_{b23} & sM_{a1b3} - sM_{b34} - sL_{b3} - R_{b3} & sM_{a1b4} - R_{b4} - sL_{b4} - sM_{b34} \\ \frac{1}{sC_{ab1}} + \frac{1}{sC_{ab2}} + R_{b1} + sL_{b1} + sM_{b12} + R_{b2} + sL_{b2} + sM_{b12} & -R_{b1} - sL_{b1} - sM_{b12} & -sM_{b12} - R_{b2} - sL_{b2} & -sM_{b13} - sM_{b23} & -sM_{b14} - sM_{b24} \\ -R_{b1} - sL_{b1} - sM_{b12} & R_{b1} + \frac{1}{sC_{b1}} + sL_{b1} & sM_{b12} & sM_{b13} & sM_{b14} \\ -R_{b2} - sL_{b2} - sM_{b12} & sM_{b12} & R_{b2} + \frac{1}{sC_{b2}} + sL_{b2} & sM_{b23} & sM_{b24} \\ -sM_{b13} - sM_{b23} & sM_{b13} & sM_{b23} & R_{b3} + \frac{1}{sC_{b3}} + sL_{b3} & sM_{b34} \\ -sM_{b14} - sM_{b24} & sM_{b14} & sM_{b24} & sM_{b34} & R_{b4} + \frac{1}{sC_{b4}} + sL_{b4} \\ 0 & \frac{-1}{sC_{b1}} & \frac{-1}{sC_{b2}} & 0 & 0 \\ 0 & 0 & 0 & \frac{-1}{sC_{b3}} & \frac{-1}{sC_{b4}} \\ 0 & 0 & 0 & 0 & 0 \\ -sM_{b1bc} - sM_{b2bc} & sM_{b1bc} & sM_{b2bc} & sM_{b3bc} & sM_{b4bc} \\ 0 & 0 & 0 & 0 & 0 \\ sM_{b1bc} + sM_{b2bc} & -sM_{b1bc} & -sM_{b2bc} & -sM_{b3bc} & -sM_{b4bc} \end{bmatrix} \tag{H.10}$$

$$Z^3_{hvsc} = \begin{bmatrix} 0 & 0 & 0 & -sM_{a1bc} & \frac{-1}{sC_{a10}} & sM_{a1bc} \\ 0 & 0 & 0 & sM_{a1bc} - sM_{b4bc} - sM_{b3bc} & 0 & -sM_{a1bc} + sM_{b3bc} + sM_{b4bc} \\ 0 & 0 & 0 & -sM_{b1bc} - sM_{b2bc} & 0 & sM_{b1bc} + sM_{b2bc} \\ \frac{-1}{sC_{b1}} & 0 & 0 & sM_{b1bc} & 0 & -sM_{b1bc} \\ \frac{-1}{sC_{b2}} & 0 & 0 & sM_{b2bc} & 0 & -sM_{b2bc} \\ 0 & \frac{-1}{sC_{b3}} & 0 & sM_{b3bc} & 0 & -sM_{b3bc} \\ 0 & \frac{-1}{sC_{b4}} & 0 & sM_{b4bc} & 0 & -sM_{b4bc} \\ \frac{1}{sC_{b1}} + \frac{1}{sC_{b2}} + \frac{1}{sC_{b12}} & 0 & \frac{-1}{sC_{b12}} & 0 & 0 & 0 \\ 0 & \frac{1}{sC_{b3}} + \frac{1}{sC_{b4}} + \frac{1}{sC_{b34}} & \frac{-1}{sC_{b34}} & 0 & 0 & 0 \\ \frac{-1}{sC_{b12}} & \frac{-1}{sC_{b34}} & \frac{1}{sC_{b12}} + \frac{1}{sC_{b34}} + \frac{1}{sC_{b10}} & 0 & 0 & \frac{-1}{sC_{b10}} \\ 0 & 0 & 0 & R_c + sL_c & 0 & -R_c - sL_c \\ 0 & 0 & 0 & 0 & \frac{-1}{sC_{a10}} & 0 \\ 0 & 0 & \frac{-1}{sC_{b10}} & -R_c - sL_c & 0 & \frac{1}{sC_{b10}} + R_c + sL_c \end{bmatrix} \tag{H.11}$$

$$Z_{hvsc} = \begin{bmatrix} Z^1_{hvsc} & Z^2_{hvsc} & Z^3_{hvsc} \end{bmatrix} \tag{H.12}$$

$$Z_{hvoc}^{1} = \begin{bmatrix} \frac{1}{sC_{a10}} + R_{a1} + sL_{a1} & -R_{a1} - sL_{a1} + sM_{a1b3} + sM_{a1b4} \\ -R_{a1} - sL_{a1} + sM_{a1b4} + sM_{a1b3} & \frac{1}{sC_{ab1}} + R_{a1} + sL_{a1} - sM_{a1b3} - sM_{a1b4} + R_{b4} + sL_{b4} - sM_{a1b4} + sM_{b34} + R_{b3} + sL_{b3} - sM_{a1b3} + sM_{b34} \\ sM_{a1b1} + sM_{a1b2} & \frac{-1}{sC_{ab1}} - sM_{a1b1} + sM_{b13} + sM_{b14} - sM_{a1b2} + sM_{b23} + sM_{b24} \\ -sM_{a1b1} & -sM_{b13} - sM_{b14} + sM_{a1b1} \\ -sM_{a1b2} & -sM_{b23} - sM_{b24} + sM_{a1b2} \\ -sM_{a1b3} & -R_{b3} - sL_{b3} - sM_{b34} + sM_{a1b3} \\ -sM_{a1b4} & -R_{b4} - sL_{b4} - sM_{b34} + sM_{a1b4} \\ 0 & 0 \\ 0 & 0 \\ 0 & 0 \\ -sM_{a1bc} & sM_{a1bc} - sM_{b3bc} - sM_{b4bc} \\ sM_{a1bc} & -sM_{a1bc} + sM_{b3bc} + sM_{b4bc} \end{bmatrix} \tag{H.13}$$

$$Z_{hvoc}^{2} = \begin{bmatrix} sM_{a1b1} + sM_{a1b2} & -sM_{a1b1} & -sM_{a1b2} & -sM_{a1b3} & -sM_{a1b4} \\ \frac{-1}{sC_{ab1}} - sM_{a1b1} - sM_{a1b2} + sM_{b13} + sM_{b23} + sM_{b14} + sM_{b24} & sM_{a1b1} - sM_{b14} - sM_{b13} & sM_{a1b2} - sM_{b24} - sM_{b23} & sM_{a1b3} - sM_{b34} - sL_{b3} - R_{b3} & sM_{a1b4} - R_{b4} - sL_{b4} - sM_{b34} \\ \frac{1}{sC_{ab1}} + \frac{1}{sC_{ab2}} + R_{b1} + sL_{b1} + sM_{b12} + R_{b2} + sL_{b2} + sM_{b12} & -R_{b1} - sL_{b1} - sM_{b12} & -sM_{b12} - R_{b2} - sL_{b2} & -sM_{b13} - sM_{b23} & -sM_{b14} - sM_{b24} \\ -R_{b1} - sL_{b1} - sM_{b12} & R_{b1} + \frac{1}{sC_{b1}} + sL_{b1} & sM_{b12} & sM_{b13} & sM_{b14} \\ -R_{b2} - sL_{b2} - sM_{b12} & sM_{b12} & R_{b2} + \frac{1}{sC_{b2}} + sL_{b2} & sM_{b23} & sM_{b24} \\ -sM_{b13} - sM_{b23} & sM_{b13} & sM_{b23} & R_{b3} + \frac{1}{sC_{b3}} + sL_{b3} & sM_{b34} \\ -sM_{b14} - sM_{b24} & sM_{b14} & sM_{b24} & sM_{b34} & R_{b4} + \frac{1}{sC_{b4}} + sL_{b4} \\ 0 & \frac{-1}{sC_{b1}} & \frac{-1}{sC_{b2}} & 0 & 0 \\ 0 & 0 & 0 & \frac{-1}{sC_{b3}} & \frac{-1}{sC_{b4}} \\ 0 & 0 & 0 & 0 & 0 \\ -sM_{b1bc} - sM_{b2bc} & sM_{b1bc} & sM_{b2bc} & sM_{b3bc} & sM_{b4bc} \\ sM_{b1bc} + sM_{b2bc} & -sM_{b1bc} & -sM_{b2bc} & -sM_{b3bc} & -sM_{b4bc} \end{bmatrix} \tag{H.14}$$

$$Z_{hvoc}^{3} = \begin{bmatrix} 0 & 0 & 0 & -sM_{a1bc} & sM_{a1bc} & \\ 0 & 0 & 0 & sM_{a1bc} - sM_{b4bc} - sM_{b3bc} & -sM_{a1bc} + sM_{b3bc} + sM_{b4bc} & \\ 0 & 0 & 0 & -sM_{b1bc} - sM_{b2bc} & 0 & sM_{b1bc} + sM_{b2bc} \\ \frac{-1}{sC_{b1}} & 0 & 0 & sM_{b1bc} & -sM_{b1bc} & \\ \frac{-1}{sC_{b2}} & 0 & 0 & sM_{b2bc} & -sM_{b2bc} & \\ 0 & \frac{-1}{sC_{b3}} & 0 & sM_{b3bc} & -sM_{b3bc} & \\ 0 & \frac{-1}{sC_{b4}} & 0 & sM_{b4bc} & -sM_{b4bc} & \\ \frac{1}{sC_{b1}} + \frac{1}{sC_{b2}} + \frac{1}{sC_{b12}} & 0 & \frac{-1}{sC_{b12}} & 0 & 0 & \\ 0 & \frac{1}{sC_{b3}} + \frac{1}{sC_{b4}} + \frac{1}{sC_{b34}} & \frac{-1}{sC_{b34}} & 0 & 0 & \\ \frac{-1}{sC_{b12}} & \frac{-1}{sC_{b34}} & \frac{1}{sC_{b12}} + \frac{1}{sC_{b34}} + \frac{1}{sC_{b10}} & 0 & \frac{-1}{sC_{b10}} & \\ 0 & 0 & 0 & R_c + sL_c & -R_c - sL_c & \\ 0 & 0 & \frac{-1}{sC_{b10}} & -R_c - sL_c & \frac{1}{sC_{b10}} + R_c + sL_c & \end{bmatrix} \tag{H.15}$$

$$Z_{hvoc} = \begin{bmatrix} Z_{hvoc}^{1} & Z_{hvoc}^{2} & Z_{hvoc}^{3} \end{bmatrix} \tag{H.16}$$

Appendix I

Case Study 2: Attempt 1 Analytical Validation

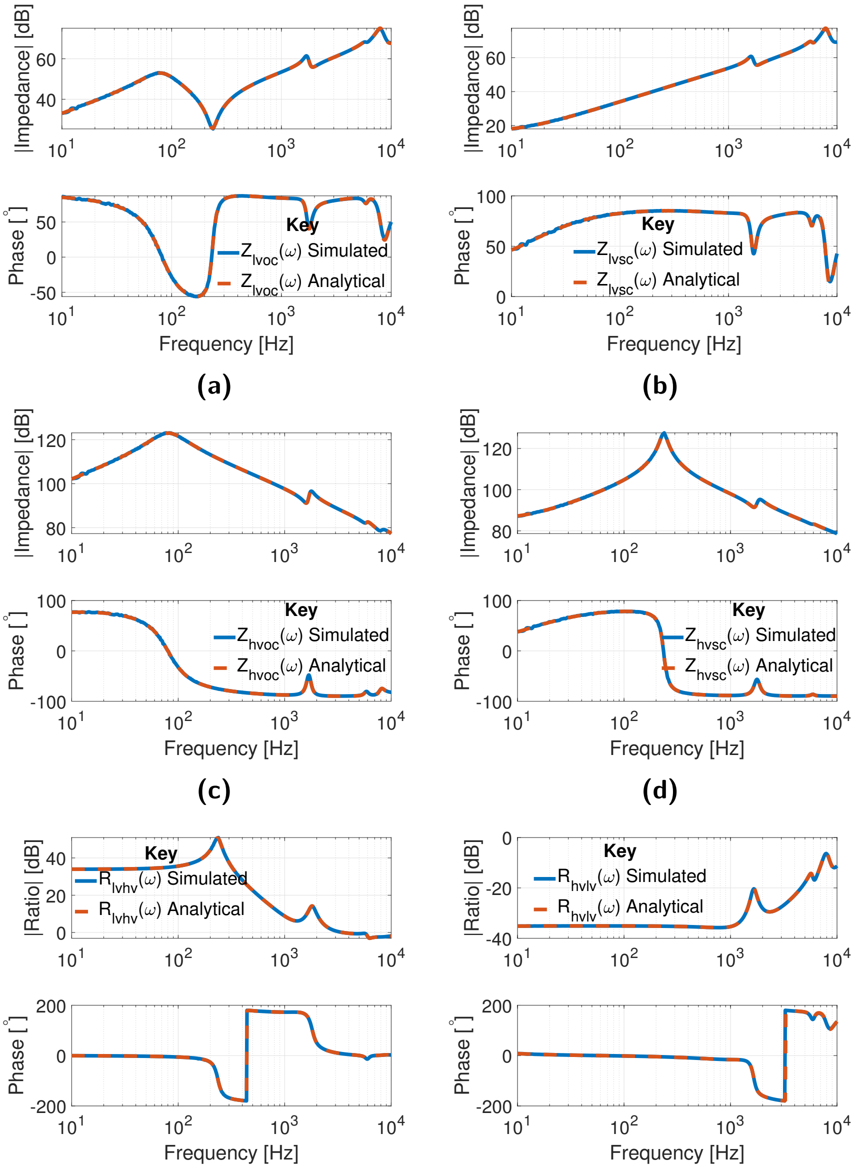

(a) **(b)** **(c)** **(d)** **(e)** **(f)**

Figure I.1: Magnitude and phase responses of **(a)**$Z_{lvoc}(\omega)$, **(b)**$Z_{lvsc}(\omega)$, **(c)**$Z_{hvoc}(\omega)$, **(d)**$Z_{hvsc}(\omega)$, **(e)**$R_{lvhv}(\omega)$ and **(f)**$R_{hvlv}(\omega)$ obtained analytically and through simulated PRIS perturbation of the model presented in Fig. 5.14 for a random set of parameters.

Appendix J

Case Study 2: Attempt 2 Impedance Matrices

$$Z^1_{lvsc} = \begin{bmatrix} \frac{1}{sC_{a10}} + R_{a1} + sL_{a1} & -R_{a1} - sL_{a1} + sM_{a1b4} & sM_{a1b2} + sM_{a1b3} \\ -R_{a1} - sL_{a1} + sM_{a1b4} & \frac{1}{sC_{ab1}} + R_{a1} + sL_{a1} - sM_{a1b4} + R_{b4} + sL_{b4} - sM_{a1b4} & \frac{-1}{sC_{ab1}} - sM_{a1b2} - sM_{a1b3} + sM_{b24} + sM_{b34} \\ sM_{a1b2} + sM_{a1b3} & \frac{-1}{sC_{ab1}} - sM_{a1b2} + sM_{b24} - sM_{a1b3} + sM_{b34} & \frac{1}{sC_{ab1}} + \frac{1}{sC_{ab2}} + R_{b2} + sL_{b2} + sM_{b23} + R_{b3} + sL_{b3} + sM_{b23} \\ -sM_{a1b1} & -sM_{b14} + sM_{a1b1} & -sM_{b13} - sM_{b12} \\ -sM_{a1b2} & -sM_{b24} + sM_{a1b2} & -R_{b2} - sL_{b2} - sM_{b23} \\ -sM_{a1b3} & -sM_{b34} + sM_{a1b3} & -R_{b3} - sL_{b3} - sM_{b23} \\ -sM_{a1b4} & -R_{b4} - sL_{b4} + sM_{a1b4} & -sM_{b34} - sM_{b24} \\ 0 & 0 & 0 \\ 0 & 0 & 0 \\ 0 & 0 & 0 \\ -sM_{a1bc} & sM_{a1bc} - sM_{b4bc} & -sM_{b2bc} - sM_{b3bc} \\ sM_{a1bc} & -sM_{a1bc} + sM_{b4bc} & sM_{b2bc} + sM_{b3bc} \\ \frac{1}{sC_{a10}} & 0 & 0 \end{bmatrix} \tag{J.1}$$

$$Z^2_{lvsc} = \begin{bmatrix} -sM_{a1b1} & -sM_{a1b2} & -sM_{a1b3} & -sM_{a1b4} & 0 \\ sM_{a1b1} - sM_{b14} & sM_{a1b2} - sM_{b24} & sM_{a1b3} - sM_{b34} & sM_{a1b4} - R_{b4} - sL_{b4} & 0 \\ -sM_{b12} - sM_{b13} & -sM_{b23} - R_{b2} - sL_{b2} & -sM_{b23} - R_{b3} - sL_{b3} & -sM_{b24} - sM_{b34} & 0 \\ R_{b1} + \frac{1}{sC_{b1}} + sL_{b1} & sM_{b12} & sM_{b13} & sM_{b14} & \frac{-1}{sC_{b1}} \\ sM_{b12} & R_{b2} + \frac{1}{sC_{b2}} + sL_{b2} & sM_{b23} & sM_{b24} & \frac{-1}{sC_{b2}} \\ sM_{b13} & sM_{b23} & R_{b3} + \frac{1}{sC_{b3}} + sL_{b3} & sM_{b34} & 0 \\ sM_{b14} & sM_{b24} & sM_{b34} & R_{b4} + \frac{1}{sC_{b4}} + sL_{b4} & 0 \\ \frac{-1}{sC_{b1}} & \frac{-1}{sC_{b2}} & 0 & 0 & \frac{1}{sC_{b1}} + \frac{1}{sC_{b2}} + \frac{1}{sC_{b12}} \\ 0 & 0 & \frac{-1}{sC_{b3}} & \frac{-1}{sC_{b4}} & 0 \\ 0 & 0 & 0 & 0 & \frac{-1}{sC_{b12}} \\ sM_{b1bc} & sM_{b2bc} & sM_{b3bc} & sM_{b4bc} & 0 \\ -sM_{b1bc} & -sM_{b2bc} & -sM_{b3bc} & -sM_{b4bc} & 0 \\ 0 & 0 & 0 & 0 & 0 \end{bmatrix} \tag{J.2}$$

$$Z^3_{lvsc} = \begin{bmatrix} 0 & 0 & -sM_{a1bc} & sM_{a1bc} & \frac{-1}{sC_{a10}} \\ 0 & 0 & sM_{a1bc} - sM_{b4bc} & -sM_{a1bc} + sM_{b4bc} & 0 \\ 0 & 0 & -sM_{b2bc} - sM_{b3bc} & sM_{b2bc} + sM_{b3bc} & 0 \\ 0 & 0 & sM_{b1bc} & -sM_{b1bc} & 0 \\ 0 & 0 & sM_{b2bc} & -sM_{b2bc} & 0 \\ \frac{-1}{sC_{b3}} & 0 & sM_{b3bc} & -sM_{b3bc} & 0 \\ \frac{-1}{sC_{b4}} & 0 & sM_{b4bc} & -sM_{b4bc} & 0 \\ 0 & \frac{-1}{sC_{b12}} & 0 & 0 & 0 \\ \frac{1}{sC_{b3}} + \frac{1}{sC_{b4}} + \frac{1}{sC_{b34}} & \frac{-1}{sC_{b34}} & 0 & 0 & 0 \\ \frac{-1}{sC_{b34}} & \frac{1}{sC_{b12}} + \frac{1}{sC_{b34}} + \frac{1}{sC_{b10}} & 0 & \frac{-1}{sC_{b10}} & 0 \\ 0 & 0 & R_c + sL_c & -R_c - sL_c & 0 \\ 0 & \frac{-1}{sC_{b10}} & -R_c - sL_c & \frac{1}{sC_{b10}} + R_c + sL_c & 0 \\ 0 & 0 & 0 & 0 & \frac{-1}{sC_{a10}} \end{bmatrix} \tag{J.3}$$

$$Z_{lvsc} = \begin{bmatrix} Z^1_{lvsc} & Z^2_{lvsc} & Z^3_{lvsc} \end{bmatrix} \tag{J.4}$$

$$Z^1_{lvoc} = \begin{bmatrix} \frac{1}{sC_{a10}} + R_{a1} + sL_{a1} & -R_{a1} - sL_{a1} + sM_{a1b4} & sM_{a1b2} + sM_{a1b3} \\ -R_{a1} - sL_{a1} + sM_{a1b4} & \frac{1}{sC_{ab1}} + R_{a1} + sL_{a1} - sM_{a1b4} + R_{b4} + sL_{b4} - sM_{a1b4} & \frac{-1}{sC_{ab1}} - sM_{a1b2} - sM_{a1b3} + sM_{b24} + sM_{b34} \\ sM_{a1b2} + sM_{a1b3} & \frac{-1}{sC_{ab1}} - sM_{a1b2} + sM_{b24} - sM_{a1b3} + sM_{b34} & \frac{1}{sC_{ab1}} + \frac{1}{sC_{ab2}} + R_{b2} + sL_{b2} + sM_{b23} + R_{b3} + sL_{b3} + sM_{b23} \\ -sM_{a1b1} & -sM_{b14} + sM_{a1b1} & -sM_{b13} - sM_{b12} \\ -sM_{a1b2} & -sM_{b24} + sM_{a1b2} & -R_{b2} - sL_{b2} - sM_{b23} \\ -sM_{a1b3} & -sM_{b34} + sM_{a1b3} & -R_{b3} - sL_{b3} - sM_{b23} \\ -sM_{a1b4} & -R_{b4} - sL_{b4} + sM_{a1b4} & -sM_{b34} - sM_{b24} \\ 0 & 0 & 0 \\ 0 & 0 & 0 \\ 0 & 0 & 0 \\ -sM_{a1bc} & sM_{a1bc} - sM_{b4bc} & -sM_{b2bc} - sM_{b3bc} \\ \frac{1}{sC_{a10}} & 0 & 0 \end{bmatrix} \tag{J.5}$$

$$Z^2_{lvoc} = \begin{bmatrix} -sM_{a1b1} & -sM_{a1b2} & -sM_{a1b3} & -sM_{a1b4} & 0 \\ sM_{a1b1} - sM_{b14} & sM_{a1b2} - sM_{b24} & sM_{a1b3} - sM_{b34} & sM_{a1b4} - R_{b4} - sL_{b4} & 0 \\ -sM_{b12} - sM_{b13} & -sM_{b23} - R_{b2} - sL_{b2} & -sM_{b23} - R_{b3} - sL_{b3} & -sM_{b24} - sM_{b34} & 0 \\ R_{b1} + \frac{1}{sC_{b1}} + sL_{b1} & sM_{b12} & sM_{b13} & sM_{b14} & \frac{-1}{sC_{b1}} \\ sM_{b12} & R_{b2} + \frac{1}{sC_{b2}} + sL_{b2} & sM_{b23} & sM_{b24} & \frac{-1}{sC_{b2}} \\ sM_{b13} & sM_{b23} & R_{b3} + \frac{1}{sC_{b3}} + sL_{b3} & sM_{b34} & 0 \\ sM_{b14} & sM_{b24} & sM_{b34} & R_{b4} + \frac{1}{sC_{b4}} + sL_{b4} & 0 \\ \frac{-1}{sC_{b1}} & \frac{-1}{sC_{b2}} & 0 & 0 & \frac{1}{sC_{b1}} + \frac{1}{sC_{b2}} + \frac{1}{sC_{b12}} \\ 0 & 0 & \frac{-1}{sC_{b3}} & \frac{-1}{sC_{b4}} & 0 \\ 0 & 0 & 0 & 0 & \frac{-1}{sC_{b12}} \\ sM_{b1bc} & sM_{b2bc} & sM_{b3bc} & sM_{b4bc} & 0 \\ 0 & 0 & 0 & 0 & 0 \end{bmatrix} \tag{J.6}$$

$$Z^3_{lvoc} = \begin{bmatrix} 0 & 0 & -sM_{a1bc} & \frac{-1}{sC_{a10}} \\ 0 & 0 & sM_{a1bc} - sM_{b4bc} & 0 \\ 0 & 0 & -sM_{b2bc} - sM_{b3bc} & 0 \\ 0 & 0 & sM_{b1bc} & 0 \\ 0 & 0 & sM_{b2bc} & 0 \\ \frac{-1}{sC_{b3}} & 0 & sM_{b3bc} & 0 \\ \frac{-1}{sC_{b4}} & 0 & sM_{b4bc} & 0 \\ 0 & \frac{-1}{sC_{b12}} & 0 & 0 \\ \frac{1}{sC_{b3}} + \frac{1}{sC_{b4}} + \frac{1}{sC_{b34}} & \frac{-1}{sC_{b34}} & 0 & 0 \\ \frac{-1}{sC_{b34}} & \frac{1}{sC_{b12}} + \frac{1}{sC_{b34}} + \frac{1}{sC_{b10}} & 0 & 0 \\ 0 & 0 & R_c + sL_c & 0 \\ 0 & 0 & 0 & \frac{-1}{sC_{a10}} \end{bmatrix} \tag{J.7}$$

$$Z_{lvoc} = \begin{bmatrix} Z^1_{lvoc} & Z^2_{lvoc} & Z^3_{lvoc} \end{bmatrix} \tag{J.8}$$

$$Z^1_{hvsc} = \begin{bmatrix} \frac{1}{sC_{a10}} + R_{a1} + sL_{a1} & -R_{a1} - sL_{a1} + sM_{a1b4} & sM_{a1b2} + sM_{a1b3} \\ -R_{a1} - sL_{a1} + sM_{a1b4} & \frac{1}{sC_{ab1}} + R_{a1} + sL_{a1} - sM_{a1b4} + R_{b4} + sL_{b4} - sM_{a1b4} & \frac{-1}{sC_{ab1}} - sM_{a1b2} - sM_{a1b3} + sM_{b24} + sM_{b34} \\ sM_{a1b2} + sM_{a1b3} & \frac{-1}{sC_{ab1}} - sM_{a1b2} + sM_{b24} - sM_{a1b3} + sM_{b34} & \frac{1}{sC_{ab1}} + \frac{1}{sC_{ab2}} + R_{b2} + sL_{b2} + sM_{b23} + R_{b3} + sL_{b3} + sM_{b23} \\ -sM_{a1b1} & -sM_{b14} + sM_{a1b1} & -sM_{b13} - sM_{b12} \\ -sM_{a1b2} & -sM_{b24} + sM_{a1b2} & -R_{b2} - sL_{b2} - sM_{b23} \\ -sM_{a1b3} & -sM_{b34} + sM_{a1b3} & -R_{b3} - sL_{b3} - sM_{b23} \\ -sM_{a1b4} & -R_{b4} - sL_{b4} + sM_{a1b4} & -sM_{b34} - sM_{b24} \\ 0 & 0 & 0 \\ 0 & 0 & 0 \\ 0 & 0 & 0 \\ -sM_{a1bc} & sM_{a1bc} - sM_{b4bc} & -sM_{b2bc} - sM_{b3bc} \\ \frac{1}{sC_{a10}} & 0 & 0 \\ sM_{a1bc} & -sM_{a1bc} + sM_{b4bc} & sM_{b2bc} + sM_{b3bc} \end{bmatrix} \tag{J.9}$$

$$Z^2_{hvsc} = \begin{bmatrix} -sM_{a1b1} & -sM_{a1b2} & -sM_{a1b3} & -sM_{a1b4} & 0 \\ sM_{a1b1} - sM_{b14} & sM_{a1b2} - sM_{b24} & sM_{a1b3} - sM_{b34} & sM_{a1b4} - R_{b4} - sL_{b4} & 0 \\ -sM_{b12} - sM_{b13} & -sM_{b23} - R_{b2} - sL_{b2} & -sM_{b23} - R_{b3} - sL_{b3} & -sM_{b24} - sM_{b34} & 0 \\ R_{b1} + \frac{1}{sC_{b1}} + sL_{b1} & sM_{b12} & sM_{b13} & sM_{b14} & \frac{-1}{sC_{b1}} \\ sM_{b12} & R_{b2} + \frac{1}{sC_{b2}} + sL_{b2} & sM_{b23} & sM_{b24} & \frac{-1}{sC_{b2}} \\ sM_{b13} & sM_{b23} & R_{b3} + \frac{1}{sC_{b3}} + sL_{b3} & sM_{b34} & 0 \\ sM_{b14} & sM_{b24} & sM_{b34} & R_{b4} + \frac{1}{sC_{b4}} + sL_{b4} & 0 \\ \frac{-1}{sC_{b1}} & \frac{-1}{sC_{b2}} & 0 & 0 & \frac{1}{sC_{b1}} + \frac{1}{sC_{b2}} + \frac{1}{sC_{b12}} \\ 0 & 0 & \frac{-1}{sC_{b3}} & \frac{-1}{sC_{b4}} & 0 \\ 0 & 0 & 0 & 0 & \frac{-1}{sC_{b12}} \\ sM_{b1bc} & sM_{b2bc} & sM_{b3bc} & sM_{b4bc} & 0 \\ 0 & 0 & 0 & 0 & 0 \\ -sM_{b1bc} & -sM_{b2bc} & -sM_{b3bc} & -sM_{b4bc} & 0 \end{bmatrix} \tag{J.10}$$

$$Z^3_{hvsc} = \begin{bmatrix} 0 & 0 & -sM_{a1bc} & \frac{-1}{sC_{a10}} & sM_{a1bc} \\ 0 & 0 & sM_{a1bc} - sM_{b4bc} & 0 & -sM_{a1bc} + sM_{b4bc} \\ 0 & 0 & -sM_{b2bc} - sM_{b3bc} & 0 & sM_{b2bc} + sM_{b3bc} \\ 0 & 0 & sM_{b1bc} & 0 & -sM_{b1bc} \\ 0 & 0 & sM_{b2bc} & 0 & -sM_{b2bc} \\ \frac{-1}{sC_{b3}} & 0 & sM_{b3bc} & 0 & -sM_{b3bc} \\ \frac{-1}{sC_{b4}} & 0 & sM_{b4bc} & 0 & -sM_{b4bc} \\ 0 & \frac{-1}{sC_{b12}} & 0 & 0 & 0 \\ \frac{1}{sC_{b3}} + \frac{1}{sC_{b4}} + \frac{1}{sC_{b34}} & \frac{-1}{sC_{b34}} & 0 & 0 & 0 \\ \frac{-1}{sC_{b34}} & \frac{1}{sC_{b12}} + \frac{1}{sC_{b34}} + \frac{1}{sC_{b10}} & 0 & 0 & \frac{-1}{sC_{b10}} \\ 0 & 0 & R_c + sL_c & 0 & -R_c - sL_c \\ 0 & 0 & 0 & \frac{-1}{sC_{a10}} & 0 \\ 0 & \frac{-1}{sC_{b10}} & -R_c - sL_c & 0 & \frac{1}{sC_{b10}} + R_c + sL_c \end{bmatrix} \tag{J.11}$$

$$Z_{hvsc} = \begin{bmatrix} Z^1_{hvsc} & Z^2_{hvsc} & Z^3_{hvsc} \end{bmatrix} \tag{J.12}$$

$$Z^1_{hvoc} = \begin{bmatrix} \frac{1}{sC_{a10}} + R_{a1} + sL_{a1} & -R_{a1} - sL_{a1} + sM_{a1b4} & sM_{a1b2} + sM_{a1b3} \\ -R_{a1} - sL_{a1} + sM_{a1b4} & \frac{1}{sC_{ab1}} + R_{a1} + sL_{a1} - sM_{a1b4} + R_{b4} + sL_{b4} - sM_{a1b4} & \frac{-1}{sC_{ab1}} - sM_{a1b2} - sM_{a1b3} + sM_{b24} + sM_{b34} \\ sM_{a1b2} + sM_{a1b3} & \frac{-1}{sC_{ab1}} - sM_{a1b2} + sM_{b24} - sM_{a1b3} + sM_{b34} & \frac{1}{sC_{ab1}} + \frac{1}{sC_{ab2}} + R_{b2} + sL_{b2} + sM_{b23} + R_{b3} + sL_{b3} + sM_{b23} \\ -sM_{a1b1} & -sM_{b14} + sM_{a1b1} & -sM_{b13} - sM_{b12} \\ -sM_{a1b2} & -sM_{b24} + sM_{a1b2} & -R_{b2} - sL_{b2} - sM_{b23} \\ -sM_{a1b3} & -sM_{b34} + sM_{a1b3} & -R_{b3} - sL_{b3} - sM_{b23} \\ -sM_{a1b4} & -R_{b4} - sL_{b4} + sM_{a1b4} & -sM_{b34} - sM_{b24} \\ 0 & 0 & 0 \\ 0 & 0 & 0 \\ 0 & 0 & 0 \\ -sM_{a1bc} & sM_{a1bc} - sM_{b4bc} & -sM_{b2bc} - sM_{b3bc} \\ sM_{a1bc} & -sM_{a1bc} + sM_{b4bc} & sM_{b2bc} + sM_{b3bc} \end{bmatrix} \tag{J.13}$$

$$Z^2_{hvoc} = \begin{bmatrix} -sM_{a1b1} & -sM_{a1b2} & -sM_{a1b3} & -sM_{a1b4} & 0 \\ sM_{a1b1} - sM_{b14} & sM_{a1b2} - sM_{b24} & sM_{a1b3} - sM_{b34} & sM_{a1b4} - R_{b4} - sL_{b4} & 0 \\ -sM_{b12} - sM_{b13} & -sM_{b23} - R_{b2} - sL_{b2} & -sM_{b23} - R_{b3} - sL_{b3} & -sM_{b24} - sM_{b34} & 0 \\ R_{b1} + \frac{1}{sC_{b1}} + sL_{b1} & sM_{b12} & sM_{b13} & sM_{b14} & \frac{-1}{sC_{b1}} \\ sM_{b12} & R_{b2} + \frac{1}{sC_{b2}} + sL_{b2} & sM_{b23} & sM_{b24} & \frac{-1}{sC_{b2}} \\ sM_{b13} & sM_{b23} & R_{b3} + \frac{1}{sC_{b3}} + sL_{b3} & sM_{b34} & 0 \\ sM_{b14} & sM_{b24} & sM_{b34} & R_{b4} + \frac{1}{sC_{b4}} + sL_{b4} & 0 \\ \frac{-1}{sC_{b1}} & \frac{-1}{sC_{b2}} & 0 & 0 & \frac{1}{sC_{b1}} + \frac{1}{sC_{b2}} + \frac{1}{sC_{b12}} \\ 0 & 0 & \frac{-1}{sC_{b3}} & \frac{-1}{sC_{b4}} & 0 \\ 0 & 0 & 0 & 0 & \frac{-1}{sC_{b12}} \\ sM_{b1bc} & sM_{b2bc} & sM_{b3bc} & sM_{b4bc} & 0 \\ -sM_{b1bc} & -sM_{b2bc} & -sM_{b3bc} & -sM_{b4bc} & 0 \end{bmatrix} \tag{J.14}$$

$$Z^3_{hvoc} = \begin{bmatrix} 0 & 0 & -sM_{a1bc} & sM_{a1bc} \\ 0 & 0 & sM_{a1bc} - sM_{b4bc} & -sM_{a1bc} + sM_{b4bc} \\ 0 & 0 & -sM_{b2bc} - sM_{b3bc} & sM_{b2bc} + sM_{b3bc} \\ 0 & 0 & sM_{b1bc} & -sM_{b1bc} \\ 0 & 0 & sM_{b2bc} & -sM_{b2bc} \\ \frac{-1}{sC_{b3}} & 0 & sM_{b3bc} & -sM_{b3bc} \\ \frac{-1}{sC_{b4}} & 0 & sM_{b4bc} & -sM_{b4bc} \\ 0 & \frac{-1}{sC_{b12}} & 0 & 0 \\ \frac{1}{sC_{b3}} + \frac{1}{sC_{b4}} + \frac{1}{sC_{b34}} & \frac{-1}{sC_{b34}} & 0 & 0 \\ \frac{-1}{sC_{b34}} & \frac{1}{sC_{b12}} + \frac{1}{sC_{b34}} + \frac{1}{sC_{b10}} & 0 & \frac{-1}{sC_{b10}} \\ 0 & 0 & R_c + sL_c & -R_c - sL_c \\ 0 & \frac{-1}{sC_{b10}} & -R_c - sL_c & \frac{1}{sC_{b10}} + R_c + sL_c \end{bmatrix} \tag{J.15}$$

$$Z_{hvoc} = \begin{bmatrix} Z^1_{hvoc} & Z^2_{hvoc} & Z^3_{hvoc} \end{bmatrix} \tag{J.16}$$

Appendix K

Case Study 2: Attempt 2 Analytical Validation

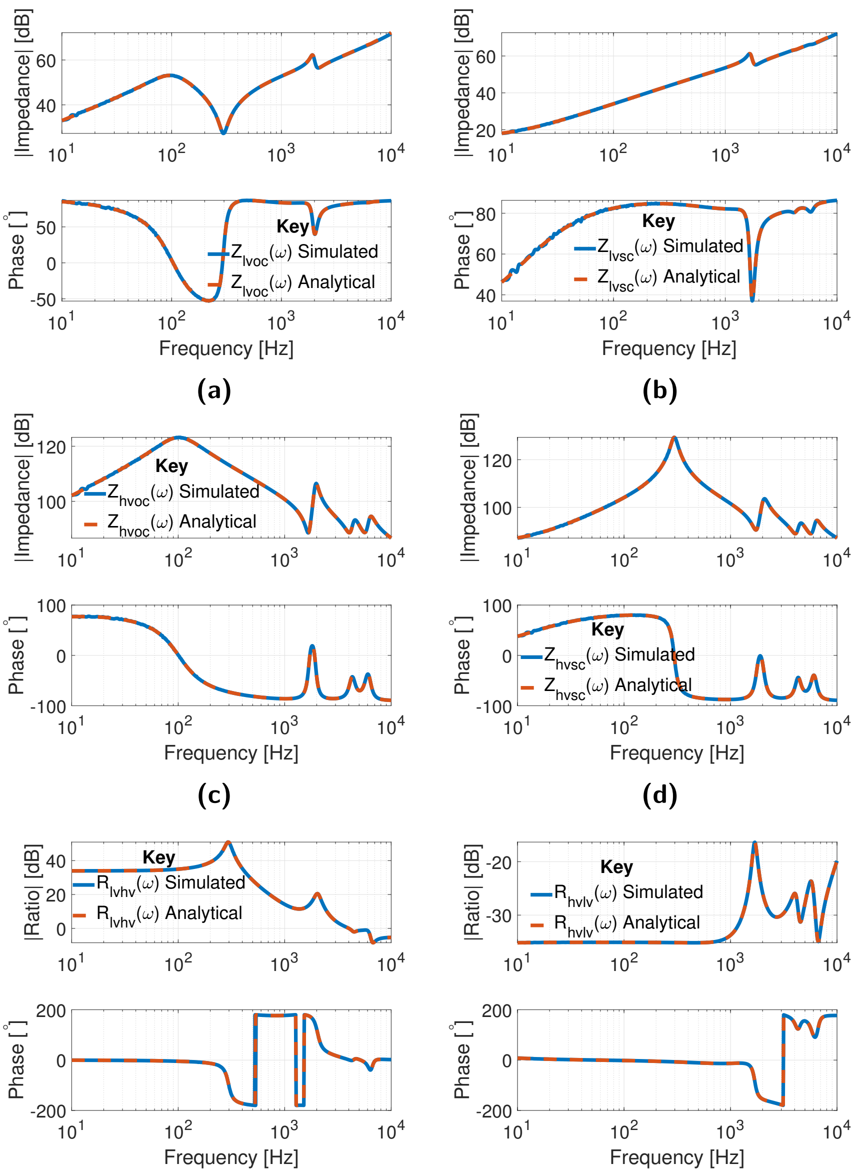

(a) **(b)**

(c) **(d)**

(e) **(f)**

Figure K.1: Magnitude and phase responses of **(a)**$Z_{lvoc}(\omega)$, **(b)**$Z_{lvsc}(\omega)$, **(c)**$Z_{hvoc}(\omega)$, **(d)**$Z_{hvsc}(\omega)$, **(e)**$R_{lvhv}(\omega)$ and **(f)**$R_{hvlv}(\omega)$ obtained analytically and through simulated PRIS perturbation of the model presented in Fig. 5.16 for a random set of parameters.

Appendix L

Case Study 3: Impedance Matrices

$$Z_{lvsc}^{1} = \begin{bmatrix} \frac{1}{sC_{a10}} + R_{a1} + sL_{a1} & -R_{a1} - sL_{a1} + sM_{a1b4} + sM_{a1b5} + sM_{a1b6} \\ -R_{a1} - sL_{a1} + sM_{a1b6} + sM_{a1b5} + sM_{a1b4} & Z_{22} \\ -sM_{a1b1} & sM_{a1b1} - sM_{b14} - sM_{b15} - sM_{b16} \\ -sM_{a1b2} & sM_{a1b2} - sM_{b24} - sM_{b25} - sM_{b26} \\ -sM_{a1b3} & sM_{a1b3} - sM_{b34} - sM_{b35} - sM_{b36} \\ -sM_{a1b4} & -R_{b4} - sL_{b4} + sM_{a1b4} - sM_{b45} - sM_{b46} \\ -sM_{a1b5} & -R_{b5} - sL_{b5} + sM_{a1b5} - sM_{b45} - sM_{b56} \\ -sM_{a1b6} & -R_{b6} - sL_{b6} + sM_{a1b6} - sM_{b46} - sM_{b56} \\ 0 & 0 \\ 0 & 0 \\ 0 & 0 \\ -sM_{a1bc} & sM_{a1bc} - sM_{b4bc} - sM_{b5bc} - sM_{b6bc} \\ sM_{a1bc} & -sM_{a1bc} + sM_{b4bc} + sM_{b5bc} + sM_{b6bc} \\ \frac{1}{sC_{a10}} & 0 \end{bmatrix} \tag{L.1}$$

$$Z_{22} = \frac{1}{sC_{ab1}} + R_{a1} + R_{b6} + R_{b5} + R_{b4} + sL_{a1} - sM_{a1b4} - sM_{a1b5} - sM_{a1b6} + sL_{b6} - sM_{a1b6} + sM_{b46} + sM_{b56} + sL_{b5} - sM_{a1b5} + sM_{b45} + sM_{b56} + sL_{b4} - sM_{a1b4} + sM_{b45} + sM_{b46} \tag{L.2}$$

$$Z_{lvsc}^{2} = \begin{bmatrix} -sM_{a1b1} & -sM_{a1b2} & -sM_{a1b3} & & \\ sM_{a1b1} - sM_{b16} - sM_{b15} - sM_{b14} & sM_{a1b2} - sM_{b26} - sM_{b25} - sM_{b24} & sM_{a1b3} - sM_{b36} - sM_{b35} - sM_{b34} & -R_{b4} + sM_{a1b4} - sM_{b46} - sM_{b45} - sL_{b4} & \\ R_{b1} + \frac{1}{sC_{b1}} + sL_{b1} & sM_{b12} & sM_{b13} & sM_{b14} & \\ sM_{b12} & R_{b2} + \frac{1}{sC_{b2}} + sL_{b2} & sM_{b23} & sM_{b24} & \\ sM_{b13} & sM_{b23} & R_{b3} + \frac{1}{sC_{b3}} + sL_{b3} & sM_{b34} & \\ sM_{b14} & sM_{b24} & sM_{b34} & R_{b4} + \frac{1}{sC_{b4}} + sL_{b4} & \\ sM_{b15} & sM_{b25} & sM_{b35} & sM_{b45} & \\ sM_{b16} & sM_{b26} & sM_{b36} & sM_{b46} & sM_{b56} \\ \frac{-1}{sC_{b1}} & \frac{-1}{sC_{b2}} & \frac{-1}{sC_{b3}} & 0 & \\ 0 & 0 & 0 & \frac{-1}{sC_{b4}} & \\ 0 & 0 & 0 & 0 & \\ sM_{b1bc} & sM_{b2bc} & sM_{b3bc} & sM_{b4bc} & \\ -sM_{b1bc} & -sM_{b2bc} & -sM_{b3bc} & -sM_{b4bc} & \\ 0 & 0 & 0 & 0 & \end{bmatrix} \tag{L.3}$$

$$Z^3_{lvsc} = \begin{bmatrix} -sM_{a1b5} & -sM_{a1b6} & 0 & 0 \\ -R_{b5} + sM_{a1b5} - sM_{b56} - sL_{b5} - sM_{b45} & -R_{b6} + sM_{a1b6} - sL_{b6} - sM_{b56} - sM_{b46} & 0 & 0 \\ sM_{b15} & sM_{b16} & \frac{-1}{sC_{b1}} & 0 \\ sM_{b25} & sM_{b26} & \frac{-1}{sC_{b2}} & 0 \\ sM_{b35} & sM_{b36} & \frac{-1}{sC_{b3}} & 0 \\ sM_{b45} & sM_{b46} & 0 & \frac{-1}{sC_{b4}} \\ R_{b5} + \frac{1}{sC_{b5}} + sL_{b5} & sM_{b56} & 0 & \frac{-1}{sC_{b5}} \\ sM_{b56} & R_{b6} + \frac{1}{sC_{b6}} + sL_{b6} & 0 & \frac{-1}{sC_{b6}} \\ 0 & 0 & \frac{1}{sC_{b1}} + \frac{1}{sC_{b2}} + \frac{1}{sC_{b3}} + \frac{1}{sC_{b13}} & 0 \\ \frac{-1}{sC_{b5}} & \frac{-1}{sC_{b6}} & 0 & \frac{1}{sC_{b4}} + \frac{1}{sC_{b5}} + \frac{1}{sC_{b6}} + \frac{1}{sC_{b46}} \\ 0 & 0 & \frac{-1}{sC_{b13}} & \frac{-1}{sC_{b46}} \\ sM_{b5bc} & sM_{b6bc} & 0 & 0 \\ -sM_{b5bc} & -sM_{b6bc} & 0 & 0 \\ 0 & 0 & 0 & 0 \end{bmatrix} \tag{L.4}$$

$$Z^4_{lvsc} = \begin{bmatrix} 0 & -sM_{a1bc} & sM_{a1bc} & \frac{-1}{sC_{a10}} \\ 0 & sM_{a1bc} - sM_{b6bc} - sM_{b5bc} - sM_{b4bc} & -sM_{a1bc} + sM_{b6bc} + sM_{b5bc} + sM_{b4bc} & 0 \\ 0 & sM_{b1bc} & -sM_{b1bc} & 0 \\ 0 & sM_{b2bc} & -sM_{b2bc} & 0 \\ 0 & sM_{b3bc} & -sM_{b3bc} & 0 \\ 0 & sM_{b4bc} & -sM_{b4bc} & 0 \\ 0 & sM_{b5bc} & -sM_{b5bc} & 0 \\ 0 & sM_{b6bc} & -sM_{b6bc} & 0 \\ \frac{-1}{sC_{b13}} & 0 & 0 & 0 \\ \frac{-1}{sC_{b46}} & 0 & 0 & 0 \\ \frac{1}{sC_{b13}} + \frac{1}{sC_{b46}} + \frac{1}{sC_{b10}} & 0 & \frac{-1}{sC_{b10}} & 0 \\ 0 & R_c + sL_c & -R_c - sL_c & 0 \\ \frac{-1}{sC_{b10}} & -R_c - sL_c & \frac{1}{sC_{b10}} + R_c + sL_c & 0 \\ 0 & 0 & 0 & \frac{-1}{sC_{a10}} \end{bmatrix} \tag{L.5}$$

$$Z_{lvsc} = \begin{bmatrix} Z^1_{lvsc} & Z^2_{lvsc} & Z^3_{lvsc} & Z^4_{lvsc} \end{bmatrix} \tag{L.6}$$

$$Z^{1}_{lvoc} = \begin{bmatrix} \frac{1}{sC_{a10}} + R_{a1} + sL_{a1} & -R_{a1} - sL_{a1} + sM_{a1b4} + sM_{a1b5} + sM_{a1b6} \\ -R_{a1} - sL_{a1} + sM_{a1b6} + sM_{a1b5} + sM_{a1b4} & Z_{22} \\ -sM_{a1b1} & sM_{a1b1} - sM_{b14} - sM_{b15} - sM_{b16} \\ -sM_{a1b2} & sM_{a1b2} - sM_{b24} - sM_{b25} - sM_{b26} \\ -sM_{a1b3} & sM_{a1b3} - sM_{b34} - sM_{b35} - sM_{b36} \\ -sM_{a1b4} & -R_{b4} - sL_{b4} + sM_{a1b4} - sM_{b45} - sM_{b46} \\ -sM_{a1b5} & -R_{b5} - sL_{b5} + sM_{a1b5} - sM_{b45} - sM_{b56} \\ -sM_{a1b6} & -R_{b6} - sL_{b6} + sM_{a1b6} - sM_{b46} - sM_{b56} \\ 0 & 0 \\ 0 & 0 \\ 0 & 0 \\ -sM_{a1bc} & sM_{a1bc} - sM_{b4bc} - sM_{b5bc} - sM_{b6bc} \\ \frac{1}{sC_{a10}} & 0 \end{bmatrix} \tag{L.7}$$

$$Z_{22} = \frac{1}{sC_{ab1}} + R_{a1} + R_{b6} + R_{b5} + R_{b4} + sL_{a1} - sM_{a1b4} - sM_{a1b5} - sM_{a1b6} + sL_{b6} - sM_{a1b6} + sM_{b46} + sM_{b56} + sL_{b5} - sM_{a1b5} + sM_{b45} + sM_{b56} + sL_{b4} - sM_{a1b4} + sM_{b45} + sM_{b46} \tag{L.8}$$

$$Z^{2}_{lvoc} = \begin{bmatrix} -sM_{a1b1} & -sM_{a1b2} & -sM_{a1b3} & & \\ sM_{a1b1} - sM_{b16} - sM_{b15} - sM_{b14} & sM_{a1b2} - sM_{b26} - sM_{b25} - sM_{b24} & sM_{a1b3} - sM_{b36} - sM_{b35} - sM_{b34} & -R_{b4} + sM_{a1b4} - sM_{b46} - sM_{b45} - sL_{b4} & \\ R_{b1} + \frac{1}{sC_{b1}} + sL_{b1} & sM_{b12} & sM_{b13} & sM_{b14} & \\ sM_{b12} & R_{b2} + \frac{1}{sC_{b2}} + sL_{b2} & sM_{b23} & sM_{b24} & \\ sM_{b13} & sM_{b23} & R_{b3} + \frac{1}{sC_{b3}} + sL_{b3} & sM_{b34} & \\ sM_{b14} & sM_{b24} & sM_{b34} & R_{b4} + \frac{1}{sC_{b4}} + sL_{b4} & \\ sM_{b15} & sM_{b25} & sM_{b35} & sM_{b45} & \\ sM_{b16} & sM_{b26} & sM_{b36} & sM_{b46} & sM_{b56} \\ \frac{-1}{sC_{b1}} & \frac{-1}{sC_{b2}} & \frac{-1}{sC_{b3}} & 0 & \\ 0 & 0 & 0 & \frac{-1}{sC_{b4}} & \\ 0 & 0 & 0 & 0 & \\ sM_{b1bc} & sM_{b2bc} & sM_{b3bc} & sM_{b4bc} & \\ 0 & 0 & 0 & 0 & \end{bmatrix} \tag{L.9}$$

$$Z_{lvoc}^3 = \begin{bmatrix} -sM_{a1b5} & -sM_{a1b6} & 0 & 0 \\ -R_{b5} + sM_{a1b5} - sM_{b56} - sL_{b5} - sM_{b45} & -R_{b6} + sM_{a1b6} - sL_{b6} - sM_{b56} - sM_{b46} & 0 & 0 \\ sM_{b15} & sM_{b16} & \frac{-1}{sC_{b1}} & 0 \\ sM_{b25} & sM_{b26} & \frac{-1}{sC_{b2}} & 0 \\ sM_{b35} & sM_{b36} & \frac{-1}{sC_{b3}} & 0 \\ sM_{b45} & sM_{b46} & 0 & \frac{-1}{sC_{b4}} \\ R_{b5} + \frac{1}{sC_{b5}} + sL_{b5} & sM_{b56} & 0 & \frac{-1}{sC_{b5}} \\ sM_{b56} & R_{b6} + \frac{1}{sC_{b6}} + sL_{b6} & 0 & \frac{-1}{sC_{b6}} \\ 0 & 0 & \frac{1}{sC_{b1}} + \frac{1}{sC_{b2}} + \frac{1}{sC_{b3}} + \frac{1}{sC_{b13}} & 0 \\ \frac{-1}{sC_{b5}} & \frac{-1}{sC_{b6}} & 0 & \frac{1}{sC_{b4}} + \frac{1}{sC_{b5}} + \frac{1}{sC_{b6}} + \frac{1}{sC_{b46}} \\ 0 & 0 & \frac{-1}{sC_{b13}} & \frac{-1}{sC_{b46}} \\ sM_{b5bc} & sM_{b6bc} & 0 & 0 \\ 0 & 0 & 0 & 0 \end{bmatrix} \tag{L.10}$$

$$Z_{lvoc}^4 = \begin{bmatrix} 0 & -sM_{a1bc} & \frac{-1}{sC_{a10}} \\ 0 & sM_{a1bc} - sM_{b6bc} - sM_{b5bc} - sM_{b4bc} & 0 \\ 0 & sM_{b1bc} & 0 \\ 0 & sM_{b2bc} & 0 \\ 0 & sM_{b3bc} & 0 \\ 0 & sM_{b4bc} & 0 \\ 0 & sM_{b5bc} & 0 \\ 0 & sM_{b6bc} & 0 \\ \frac{-1}{sC_{b13}} & 0 & 0 \\ \frac{-1}{sC_{b46}} & 0 & 0 \\ \frac{1}{sC_{b13}} + \frac{1}{sC_{b46}} + \frac{1}{sC_{b10}} & 0 & 0 \\ 0 & R_c + sL_c & 0 \\ 0 & 0 & \frac{-1}{sC_{a10}} \end{bmatrix} \tag{L.11}$$

$$Z_{lvoc} = \begin{bmatrix} Z_{lvoc}^1 & Z_{lvoc}^2 & Z_{lvoc}^3 & Z_{lvoc}^4 \end{bmatrix} \tag{L.12}$$

$$Z_{hvsc}^{1} = \begin{bmatrix} \frac{1}{sC_{a10}} + R_{a1} + sL_{a1} & -R_{a1} - sL_{a1} + sM_{a1b4} + sM_{a1b5} + sM_{a1b6} \\ -R_{a1} - sL_{a1} + sM_{a1b6} + sM_{a1b5} + sM_{a1b4} & Z_{22} \\ -sM_{a1b1} & sM_{a1b1} - sM_{b14} - sM_{b15} - sM_{b16} \\ -sM_{a1b2} & sM_{a1b2} - sM_{b24} - sM_{b25} - sM_{b26} \\ -sM_{a1b3} & sM_{a1b3} - sM_{b34} - sM_{b35} - sM_{b36} \\ -sM_{a1b4} & -R_{b4} - sL_{b4} + sM_{a1b4} - sM_{b45} - sM_{b46} \\ -sM_{a1b5} & -R_{b5} - sL_{b5} + sM_{a1b5} - sM_{b45} - sM_{b56} \\ -sM_{a1b6} & -R_{b6} - sL_{b6} + sM_{a1b6} - sM_{b46} - sM_{b56} \\ 0 & 0 \\ 0 & 0 \\ 0 & 0 \\ -sM_{a1bc} & sM_{a1bc} - sM_{b4bc} - sM_{b5bc} - sM_{b6bc} \\ \frac{1}{sC_{a10}} & 0 \\ sM_{a1bc} & -sM_{a1bc} + sM_{b4bc} + sM_{b5bc} + sM_{b6bc} \end{bmatrix} \tag{L.13}$$

$$Z_{22} = \frac{1}{sC_{ab1}} + R_{a1} + R_{b6} + R_{b5} + R_{b4} + sL_{a1} - sM_{a1b4} - sM_{a1b5} - sM_{a1b6} + sL_{b6} - sM_{a1b6} + sM_{b46} + sM_{b56} + sL_{b5} - sM_{a1b5} + sM_{b45} + sM_{b56} + sL_{b4} - sM_{a1b4} + sM_{b45} + sM_{b46} \tag{L.14}$$

$$Z_{hvsc}^{2} = \begin{bmatrix} -sM_{a1b1} & -sM_{a1b2} & -sM_{a1b3} & & \\ sM_{a1b1} - sM_{b16} - sM_{b15} - sM_{b14} & sM_{a1b2} - sM_{b26} - sM_{b25} - sM_{b24} & sM_{a1b3} - sM_{b36} - sM_{b35} - sM_{b34} & -R_{b4} + sM_{a1b4} - sM_{b46} - sM_{b45} - sL_{b4} & \\ R_{b1} + \frac{1}{sC_{b1}} + sL_{b1} & sM_{b12} & sM_{b13} & sM_{b14} & \\ sM_{b12} & R_{b2} + \frac{1}{sC_{b2}} + sL_{b2} & sM_{b23} & sM_{b24} & \\ sM_{b13} & sM_{b23} & R_{b3} + \frac{1}{sC_{b3}} + sL_{b3} & sM_{b34} & \\ sM_{b14} & sM_{b24} & sM_{b34} & R_{b4} + \frac{1}{sC_{b4}} + sL_{b4} & \\ sM_{b15} & sM_{b25} & sM_{b35} & sM_{b45} & \\ sM_{b16} & sM_{b26} & sM_{b36} & sM_{b46} & sM_{b56} \\ \frac{-1}{sC_{b1}} & \frac{-1}{sC_{b2}} & \frac{-1}{sC_{b3}} & 0 & \\ 0 & 0 & 0 & \frac{-1}{sC_{b4}} & \\ 0 & 0 & 0 & 0 & \\ sM_{b1bc} & sM_{b2bc} & sM_{b3bc} & sM_{b4bc} & \\ 0 & 0 & 0 & 0 & \\ -sM_{b1bc} & -sM_{b2bc} & -sM_{b3bc} & -sM_{b4bc} & \end{bmatrix} \tag{L.15}$$

$$Z^3_{hvsc} = \begin{bmatrix} -sM_{a1b5} & -sM_{a1b6} & 0 & 0 \\ -R_{b5} + sM_{a1b5} - sM_{b56} - sL_{b5} - sM_{b45} & -R_{b6} + sM_{a1b6} - sL_{b6} - sM_{b56} - sM_{b46} & 0 & 0 \\ sM_{b15} & sM_{b16} & \frac{-1}{sC_{b1}} & 0 \\ sM_{b25} & sM_{b26} & \frac{-1}{sC_{b2}} & 0 \\ sM_{b35} & sM_{b36} & \frac{-1}{sC_{b3}} & 0 \\ sM_{b45} & sM_{b46} & 0 & \frac{-1}{sC_{b4}} \\ R_{b5} + \frac{1}{sC_{b5}} + sL_{b5} & sM_{b56} & 0 & \frac{-1}{sC_{b5}} \\ sM_{b56} & R_{b6} + \frac{1}{sC_{b6}} + sL_{b6} & 0 & \frac{-1}{sC_{b6}} \\ 0 & 0 & \frac{1}{sC_{b1}} + \frac{1}{sC_{b2}} + \frac{1}{sC_{b3}} + \frac{1}{sC_{b13}} & 0 \\ \frac{-1}{sC_{b5}} & \frac{-1}{sC_{b6}} & 0 & \frac{1}{sC_{b4}} + \frac{1}{sC_{b5}} + \frac{1}{sC_{b6}} + \frac{1}{sC_{b46}} \\ 0 & 0 & \frac{-1}{sC_{b13}} & \frac{-1}{sC_{b46}} \\ sM_{b5bc} & sM_{b6bc} & 0 & 0 \\ 0 & 0 & 0 & 0 \\ -sM_{b5bc} & -sM_{b6bc} & 0 & 0 \end{bmatrix} \tag{L.16}$$

$$Z^4_{hvsc} = \begin{bmatrix} 0 & -sM_{a1bc} & \frac{-1}{sC_{a10}} & sM_{a1bc} \\ 0 & sM_{a1bc} - sM_{b6bc} - sM_{b5bc} - sM_{b4bc} & 0 & -sM_{a1bc} + sM_{b6bc} + sM_{b5bc} + sM_{b4bc} \\ 0 & sM_{b1bc} & 0 & -sM_{b1bc} \\ 0 & sM_{b2bc} & 0 & -sM_{b2bc} \\ 0 & sM_{b3bc} & 0 & -sM_{b3bc} \\ 0 & sM_{b4bc} & 0 & -sM_{b4bc} \\ 0 & sM_{b5bc} & 0 & -sM_{b5bc} \\ 0 & sM_{b6bc} & 0 & -sM_{b6bc} \\ \frac{-1}{sC_{b13}} & 0 & 0 & 0 \\ \frac{-1}{sC_{b46}} & 0 & 0 & 0 \\ \frac{1}{sC_{b13}} + \frac{1}{sC_{b46}} + \frac{1}{sC_{b10}} & 0 & 0 & \frac{-1}{sC_{b10}} \\ 0 & R_c + sL_c & 0 & -R_c - sL_c \\ 0 & 0 & \frac{-1}{sC_{a10}} & 0 \\ \frac{-1}{sC_{b10}} & -R_c - sL_c & 0 & \frac{1}{sC_{b10}} + R_c + sL_c \end{bmatrix} \tag{L.17}$$

$$Z_{hvsc} = \begin{bmatrix} Z^1_{hvsc} & Z^2_{hvsc} & Z^3_{hvsc} & Z^4_{hvsc} \end{bmatrix} \tag{L.18}$$

$$Z^1_{hvoc} = \begin{bmatrix} \frac{1}{sC_{a10}} + R_{a1} + sL_{a1} & -R_{a1} - sL_{a1} + sM_{a1b4} + sM_{a1b5} + sM_{a1b6} \\ -R_{a1} - sL_{a1} + sM_{a1b6} + sM_{a1b5} + sM_{a1b4} & Z_{22} \\ -sM_{a1b1} & sM_{a1b1} - sM_{b14} - sM_{b15} - sM_{b16} \\ -sM_{a1b2} & sM_{a1b2} - sM_{b24} - sM_{b25} - sM_{b26} \\ -sM_{a1b3} & sM_{a1b3} - sM_{b34} - sM_{b35} - sM_{b36} \\ -sM_{a1b4} & -R_{b4} - sL_{b4} + sM_{a1b4} - sM_{b45} - sM_{b46} \\ -sM_{a1b5} & -R_{b5} - sL_{b5} + sM_{a1b5} - sM_{b45} - sM_{b56} \\ -sM_{a1b6} & -R_{b6} - sL_{b6} + sM_{a1b6} - sM_{b46} - sM_{b56} \\ 0 & 0 \\ 0 & 0 \\ 0 & 0 \\ -sM_{a1bc} & sM_{a1bc} - sM_{b4bc} - sM_{b5bc} - sM_{b6bc} \\ sM_{a1bc} & -sM_{a1bc} + sM_{b4bc} + sM_{b5bc} + sM_{b6bc} \end{bmatrix} \tag{L.19}$$

$$Z_{22} = \frac{1}{sC_{ab1}} + R_{a1} + R_{b6} + R_{b5} + R_{b4} + sL_{a1} - sM_{a1b4} - sM_{a1b5} - sM_{a1b6} + sL_{b6} - sM_{a1b6} + sM_{b46} + sM_{b56} + sL_{b5} - sM_{a1b5} + sM_{b45} + sM_{b56} + sL_{b4} - sM_{a1b4} + sM_{b45} + sM_{b46} \tag{L.20}$$

$$Z^2_{hvoc} = \begin{bmatrix} -sM_{a1b1} & -sM_{a1b2} & -sM_{a1b3} & & \\ sM_{a1b1} - sM_{b16} - sM_{b15} - sM_{b14} & sM_{a1b2} - sM_{b26} - sM_{b25} - sM_{b24} & sM_{a1b3} - sM_{b36} - sM_{b35} - sM_{b34} & -R_{b4} + sM_{a1b4} - sM_{b46} - sM_{b45} - sL_{b4} & \\ R_{b1} + \frac{1}{sC_{b1}} + sL_{b1} & sM_{b12} & sM_{b13} & sM_{b14} & \\ sM_{b12} & R_{b2} + \frac{1}{sC_{b2}} + sL_{b2} & sM_{b23} & sM_{b24} & \\ sM_{b13} & sM_{b23} & R_{b3} + \frac{1}{sC_{b3}} + sL_{b3} & sM_{b34} & \\ sM_{b14} & sM_{b24} & sM_{b34} & R_{b4} + \frac{1}{sC_{b4}} + sL_{b4} & \\ sM_{b15} & sM_{b25} & sM_{b35} & sM_{b45} & \\ sM_{b16} & sM_{b26} & sM_{b36} & sM_{b46} & sM_{b56} \\ \frac{-1}{sC_{b1}} & \frac{-1}{sC_{b2}} & \frac{-1}{sC_{b3}} & 0 & \\ 0 & 0 & 0 & \frac{-1}{sC_{b4}} & \\ 0 & 0 & 0 & 0 & \\ sM_{b1bc} & sM_{b2bc} & sM_{b3bc} & sM_{b4bc} & \\ -sM_{b1bc} & -sM_{b2bc} & -sM_{b3bc} & -sM_{b4bc} & \end{bmatrix} \tag{L.21}$$

$$Z_{hvoc}^{3} = \begin{bmatrix} -sM_{a1b5} & -sM_{a1b6} & 0 & 0 \\ -R_{b5} + sM_{a1b5} - sM_{b56} - sL_{b5} - sM_{b45} & -R_{b6} + sM_{a1b6} - sL_{b6} - sM_{b56} - sM_{b46} & 0 & 0 \\ sM_{b15} & sM_{b16} & \frac{-1}{sC_{b1}} & 0 \\ sM_{b25} & sM_{b26} & \frac{-1}{sC_{b2}} & 0 \\ sM_{b35} & sM_{b36} & \frac{-1}{sC_{b3}} & 0 \\ sM_{b45} & sM_{b46} & 0 & \frac{-1}{sC_{b4}} \\ R_{b5} + \frac{1}{sC_{b5}} + sL_{b5} & sM_{b56} & 0 & \frac{-1}{sC_{b5}} \\ sM_{b56} & R_{b6} + \frac{1}{sC_{b6}} + sL_{b6} & 0 & \frac{-1}{sC_{b6}} \\ 0 & 0 & \frac{1}{sC_{b1}} + \frac{1}{sC_{b2}} + \frac{1}{sC_{b3}} + \frac{1}{sC_{b13}} & 0 \\ \frac{-1}{sC_{b5}} & \frac{-1}{sC_{b6}} & 0 & \frac{1}{sC_{b4}} + \frac{1}{sC_{b5}} + \frac{1}{sC_{b6}} + \frac{1}{sC_{b46}} \\ 0 & 0 & \frac{-1}{sC_{b13}} & \frac{-1}{sC_{b46}} \\ sM_{b5bc} & sM_{b6bc} & 0 & 0 \\ -sM_{b5bc} & -sM_{b6bc} & 0 & 0 \end{bmatrix} \tag{L.22}$$

$$Z_{hvoc}^{4} = \begin{bmatrix} 0 & -sM_{a1bc} & sM_{a1bc} \\ 0 & sM_{a1bc} - sM_{b6bc} - sM_{b5bc} - sM_{b4bc} & -sM_{a1bc} + sM_{b6bc} + sM_{b5bc} + sM_{b4bc} \\ 0 & sM_{b1bc} & -sM_{b1bc} \\ 0 & sM_{b2bc} & -sM_{b2bc} \\ 0 & sM_{b3bc} & -sM_{b3bc} \\ 0 & sM_{b4bc} & -sM_{b4bc} \\ 0 & sM_{b5bc} & -sM_{b5bc} \\ 0 & sM_{b6bc} & -sM_{b6bc} \\ \frac{-1}{sC_{b13}} & 0 & 0 \\ \frac{-1}{sC_{b46}} & 0 & 0 \\ \frac{1}{sC_{b13}} + \frac{1}{sC_{b46}} + \frac{1}{sC_{b10}} & 0 & \frac{-1}{sC_{b10}} \\ 0 & R_c + sL_c & -R_c - sL_c \\ \frac{-1}{sC_{b10}} & -R_c - sL_c & \frac{1}{sC_{b10}} + R_c + sL_c \end{bmatrix} \tag{L.23}$$

$$Z_{hvoc} = \begin{bmatrix} Z_{hvoc}^{1} & Z_{hvoc}^{2} & Z_{hvoc}^{3} & Z_{hvoc}^{4} \end{bmatrix} \tag{L.24}$$

Appendix M

Case Study 3: Analytical Validation

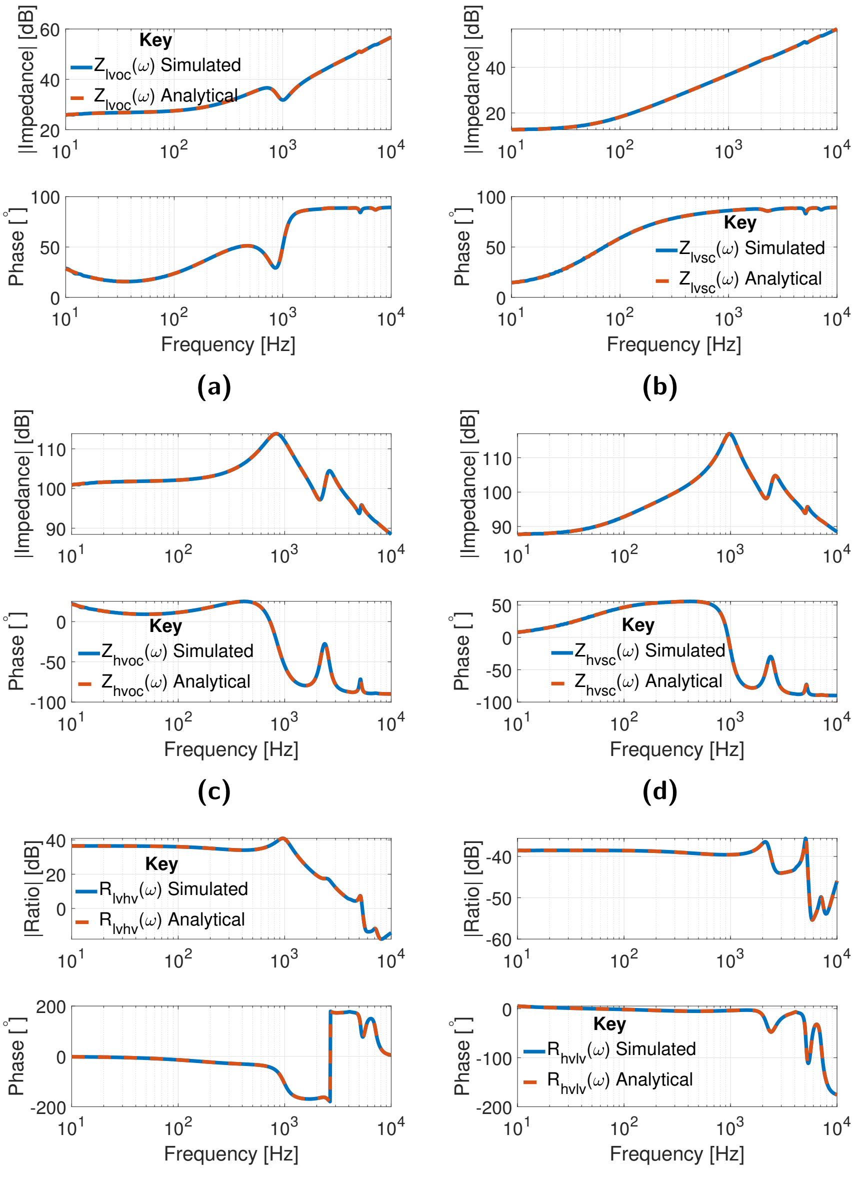

(a) **(b)**

(c) **(d)**

(e) **(f)**

Figure M.1: Magnitude and phase responses of **(a)**$Z_{lvoc}(\omega)$, **(b)**$Z_{lvsc}(\omega)$, **(c)**$Z_{hvoc}(\omega)$, **(d)**$Z_{hvsc}(\omega)$, **(e)**$R_{lvhv}(\omega)$ and **(f)**$R_{hvlv}(\omega)$ obtained analytically and through simulated PRIS perturbation of the model presented in Fig. 5.18 for a random set of parameters.